Development and characterisation of affinity devices for cell detection and separation

William Bowen

Chemical Engineering, Loughborough

A thesis submitted in partial fulfilment of the requirements for the award of Doctor of Philosophy at Loughborough University

February 2015

Loughborough University

.

Certificate of Originality

Thesis Access Conditions and Deposit Agreement

Students should consult the guidance notes on the electronic thesis deposit and the access conditions in the University's Code of Practice on Research Degree Programmes

Author……..……..

Title……..

I [Please insert name and address], "the Depositor",

would like to deposit [Please insert title of dissertation], hereafter referred to as the "Work", once it has successfully been examined in Loughborough University Institutional Repository

Status of access OPEN / RESTRICTED / CONFIDENTIAL

Moratorium Period……years, ending……../……20…….

Status of access approved by (CAPITALS):……

Supervisor (Signature)……..

School of……

Author's Declaration *I confirm the following :*

CERTIFICATE OF ORIGINALITY

This is to certify that I am responsible for the work submitted in this thesis, that the original work is my own except as specified in acknowledgements or in footnotes, and that neither the thesis nor the original work therein has been submitted to this or any other institution for a degree

NON-EXCLUSIVE RIGHTS

The licence rights granted to Loughborough University Institutional Repository through this agreement are entirely non-exclusive and royalty free. I am free to publish the Work in its present version or future versions elsewhere. I agree that Loughborough University Institutional Repository administrators or any third party with whom Loughborough University Institutional Repository has an agreement to do so may, without changing content, convert the Work to any medium or format for the purpose of future preservation and accessibility.

DEPOSIT IN LOUGHBOROUGH UNIVERSITY INSTITUTIONAL REPOSITORY

I understand that open access work deposited in Loughborough University Institutional Repository will be accessible to a wide variety of people and institutions - including automated agents - via the

.

World Wide Web. An electronic copy of my thesis may also be included in the British Library Electronic Theses On-line System (EThOS).

I understand that once the Work is deposited, a citation to the Work will always remain visible. Removal of the Work can be made after discussion with Loughborough University Institutional Repository, who shall make best efforts to ensure removal of the Work from any third party with whom Loughborough University Institutional Repository has an agreement. Restricted or Confidential access material will not be available on the World Wide Web until the moratorium period has expired.

- That I am the author of the Work and have the authority to make this agreement and to hereby give Loughborough University Institutional Repository administrators the right to make available the Work in the way described above.

- That I have exercised reasonable care to ensure that the Work is original, and does not to the best of my knowledge break any UK law or infringe any third party's copyright or other Intellectual Property Right. I have read the University's guidance on third party copyright material in theses.

- The administrators of Loughborough University Institutional Repository do not hold any obligation to take legal action on behalf of the Depositor, or other rights holders, in the event of breach of Intellectual Property Rights, or any other right, in the material deposited.

*The statement below shall apply to **ALL** copies:*

.

Author's signature……..Date……..……

user's declaration: for signature during any Moratorium period (Not Open work): ***I undertake to uphold the above conditions:***			
Date	Name (CAPITALS)	Signature	Address

.

Abstract

This thesis seeks to demonstrate technologies capable of improving the purity of pluripotent-derived cells. Such cells offer an enormous opportunity for medical science. However, it is anticipated that a higher proportion of undifferentiated pluripotent cells will remain when manufacturing at scale. As indicated in the literature, the *in vivo* transplantation of undifferentiated cells is a threat to patient safety and is considered a limiting factor for large-scale manufacture.

Pluripotent undifferentiated cells can be identified and removed based on an affinity interaction with the SSEA-4 antigen, which is down-regulated on differentiated cells. Using CD20+ and CD20- (HLA-A2+) lymphocyte cells as a cost-effective alternative, where the CD20+ cells are target impurities and the HLA-A2+ cells are product-designated cells, this thesis presents two technologies to minimise the proportion of undifferentiated cells during manufacture. These technologies rely upon shear stress-induced affinity separation to differentiate between cells with and without target antigens. A small-scale model is used to identify a range of shear stresses (0 – 25 dynes/cm^2) with which these differences can be elucidated. These technologies are:

(1) a quartz crystal microbalance (QCM) biosensor to detect pluripotent cell differentiation over a multi-day period, particularly during process development. The limit of quantitation (LoQ) was estimated to be 5,000 cells, which would enable the measurement of target cell purities in excess of 4 %. Findings provide the basis for such a system, but also highlight the technical challenges of development, in particular variability.

.

(2) two affinity membranes (hollow fibre and flat sheet) were used to deplete cells positive for the target antigen, demonstrating a possible downstream-purification tool in instances where clinical purity does not suffice. The shear stress-induced detachment of adsorbed cells incubated for 30 minutes was investigated over 1 – 25 dynes/cm^2 and 1 – 10 dynes/cm^2 for the hollow fibre and flat sheet membranes respectively. Measured output included cell purity, which showed an increase in the relative change in purity (RCP) of 0.2 – 0.5 for the hollow fibre modules at 5 dynes/cm^2 (n = 5) and was as high as 11.8 at 10 dynes/cm^2 for the flat sheet membrane cassette (n = 1). A loss of cell membrane integrity, where up to 5 % in hollow fibres and up to 55 % in the flat sheet membrane were observed.

.

Acknowledgements

First and foremost, I must thank the following people who have provided a great deal of help along the way:

Especially helpful have been Tony Eyre, Monica Pietrzak, Rob Bentham and David Smith for helping to make things run smoothly in the Chemical engineering department. Likewise, the same gratitude must go to Kulvindar Sikand, Amit Chandra and Paul Hoard in the Centre for Biological Engineering.

Much appreciation should also go to Patricia Cropper and David Grandy at the Loughborough Materials Centre for their help in using XPS and AFM instrumentation.

I must also express my gratitude to Dr Peter Levison at Pall Life Sciences for guidance, encouragement and technical advice. I am also greatly indebted to Pall Life Sciences for the supply of membrane materials and constructs fundamental to this project.

As a supervisor, I must also thank Dr Eirini Theodosiou for having faith in me, as well as providing encouragement and valuable advice when times were very hard. Likewise, I must also thank Professor Christopher Hewitt and Dr Karen Coopman for providing encouragement, feedback and guidance. Gratitude must also go to Dr Andrew Picken for his biological insight and helpful advice, not to mention taking the time out to read this thesis.

Lastly, I must thank my family and friends for their consistent, unwavering support.

.

Contents

. 1

Thesis Access Conditions and Deposit Agreement 2

Chapter 1: Literature review 20

1.1. Cell therapies 20

1.2. Types of cell therapies 20

Chapter Scope 22

1.3. Regulatory constraints 22

1.4. Defining a cell therapy product 23

1.5. Cost of goods 25

1.6. Manufacturing process 26

1.6.1. Upstream processing 27

1.6.1.1. Tissue acquisition and primary cell isolation 27

1.6.1.2. Cell expansion 28

1.6.1.3. Differentiation 32

1.6.2. Downstream processing 33

1.6.2.1. Harvesting, volume reduction and washing 34

1.6.2.2. Purification 36

1.6.2.3. Formulation, filling and cryopreservation 37

1.7. Opportunities for new technologies 38

1.7.1. Technologies to control cell purity 40

1.7.1.1. Biosensors 41

1.7.1.2. Elimination and removal of unwanted cells 47

1.8. Technological approach 53

1.9. Biological impact 55

1.10. Theoretical considerations 57

1.10.1. Cell transport 57

1.10.2. Cell-substrate interactions 58

1.10.3. Creating an affinity support matrix 60

1.10.4. Cell adsorption 62

1.10.5. Force-induced cell detachment 62

1.10.6. Calculating shear stress 63

1.10.7. Force acting on cells 64

.

1.10.8. Equilibrium dissociation constant 64
1.10.9. Cell adhesion strength 66
1.10.10. Detachment mechanisms 69
1.11. Summary 69
Chapter 2. Flow tube model 71
2.1. Introduction 71
2.2. Materials and methods 74
2.2.1. Glass surface chemical modification 74
2.2.2. Cleaning 74
2.2.3. Amination 74
2.2.4. Aldehyde functionalization 75
2.2.5. Protein adsorption 75
2.2.5.1. Recombinant Protein A (rPrA) and bovine serum albumin (BSA) 75
2.2.5.2. IgG antibody adsorption 76
2.2.5.3. Glass flow tube modification 76
2.2.5.4. Chemical modification 76
2.2.5.5. PrA and BSA protein adsorption 77
2.2.6. Cell detachment studies 77
2.2.6.1. Process setup 77
2.2.6.2. Cell culture 78
2.2.6.3. Cell detachment 79
2.3. Theoretical considerations 81
2.3.1. Shear stress 81
2.4. Analysis and characterisation 82
2.4.1. Atomic force microscopy 82
2.4.2. X-ray photoelectron microscopy (XPS) 82
2.4.3. TNBS assay 83
2.4.4. Silver mirror test 83
2.4.5. BCA assay 84
2.4.6. Contact angle 84
2.4.7. BET surface area 84
2.4.8. Fluorescent IgG staining and binding to cells 85
2.4.9. Cell counting 85
2.5. Results and Discussion 85

.

2.5.1. Surface analysis 87
2.5.2. Chemical group functionality measurements 90
2.5.3. Static protein binding studies 91
2.5.4. IgG binding capacity 92
2.5.5. IgG binding to cells 93
2.5.6. Cell detachment studies 94
2.5.7. Counting adherent cells 95
2.5.8. Cell detachment as a function of shear stress 96
2.5.9. Cell detachment in real time 101
2.5.10. Cell viability 103
2.5.11. Projected performances 104
2.5.12. Large-scale separation device 105
2.5.13. Biosensor development 108
2.6. Conclusions 116
Chapter 3. Biosensor development 118
3.1. Introduction 118
3.2. Materials and methods 120
3.2.1. Chemical modification 120
3.2.2. System operation 121
3.2.3. Surface characterisation 121
3.2.3.1. Contact angle measurements 121
3.2.3.2. Surface charge 121
3.2.4. Protein adsorption 121
3.2.5. Cell adsorption studies 122
3.2.5.1. Cell culture 122
3.2.5.2. Cell adsorption 123
3.3. Theoretical considerations 123
3.4. Results 124
3.4.1. Computational modelling 124
3.4.2. Surface characterisation 125
3.4.3. Protein binding 126
3.4.4. Cell binding 129
3.5. Discussion 130
3.5.1. Surface hydrophobicity and charge 130

.

3.5.2. Protein L and Protein A 131
3.5.3. Cell adsorption 131
3.5.4. Quantifying adherent cells 132
3.5.5. System feasibility 136
3.5.5.1. Operation 137
3.6. Conclusion 141
Chapter 4. Affinity membrane development 143
4.1. Introduction 143
4.2. Materials and methods 144
4.2.1. Chemical modification 145
4.2.1.1. Hollow fibre aldehyde functionalisation 145
4.2.2. Chemical assays 146
4.2.2.1. TNBS 146
4.2.2.2. Silver mirror test 146
4.2.2.3. Fourier Transform Infra-Red (FTIR) spectroscopy 147
4.2.2.4. BCA assay for aldehyde coating efficiency 147
4.2.3. Physical characterisation 147
4.2.3.1. Atomic Force Microscopy 148
4.2.3.2. Environmental scanning electron microscopy (ESEM) 148
4.2.3.3. Field emission scanning electron microscopy (FESEM) 148
4.2.3.4. BET surface area 149
4.2.4. Membrane sample preparation 149
4.2.4.1. Hollow fibres 149
4.2.4.2. Flat sheet microfiltration membrane 151
4.2.5. Hydraulic studies 152
4.2.5.1. Pressure loss 152
4.2.5.2. Hydraulic permeability 153
4.2.6. Protein adsorption 153
4.2.6.1. Hollow fibre membrane 153
4.2.6.2. Flat sheet membrane 156
4.3. Theoretical considerations 157
4.3.1. Hydraulic characterisation 157
4.3.2. Protein adsorption capacities 159
4.3.3. Membrane size calculations 159

.

4.4. Results and discussion 160
4.4.1. Physical 160
4.4.2. Hydraulic properties 164
4.4.3. Chemistry 164
4.4.4. rPrA and BSA protein adsorption densities 167
4.4.5. IgG binding 168
4.4.5.1. Hollow fibre Type 1 modules 169
4.4.5.2. Flat sheet microfiltration membrane 170
4.5. Conclusions 172
Chapter 5. Affinity cell separation 174
5.1. Introduction 174
5.2. Materials and methods 176
5.2.1. Cell preparation 176
5.2.1.1. Cell culture 176
5.2.1.2. Cell harvesting for separation 176
5.2.2. Separation units 177
5.2.2.2. Magnetic Activated Cell Separation (MACS) 177
5.2.2.3. Affinity membrane separation 177
5.2.3. Cell separation 181
5.2.4. Characterisation 182
5.2.4.1. Cell membrane integrity and intracellular staining 182
5.2.4.2. Cell recovery 184
5.2.4.3. Cell purity 184
5.3. Theoretical considerations 186
5.3.1. Hydrodynamic conditions 186
5.4. Results 188
5.4.1. Recovery 188
5.4.2. Purity 189
5.4.3. Cell membrane integrity and intracellular staining 193
5.5. Conclusion 204
Chapter 6. Thesis summary and future work 206
6.1. Thesis output 206
6.1.1. Flow tube model 206
6.1.2. Biosensor 206

.

6.1.3. Separation devices 206
6.2. Improvements and future work 207
6.3. New system design 208
Chapter 7. Appendix 217
Chapter 8. Appendix 226

.

List of Figures

Figure 1-1. Generic cell therapy manufacturing process 26
Figure 1-2. Quartz crystal microbalance biosensor for shear stress-induced affinity cell separation 54
Figure 1-3. Generic cell separation process 55
Figure 1-4. Example of shear stress (shear stress)-induced mechanotransduction 56
Figure 1-5. Cell separation protocol 57
Figure 1-6. Generic antibody structure and labelling sites 61
Figure 1-7. Adhesion strength per receptor present in the contact region (Ft/Rc) asa function of various dissociation constants 66
Figure 1-8. Effect of increasing ligand density and receptor number versus shear stress for a KD value of 10-6 M 68
Figure 1-9. Effect of increasing ligand density and receptor number versus shear stress for a KD value of 10-9 M 68
Figure 2-1. Reaction of cleaned glass with 3-APTES to create an amine-terminated surface 72
Figure 2-2. Reaction of glutaraldehde in the presence of sodium cyanoborohydride to reduce reversible Schiff bases into stable secondary amine bonds 72
Figure 2-3. Immobilisation of rPrA via Schiff base formation and subsequent reduction to create a stable secondary amine bond 72
Figure 2-4. Reaction of immobilised rPrA with IgG-tagged cells 72
Figure 2-5. Unit schematic for cell binding studies; 77
Figure 2-6. High resolution nitrogen 1s scans on cleaned glass, APTES-glass and APTES-glass coated with glutaraldehyde 87
Figure 2-7. High resolution XPS carbon 1s scans on cleaned glass, APTES-glass and APTES-glass coated with glutaraldehyde; 87
Figure 2-8. Contact angles for cleaned glass (A); APTES-treated glass (B) and APTES-glass treated with glutaraldehyde (C) 88
Figure 2-9. AFM images for glass (2 x 2 µm) in a two-dimensional display (A) and a three-dimensional display. 89
Figure 2-10. AFM images for aminated glass (2 x 2 µm) in a two-dimensional display (A) and a three-dimensional display. 89
Figure 2-11. AFM images for aminated glass (20 µm x 20 µm) in a two-dimensional display (A) and a three-dimensional display. 89
Figure 2-12. AFM images for aldehyde-treated aminated glass (2 x 2 µm) in a two-dimensional display (A) and a three-dimensional display. 89
Figure 2-13. Representative staining images for aldehyde functionalities using Tollen's reagent 91
Figure 2-14. Binding saturation curve for IgG adsorption onto rPrA-coupled glass beads 93
Figure 2.15. Fluorescent microscopy images at x10 magnification 94
Figure 2-16. Actual image of adsorbed cells (A) and software-modified image of cells used for cell counting (B) 95
Figure 2-17. Calibration chart comparing software-based counting to manual counting 96
Figure 2-18. HLA-A2+ detachment without CD20+ IgG affinity interaction from rPrA-coupled glass flow tubes 98
Figure 2-19. CD20+ detachment without CD20+ IgG affinity interaction from rPrA-coupled glass flow tubes 98
Figure 2-20. CD20+ detachment with CD20+ IgG affinity interaction from rPrA-coupled glass flow tubes 99
Figure 2-21. CD20 cells exposed to CD20 IgG. 100
Figure 2-22. CD20 cell adhesion without exposure to CD20 IgG. 100

.

Figure 2-23. HLA-A2 cells exposed to CD20 IgG. 100
Figure 2-24. CD20+ cells adsorbed with affinity interactions subjected to a shear stress of 5 dynes/cm^2 101
Figure 2-25. CD20+ cells adsorbed with affinity interactions subjected to a shear stress of 25 dynes/cm^2 101
Figure 2-26. HLA-A2+ cells adsorbed without affinity interactions subjected to a shear stress of 5 dynes/cm^2 102
Figure 2-27. HLA-A2+ cells adsorbed without affinity interactions subjected to a shear stress of 25 dynes/cm^2 102
Figure 2-28. Cells exposed to shear stress undergo changes in morphology 103
Figure 2-29. Projected HLA-A2+ purity as a function of shear stress 108
Figure 2-30. Total number of cells on the surface ($N_{T,n}$) as a function of shear stress 112
Figure 2-31. CD20+ cell purity on the sensor surface as a function of shear stress 113
Figure 2-32. CD20+ cell purity on the sensor surface
Figure 3-1. Key aspects of the QCM system: (A) Gold-coated quartz crystal and (B) QCM system schematic. 119
Figure 3-2. Protein A terminated surface on a gold-coated dS-PEG-OH/-biotin sensor. 122
Figure 3-3. QCM chamber schematic. 124
Figure 3-4. Top-down view of shear stress (A) and pressure (B) on the surface of the QCM chamber 125
Figure 3-5. Side-views of fluid velocity in (A) and (B) inside the QCM chamber 125
Figure 3-6. Contact angle images for (A) cleaned gold and (B) dS-PEG-OH/-biotin treated gold sensors. 126
Figure 3-7. Frequency and dissipation changes vs. time for BSA adsorption. 126
Figure 3-8. Frequency and dissipation changes vs. time for Protein L binding to CD20 IgG-based complex. 128
Figure 3-9. Frequency and dissipation vs. time Protein L binding to CD20 IgG-absent complex. 128
Figure 3-10. Frequency and dissipation vs. time for Protein A binding to CD20 IgG-based complex. 129
Figure 3-11. Frequency and dissipation vs. time for HLA-A2 B-lymphocyte cell binding to IgG complex. 130
Figure 3-12. Frequency and dissipation vs. time for red blood cell binding to IgG complex. 133
Figure 3-13. Output signal generated by difference in cell detachment. 135
Figure 3-14. Example frequency vs. time plot. 136
Figure 3-15. Sampling process for pluripotent cell differentiation towards a cardiomyocyte lineage. 137
Figure 4-1. Basic chemical structures of (A) polyethyleneimine (PEI) (linear chain) and (B) polyethersulfone (PES). 145
Figure 4-2. SEM porosity image analysis. 142
Figure 4-3. Schematic diagrams of constructed hollow fibre modules 150
Figure 4-4. Representative schematic of process setup for TFF cassette and the HFM cartridge characterisation 152
Figure 4-5. Schematic of a Type 1 hollow fibre module with immobilised rPrA for IgG binding capacity evaluation 156
Figure 4-6. Atomic force micrographs of polyethylenimine hollow fibres in (A) 2D and (B) 3D formats. 161
Figure 4-7. Atomic force micrographs of glutaraldehyde-treated polyethylenimine hollow fibres in (A) 2D and (B) 3D formats. 161
Figure 4-8. Atomic force micrographs of polyethersulfone segments in (A) 2D and (B) 3D formats. 161
Figure 4-9. Representative images of hollow fibre membrane surfaces 162

.

Figure 4-10. SEM Cross-sectional images of raw PES membranes 163
Figure 4-11. FTIR spectra for unmodified PEI membrane and aldehyde-functionalised PEI membrane. 165
Figure 4-12. Representative staining images of untreated PEI fibres (A) and (C) and glutaraldehyde-treated fibres (B) and (D) stained with TNBS and Tollen's reagent respectively 166
Figure 4-13. The elution of IgG from both rPrA-coupled (blue) and rPrA-free (red) Type 1 modules over three washes 170
Figure 4-14. IgG binding curve 171
Figure 5-1. Hollow fibre membrane cell separation process 179
Figure 5-2. Flat sheet membrane cell separation process schematic 181
Figure 5-3. Process diagram for cell separation 182
Figure 5-4. Cell staining histograms 185
Figure 5-5. HLA-A2+ cell recovery across tested units 189
Figure 5-6. Scatter plots and histograms for separation devices 191
Figure 5-7. Percent cell uptake of trypan blue 194
Figure 5-8. Scatter plots showing DAPI staining 195
Figure 5-9. Percent cell uptake of DAPI as a function of shear stress 196
Figure 5-10. Scatter plots of B-lymphocyte cells showing VB-48 intensity vs. PI staining intensity before and after magnetic depletion using MACS MS columns 198
Figure 5-11. Scatter plots of gated cells before and after cell separation in hollow fibre and flat sheet membranes over ranges of 1 – 25 and 1 – 10 dynes/cm2 respectively 198
Figure 5-12. Percent cell uptake of 7-AAD as a function of shear stress 199
Figure 5-13. Dissected hollow fibre membrane modules post-separation. 202
Figure 6-1. Individual cartridge components 209
Figure 6-2. Top-down view of basic setup for 10 cartridges 211
Figure 6-3. Cell separation system size and dimensions. 211
Figure 6-4. Operating regime for an individual cartridge. 212
Figure 6-5. Operating regime for 10 cartridges in series. 212
Figure 6-6. System performance projections 214
Figure 6-7. Internal volumes inside the 100 cartridge units 216
Figure 7-1. Calibration chart for rPrA quantification (aldehyde beads) 217
Figure 7-2. Calibration chart for BSA quantification (aldehyde beads) 218
Figure 7-3. TNBS calibration chart 218
Figure 7-4. Comparison of actual purities versus those 220
Figure 7-5. Calibration chart for rPrA quantification (aldehyde hollow fibres) 221
Figure 7-6. Calibration chart for BSA quantification (aldehyde hollow fibres) 222
Figure 7-7. Calibration chart for rPrA quantification (aldehyde PES segments) 222
Figure 7-8. Calibration chart for rPrA quantification (aldehyde PES segments) 223
Figure 7-9. CD20+ cell recovery across tested units 224
Figure 7-10. Individual cell recoveries from hollow fibre membranes 225

.

List of Tables

Table 1-1. Cell Critical Quality Attributes (CQA) 24
Table 1-2. Technology requirements recommended for implementation into a cell therapy manufacturing process 27
Table 1-3. Recommended expansion formats for allogenic mesenchymal stem cell manufacture 30
Table 1-4. Differentiation of pluripotent human cells to cardiomyocytes 33
Table 1-5. Volume reduction and washing technologies for various batch sizes 34
Table 1-6. Cryopreservation technology recommended for various batch sizes 38
Table 1-7. Fluorescent methods for measuring cell purity 43
Table 1-8. Label-free detection for measuring cell purity 45
Table 1-9. Acoustic methods for measuring cell purity 47
Table 1-10. Fluorescence-based cell separation technologies 49
Table 1-11. Magnetic bead separation technologies 50
Table 1-12. Membrane-based separation technologies 51
Table 1-13. Monolith-based cell separation technologies 52
Table 2-1. Cell types and properties 79
Table 2-2. XPS elemental composition of the first 100 nm depth of modified glass slides and contact angle measurements for modified glass slides 87
Table 2-3. Contact angle measurements for chemically modified glass slides 88
Table 2-4. Surface roughness for modified glass slides using AFM 88
Table 2-5. Number of APTES deposits on APTES and glutaraldehyde-treated APTES glass beads 91
Table 2-6. Protein binding onto aldehyde-functionalised glass beads 92
Table 2-7. Cell viability assay using trypan blue staining 93
Table 2-8. Projected cell depletion and recovery performance as a function of hydrodynamic force 103
Table 2.9. Projected cell depletion and recovery performance as a function of shear stress. 107
Table 2.10. Parameters used to determine cell purity. 115
Table 3-1. Analyte and component deposition 122
Table 3-2. Cell adsorption study conditions 123
Table 3-3. Contact angle and frequency shifts for cleaned gold and dS-PEG-OH/-biotin (1%) treated gold sensors 126
Table 3-4. Protein L and Protein A analyte responses during QCM-D runs in the presence and absence of CD20 IgG antibody 127
Table 3-5. Signal responses generated by cell adsorption onto IgG coupled surfaces 129
Table 3-6. Protocol proposed for the detection of cells using the QCM biosensor 137
Table 3-7. Performance constraints used to define a biosensor 139
Table 3-8. Limitations and potential solutions for the QCM biosensor 140
Table 4-1. Comparison of hollow fibre and flat sheet microfiltration membranes 145
Table 4-2. Membrane roughness for hollow fibre and flat sheet membrane formats 161
Table 4-3. Measured properties of aldehyde-functionalised hollow fibres 162
Table 4-4. Morphological properties of PES membranes 163
Table 4-5. Pressure drop and hydraulic permeability 164
Table 4-6. Selected bands of diagnostic importance from FTIR spectra of PEI and aldehyde-functionalised PEI 165
Table 4-7. Net change in absorbance between unmodified and aldehyde-functionalised PEI hollow fibre membranes 167
Table 4-8. rPrA and BSA adsorption onto aldehyde-functionalised hollow fibre 168

.

membranes
Table 4-9. rPrA and BSA adsorption onto aldehyde-functionalised PES membranes 168
Table 4-10. Net IgG content for rPrA-coupled aldehyde-functionalised fibres 171
Table 4-11. IgG adsorption capacity data for rPrA-coupled PES membranes 172
Table 5-1. Hollow fibre module properties 178
Table 5-2. Flat sheet membrane properties 180
Table 5-3. Operating parameters for cell separation 181
Table 5-4. Relative change in purity for each collected fraction 192
Table 5-5. HLA-A2 cell purification data for each fraction 193
Table 5-6. Flat sheet membrane purification performance 193
Table 5-7. Cell staining based on VB-48/PI 199
Table 6-1. Separation system properties 209
Table 6-2. System requirements for two cell separation scenarios. 210
Table 6-3. Technology requirements 212
Table 6-4. Cell adsorption capacity per cartridge 214
Table 6-5. Large-scale cell adsorption capacity per 100-cartridge system 215

.

Thesis outline

Chapter 1 (Literature review): provides an overview of the challenges facing the cell therapy manufacturing industry. It also highlights the potential for developing new technology to detect and remove unwanted cell types using immunoaffinity interactions.

Chapter 2 (Flow tube model): shear stresses capable of differentiating between affinity and non-affinity interactive cells are identified in a small-scale glass flow tube model.

Chapter 3 (Biosensor development): presents a quartz crystal microbalance biosensor with a proposed method for measuring cell purity

Chapter 4 (Affinity membrane development): outlines the development and characterisation of two units: a hollow fibre and flat sheet membrane to be used for cell separation studies in Chapter 5.

Chapter 5 (Affinity cell separation): provides a performance comparison of immunoaffinity membranes developed in Chapter 4 and compares their purification performance against the existing benchmark technology.

Chapter 6 (Thesis summary and future work): summarises the work of this thesis and proposes the design of a new system for affinity cell separation.

Chapter 1: Literature review

1.1. Cell therapies

Cell therapies involve the administration of human cells into the body to replace, repair, regenerate, or enhance the function of tissues (Mason and Dunnill, 2009). Their therapeutic effect is thought to exploit the cell's natural ability to differentiate and transdifferentiate into tissue-specific cells, to secrete paracrine factors to stimulate the survival and recovery of localised cells, or to regulate the microenvironment and immune response (Herdrich et al., 2008, Li and Fu, 2012).

The economic potential of the cell therapy industry is also apparent: over 50 publically traded companies operate with a combined market capitalization in excess of $7B as of 2013 with growth projections of 39.5 % (CAGR) from 2015 to 2020. (Mason et al., 2012).

1.2. Types of cell therapies

Two forms of human cell transplantion exist: (1) autologous therapies, where patient-derived cells are re-infused back into the patient with or without manipulation. Autologous transplants involve simple operating processes at the expense of more complex regulatory constraints (Hourd et al., 2014); and (2) allogeneic cell therapies, where cells are derived and expanded from a pool of screened donor material and applied to multiple patients, delivering 'off-the-shelf' capability. Product scale-up in a cost-effective manner whilst identifying and maintaining cell critical quality attributes (CQA) is crucial (Brandenberger, 2011, Rowley, 2012). Several types of cell therapies exist and are detailed accordingly:

T-cells

T-cell therapy is a form of immunotherapy designed to control the immune system response. T-cell transplants aim to induce cytotoxic responses to attack cancer cells via autologous immune enhancement therapy or genetic engineering (O'Garra and Vieira, 2004). T cell therapies have demonstrated clinical efficacy in certain types of leukaemia (Lee et al., 2013), but face significant safety constraints related to cytokine release syndrome (CRS), a life-threatening infusion reaction caused by the release of cytokines by the patient (Davila and Papapetrou, 2014).

Pluripotent stem cells

First reported in 1998 as embryonic stem cells, pluripotent stem cells have the capacity to differentiate into almost any cell type in the body, forming all three germ layers (mesoderm, endoderm and ectoderm) (Thomson et al., 1998). Ethical concerns, owing to the derivation of cells from embryos, were mitigated when induced pluripotent stem cells (iPSCs) were derived through the insertion of four genes (Oct3/4, Sox2, Klf4, c-Myc), leading to the formation of patient-derived immature pluripotent cells with the same therapeutic differentiation ability as embryonic stem cells (Yamanaka and Takahashi, 2011).

Their pluripotent nature allows near endless supplies of these cells to be created making them attractive for pharmacology, disease treatment and drug modelling (Mason and Dunnill, 2009). Clinical efforts thus far have been restricted to very small-scale trials, with teratoma formation due to impure cell populations being a possible drawback (Lebkowski, 2011, Schriebl et al., 2012).

Mesenchymal stem cells

Mesenchymal stem cells are primarily sourced from perivascular niches (Hass et al., 2011). They have the capacity to differentiate into specialised cells, but to a lesser degree than embryonic stem cells (Uccelli et al., 2008). They are thought to have vital roles in the repair of disease or damaged tissue (Shi et al., 2010, Gupta et al., 2012) and express anti-inflammatory and immunomodulatory characteristics (Ma et al., 2014).

Haematopoetic stem cells

Haematopoetic stem cells are primarily derived from bone marrow. Transplants were originally conceived as a treatment for haematological and lyphoid cancers (Mikkola and Orkin, 2006). They have the potential to treat genetic and acquired diseases like automimmune and neurodegenerative disorders as well as cancer (Ness et al., 2005, Atkins and Freedman, 2013).

Chapter Scope

Whilst many different cell therapies exist, this chapter concerns the manufacture of pluripotent stem cells and their derivatives (e.g. pluripotent-derived cardiomyocytes). However, owing to the lack of scalable or commercial ventures using pluripotent stem cells to date, the biological and technical gains made in traditional bioprocessing (Varley and Birch, 1999, Velez-Suberbie et al., 2013) and in non-pluripotent stem cell manufacture (Rafiq et al., 2013) are considered where relevant and opportunities for implementing new technology highlighted.

1.3. Regulatory constraints

Governing bodies in respective nations provide oversight on cell therapy products, the purpose being to regulate the safe, efficacious supply of treatments to patients. For

instance, the Food and Drug Administration (FDA) in the United States, the European Medical Agency (EMA) in Europe and the Ministry of Health, Labour and Welfare (MHLW) in Japan.

Cell therapy manufacture must comply with advanced therapy medicinal product (ATMP) regulations. The regulatory framework for the United States is in Part 1271 of Title 21 of the Code of Federal Regulations (21 CFR Part 127 1): Human Cellular and Tissue-based Products; for the European Union it is in Regulation (EC) No. 1394/2007 on Advanced Therapy Medicinal Products (ATMPs); and for Japan in the Pharmaceutical Affairs Law (PAL); Act regarding Ensuring of Safety of Regenerative Medicine (Regenerative Medicine Law).

The majority of these regulations are adaptations of existing standard measures for pharmaceutical and biological products. Therefore efforts to provide more specific regulatory interpretations relevant to the European Union and United States (Table 1-1) (PAS 93, 2011, PAS83, 2012) and through case studies performed on commercial-grade cell therapy products (Bravery et al., 2013) and FDA recommendations (CFR Title 21) have been made.

1.4. Defining a cell therapy product

Characterisation is a fundamental part of Cell Therapy Product (CTP) development and commercialisation. The purpose is to identify and subsequently quantify cell Critical Quality Attributes (CQA) influential in the therapeutic action of the cell Table 1-1). Such assays need to be developed early – ideally before Phase 2 and absolutely before Phase 3 in compliance with regulatory constraints (PAS93, 2011, Bravery et al., 2013). Quantified CQAs serve as a performance benchmark when investigating the effect of processing conditions on the CTP.

Table 1-1. Cell Critical Quality Attributes (CQA)

Attribute	Description	Characteristics used to define attributes
Safety	Transplanted cells must be free of genetic abnormalities, microbial contamination, as well as undesired cell types[b].	Karyotype; sterility; tumorigenic potential
Purity[a]	The cell population should comprise the maximum number of desirable cells exhibiting the required medicinal action. It should exhibit little or no undesirable cells or non-cell-based contaminants such as biodegradable materials, human- or animal-derived proteins, or enzymatic components such as trypsin (PAS93, 2011).	Genotype; gene expression; cell surface marker (antigen) expression profile; morphology; size
Identity[a]	Cells exhibiting the required medicinal action of the cell therapy product must be present in the product in sufficient quantity.	
Potency	Transplanted cells must exert an acceptable level of efficacy through defined by biological functionality or better yet therapeutic outcome.	Cytokine secretion; cell-to-cell interactions;

[a]It is acknowledged that purity and identity are closely linked and the tests used to confirm both overlap with each other (PAS93, 2011, PAS83, 2012, Bravery et al., 2013); [b]in the case of cells derived from pluripotent stem cells, undesired cells would manifest themselves as undifferentiated or spontaneously differentiated cells.

Non-pluripotent cells

For non-pluripotent cells, such as mesenchymal stem cells, minimum identification criteria includes plastic adherence and in vitro trilineage differentiation, as well as CD105, CD73 and CD90 expression and the absence of CD45, CD19, CD79 and HLA-DR extracellular antigens (Dominici et al., 2006, Keating, 2012). Commercial CTPs are defined by the expression of certain extracellular markers to define product cells (Maziarz et al., 2012), along with the secretion of growth factors and cytokines specific to the therapeutic application (Bravery et al., 2013).

Pluripotent cells

Pluripotent cells must satisfy constraints presented previously, centring on the expression of extracellular antigens (SSEA-3 and 4, TRA-1-60, TRA-1-81), and the absence of SSEA-1, the presence of intracellular markers (OCT-4, SOX2 and NANOG), a high cytoplasm-to-cell ratio, normal karyotype, the ability to form all three germ layers and the ability to retain a pluripotent state for multiple passages (>10) (Thomson et al., 1998). Pluripotent-derived stem cells must satisfy criteria specific to each cell type and demonstrate an absence of the

aforementioned pluripotent characteristics. Fully differentiated cardiomyocytes, for instance, must express an array of markers (MLC2V, VCAM, MYH6, cTnT, SIRPA, ctNL) and demonstrate comparable electrophysiology to in naturally sourced cardiomyocytes (Blazeski et al., 2012, Chen et al., 2014).

1.5. Cost of goods

Cost of goods (COG) in cell therapy manufacturing concerns the value of the therapeutic product being manufactured. Given the high cost and high risk of failure for cell therapy product (CTP) development, optimising COGs is imperative in the scaled commercialisation of cell therapeutics.

Key features in medical drug manufacture are high costs (> $1.3 – 1.7 billion) and long (~ 15 years) developmental periods (Collier, 2009). Therefore, the bioprocessing industry has implemented different cost structures to that of other industries. The ratio of COGS to sales in the automotive sector, for instance, is in excess of 70 %, yet in many pharmaceutical and biotechnology companies it is between 15 and 30 % (Basu et al., 2008) due to the high cost of product manufacture.

Large-scale cell therapy manufacturing is dictated by economies of scale (Mason and Hoare, 2006). The estimated costs for an allogenic cell therapy (for insulin-dependent diabetes) in 2009 was $20 per 10^6 cells (Mason and Dunnill, 2009). Technical advances are projected reduce the cost to $1 – 5 or less (Rowley, 2014). Future technical advances will no doubt lower COGs for cell therapy products, but extracting maximum value from existing bioprocessing expertise and technology should be sought throughout the developmental process.

1.6. Manufacturing process

Proposed allogeneic cell therapy manufacturing processes (Figure 1-1) resemble traditional bioprocesses where mammalian cells are expanded upstream (Velez-Suberbie et al., 2013) and retrieved downstream (Gronemeyer, 2014). Owing to the nature of a cell therapy, where the cell is a product rather than the host of a product, processing conditions complementary to cell physiology are required (Quintanilla, 2013, Wolfe and Ahsan, 2013).

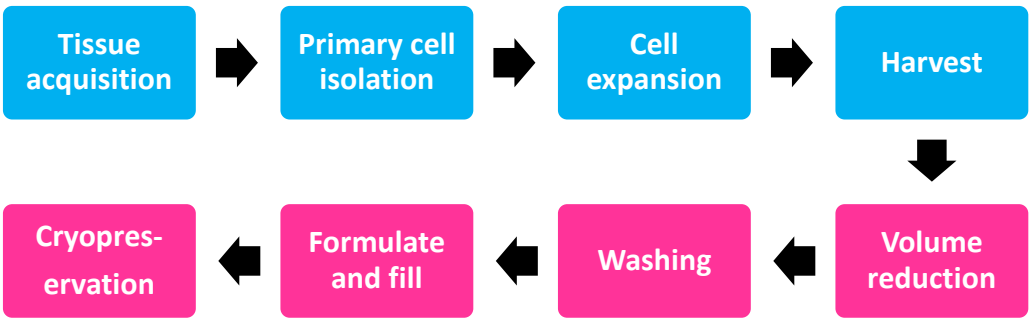

Figure 1-1. Generic cell therapy manufacturing process. The manufacturing process is largely split into three different stages: (Blue = upstream) cell sourcing and expansion; (Pink = downstream) cell separation and cryopreservation. Tissue acquisition = selection, screening and extraction of cellular material; primary cell isolation = identification and isolution of product-related cells; cell expansion = increased quantity and maintained quality of product-related cells; harvesting = recovery of cells from expansion system; volume reduction = concentration of cellular product; washing = removal of waste-related components; formulate and fill = the filling of multiple vials containing cryopreservation medium; = cryopreservation = freezing process for long-term product storage (Rowley, 2012).

Technology used in a cell therapy manufacturing process should also satisfy the following considerations (Table 1-2) to provide safe, cost-effective and consistent performance compliant with regulatory standards (Brindley, 2014). The following section selectively discusses each of these steps based on their location (upstream or downstream) and the technical challenges facing them.

Table 1-2. Technology requirements recommended for implementation into a cell therapy manufacturing process.

Property	Description
Closed system	Functionally closed unit permitting operation in non-GMP settings.
Single-use	Disposable device
Cost-effective	Exert minimal costs on process development or operation
Scalable	Capacity to increase batch sizes whilst maintaining process performance
Capable of automated operation	Integration into robotic processing steps
GMP compliant	Consistent with regulatory constraints surrounding product manufacture
ISO 9000 certification	Demonstration of dependable quality

1.6.1. Upstream processing

Upstream processing involves sourcing a cell line for expansion and possible differentiation towards a specific lineage. The purpose is to expand cells to a quantity and quality deemed sufficient to meet intended supply in a cost-effective manner. Approximately 10^6 – 10^9 cells will be required per patient dose for each disease, with up to 10,000 to 100,000 patients being treated annually (Le Blanc et al., 2008, Braam et al., 2010). Such quantities necessitate the use of more cost-effective and scalable technologies.

1.6.1.1. Tissue acquisition and primary cell isolation

Cell line selection influences both the efficacy and safety of the CTP. Donor and ingredient screening must maximise the CQAs of selected lines to provide a platform for cell bank creation and standardised product development (PAS93, 2011, PAS83, 2012, Bravery et al. 2013). Requirements for both pluripotent and non-pluripotent cells are detailed below.

Non-pluripotent stem cells

Non-pluripotent stem cell isolation is often performed based on differences in density and antigen expression. Density-based separation has been used to isolate stem cells from bone marrow (Juopperi et al., 2007) and umbilical cord blood (Sato et al., 1995). More precise methods utilise affinity interactions between extracellular receptors and corresponding ligands, such as magnetic and fluorescence-based cell sorting (detailed in Section 1.7.2.2.),

offering higher purities. Athersys' Multistem® utilises magnetic beads to achieve cell purities in excess of 99.5 % based on CD45+ and Glycophorin A antigens (Maziarz et al., 2012). The company, Osiris uses a combination of anti-fibroblast magnetic beads and fluorescence-activated cell sorting (FACS) to achieve purities in excess of 99.5 % (Davis-Sproul et al., 1999, Jones et al., 2002) for its OTI-010 product. Similarly, Pluristem's PLX, using cells derived from the placenta, relies upon magnetic beads and FACS to sort cells based on CD44+, CD45+, CD73+ and CD90+ expression for a purity above 98 % (Duda et al., 2013).

Pluripotent stem cells

Embryonic stem cells are sourced from a 3 – 5 day-old blastocyst (Thomson et al., 1998). Induced pluripotent stem cells are derived from fibroblasts using a combination of reprogramming genes (Yamanaka and Takahashi, 2011). Both cell types are assessed based on cell morphology, the retention of their pluripotent state across multiple passages, karotypic and genetic stability, antigen expression, sterility and the ability to form each of the three germ layers (Thomson et al., 1998, Davidson, 2008). More recent attempts to improve product quality have occurred through the removal of cells positive for certain antigens associated with teratoma formation (SSEA-5 plus two of the following antigenic markers: CD9, CD30, CD50 and CD200) (Tang et al., 2011). Cells that meet these criteria are used to create a cell bank for the deployment of research and developmental studies.

1.6.1.2. Cell expansion

Cell expansion seeks to increase the quantity of cells produced either through scale-out or scale-up strategies, depending upon projected requirements and process performance (Table 1-3). In scale-out strategies, the expansion of cells in multiple systems of smaller batches and is more applicable to low-dosage treatments that require few cells ($<10^6$ cells)

(Thomas et al., 2009, Schwartz et al., 2012). Large dosage treatments (>10^6 cells) and high patient demand (>10,000 treatments/year) require scale-up approaches where cells are expanded in three-dimensional formats to capacities up to 5 x 10^{12} cells per batch, which present significant technical challenges (Rowley, 2012).

The majority of adherent cell culture scale-up challenges are being addressed through non-pluripotent cell culture (Rafiq et al., 2013) as opposed to pluripotent cell culture (Prowse et al., 2014), owing to the inhibitive cost and understanding of the latter. For instance, mesenchymal stem cells are closer to requiring scalable manufacturing technology, not only because of clinical progress, but also because of high surface areas for cell growth (2 x 10^4 cells/cm^2) and high dosages (0.4 – 1 x 10^6 cells) per patient (Le Blanc et al., 2008, Macmillan et al., 2009) are required. In contrast 6 – 8 x 10^6 cells/cm^2 are possible for pluripotent cells with dosages of 10^5 – 10^6 per patient (Schwartz et al., 2012). Therapies requiring larger dosages (10^8 – 10^9 cells) are in a less advanced state (Braam et al., 2010), so the use of large-scale (>10^{11} cells/batch) culture units for pluripotent cell culture is not considered an immediate necessity.

Reactors

Beyond a certain batch size (approximately 1 – 5 x 10^{11} cells) two-dimensional culture systems are not practical (Rowley, 2012). Therefore, a transition towards larger culture systems enabling higher surface area-to-volume ratios are required (Table 1-3) (Rowley, 2012).

Table 1-3. Recommended expansion formats for allogenic mesenchymal stem cell manufacture (Rowley, 2012).

Scale (Billion cells/lot)	**1**	**10**	**50**	**100**	**≥500**
Cell culture tool	T-flask, hyper-flask (10-layer)	10 and 40 layer hyper-flasks, robotics	40 layer hyperstack + robotics	Automation of 40-layer hyperflasks; hollow fibre bioreactors	Suspension bioreactors

A cost per number of cells is often cited as determining the cost-effective manufacture of cells. Indeed, progress has demonstrated large-scale expansion of MSCs, albeit without their integration into a process. Potential limitations concern the replication of the cells in the 3D environment.

The configuration of scalable bioreactors applicable to adherent cell therapy culture are summarised below. However, transitioning to these larger systems presents several technical challenges, relating to heterogeneity (Donati, 1997, Lara et al., 2006a) and other bulk processing side-effects such as fouling (Drews, 2010) and clumping (Serra et al., 2009). Several reactors are relevant for the expansion of adherent stem cells and are detailed below.

Hollow fibre perfusion

Hollow fibre bioreactors are cylindrical vessels packed with thousands of thin microporous fibres. These fibres offer mechanical strength while allowing selective molecule transition (Guardia, 1999). During culture, cells are localised on the shell side of the fibres, whilst culture medium is circulated through the module, facilitating mass transfer across the membrane (Eibl, 2009). Clinical-grade cell lines have also been tested on these devices. Athersys' Multistem® product was recently used to expand 10^7 cells to over 7.5 x 10^8 per reactor. Whilst restricted to around 200 mL per unit due to mass transport limitations, scale-out procedures do allow operation at up to 20 cartridges per culture unit (Davis, 2007). Cost-effectiveness is estimated to be at \$10 – 15 per 10^6 non-pluripotent cells (versus \$50 – 100 for two-dimensional monolayer culture systems) (Rowley, 2014).

Stirred tank

Stirred tank bioreactors are commonly used for the cultivation of mammalian cells in suspension (Adamson, 1998). They are typically operated using suspension-grade cells (Adamson, 1998), but also enable adherent cell culture through microcarriers (Rafiq et al., 2013). The basic setup ensures adequate mixing, heating and cooling and includes sensors for parameter monitoring. Care must be taken during scale-up to avoid shear stress-induced cell damage (Kretzmer and Schügerl, 1991). Given the potential costs associated with scaled operation, small-scale (7 mL vessels), high-throughput (up to 24 vessels) systems have been developed to overcome these limitations (Warr, 2014). The cost is estimated to be at $1 – 5 per 10^6 non-pluripotent cells, which is significantly below that estimated for both hollow fibre ($10 - 15) and monolayer ($50 – 100) culture systems (Rowley, 2014), demonstrating cost effectiveness.

Microcarriers

Microcarriers are polymer-based beads or chips used to enable two-dimensional adherent cell culture in a three-dimensional format. They are usually 10 – 200 µm in size and exhibit surface functionalities, morphologies and densities necessary to promote cell adhesion and proliferation (Chen et al., 2011, dos Santos et al., 2011).

Embryoid bodies

Embryoid bodies are three-dimensional aggregates of pluripotent stem cells. Whilst pluripotent cell culture in two-dimensional culture systems is possible, effective scale-up in three-dimensional culture systems requires microencapsulation into microbeads to overcome heterogeneity (Niwa, 2006, Jing et al., 2010).

1.6.1.3. Differentiation

Cell differentiation involves the controlled transition of an immature cell towards a more mature specific lineage (Sathananthan and Trounson, 2005, Murry and Keller, 2008). The necessity for differentiation depends upon the maturity of the cell and its application.

Non-pluripotent stem cell differentiation

Non-pluripotent stem cells, namely mesenchymal stem cells (MSCs), are multipotent with the capacity to differentiate towards osteogenic, adipogenic and chondrogenic cell types. Differentiation is considered a key characteristic of MSCs (Dominici et al., 2006), although the clinical application occurs in an undifferentiated state (Kim and Cho, 2013).

Pluripotent stem cell differentiation

Pluripotent cell differentiation involves a series of complex molecular signalling pathways to be initiated by growth factors and small molecule inhibitors (Wagner and Siddiqui, 2007a, Wagner and Siddiqui, 2007b, Chen et al., 2014) (Table 1-4). Cells may be differentiated as embryoid bodies (Kurosawa, 2007), on flat surfaces under static (Mummery et al., 2003) or flow-based conditions (Liu et al., 2013) ideally in three-dimensional arrangements (Lecina et al., 2010).

Table 1-4. Differentiation of pluripotent human cells to cardiomyocytes (adapted from (Chen et al., 2014).

	Pluripotent cell expansion	**Cardiomyocyte differentiation**		
Stage	**1**	**2 (Day 0 – 4)**	**3 (Day 4 - 8)**	**4 (Day 8+)**
Cell specification	Pluripotent cell	Mesoderm / cardiac mesoderm	Cardiac progenitors	Cardiomyocytes
Markers	SSEA-4, Tra-1-60, OCT4, SOX2, NANOG	MESP1, KDR, PDGFRA, C-KIT	ISL1, GATA4, NKX2.5, TBX5, MEF2C, TBX20	MLC2V, VCAM, MYH6, cTnT, SIRPA, cTnI
Biomolecules	FGF2, Activin A, Insulin	BMP4, Activin A, SB203580, GSK-3β inhibitors, TGF-β1 inhibitors	VEGF, FGF2, DKK1, WNT inhibitors	Insulin

Biomolecules (growth factors and small molecules) direct pluripotent cell differentiation towards a cardiomyocyte lineage. Intracellular and extracellular markers associated with each of the three main stages can be used to monitor cell differentiation.

For cardiomyocytes, a range of differentiation efficiencies have been reported, varying greatly according to the culture methods, with two-dimensional monolayer cultures achieving 25 % (Wong and Bernstein, 2010) and 97.7 % (Minami et al., 2012), embryoid bodies achieving 23.6 % (Burridge et al., 2007) to 95.8 % (Takei et al., 2009) with around 20 % being acheived using microcarriers (Lecina et al., 2010). Improved process understanding will no doubt lead to increased purity, but the threat of impure cell populations due to reactor heterogenity, either as spontaneously differentiated cells (Sathananthan and Trounson, 2005) or those retaining pluripotency attributes (Thomson et al., 1998, Schriebl et al., 2012) is of particular concern due to the potential for teratoma formation *in vivo* (Lebkowski, 2001, Schriebl et al., 2012).

1.6.2. Downstream processing

The downstream processing of biological products have traditionally centred on cell membrane disruption to recover intracellular components, prior to purification using

chromatographic techniques (Moser and Hage, 2010). Since the cell is the product, rather than the host, methods to maintain or increase the proportion of cells with these attributes are desired. Ideally, high-specificity purification methods such as those using affinity-based interactions are not needed, with downstream processing instead focussing on undesirable waste removal prior to storage.

1.6.2.1. Harvesting, volume reduction and washing

Following upstream processing, adherent cells are typically recovered using enzymatic digestion. Regulatory requirements stipulate the removal of cell processing medium waste components (e.g. cell debris, enzymatic agents xenogenic proteins, etc.) to concentrations as low as 1:1,000,000 according to Chapter 21 CFR610.15 on constituent materials of the FDA Centre for Biologics Evaluation and Research. Such procedures are simple at small lab-based scales, but as upstream capacities are expected to increase, larger harvest volumes are expected (100 to 1,000 L), rendering conventional equipment for volume reduction redundant and necessitating the use of larger, re-designed systems (Table 1-5) to concentrate cells to 10^7 – 10^8 cells/mL (Pattasseril, 2013).

Table 1-5. Volume reduction and washing technologies for various batch sizes (adapted from (Rowley, 2012).

Batch Scale		**10^9**	**10^{10}**	**5 x 10^{10}**	**10^{11}**	**5 x 10^{11}**
Volume reduction and washing		Centrifugation	Centrifugation, blood processing equipment	Tangential Flow Filtration, continuous centrifugation	Tangential Flow Filtration, continuous centrifugation	Continuous centrifugation
Input concentration (L)[a]		0.3	3.3	17	33	167
Output concentration volume (L)	A	0.1	1	5	10	50
	B	0.01	0.1	0.5	1	5

[a] Estimated input concentration post-upstream processing. Estimated output concentration based on a requirement of: (A) 10^7 to (B) 10^8 cells/mL (Pattasseril, 2013).

Centrifugation

Centrifugation is used to separate cells from surrounding waste, usually within a few minutes (Juopperi et al., 2007) by exploiting differences in cell density relative to the surrounding fluid (Fair, 1984). Such devices, typically disc bowl centrifuges, can process thousands of litres of cell suspension, offering clean-in-place procedures (Kempken et al., 1995). However, such devices were designed to recover proteins from inside cells, whilst CTP manufacture requires the maintenance of cell integrity, concentration of cells and removal of surrounding waste medium (Pattasseril, 2013). Therefore, alternative centrifugation systems capable of imparting low physical stress during waste removal are desired (Rowley et al., 2013) and have been described (Mehta et al., 2011).

Membranes

Membranes are typically used to separate cells or colloids using size exclusion across a porous barrier. When applied in cross-flow filtration, the potential to accomodate larger cell suspension volumes, particularly in the form of hollow fibre or flat sheet membranes that have pore sizes ranging from 0.1 to 10 μm, is possible (Shukla, 2007). Unlike simpler depth filters, which are prone to fouling, cross-flow minimises fouling by simultaneously disrupting surface-bound debris, effectively regenerating the surface whilst driving waste impurities to the filtrate side of the membrane through differences in transmembrane pressure (Prasad, 2012). However, as with centrifugation, cross flow filtration units must separate cells from surrounding medium whilst preserving cell integrity. Conventional ultrafiltration filtration membranes utilise higher shear rates (~14,000 s^{-1}), which would translate to higher shear stresses (~120 dynes/cm^2) and smaller pore sizes (0.1 μm) owing to the greater robustness of the cells (Trinh and Shiloach, 1995). For stem cell separation, lower shear rates (2,000 –

4,000 s^{-1} equivalent to ~17 – 35 dynes/cm^2) combined with larger pore sizes are preferred (0.65 μm), providing greater transmembrane flux yet maintaining cells in suspension and minimining shear-induced damage (Rowley et al., 2012).

1.6.2.2. Purification

Cell purification (also known as cell separation) in this context refers to the removal of undesired cells from a population of product-designated cells using highly selective affinity-interactive methods. Unlike traditional bioprocessing, where affinity purifications are a necessity (Dancette et al., 1999, Hahn et al., 2003), it is absent from downstream processing. It is anticpated that cell purity will be controlled upstream using pre-determined conditions complementary to cell physiology without resorting to selective purification methods (Pinxteren and Craeye, 2012, Schwartz et al., 2012). However, since cell therapy manufacturing is an immature industry, overlooking downstream purification is considered unwise when reflecting upon previous downstream bottlenecks in traditional bioprocessing, where such costs accounted for up to 80 % of overall processing costs (Kelley, 2007, Gronemeyer, 2014). Therefore, purification technology to remove unwanted cells is considered accordingly.

Non-pluripotent stem cells

An affinity separation step is considered unnecessary during non-pluripotent cell therapy manufacture, largely due to the absence of a differentiation step and ability to achieve sufficient purities. High cell purity (>98 %) is possible in scalable stirred tank bioreactors, where cell densities of 1.36 – 1.48 x 10^5 cells/mL were acheived (albeit at a 2.5 L working volume) (Nienow et al., 2014) and cell CQAs satisfied a universal standard (Dominici et al., 2006). Product-specific CQAs have also been obtained commercially in scalable formats,

without the need for purification. In hollow fibres, for instance, 10^7 non-pluripotent stem cells were expanded to 7.5 – 7.8 x 10^8 cells (Pinxteren and Craeye, 2012) for Athersys' Multistem® product, notably, satisfying relevant CQA in the absence of any affinity purification step post expansion.

Pluripotent stem cells

A fundamental part of pluripotent cell manufacture will be the controlled differentiation of cells towards a specific lineage *in vitro*. As detailed in Section 1.6.1.3., spontaneous differentiation or the retention of a pluripotent state post-differentiation, particularly at larger scales (>10^{11} cells), will generate impure cells with a carcinogenic potential (Schriebl et al., 2010b, Schriebl et al., 2012). Small scales and low dosage requirements do not necessitate downstream purification steps post-expansion and differentiation. For instance, Geron's oligodendrocytes (Nistor and Keirstead, 2004) and ACT's retinal pigment epithelial cells (Schwartz et al., 2012) were considered 99 % pure post-expansion (<10^6 per T-flask) and did not form tumours in human studies. However, in larger three-dimensional systems (>10^{11} cells per batch), where heterogeneity is harder to control (Donati, 1997, Lara et al., 2006a) without undergoing cell losses, inefficient differentiation efficiencies are expected and the need for purification may be required.

1.6.2.3. Formulation, filling and cryopreservation

The final stage of downstream processing concerns the transfer of concentrated cells into vessels for cryopreservation and storage. This provides an 'off-the-shelf' capability allowing large batches of cells to be stored for extended periods (Mandalam, 2005). Scale-out rather than scale-up is required to process cells of larger quantities, since the end product is dependent on the number of cells per patient dose (10^5 – 10^{12}). Existing technology requires

a transition from small lab-scale devices to larger systems able to process much larger batch sizes without compromising cell CQAs (Table 1-6).

Table 1-6. Cryopreservation technology recommended for various batch sizes (Rowley, 2012).

Scale (Billion cells/lot)	**1**	**10**	**50**	**100**	**500**
Number of vials[a]	10^2	10^3	5×10^3	10^4	5×10^4
Volume reduction and washing	Bench-controlled rate-freezer	Bench controlled rate-freezer	Large-scale controlled rate freezer	Large-scale controlled rate freezer	Scale-out, large-scale controlled-rate freezer

Based on 10^7 cells/vial

Cryoprotective agent, such as dimethyl sulfoxide (DMSO) is used to penetrate cells and prevent ice formation during freezing, at the expense of cell health (Mazur, 1984, Mazur, 1988, Meryman, 2007). Owing to the detrimental effect of cryopreservation on cells, multi-parameter studies are favoured to mitigate cell loss (Mitchell et al., 2014).

1.7. Opportunities for new technologies

Manufacturing a CTP requires a careful appreciation of how the cell product – in particular its critical quality attributes (CQA) is affected by the processing environment. One of the four CQA categories presented in Section 1.4 concerns cell purity, which can be correlated with clinical outcome (Handgretinger et al., 2002) and in some instances cell potency (Maziarz et al., 2012).

As Section 1.6.2.2. detailed, the purity of non-pluripotent cells is easier to attain as a differentiation step post-expansion is ommitted. Yet in the manufacture of pluripotent-derived cells, differentiation is required (Zandstra et al., 2003, Jing et al., 2010, Zandstra et al., 2010). During this process, pluripotent cells may differentiate spontaneously towards an undesired lineage different to the targeted tissue (Sathananthan and Trounson, 2005) or remain pluripotent (failing to differentiate) (Zandstra et al., 2003, King and Miller, 2007).

The administration of such cell into a patient could induce teratoma formation – a major safety and regulatory concern ((CTGTAC), 2008). Bypassing the ethical constraints in humans, thresholds based on the proportion of impure cells necessary to induce teratoma formation have been made in animals. Geron's human embryonic-derived oligodendrocyte cells (spiked with 10 % undifferentiated cells) formed teratomas in 4/31 immuno-suppressed mice, whilst lower proportions (1 and 5 %) demonstrated no teratoma formation (Lebkowski, 2011). Slightly higher thresholds were observed in other mouse models: purities of 99.1 – 100 % yielded no teratoma formation; a reduced range of 97.1 – 99.7 % containing more pluripotent cells yielded teratomas in 1/9 (Schriebl et al., 2012). Generally, comparison and extrapolation to humans is limited by study inconsistency, the size of the species in question (humans are ~3000 times larger than mice, whose metabolic function is significantly faster, leading to less stable homeostasis and therefore a different rate of scenesence) (Demetrius, 2005), as well as the different response of the species to tumourogenic material (Mak et al., 2014). At best, the existence of a purity threshold in humans may be hypothesized, but this could be patient-dependent.

Conservative estimates from human haematopoetic stem cell transplants suggest that 1 cancerous cell per 3.5 x 10^6 pure cells is tumour-inducing (Prockop, 2010). Even higher purities of 1 impure cell per 10^8 cells have been suggested elsewhere (Schriebl et al., 2010a). Human transplants using induced pluripotent stem cells (iPSCs) (albeit delivering only 5 x 10^4 cells) showed that threshold purities in excess of 99 % sufficed without teratoma formation (Schwartz et al., 2012). However, these findings provide early-stage results and may not be universal. For instance, teratoma formation may be both location- and cell-dependent: subcutaneous infusion yielded teratomas in 84 % of mice, whilst intratesticular

infusion yielded 94 % for embryonic stem cells; iPSCs were more aggressive, generating teratomas in all instances (Gutierrez-Aranda et al., 2010).

Overcoming inefficient conversion is considered a significant technical challenge in pluripotent cell manufacture (Schriebl et al., 2012, Chen et al., 2014). At larger scales (>10^{11} cells per batch) where homogeneous bioreactor conditions are harder to maintain (Donati, 1997) without compromising cell physiology (Lara et al., 2006a), it is predictable that a larger proportion of cells will remain pluripotent. Therefore, methods to prevent, suppress or remove such cells are of particular interest.

Of the characteristics used to define pluripotent cells (Section 1.4.), the extracellular Stage Specific Embryonic Antigen 4 (SSEA-4) is highly representative and is expressed on up to 95 % of cells considered pluripotent (Thomson et al., 1998, Shibata et al., 2006, Fong et al., 2009). The use of this – and/or any other universal pluripotency extracellular marker (e.g. SSEA-3 or SSEA-4) currently in existance is considered an ideal characteristic to address these challenges.

1.7.1. Technologies to control cell purity

The previous section has outlined the challenges in achieving cell purity in a large-scale manufacturing process. This section introduces two new technologies to overcome these challenges: (1) biosensors, to better understand cell differentiation through regular sampling or real-time sensing; and (2) methods to destroy or remove impure cells during or after differentiation. In both instances, the technology will focus upon the use of an antigenic marker – in this case the SSEA-4 antigen, which is considered the most resolute characteristic for cell identification and separation, but will also consider more novel ones.

1.7.1.1. Biosensors

Biosensors are analytical devices that connect biological interactions to physicochemical detection systems to generate output signals (Scheller et al., 1991). Their ability to reliably measure certain analytes is subject to device accuracy and precision, as well as robustness and reproducibility (Kisaalita, 1992). Such devices are considered vital to manufacturing a CTP and have been encouraged through the FDA's Process Analytical Technology (PAT) to create "a system for designing, analysing, and controlling manufacturing through timely measurements of critical quality and performance attribute of raw and in-process materials and processes, with the goal of ensuring final quality."

In cell culture, conventional sensors allow favourable conditions for mammalian cell culture to be established and maintained, typically based on pH, dissolved oxygen and metabolite monitoring in culture systems (Hanson et al., 2007). However, feedback regarding cell CQA (Section 1.4), such as antigen and gene expression, karyotype, morphology and biological functionality, which should form the basis of a CTP (Section 1.4) (Bravery et al., 2013) are not provided. Instead, such attributes are measured using separate instruments (e.g. flow cytometers, fluorescent microscopes and polymerase chain reaction (PCR) techniques) that are often expensive, time consuming and complex to use. More informative sensors with faster feedback times and smaller, more integrated designs are desirable. The following section reviews technologies with potential as biosensors for cell detection.

Optical

Optical biosensors measure a range of parameters including light absorption, fluorescence, Raman scattering and reflectance, etc (Scheller et al., 1991, Shantilatha, 2003). In this instance they are categorised as either fluorescent or label-free methods.

Fluorescence-based detection

In fluorescence-based detection, target components (e.g. intra- or extra-cellular markers) are labelled with fluorescent ligand-based conjugates for identification and quantitation based on emitted light (Resch-Genger et al., 2008) (Table 1-7). This is commonly exploited in flow cytometry, which offers very high resolution (allowing the identification of single cells) and the capacity to identify (and sort) cells based on multiple markers (Fong et al., 2009, Basu et al., 2010). However, substantial training is required for operation and maintainence, systems typically cost around £60 k.

More novel devices utilising micro-electro mechanical systems (MEMS) in closed-system setups offer alternative means of detection and sorting. These micro-electro mechanical systems (MEMS), exemplified by Miltenyi's recently launched MACSQuant system purportedly have the capacity to measure (and if necessary purify) cells based on intra- or extra-cellular fluorescence (Foster et al., 2014). Cells are categorised and gated using the MEMS actuator based on measured fluorescence (Foster and Grummitt, 2014). Whilst promising, demonstrable performance is absent and these devices appear to require similar bench space to flow cytometers (their primary purpose is sterile sorting), possess similar pricing structures and also require extensive operator training.

Table 1-7. Fluorescent methods for measuring cell purity.

Type	Application	Method	Performance	State	Reference
Fluorescence microscopy	Identification and isolation of stem cells from non-stem cells	Relies on the measurement of fluorescence emitted from cells based on mitochondrial structure.	Non-quantitative	Separate unit, not integrated.	(Chuck, 2011)[a]
	Identification and isolation of pluripotent and non-pluripotent stem cells	Relies on the measurement of fluorescence emitted from intracellular lipid bodies, which act as endogeneous markers for cell pluripotency			(Panicker et al., 2014)[b]
	Identification of stem cells based on fluorescence and syncytia	Relies on measurement of fluorescence from fixed cells in absence of extraneous or exogeneously added fluorescent dyes			(Gostjeva and Thilly, 2010)
Flow cytometry	Cell sorter and purity measurement	Not a closed system – cells are exposed to atmosphere (albeit in a sterile environment). Cell purity is based on fluorescence	Up to 100 % accurate	Separate unit, not integrated.	(Foster et al., 2014)
MEMS sorter (based on fluorescence)	Cell sorter and purity measurement	Closed system comprising a semi-conductor chip containing MEMS setup. Cells are tagged and separated on the basis of fluorescence.	Quantitative, performance currently unknown	Separate unit, not integrated.	(Foster et al., 2014)

[a] Isolation is not performed, rather it is cited as ; [b] isolation method is not disclosed

Label-free-based detection

Label-free spectroscopic detection methods such as Raman and Fourier Transform Infra-red (FTIR) interpret biomolecules in their natural form (Fan et al., 2008), providing a non-invasive alternative to fluorescent methods. Having been originally developed to idenitify certain bonds in chemical components (Waterhouse et al., 2001), these methods are increasingly applied to cells to measure intracellular components (Table 1-8) and are amenable to well-studied CTP lines either as quality control or research tools.

In FTIR, for instance, vibrational modes in macromolecular molecules (e.g. proteins, lipids, carbohydrates and nucleic acids) yield identifiable functional group bands, indicating relative concentrations and specific chemical structures (Pijanka et al., 2010). Recent attempts have demonstrated the utility of FTIR for elucidating differences in the spectra of human and mouse embryonic stem cells from their derivatives (Heraud et al., 2010, Cao et al., 2013).

Raman spectroscopy focusses a laser beam to illuminate particles, such that scattered light can be detected and analysed. Inelastically scattered light is called a Raman spectrum. Particle molecular composition and structure can be obtained from positions, intensities and line-widths of Raman sprecta peaks. However, the method has a low signal intensity, which must be distinguished from Rayleigh scattered light of the same frequency, but can be separated using filters, gratings or other wavelength separation devices.

However, in both techniques, complex methods of data interpretation and a lack of unity across different cell lines limits their use as a simpler lab-based tool (Sandt et al., 2012, Hung et al., 2013).

Table 1-8. Label-free detection for measuring cell purity

Type	Application	Method	State	Performance	Reference
Raman spectroscopy	Cancer cell detection	Cells are illuminated in electromagnetic radiation wherein Raman spectra are generated. Differences in spectra are used for cell analysis using Principle Component analysis. Cells are trapped using laser tweezers and a Raman spectrum is obtained from cells.	Portable	95.5 – 98.3 % cell detection accuracy; based on differences in intracellular DNA and protein concentration; 3 minute evaluation time per cell.	(Chan et al., 2010)
	Identification and isolation of cells based on pluripotency	Cells illuminated in incident light, where differentiated cell generates a different second-harmonic light from the undifferentiated cell. Potential to detect cells in fluid flow also cited	Separate unit, not integrated.	Differentiated cell accuracy ~97.1 %; correlated with osteogenic induction time and differentiation maturation level during osteogenesis in MSCs; 5 regions per 30 seconds	(Chan and Lieu, 2013) (Hung et al., 2013)
FTIR spectroscopy	Pluripotent cell screening to detect cellular phenotypes	Utilises vibrational modes in macromolecular functional groups within cells to generate identifiable bands within FTIR spectrum. Methods are combined with principle component analysis to facilitate the identification of patterns evident between different cell types and states.		63 – 100 % prediction accuracy depending on cell type; antigen expression and intracellular gene expression.	(Cao et al., 2013)
				86.4 – 88.6 % prediction accuracy in under 5 minutes. Validated based on cytochemical assays	(Ami et al., 2008)

Acoustic biosensors

Acoustic sensors are a class of biosensor that measure acoustic waves to detect a physical phenomenon (Marx et al., 2003). Signal generation by an acoustic unit, typically a quartz crystal microbalance (QCM) exploits the piezoelectric effect of quartz whereby changes in the inertia of the vibrating quartz crystal alter the resonance frequency, allowing surface-

localised interactions to be detected (Voinova et al., 2002, Lucklum and Hauptmann, 2006). Applying an AC voltage causes the sensor to resonate at a fundamental resonance frequency, generating a transverse standing shear wave across the crystal (Babacan et al., 2002).

Adsorbed components are quantified through changes in the frequency and dissipation of the crystal via mass (Sauerbrey, 1959) and/or viscosity (Malmström et al., 2007). Applications include the measurement of certain chemicals in gases (Brousseau and Mallouk, 1997) and liquids (Ying et al., 2008) through chemical reactions, as well as biomolecules based on affinity interactions (Shantilatha, 2003, Nileback et al., 2011). Those involving cells have typically comprised two methods where: (1) cells are cultured on the sensor surface, creating living biosensors to monitor cell growth (Reyes et al., 2013, Lee et al., 2012), or (2) where certain cell types are detected in mixed cell suspensions, as demonstrated with aptamer-conjugated to magnetic beads to target leukemia cells (Pan et al., 2010) or microbial contaminants (Table 1-9).

Table 1-9. Acoustic methods for measuring cell purity.

Application	Method	State	Performance	Method of quantification	Reference
Detection and identification of bacteria and micro-organisms	Relies upon an interaction between specific analytes to detect and quantify specific molecules on the surface based on the piezoelectric effect	Portable hand held	Not disclosed	Presumed to be a correlation between frequency and molecule number, through various equations that convert frequency into yield as a function of component physical attributes. One instance could be through the Sauerbrey equation (Sauerbrey, 1959) or viscosity equation (Malmström et al., 2007) for piezoelectric sensors, or through a calibration chart created using known component samples.	(Edmonson et al., 2010)
Detection of particles such as molecules and microbial cells in a fluid		Portable or bench-top instrument	Not disclosed		(Sheppard et al., 2005)
Detection of particles in a fluid	Utilises living cells on the sensor surface to detect changes induced by drugs or biomolecules in real-time via the piezoelectric effect	Not disclosed	N/A		(Marx et al., 2003)
Measurement technique for the binding of cell membrane-localised molecules	Monitors change in cell signal in response to specific bonds formed between target molecules and immobilised ligands	Not disclosed	N/A		(Gizeli and Saitakis, 2009)
Selective detection of human acute leukemia cells	Cell detection performed using magnetic beads conjugated with aptamers to attach target cells to magnetised quartz sensor	Bench top instrument	LOD[a] = 8 x 10^3 cells/mL	Calibration chart created using known component samples.	(Pan et al., 2010)

[a] LOD = limit of detection

1.7.1.2. Elimination and removal of unwanted cells

Beyond improved process understanding and control, several methods exist to minimise cell-based impurities based on either elimination or purification, where unwanted purities are removed from the cell suspension.

Elimination

Alternatives to affinity-based cell separation centre on the targeted destruction of cells positive for a certain marker using a cytotoxic component (Schriebl et al., 2012), which could

either replace or enhance separation technologies. Such methods would also need to demonstrate that the cytotoxic component does not affect the biological characteristics of the product cells. Other systems explore the possibility of embryonic stem cell destruction based on their metabolic state (Alexander et al., 2011) or through gene transfer for enhanced differentiation (Zandstra et al., 2003). Whilst exhibiting the potential to increase purity, the implementation of such methods into the manufacture of a clinical product would require extensive evaluation to ensure that the product cells remain safe and efficacious.

Purification

The following section considers the use of affinity-based cell purification technology to improve cell purity during scaled manufacture. Several types exist and are discussed accordingly.

Fluorescence-activated cell sorting (FACS)

Fluorescence-activated cell sorting (FACS) involves the separation of fluorescently-conjugated cells from unconjugated cells. Cells are injected into a laser-based sorter, where they are assigned an electrostatic charge based on their measured fluorescence, enabling flow-based separation (Fukuda et al., 2006). Extremely high purities (up to 100 %) are possible (Table 1-10), although separation is very slow (10^4 cells/s = ~2 x 10^9 cells/hr), the device is not a closed system and shear stress exposure during processing may be detrimental to cells, either through membrane rupture (Fong et al., 2009) or more subtle changes associated with cell functionality (Li et al., 2012). The latter point should be considered irrespective of scale and is perhaps why certain companies such as Athersys prefer magnetic separation instead (Maziarz et al., 2012). Flow cytometry sorters also

occupy large bench spaces, require extensive operator training, device maintenance and are extremely expensive (> £100 k).

Table 1-10. Fluorecence-based cell separation technologies.

Method[a]	Cells	Performance	Scale	Clinical output	Reference
FACS with SSEA-4 IgG antibody	Heptocellular carcinoma cells spiked with undifferentiated ESCs	100 %	2 x 10^5 cells	N/A	(Fong et al., 2009)
FACS with Sox1 antibody	Dopaminergic neurons from mouse embryonic stem cells	100 %	2 x 10^5 cells	Cells expressing	(Fukuda et al., 2006)
FACS with SSEA-4 IgG antibody removed from haematopoetic precursor cells	Monkey embryonic stem cell-derived haematopoetic precursors	100 %	0.16 – 78 x 10^6 cells	Tumour formation in unsorted cell populations. Absence of tumour formation in sorted cell populations.	(Shibata et al., 2006)

[a]Performance is based solely on antigen expression.

Magnetic-activated cell sorting (MACS)

Magnetic separation involves the incubation of antibody-coated ferromagnetic iron oxide particles with cell suspensions (Miltenyi et al., 1990). Here, cells positive for the target antigen are tagged with beads via an affinity interaction, whilst cells negative are not. The injection of cells into the magnetic column leads to the retention of cells conjugated to beads based on magnetic force, whilst unlabelled cells pass through. Presumably, magnetic beads are detached or absorbed and digested by cells, posing no obvious effect on the cell (Miltenyi et al., 1990, Grutzkau and Radbruch, 2010).

Log10 clearance rates in the range of 2.8 – 4.1 with recoveries of 45 – 95 % having been reported for various cell types (Table 1-11) (Handgretinger et al., 2002, Schriebl et al., 2010b), demonstrating clinical efficacy (Gratwohl, 2010). Whilst apt for single patient transplants, magnetic limitations (the magnetic field strength decreases as a function of the distance squared from the magnet, leading to reduced pulling strength) (Zborowski, 2008)

and so-called 'drafting', whereby untagged cells become trapped and drawn to the magnet by tagged cells (Lara et al., 2006b), limit the ability to process larger quantities beyond 10^{11} cells, with the rate of separation being approximately 10^7 cells/s, making them unacceptable for batches in excess of 10^{11} cells. Magnetic separation is cost-effective as a lab-based tool, but is more expensive at larger scales (>10^{10} cells), owing to the increased consumption of antibodies. Bead toxicity has been reported, but such instances are attributed to excessive concentrations and such findings would contradict clinical studies (Handgretinger et al., 2002, Tiwari et al., 2003, Gratwohl, 2010).

Table 1-11. Magnetic bead separation technologies.

Method	Cells	Performance	Scale	Clinical output	Reference
CliniMACS system using anti-CD34 antibody-conjugated beads	Human CD34+ stem cell enrichment	81.7 – 99.7 %; recovery = 14 – 77 %; log10 depletion = 2.0 – 4.4.	31 – 450 x 10^8 cells	9/18 patients free of disease over 55-month median follow-up	(Handgretinger et al., 2002)
MS MiniMACS using anti-SSEA-1 IgG IgM antibody –conjugated beads	Murine pluripotent (SSEA-1 positive) depletion[a]	95 - 99 %; recovery = 85 – 95 %. Log_{10} depletion = 0.05 – 0.5	2.2 – 22 x 10^6 cells	N/A	(Schriebl et al., 2010b)
		97.2 – 99.7 %; recovery = 63 – 91 %. Purity: 9.1 – 100 %[b]	1.0 – 2.5 x 10^7 cells	1/9 animals possessed tumours[c] 0/9 animals possessed tumours[c]	(Schriebl et al., 2012)

[a] = murine cells express SSEA-1 antigen when in a pluripotent state, in contrast to human pluripotent cells; [b] = study combined with cytotoxic antibody; [c] 100 % of animals in a control model developed tumours.

Membranes

Membranes are used extensively for filtration purposes to isolate cells from surrounding waste medium (Section 1.6.2.1.). Their convective geometry, favouring low mass transport resistance and high throughput has also been exploited for affinity-based cell separation. Cell enrichment using shear stress has been applied to recover cells adsorbed on the inner lumen of hollow fibres at values up to 200 dynes/cm^2 (Slowiaczek, 1998), as well as the application of shell-side back-pressure (Colton, 1996), enzymatic digestion (Nordon et al.,

1996) and acidic elution (pH 1) (Mandrusov et al., 1995) being utilised. Such instances demonstrated performance similar to magnetic separation (Table 1-12), but were not commercialised owing to no identifiable performance- or cost-related benefits versus the benchmark CliniMACS® magnetic separation technology. Nevertheless, such membranes are scalable and could be used to process larger batch sizes (>10^{11}) cells, either through scale-up and/or scale-out procedures where up to 20 vessels may be used (Davis, 2007), particularly when considering that axial mass transport, a common limitation in hollow fibre bioreactors (Pinxteren and Craeye, 2012), is neglected in shear stress-induced cell separation (Nordon et al., 1996, Nordon et al., 2004).

Table 1-12. Membrane-based separation technologies.

Method	Cells	Performance	Reference
Hollow fibre membrane. Oxidised IgG immobilisation onto hydrazide-functionalised fibres. Back-pressure-induced elution.	HLA-60 cells	Selectivity: 93.4 %[a]; viability: 90 ± 10 % (mean± SEM);	(Colton, 1996)[c]
Immobilisation of rPrA onto epoxy-functionalised fibres. Back-pressure-induced elution.		Selectivity: 99.8 %[a]; viability: 80 – 97 %; 400 – 500 cells per cm fibre[b].	
Hollow fibre membrane. Oxidised IgG immobilisation onto hydrazide-functionalised fibres. Enzymatic digestion-induced cell elution coupled with shear stress (0.2 – 10 dynes/cm^2).	CD34+ enrichment	Purity: 86.1 – 93.1 %; enrichment factor: 400 – 600; recovery: 53 – 60 %; capacity: 1.67 x 10^8 cells.	(Slowiaczek, 1998)
		94.4 ± 3.1 % (mean ± SEM); 3.3 ± 0.1 log_{10} depletion; recovery: 61 ± 9 % (mean ± SEM); viability: > 95 %; 1.3 ± 0.2 x 10^8 (mean ± SEM)	(Nordon et al., 1996)

No clinical output. [a] = selectivity [b] = surface area was 7.9 and 4.1 m2/mL mv for hydrazide and epoxy fibres respectively; [c] cells were separated based on differences in adhesion strength in individual studies.

Monoliths

Monoliths are polymer-based gels of highly interconnected pores (typically in the range of 1,000 to 100,000 nm) making them suitable for cell separation. They are considered alternatives to traditional beaded formats for protein purification, especially larger molecules such as pDNA, IgM antibodies and viral particles (Willoughby, 2009). Whilst

beaded formats rely upon molecule diffusion into and out of their pores, leading to mass transport restrictions, monoliths have fewer dead-end zones, promoting convective mass transport (Jungbauer and Hahn, 2004). Therefore, the interaction of molecules with an affinity-activated substrate occurs parallel to the direction of fluid flow (Pfaunmiller et al., 2013), reducing processing times and shifting the rate limiting step to a kinetic, rather than mass transport one, making them ideal for Protein A–IgG separations (Leblebici et al., 2014).

Larger pore sizes and the potential for convection-driven separation makes the monolith format suitable for cell separation. Demonstrations have centred on yeast and CD34+ cell separation achieving recoveries in excess of 95 % and incurring viability losses less than 10 % for yields of 2 x 10^7 cells (Kumar et al., 2003, Kumar and Srivastava, 2010, Mattiasson, 2011) (Table 1-13). Such units offer the potential for scaled separation, with sizes up to 8 litres being cited as possible (Jungbauer and Hahn, 2004). However, significant developmental and demonstrative investment is required to present them as competitive alternatives to magnetic separation or as scalable units.

Table 1-13. Monolith-based cell separation technologies.

Type and method	Cells	Performance	Reference
Protein A-coupled epoxy-activated polyacrylamide-based cryogel. Used to enrich IgG-tagged cells via bind and elute mechanisms.[a,b]	Yeast	Recovery: (1) flow-induced detachment = 9 - 29 %; (2) eluent = 9 - 36 %; (3) squeezing: 35 – 82 %. Separation time: < 20 minutes	(Mattiasson, 2011)
	Lymphocytes (CD34+ enrichment)	Recovery: 60 – 70 %; Viability: 90 %. Separation time: < 30 minutes	(Kumar et al., 2003)
		Binding: Recovery: 70 - 95 %; purity: >90 %; viability ~90 %; separation time: < 30 minutes. 1.6 x 10^6 cells/mL adsorbent	(Kumar and Srivastava, 2010)

[a] = bind and elute constitutes competitive elution or cryogel compression; [b] performance only evaluated in columns ≤ 2 mL in volume, although column sizes up to 15 mL are cited as being possible.

1.8. Technological approach

Identifying and separating cells based on their phenotype requires the identification of a reliable and interactive characteristic. This is important to distinguish pluripotent-derivatives from their undifferentiated counterparts. In pluripotent cells, several unique characteristics exist relating to gene expression, growth characteristics and physical structure (Section 1.4), but are hard to exploit.

Of the characteristics previously considered, the SSEA-4 antigen expressed by pluripotent cells and down-regulated by their derivatives (Thomson et al., 1998, Schriebl et al., 2010b) does provide the basis for selective identification and separation (up to 95 %) (Fong et al., 2009). Using a previously demonstrated method of shear stress-induced affinity separation (Nordon et al., 1996, Nordon et al., 2004), it may be possible to differentiate between cells positive and negative for the SSEA-4 antigen, providing a basis for identification and purification.

As the previous section has shown, many methods exist to detect cells using biosensors. Optical, label-free methods are particularly attractive, relying solely upon light emittance for non-invasive cell analysis. However, a lack of technical maturity, overly complex analytical requirements and intellectual property restrictions limit spectroscopic methods. Acoustic sensors, in particular the quartz crystal microbalance (QCM), are simple to use and interpret, cost-effective (as little as £20 k) and could provide adequate resolution as affinity cell detection tools.

In affinity cell separation devices, the lack of scalability in existing systems (magnetic- and fluorescent-based sorting) limits their deployment at larger scales (>10^{11} cells per batch). However, convection-driven systems such as membranes that employ flow-based means of

separation are attractive owing to their capacity for scale-up, provided that relevant hydrodynamic conditions can be satisfied.

In both instances, shear stress-induced affinity separation can be used for selective cell identification and purification. More explicitly, this method relies upon the application of hydrodynamic force to differentiate between cells adsorbed with and without affinity interactions. Its application may be two-fold: (1) as a means to identify cells based on their pluripotency, whereby net changes in cells adherent on the sensor surface before-after shear stress indicate those with affinity interactions (Figure 1-2), and (2) for the depletion of unwanted cells through retention, thus increasing the purity of product cells that would be recovered (Figure 1-3). As such, shear stress-induced affinity cell separation will therefore be the underlying theme of this thesis. The theoretical challenges are detailed in the following section.

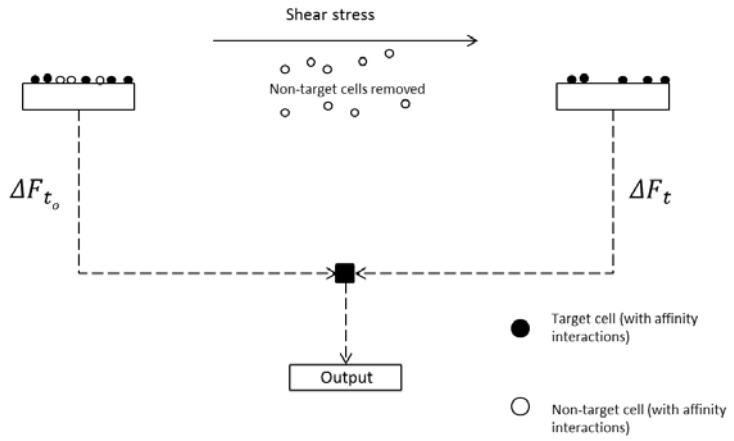

Figure 1-2. Quartz crystal microbalance biosensor for shear stress-induced affinity cell separation. Measurements would be performed in real-time. The net change in cells on the surface would be used to indicate those with affinity interactions (i.e. those with the target antigen), thus indicating cell purity. Letters are denoted accordingly: F = frequency; t_o = time prior to shear stress exposure; t = time after shear stress exposure.

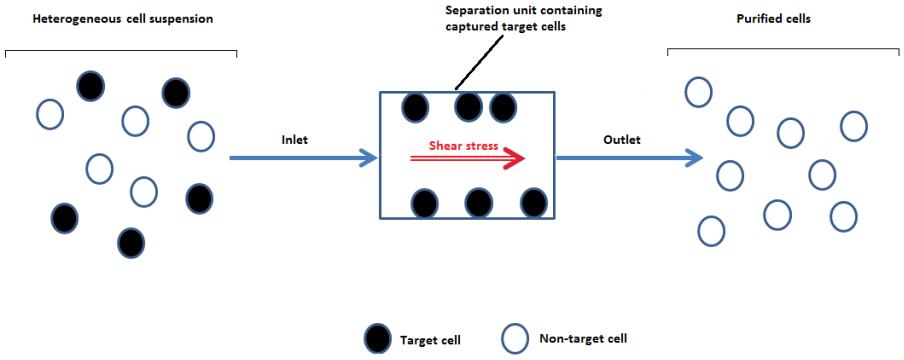

Figure 1-3. Generic cell separation process to retain impure cells through affinity interactions and permit the recovery of product cells, thereby increasing purity.

1.9. Biological impact

Understanding the biological impact of shear stress-induced affinity separation on recovered cells is vital to determine process feasibility. Primary sources of physiological stress are anticipated to be: (1) external hydrodynamic forces acting on the cell membrane due to shearing effects, (Kretzmer and Schügerl, 1991, Chisti, 2000, Avraham-Chakim et al., 2013) or (2) force-induced detachment of the cell from the surface (Christ, 2011), which could lead to membrane tearing (Rubbi et al., 1993, Xia et al., 1994), which is associated with cell death (Kroemer et al., 2009).

When subjected to shear stress, cellular membranes morphologically change, spreading or forming ellipsoid structures, leading to intracellular changes – the extent of which being determined by the severity of the forces applied. Milder shear stress, resembling the natural environment of the cell can induce physiological changes that can be exploited. For instance, shear stresses of 1.5 – 15 dynes/cm^2, applied over several days up-regulated endothelial marker genes (Nsiah et al., 2014) and encouraged differentiation towards cardiac and vascular cell types (Yamamoto et al., 2005, Adamo et al., 2009), by activating signalling pathways (Stolberg and McCloskey, 2009).

Shear stress can also be detrimental to the cell, leading to disease or death via mechanotransduction (Jaalouk and Lammerding, 2009). Mechanotransduction concerns cellular processes that convert mechanical stimuli, such as sound waves, pressure and gravity into biochemical signals allowing cells to adapt to their environments through physiological processes (Figure 1-4) (Ingber, 2006, Wang et al., 2009).

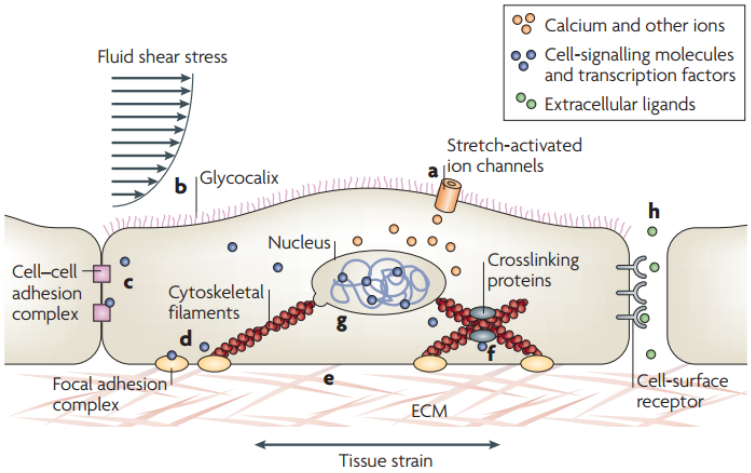

Figure 1-4. Various examples of mechanotransduction extracted from (Jaalouk and Lammerding, 2009). **a**: stretch-activated ion channels in the plasma membrane open in response to membrane strain and allow the influx of calcium and other ions; **b**: in endothelial cells, the glycocalix, a layer of carbohydrate-rich proteins on the cell surface, can mediate mechanotransduction signalling in response to fluid shear stress; **c + d**: cell-cell junctional receptors or extracellular (ECM)-cell focal adhesions allow cells to probe their environments; **e**: force-induced unfolding of ECM proteins, such as fibronectin, can initiate mechanotransduction signalling outside the cell; **f**: intracellular strain can induce conformational changes in cytoskeletal elements such as filaments, crosslinkers or motor proteins, thereby changing binding affinities to specific molecules and activating signalling pathways; **g**: the nucleus itself has been proposed to act as a mechanosensor. Intracellular deformations can alter chromatin conformation and modulate access to transcription factors or transcriptional machinery; **h**: compression of the intracellular space can alter the effective concentration of autocrine and paracrine signalling molecules.

Detrimental effects are also dependent on the intensity and duration of shear stress exposure, (Kretzmer and Schügerl, 1991, Zoro et al., 2008, Mulhall et al., 2011), as well as cell size, with larger cells being more susceptible to damage (Born et al., 1992, Al-Rubeai, 1995). Quantitative estimates have indicated that the membranes of red blood cells may

withstand up to 20 dynes/cm for short periods (Rand, 1964), although the membranes of most mammalian cells are likely to fail beyond 4-6 dynes/cm (Vlahakis and Hubmayr, 2000).

1.10. Theoretical considerations

The theoretical considerations of shear stress-induced affinity cell separation are presented below. They comprise three main stages (Figure 1-5): (1) cell transportation; (2) cell adsorption and affinity interaction; and (3) the retention of cells with affinity interactions and detachment of cells without affinity interactions using fluid flow.

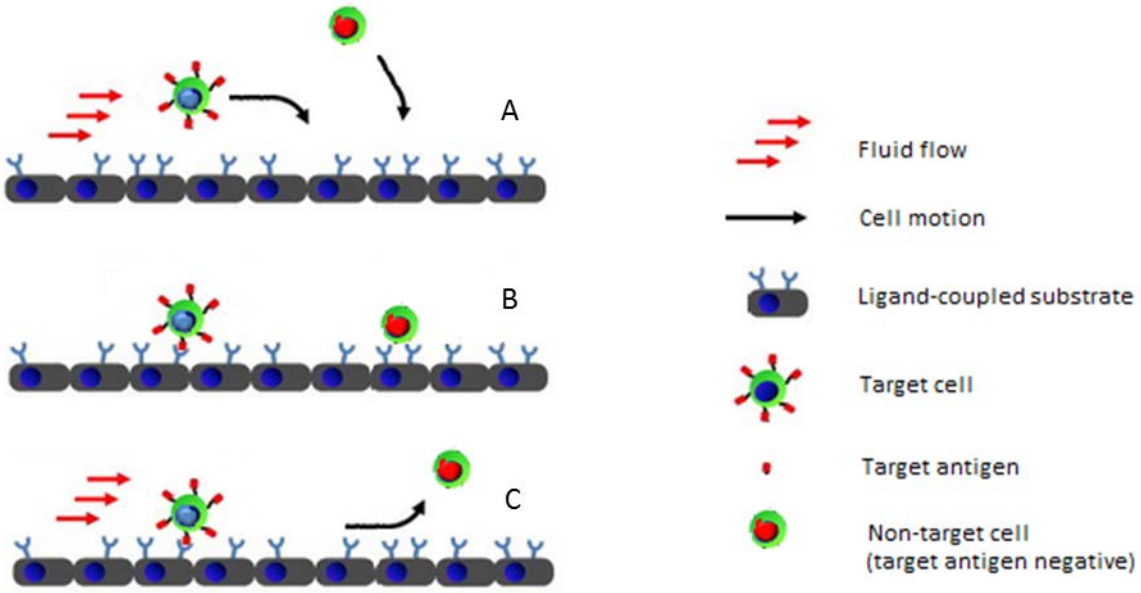

Figure 1-5. Cell separation protocol describing the transport of cells to a ligand-coupled surface under fluid flow (A); the adsorption of cells to the surface with and without affinity interactions under static adsorption conditions (B); and the selective detachment of cells without affinity interactions and retention of cells with affinity interactions in response to fluid flow (C).

1.10.1. Cell transport

Cells are highly dynamic in nature, with a membrane that changes according to external forces (Kasza et al., 2007). Their transport depends primarily on: (1) convection, owing to the size of the cell (5 – 20 µm) and density similar to that of water (1,077 vs. 1,000 kg/m^3) and (2) sedimentation, consistent with Stoke's Law (Howe, 2006). Separation devices, such

as membranes exploit these mechanisms by encouraging convective mass transport and providing a high surface area-to-volume ratio.

1.10.2. Cell-substrate interactions

In affinity separations, cell-substrate interactions comprise affinity and non-affinity interactions which are dependent on the cell-substrate contact area.

Non-affinity interaction

Three forces constitute non-affinity interactions between the cell and the substrate surface: (1) electrostatic forces; (2) steric stabilisation; and (3) van der Waals forces (Christ, 2011). Other factors determine the extent of these forces. *In vivo* cell adhesion is facilitated by the extracellular matrix (ECM), a collagen-based biological scafold which is critical to cell proliferation, migration and functionality (Engler et al., 2009). Cells adherent to ECM-coated surfaces are more resistant to detachment, owing to a variety of extracellular adhesion molecules that anchor cells to the surface (Freeman, 2000). The adhesion strength of a cell to a synthetic material via non-affinity interactions is estimated to be approximately 100 pN per μm^2 cell-surface contact area (Bell, 1978, Bell et al., 1984, Bryers, 2005). It is influenced by three properties that enhance adhesion strength as a function of time: (1) surface charge: cells are negatively charged entities electrostatically attracted to positively charged surfaces and are repulsed by negatively charged ones such as glutaraldehyde (Gallant et al., 2005); (2) hydrophobicity: moderately hydrophilic surfaces promote the deposition and adsorption of cell attachment proteins such as fibronectin, in turn promoting greater cell adhesion strength (van Oss, 2006, Bacakova et al., 2011); (3) cell type: certain cells are more prone to spreading as a function of time or physical force than others, thus leading to a larger cell-surface contact area and therefore more adhesive connections (Christ, 2011).

Minimising the adhesion strength of non-affinity interactions between the cell and the substrate is a desirable method for increasing selectivity during affinity-based separation. Selective cell adsorption onto an oxidised IgG-hydrazide surface was lower (85.3 %) versus an aldehyde-terminated surface relying upon cell-tagged IgG binding to surface-coupled Protein A (99.1 +/- 0.4 %) (Colton, 1996). Lower adhesion strengths can be achieved by selecting surfaces with a negative charge, such as glutaraldehyde to repel cells (Henry, 2009). Blocking agents such as bovine serum albumin (BSA) are also used to enhance repulsive forces (Hermanson, 1992 and 2008, Patel et al., 2008), thus improving selectivity in affinity cell separations (Colton, 1996, Kumar and Srivastava, 2010).

Affinity interactions

Affinity-based cell separation exploits an exclusive interaction between extracellular antigens localised on target cells and antibodies coupled to a support matrix (Miltenyi et al., 1990, Nordon et al., 1996) or conjugate (Fong et al., 2009). This form of separation is derived from affinity chromatography, where a ligand, such as an antibody, is immobilised onto a polymeric support for the selective capture of a receptor molecule, in this case an antigen, forming a reversible complex (Wilchek, 1999, Wilchek, 2000).

$$antigen + antibody \leftrightarrow antigen.antibody$$

An affinity interaction between an antibody and antigen comprises several forces. The binding site between the antigenic determinant on the cell (epitope) and the antigen-combining site on the antibody (paratope) recruits small sections of molecules to create a connection area of 0.4 – 0.8 nm^2. These binding sites comprise many aromatic amino acids, enabling van der Waals forces, hydrophobic interactions and less commonly hydrogen bonds. Generally, hydrophobic and van der Waals forces operate over very short ranges to

draw both regions together in a complementary shape. Electrostatic interactions between side chains and hydrogen bonds that bridge oxygen and/or nitrogen atoms, accommodate specific features or reactive groups to strengthen the overall interaction (Reverberi and Reverberi, 2007). Unlike proteins, cells possess many extracellular antigens (10^3 - 10^7) and so enable multiple affinity interctions to form between the cell and an an antibody-coupled surface.

1.10.3. Creating an affinity support matrix

Importantly, the IgG antibody has various regions and functional groups for various immobilisation or conjugation methods (Figure 1-6), the protocols of which have been detailed extensively (Hermanson, 1992). The three types of IgG antibody coupling methods are detailed accordingly:

1. Primary amines abundant across the antibody provide a simple platform for immobilisation with surface epoxy (Mateo et al., 2000) or aldehyde functionalities, with the latter reaction further stabilised through reductive amination (Yoshioka et al., 1991). However, adsorption is random causing non-orientated coupling and rendering some antigen binding sites inaccessible.

2. Carbohydrate moieties, located at the Fc region of IgG antibodies, can be oxidized in sodium meta-periodate to generate active aldehydes (Morehead et al., 1991). This enables orientated IgG coupled to a hydrazide-functionalised surface via a bond that can be further stabilised in sodium cyanoborohydride (Brillhart and Ngo, 1991, Holton and Vicalvi, 1991).

3. Conjugates may be created when a protein molecule, such as Protein A is coupled to the surface to adsorb IgG antibodies via their Fc regions (Kumar and Srivastava, 2010) derived from the purification of IgG antibodies using Protein A adsorbents (Hahn et al., 2003).

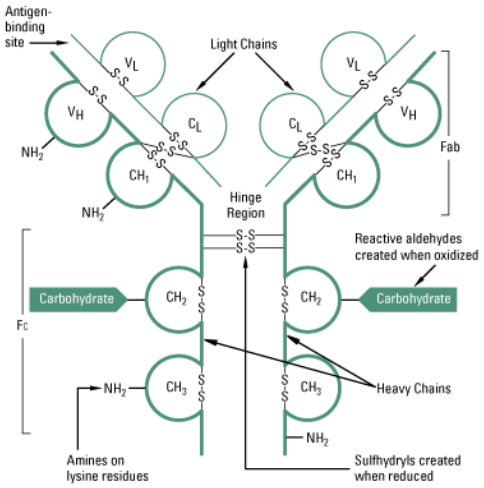

Figure 1-6. IgG antibody structure and labelling sites: they contain two identical heavy chains of about 50 kDa and two identical light chains of about 25 kDa, generating a tetrameric quaternary structure. The two heavy chains are linked to each other and to a light chain each by disulphide bonds. The resulting tetramer has two identical halves: a Fab and Fc region, which together form the characteristic Y-shape. Each end of the fork contains an identical antigen binding site capable of targeting antigens on cell. The Fc regions of IgGs bear a highly conserved N-glycosylation site (Hermanson, 1992).

Ideally, antibodies will be coupled to the substrate through strong, covalent bonds where antigen binding sites are easily accessible. Orientated coupling provides greater binding efficiencies – often several orders of magnitude higher than passive adsorption methods, particularly for smaller molecules (Wang et al., 2012b). Whilst the same principles apply to cells, the binding mechanism is different: antigens are not isolated components – instead they are expressed by the body of the cell, localised at its surface. This presents the opportunity for mutli-valent site binding and is a function of the cell-substrate contact area – itself a function of the cell's propensity for deformation.

1.10.4. Cell adsorption

Affinity and/or non-affinity bond formation will occur after cell adsorption onto the surface. Affinity bond formation under static conditions may be described mathematically:

$$\frac{dC}{dt_a} = k_f^0 N_L (R_T - C) - k_r^0 C \qquad 1.1.$$

, where C = the number of antigen-antibody complexes, t_a is the attachment time, R_T = attachment time for affinity interactions to form within the contact area, and k_f^0 and k_r^0 are the forward and reverse rate constants. k_r^0/k_f^0 = the equilibrium dissociation constant (equivalent to the reciprocal of the affinity constant, K^0) (Cozens-Roberts et al., 1990). The number of affinity interactions is also dependent on the cell-surface contact area. Whilst not a measure of its three-dimensional state, the cell-substrate contact area may be expressed as a function of shear stress and estimated accordingly (Bose, 2009):

$$r_\tau = r_{max} - (r_{max} - r_{min}) exp^{(\tau/\tau_o)} \qquad 1.2.$$

, where r_τ = contact radius of cell at applied shear stress; r_{max} = maximum contact radius of cell; r_{min} = minimum contact radius of cell; τ = applied shear stress; τ_o = measure of the rigidity of the cell.

Assuming that r_{max} = 2 µm; r_{min} = 0.5 µm; τ = 0 – 25 dynes/cm^2; τ_o = 15 dynes/cm^2 for a 10 µm cell based on (Bose, 2009), the contact radius would range from 0.2 – 1.7 µm for 0 – 25 dynes/cm^2, equating to a surface area of 0.5 – 2.3 µm^2.

1.10.5. Force-induced cell detachment

Several methods of antibody-antigen dissociation exist: pH adjustment commonly used for proteins (Wilchek and Miron, 1999) (and demonstrated for cells (Mandrusov et al., 1995)),

ionic adjustment (Ohlson et al., 1997), as well as enzymatic digestion (Firer, 2001). But such methods to enrich cells are not considered complementary to cell physiology – especially more sensitive cells such as pluripotent cells – and likely to result in damage or undesirable changes. Instead, force-induced separation is preferrable, resembling the natural environment of the cell (where the shear stress is typically <50 dynes/cm^2) (Lipowsky et al., 1978, Stolberg and McCloskey, 2009). The concept has been illustrated both theoretically (Bell, 1978, Kuo and Lauffenburger, 1993) and practically (Slowiaczek, 1998, Nordon et al., 2004). However, many instances have relied upon enrichment strategies – the use of higher forces (up to 200 dynes/cm^2) to recover cells adsorbed with affinity interactions – without much consideration beyond membrane permeability as to how the conditions might affect the cells (Nordon et al., 1996 and 2004, Slowiaczek, 1998). Instead, the depletion of unwanted cells and the recovery of product cells using lower shear stresses (≤ 25 dynes/cm^2) is preferred as it would expose cells to milder processing conditions, mitigating harmful effects.

1.10.6. Calculating shear stress

Since the cell suspension is assumed to act as a Newtonian fluid with a density of 1000 kg/m^3 (Kasza et al., 2007), laminar flow (<< 2,100) may be calculated using the Reynold's number equation (Rothfus et al., 1957):

$$Re = \frac{Q\,\rho}{D\,\mu} \qquad 1.3.$$

, where Q = flowrate (m^3/s); *p* = fluid density (kg/m^3); μ = dynamic viscosity (kg/m.s); D = chamber diameter (m). Shear stress may be calculated for both tubular (Equation 4.2) (Bird, 2007) and parallel plate (Equation 2.1) models (Bacabac et al., 2005).

1.10.7. Force acting on cells

The calculation of shear stress allows drag forces acting on adherent cells to be estimated, assuming a non-deformable sphere adjacent to the vessel wall (Goldman et al., 1967):

$$F_{drag} = 6\alpha\pi\tau_w r^2 \quad 1.4.$$

where α = 1.7, a dimensionless drag coefficient (Brooks, 1996), r = cell radius (m) and τ_w = shear stress (1 Pa = 10 dynes/cm^2). The force applied per affinity bond, may be calculated using:

$$F_b = \frac{F_{drag}}{N_b} \quad 1.5.$$

, where F_b = the force per bond; F_{drag} = the drag force acting on the non-deformable spherical cell and N_b = the number of bonds (-).

The effect of different bond densities may be considered: assume that a 10 µm diameter cell with a surface contact area of 0.5 µm^2 is subjected to a shear stress of 25 dynes/cm^2 (equivalent to a drag force of 2,000 pN). If antigen density ranges from 10^3 – 10^7 (Cozens-Roberts et al., 1990) this would equate to 1.6 – 1.6 x 10^4 possible cell-surface affinity interactions. Across this range, applied force per bond, F_b, would range from 0.12 – 1.2 x 10^3 pN, which could determine whether an adsorbed cell remains adherent or detaches in response to shear stress.

1.10.8. Equilibrium dissociation constant

The equilibrium dissociation constant (K_D), an indicator of the propensity of the cell-surface complex (in this instance an antibody-antigen interaction) to reversibly split into two

separate entities is also decisive in cell detachment and has been expressed by (Kuo and Lauffenburger, 1993):

$$\frac{F_t}{R_c} = \frac{2k_B\Theta}{I_B}\ln\left(1 + \frac{N_L}{\eta K_D}\right) \qquad 1.6.$$

, where F_t = the total force required to detach a cell; R_c = receptor number per cell in contact area; k_B = Boltzmann constant; Θ = absolute temperature; I_B = extent of bond stretch; N_L = surface ligand density; η = conversion parameter for K_D; K_D = equilibrium dissociation constant.

To demonstrate the effect of different K_D values (1 x 10^{-5} to 1 x 10^{-10} M) on cell adhesion strength, the following assumptions may be made using Equation 1.7, where N_L = 3.5 x 10^{12} #/cm^2; R_c = 1,000 #/cm^2; I_B = 8.8 Å; k_B = 1.38 x 10^{-23} J/K; Θ = 296 K (23 ^oC); η = 1.38 x 10^{-23} J/K are fixed and the data are shown in Figure 1-7, where K_D ranges from 10^{-10} – 10^{-5} M and is inversely proportional to the force per receptor required to break affinity interaction bonds (F_t/R_c). These findings are consistent with previous estimates (Bell, 1978, Bell et al., 1984), where the adhesion strength was estimated to be 1 – 10 µdynes (10 – 100 pN) per affinity interaction, which is much higher than that of ~0.4 µdynes (4 pN) per non-affinity bond (equivalent to 100 pN/μm^2 contact area).

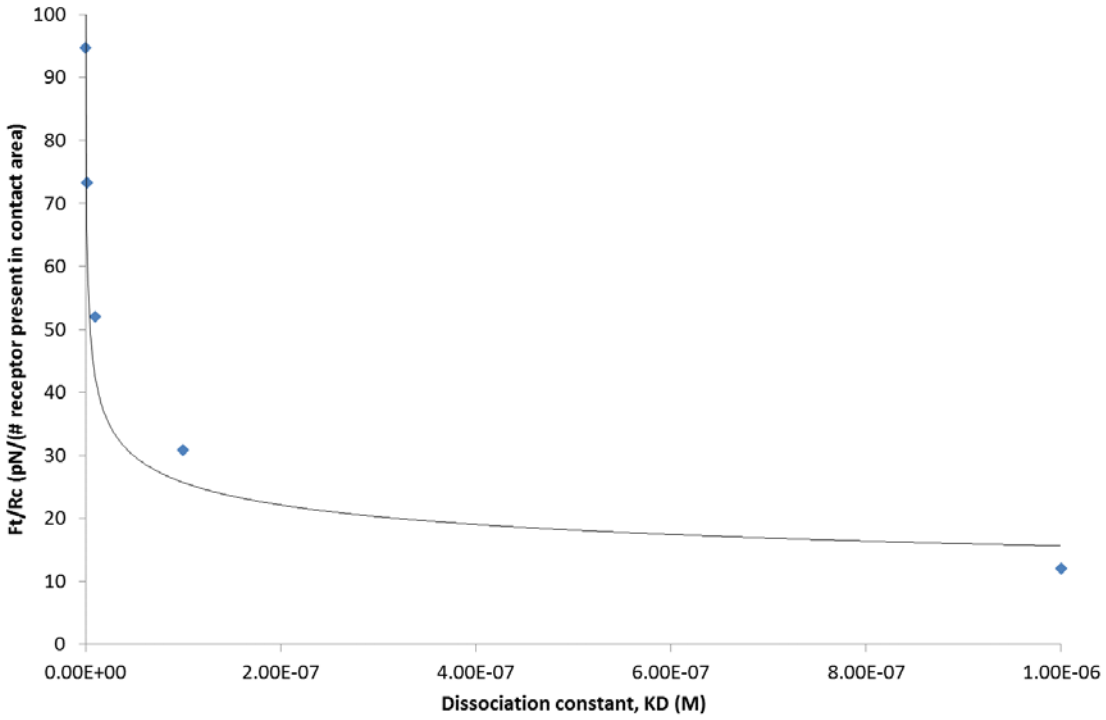

Figure 1-7. Adhesion strength per receptor present in the contact region (F_t/R_c) as a function of the dissociation constant (K_D). Adhesion strengths were determined from Equation 1.6. K_D ranges from 10^{-10} – 10^{-5} M.

1.10.9. Cell adhesion strength

The flowrate required to detach cells adherent with affinity interactions may be estimated by linking threshold bond strengths to shear stress. Drag forces required to detach a cell may be estimated by re-arranging Equation 1.7 to account for the force per cell:

$$F_t = \frac{2R_c k_B \Theta}{I_B} \ln\left(1 + \frac{N_L}{\eta K_D}\right) \qquad 1.7.$$

Quantitative output can then be converted into shear stress, as displayed in Figures 1-8 and 1-9 for high (10^{-6} M) and low (10^{-9} M) K_D values. Accounting for non-affinity adhesion forces, estimated to be ~100 pN per µm^2 contact area (Bell, 1978, Bell et al., 1984, Bryers, 2005), the shear stress required to detach cells adherent with non-affinity interactions may be

calculated by rearranging Equation 1.5 to calculate the equivalent shear stress to induce detachment:

$$\tau_w = \frac{F_{drag}}{6\alpha\pi r^2} \quad 1.8.$$

, where F_{drag} is equivalent to F_t, the force required to detach a cell from the surface, such that for a 10 µm diameter cell with a contact area of 0.5 µm^2, a drag force of ~0.12 Pa (1.2 dynes/cm^2) would be sufficient for detachment. Presented differences in the calculated adhesion strengths of cells with and without affinity interactions show good agreement with practical studies (Nordon et al., 1996 and 2004; Slowiaczek, 1998). These equations to calculate the force acting on a cell assume a hard sphere, meaning that force- (Nordon et al., 2004) or time-induced (Cuvelier et al., 2007) cell deformation is unaccounted for and actual forces acting on the cell – in particular the stressed bonds – may be lower.

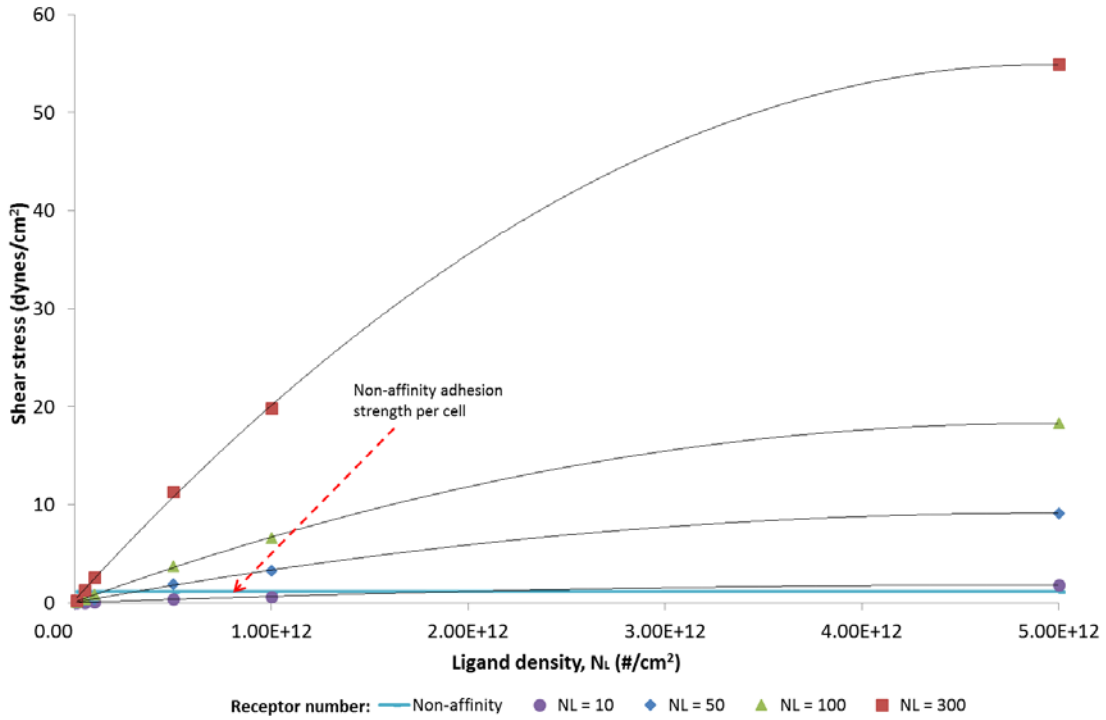

Figure 1-8. Effect of increasing ligand density and receptor number versus shear stress for a K_D value of 10^{-6} M. The ligand density ranges across from 1 x 10^{10} – 5 x 10^{12} per cm^2. The receptor density in the contact area ranges across 10, 50, 100 and 300 per cm^2. The non-affinity adhesion strength per cell is estimated to be equivalent to 1.2 dynes/cm^2. Data are calculated from Equation 1.7 and 1.8.

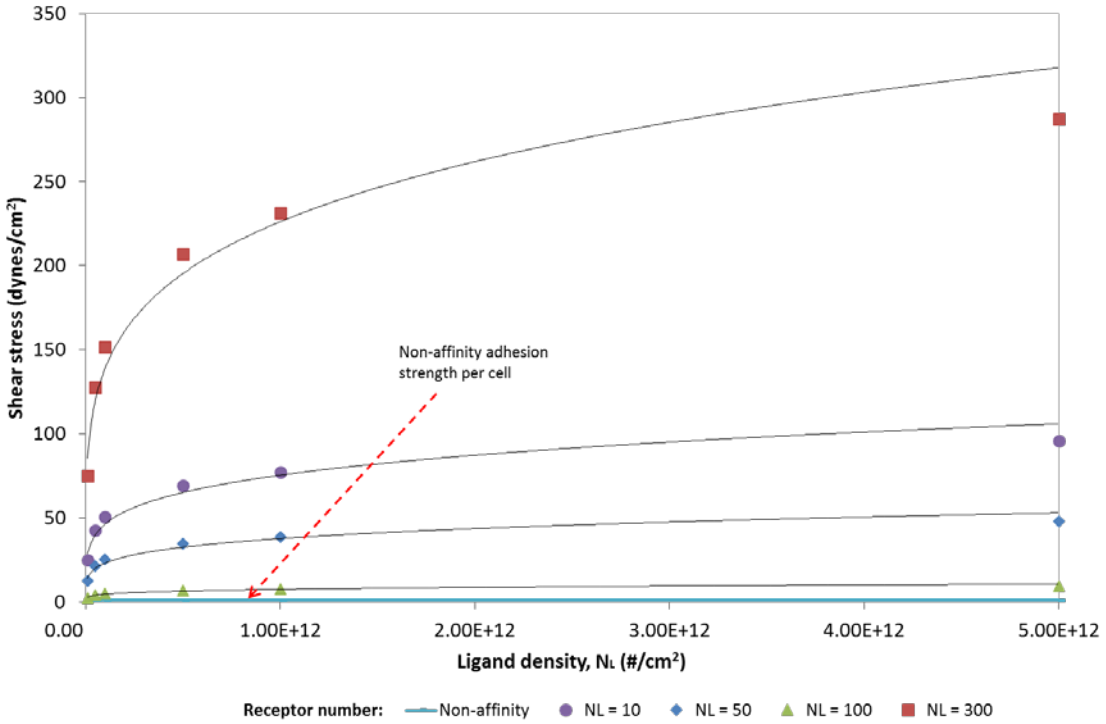

Figure 1-9. Effect of increasing ligand density and receptor number versus shear stress for a K_D value of 10^{-9} M. The ligand density ranges across from 1 x 10^{10} – 5 x 10^{12} per cm^2. The receptor density in the contact area ranges across 10, 50, 100 and 300 per cm^2. The non-affinity adhesion strength per cell is estimated to be equivalent to 1.2 dynes/cm^2. Data are calculated from Equation 1.7 and 1.8.

1.10.10. Detachment mechanisms

The precise mechanism of cell detachment is thought to occur via two possible mechanisms. The first is through a peeling mechanism; bonds at the side of the cell facing fluid flow are stressed more than those at the rear of the cell, initiating sequential rupturing (Chang and Hammer, 1996, Décavé et al., 2002). However, measurements of individual bond strengths (Dammer et al., 1996), or those using synthetic spheres coated with ligands incapable of extension (Kuo and Lauffenburger, 1993), where peeling would be more obvious, contradict this theory. In the second, the cell is assumed to adapt to shear stress through bond reinforcement (Choquet et al., 1997, Demali, 2004), resembling a tensegrity system (Ingber, 2014) where detachment occurs when the collective bond strength of all interactions is exceeded.

1.11. Summary

Many of the technical gains made by the cell therapy industry have occurred using conventional bioprocessing technology. It is anticipated that the scaled manufacture of pluripotent-derived cells will be subject to certain purity thresholds with reference to the presence of impure undifferentiated cells. These cells, caused by inefficiencient cell differentiation, can form teratomas *in vivo* and are a primary safety concern. Such impurities are expected to occupy a greater proportion of cells in larger batch sizes. Existing technologies do not have the capacity to effectively monitor or control impure cells during manufacturing at scale. Two technologies are therefore proposed to improve the performance of a pluripotent cell therapy manufacturing process: (1) a quartz crystal microbalance biosensor to detect impure cell populations either in real-time or at regular intervals during the cell differentiation process and (2) a scalable membrane to retain

impure cells and recover product cells post-differentiation, to increase cell purity to a safe level. Both systems will utilise shear stress-induced cell separation to differentiate between cells adsorbed with and without affinity interactions.

Chapter 2. Flow tube model

2.1. Introduction

For cells derived from pluripotent cells, ensuring higher purities (≥95 – 99 %) can prevent tumour formation (Lebkowski, 2011, Schriebl et al., 2012). This may be through: (1) the detection mechanisms of an acoustic biosensor to better understand the factors affecting pluripotent cell differentiation towards designated lineages or (2) through the use of a separation device to remove impure cells, thus increasing product cell purity. In pluripotent cell manufacture, the SSEA-4 antigen is present on undifferentiated pluripotent cells (Thomson et al., 1998) and is downregulated on differentiated cells (Chen et al., 2014).

Shear stress-induced affinity cell separation can be applied to differentiate between cells positive and negative for this SSEA-4 antigen. In transferring this concept to the acoustic QCM biosensor or a membrane separation device, as little as 5 dynes/cm^2 may be used to recover >95 % of product cells adsorbed without affinity interactions, with higher shear stresses (up to 200 dynes/cm^2) being required to recover cells adsorbed with affinity interactions (Slowiaczek, 1998, Nordon et al., 2004).

To study these interactions at a single-cell level, a small-scale device is necessary. Many methods exist for the study of cell-based affinity interactions, ranging from magnetic beads (Schriebl et al., 2010b) to flow cytometers (Quintanilla, 2013) and optical tweezers (Wang et al., 2011), but do not replicate the hydrodynamic environment of shear stress-induced affinity cell separation. However, transparent flow chambers provide visual and possibly quantitative feedback about how cells respond to shear stress (van Kooten et al., 1992, Xia et al., 1994). Indeed, a number of approaches have been used to study shear stress-induced

cell separation at small scales (Nordon, 1994, Pomianek, 1998, Nordon et al., 2004), providing the basis for larger separations capable of single-patient CD34+ cell transplants (Colton, 1996, Nordon et al., 1996, Slowiaczek, 1998).

To perform separation studies in glass flow tubes, antibody-coupled surfaces are required. Glass surfaces must first be modified to generate chemical functionalities, of which many methods have been presented (Vandenberg et al., 1991, Funk et al., 2012). Hydroxyl groups on cleaned glass can be chemically modified with aminosilanes, such as (3-aminopropyl)triethoxysilane to create terminal amine groups (Zhang et al., 2010, Terracciano, 2013) (Figure 2-1). Amine-functionalised surfaces provide a reactive platform to facilitate the deposition of glutaraldehyde, a homobifunctional cross-linker possessing aldehyde functionality (Figure 2-2). The aldehyde functionality can then react covalently with amine functionalities on glass and those present on proteins (Miller and Robyt, 1983, Kumar and Srivastava, 2010). However, the direct adsorption of IgG antibody onto such surfaces will lead to non-orientated immobilisation. Therefore, coupling Protein A to the surface (Figure 2-3), which has the capacity to bind IgG antibodies via their Fc base (Moks et al., 1986) would promote orientated immobilisation. Thus, when a cell suspension is introduced to the Protein A-coupled substrate, only cells tagged with IgG antibodies will be able to generate affinity interactions (Figure 2-4). Untagged cells, negative for the target antigen, will possess weaker cell-surface interactions and therefore have a higher propensity for detachment when exposed to shear stress (Nordon et al., 1996, Slowiaczek, 1998).

Figure 2-1. Reaction of cleaned glass with 3-APTES to create an amine-terminated surface.

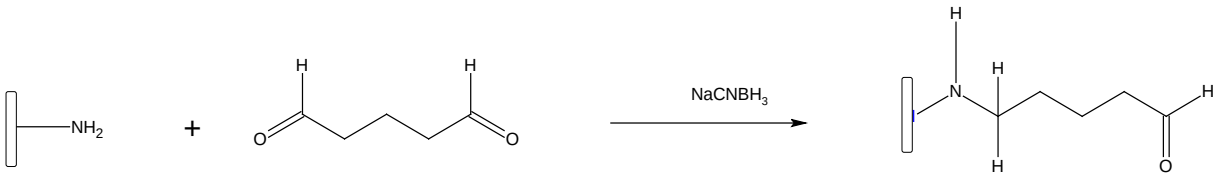

Figure 2-2. Reaction of glutaraldehde in the presence of sodium cyanoborohydride to reduce reversible Schiff bases into stable secondary amine bonds.

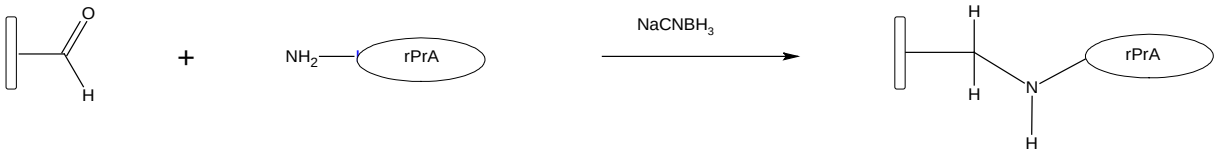

Figure 2-3. Immobilisation of rPrA via Schiff base formation and subsequent reduction to create a stable secondary amine bond.

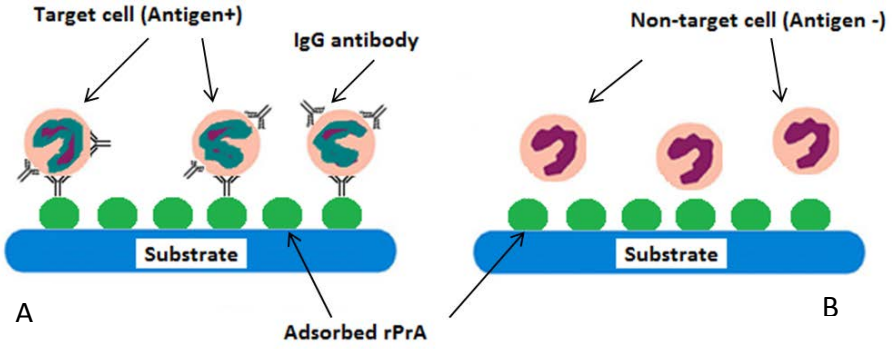

Figure 2-4. Reaction of immobilised rPrA with IgG-tagged cells. Cells adherent with multiple affinity interactions, in this instance facilitated by IgG-rPrA interactions (A), have a greater resistance to shear stress-induced detachment than those without (B).

Chapter aims and objectives:

- Develop a small-scale model to visually observe and determine a range of shear stresses capable of differentiating between cells adsorbed with and without affinity interactions

- Extract quantitative data and develop models to project cell separation inside an acoustic QCM biosensor and in a scalable separation device

2.2. Materials and methods

The following section details the materials and methods ultimately used to create, characterise and test rPrA-coupled glass flow tubes for cell adhesion studies.

2.2.1. Glass surface chemical modification

Glass microslides (borosilicate, 10 mm diameter; Fisher Scientific, Loughborough, UK) and beads (borosilicate, 212-300 µm; Sigma-Aldrich, Munich, Germany) were chemically modified to study create functional surfaces for chemical and morphological analysis and protein immobilisation.

2.2.2. Cleaning

Glass was cleaned in an ultrasonic bath first with acetone (2 minutes), followed by 95 % (v/v) ethanol and then 2 % (v/v) Liquinox (Cole-Parmer, London, UK), both for 20 minutes, before rinsing in deionised water and drying in a DCPro oven (BioCare Medical, Berkshire, UK) for 2 hours at 130 ^{o}C using a method described previously (Rowland et al., 1995).

2.2.3. Amination

Cleaned glass slides were then immersed in a 5 % (v/v) solution of 3-aminopropyltriexthoxysilane (APTES) (Sigma-Aldrich, Munich, Germany) in toluene for 1 hour, before rinsing successively in toluene and then deionised water in an ultrasonic bath for 10 minutes each. For glass micro-slides, care was taken to avoid rotation and ensure inter-batch consistency, since inverted slides exhibited different surface properties. The same procedure was repeated for glass beads, except that more vigorous washing was

implemented by manually shaking the beads aggressively before and after ultrasonic bath washing. Washed samples were then dried at 50 ^{o}C overnight in a DCPro drying oven (BioCare Medical, Berkshire, UK) (Terracciano, 2013).

2.2.4. Aldehyde functionalization

Amine-functionalised glass was immersed in 2.5 % (v/v) glutaraldehyde solution in 0.1 M sodium phosphate with 0.15 M sodium chloride (PBS) and 0.075 M sodium cyanoborohydride (pH 7) for 4 hours for glutaraldehyde deposition (Figure 2-2). Glass samples were then washed twice successively in methanol, acetone (Fisher Scientific, Loughborough, UK) and deionised water.

2.2.5. Protein adsorption

2.2.5.1. Recombinant Protein A (rPrA) and bovine serum albumin (BSA)

Recombinant Protein A (rPrA) (Prospec Bio, Ness-Ziona, Israel) was incubated with aldehyde-functionalised glass beads at a concentration of 1 mg/mL in PBS (pH 7) for 18 hours under agitation on an IKA VRX Vibrax horizontal shaking platform (Fischer Scientific, Loughborough, UK) at room temperature (~ 22 ^{o}C). rPrA-coupled glass beads were then sequentially washed in PBS, 1 M NaCl and de-ionised water, twice, using a micropipette to remove weakly adsorbed proteins. Reductive amination was then performed in 0.075 M sodium cyanoborohydride in PBS at pH 7 for 1 hour at room temperature on an orbital platform shaker (Cole-Parmer, London, UK), prior to washing in the aforementioned procedure. rPrA-coupled and rPrA-free aldehyde-functionalised glass beads were then blocked in 1 % (w/v) BSA (Sigma-Aldrich, Munich, Germany) in PBS for a further 2 hours at room temperature and rinsed in washing buffer. The adsorbed protein content of glass beads was quantified using the BCA assay (Section 2.4.5.).

2.2.5.2. IgG antibody adsorption

IgG binding capacity studies were performed using CD20 IgG antibody across a range of concentrations from 0 – 1.28 mg/mL to determine the adsorption capacity of rPrA-coupled beads. CD20 IgG antibody was purchased from The University of Birmingham Hospital (Birmingham, UK) at a concentration of 10 mg/mL (The CD20 IgG antibody is a chimeric mouse/human monoclonal antibody (mAb), comprising of a glycosylated IgG_1 kappa immunoglobulin with murine light and heavy-chain variable regions and human kappa and gamma-1 constant regions (Fc domain). It is commercially marketed as Mabthera®.) Samples were diluted in PBS (pH 7) from a 10 mg/mL stock solution and incubated for up to 2 hours in PBS with rPrA-coupled or rPrA-free aldehyde-functionalised glass beads blocked with 1 % BSA (w/v). Samples were then rinsed three times in PBS to remove unbound IgG. Adsorbed IgG was then eluted in 0.5 mL of 0.1 M sodium citrate at pH 2.5 following a 10 minute incubation period. IgG antibody in eluted samples was calculated using a Nanodrop 2000 UV spectrophotometric instrument (Thermo Scientific, Loughborough, UK) by placing 2 µL on the sensor and recording the absorbance at 280 nm.

2.2.5.3. Glass flow tube modification

The same chemical modification and rPrA coupling procedures were then transferred to transparent glass flow tubes to enable the study of cell responses to shear stress.

2.2.5.4. Chemical modification

Glass flow tubes (Camlab, Cambridge, UK) (length 5 cm; width 3 mm; thickness 0.3 mm) were treated in a similar fashion as the glass microslides and beads described above. However, chemical modification was performed under flow (5 mL/hr) using a peristaltic pump (Watson-Marlow, Falmouth, UK). Following cleaning and drying, where cells were

dipped in respective cleaning solutions outlined in Section 2.2.2., dried flow tubes were wrapped in cellophane (0.5 x 2 cm) at the inlet and connected to Gore® STA-PURE tubing (Watson-Marlow, Falmouth, UK). Tubes were then chemically modified by flowing APTES through the tube at 5 mL/hr, followed by rinsing (20 mL/hr) using both toluene and de-ionised water, applied sequentially, twice, for 10 minutes each to remove physisorbed layers (Section 2.2.3). For cleaning, tubes were removed dried separately as described for glass beads and slides. Thereafter, glutaraldehyde treatment was also performed as detailed in Section 2.2.4.

2.2.5.5. PrA and BSA protein adsorption

Aldehyde-modified glass flow tubes were then connected to a 100 µL micropipette via tygon tubing (Cole-Parmer, London, UK) and cellophane tape. A 1 mg/mL solution of rPrA in PBS (pH 7) was then injected into the tube and incubated for 4 hours at room temperature. Protein solution was agitated using a connected micropipette every 30 minutes. Following incubation, excess protein was removed by gently rinsing with PBS. Reductive amination in a 0.075 M sodium cyanoborohydride solution in PBS was then performed for 1 hour at room temperature. Excess solution was then removed and tubes were rinsed in PBS, 1 M NaCl and de-ionised water. Thereafter, tubes were blocked in 1 % (w/v) BSA for 2 hours in PBS, prior to washing in PBS, 1 M NaCl and de-ionised water prior to cell adsorption studies.

2.2.6. Cell detachment studies

2.2.6.1. Process setup

Aldehyde-functionalised flow tubes for cell adhesion studies were inserted into the process presented in Figure 2-5. The inlet and outlets were wrapped in cellophane, connected to tygon tubing at both ends and attached to a microscope slide (dimensions: 6 x 2.5 cm)

(Sigma-Aldrich, Dorset, UK) using autoclave tape. The microscope slides were then positioned underneath an inverted Nikon microscope lens which was set at x10 magnification and connected to a Nikon DS L3 LCD monitor (Nikon, Tokyo, Japan). The tube inlet was then connected to an Alaris IVAC P7000 syringe pump (CareFusion, St Albans, UK) containing a 50 mL syringe filled with 1 % BSA (w/v) in PBS via a 3-way valve. The side inlet of the 3-way valve was then attached to a 10 mL syringe containing 1 % (w/v) BSA in PBS. Tubes were washed for 5 minutes at 50 mL/hr and then incubated statically in 1 % (w/v) BSA in PBS for 2 hours. Prior to cell binding, tubes were washed in in PBS at 20 mL/h for 5 minutes to remove excess BSA.

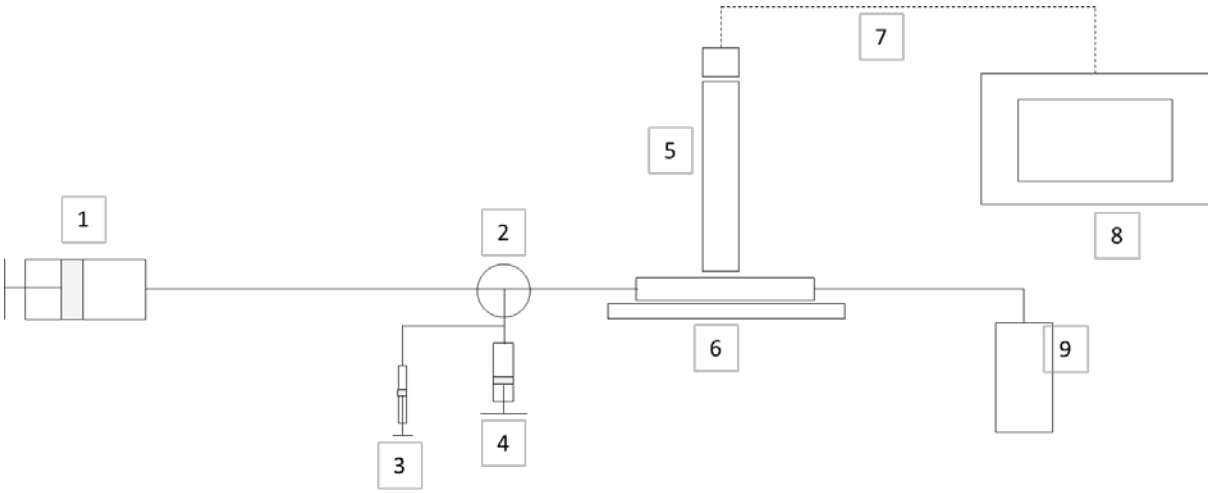

Figure 2-5. Unit schematic for cell binding studies. Components are listed as follows: 1 = 50 mL syringe connected to a syringe pump; 2 = 3-way valve; 3 = 1 mL syringe for cell injection with a needle to be injected into the side inlet tubing; 4 = 10 mL syringe; 5 = microscope connected to camera; 6 = flow tube; 7 = connection lead; 8 = camera display screen; 9 = 50 mL collection vessel.

2.2.6.2. Cell culture

Two B-lymphocyte cell lines were used: (1) Toledo CD20 antigen-positive B-lymphocytes cells from ATCC (LGC Standards, Middlesex, UK) with an affinity for the IgG CD20 antibody and (2) CCRF-HSB-2 HLA-A2 antigen-positive B-lymphocytes from Sigma-Aldrich (Dorset, UK) with no affinity for CD20 IgG.

Cells were cultured in 90 % RPMI-1640 with 2 mM glutamine and 10 % (v/v) foetal bovine serum (FBS) supplemented with 1 % Pen-Strep (Sigma-Aldrich, Munich, Germany). Cell cultures were maintained at $3x10^5$ to $1x10^6$ cells/mL in 5 % CO_2 and 95 % O_2 atmospheric content at 37 ^oC using a Heracell 150i CO_2 incubator (Thermo Scientific, Loughborough, UK) and cultured every 2-3 days.

Additional cell details are displayed in Table 2-1 below. The purpose was for the CD20+ cells to mimic pluripotent stem cells expressing the SSEA-4 antigen, whilst HLA-A2+ cells were intended to mimic pluripotent-derived cells, such as cardiomyocytes, where the SSEA-4 antigen had been down-regulated.

Table 2-1. Cell types and properties.

	Toldeo	**CCRF-HSB-2**
Cell type	B-lymphocyte	
Location	Peripheral blood	
Species	Human	
Antigen expression	CD10, CD19, CD20, CD38	HLA-A1, HLA-A2, HLA-B17, Cw2, CD5, CD7
Cell size[a]	11.0 ± 7.2 um	11.5 ± 6.0 um
Status	Target, non-product cell	Non-target, product cell
CD20 antigens	109,000[b]	-

[a] determined using a Nucleocell Counter; [b] Experimental estimate (Ginaldi, 1998)

2.2.6.3. Cell detachment

Cells were harvested on the condition that viability (based on trypan blue membrane exclusion) blue was in excess of 99 %. Cells were centrifuged in a Heraeus™ Labofuge 400 (Thermo Scientific, Loughborough, UK) at 1,200 rpm for 5 minutes and re-suspended twice in 1 % (w/v) BSA in 1 X Dulbecco's Phosphate Buffered Saline (DPBS) (Sigma-Aldrich, Dorset, UK) to a concentration of $3x10^7$ cells/mL and incubated with or without 10 µg/mL of CD20 IgG antibody at 4 ^oC for 30 minutes. Prior to injection, cells were centrifuged and re-suspended twice in 1 % (w/v) BSA in DPBS to remove unbound IgG and achieve a final concentration of $3x10^6$ cells/mL. The cell suspension was then drawn up into a 1 mL syringe,

after which a needle was attached. Air was removed by rotating the syringe vertically and tapping the needle whilst simultaneously forcing fluid out of the nozzle.

The side inlet of the 3-way valve was then positioned to allow fluid from the 10 mL syringe to enter into the tube. The cell suspension in the 1 mL syringe was then injected into the tygon tubing of the side inlet port (connected to syringe 4 in Figure 2-5). The addition of cells into the flow tube using the side inlet syringe (4) was monitored by measuring the microscopic output from the camera screen. The injection was ceased when the surface appeared saturated and cells were evenly distributed. The 3-way valve was then positioned to allow flow from the syringe pump into the tube whilst blocking side-inlet flow. Adsorbed cells were then incubated for a 30 minute period, prior to detachment studies being performed.

Detachment studies involved the sequential application of shear stress over 1, 5, 10 and 25 dynes/cm^2 for 3 minute intervals. Images of cells were taken at six regions across the flow tube following the application of each shear stress over a 2 minute period. Pooled cells were collected in a 50 mL tube and concentrated by centrifuging at 1,200 rpm. Viability, based on membrane exclusion using trypan blue, was then measured for pooled cells.

A second study was performed to qualitatively assess how adsorbed cells responded in real time to applied shear stress. Video recordings of the camera screen were performed prior to, during and after applied shear stresses of 5 and 25 dynes/cm^2 until steady state was reached.

2.3. Theoretical considerations

The controlled application of shear stress relies on the geometric arrangement inside the device as well as the volumetric flowrate. Such calculations rely on the assumption of laminar flow within the system (Re << 2100) determined using Equation 1.3 (Rothfus et al., 1957). Cells are assumed to have the same density as that of water (1,000 kg/m^3) so that the suspension resembles a Newtonian fluid, transported via convective processes with a density of 1000 kg/m^3 (Kasza et al., 2007).

2.3.1. Shear stress

Shear stresses within the flow tube were estimated at the wall of the vessel based on the equation for a parallel plate model (Bacabac et al., 2005):

$$\tau = \frac{3Q\mu}{2w(h/2)^2} \qquad 2.1.$$

, where Q = flowrate (m^3/s); μ = dynamic viscosity (kg/m.s); w = chamber width (m); h = chamber height (m); and τ = shear stress (1 Pa = 0.1 dynes/cm^2). The cell-surface contact area can be estimated as a function of shear stress (Bose, 2009) and is represented previously by Equation 1.2.

The number of moles of protein on the surface may be calculated from:

$$Moles\ of\ protein\ (mol) = \frac{mass\ protein\ (g)}{molecular\ weight\ protein\ (\frac{g}{mol})} \qquad 2.2$$

, where 1 kDa = 1,000 Da = 1,000 g/mol.

Number of moles of protein in solution may be calculated from:

$$Moles\ of\ protein\ \left(\frac{mol}{L}\right) \times molecular\ weight\ protein\left(\frac{g}{mol}\right) = mass\ of\ protein\ in\ solution\left(\frac{g}{L}\right) \quad 2.3$$

Number of protein molecules in both instances determined from Equations X and Y may be calculated from:

$$Number\ of\ molecules\ (\#) = Avogadro\ constant\ (mol^{-1})\ \times moles\ of\ protein\ (mol) \quad 2.4$$

, where the Avogadro constant = 6.02 x 10^{23} mol^{-1}.

2.4. Analysis and characterisation

2.4.1. Atomic force microscopy

An Explorer atomic force microscope (Bruker TESP, Coventry, UK) was used to assess the surface topography of modified glass at an approximate frequency of 330 kHz and k = 20-80 N/m. Duplicate images at different sites were taken for each sample.

2.4.2. X-ray photoelectron microscopy (XPS)

XPS was performed on chemically modified glass slides using a K-Alpha™ X-ray Photoelectron Spectrometer (ThermoScientific, Loughborough, UK). Photoelectrons were excited using mono-chromated Al K alpha x-rays (1486.6 eV). Spectra were collected at an electron emission angle of 90 degrees with respect to the sample surface plane. High-resolution scans (50 eV pass energy) of all elements were taken and reported as duplicates from different batches for each condition. The sampling depths at 90 degree electron take-off angles were estimated to be 100 nm. High resolution scans were performed on carbon, nitrogen, silicon and oxygen. A curve-fitting program that uses a Gaussian function was used

to deconvolute the XPS peaks. The samples were dried and stored in a desiccator prior to analysis.

2.4.3. TNBS assay

2,4,6-trinitrobenzenesulfonic acid (TNBS) was used to quantify silane deposits via a reaction with amine groups (Hermanson, 1992). A solution containing 10 µL of 1 M TNBS (Sigma-Aldrich, Munich, Germany) and 1.5 mL of 0.05 M (Borax) (Sigma-Aldrich, Munich, Germany) was mixed with glass beads and heated to 70 ^{o}C, prior to cooling. Supernatant was then removed and glass material was washed sequentially in deionised water, 50 % (v/v) acetone in deionised water, 100 % acetone and deionised water using a plastic micropipette. After washing, samples were then heated to 70 ^{o}C in 1.5 mL of 1 M NaOH and supernatant was measured at 410 nm using a UV spectrophotometer (Shimazdu, Tokyo, Japan) to quantify the amount of picricsulfonic acid eluted. A calibration chart was created using known amounts of picric acid. This was used to convert measured absorbance into amine deposits on the basis of a 1:1 reaction.

2.4.4. Silver mirror test

Aldehyde functionalities were measured using Tollen's reagent on both APTES and glutaraldehyde-treated glass (Fieser, 1987). Prior to conducting the reaction, all tubes were cleaned with 10 % (v/v) sodium hydroxide. Thereafter, 1 mL of 0.2 M sodium nitrate solution was then mixed with 1 mL of 10 % (w/v) sodium hydroxide solution (Sigma-Aldrich, Munich, Germany) to create silver oxide. Dilute ammonia solution (2 %, v/v) was then added slowly to dissolve the silver oxide. Both APTES and glutaraldehyde-treated APTES beads were then soaked in this solution in a water bath at 37 ^{o}C for 15 minutes. Beads were then removed with tweezers and rinsed in de-ionised water prior to imaging.

2.4.5. BCA assay

The adsorbed protein content of aldehyde-functionalised glass beads was determined using the BCA assay (Pierce Biotechnology, Illinois, USA) (Figure 9). Beads were incubated in 0.1 mL of PBS and 1.9 mL of working reagent for 30 minutes at 37 ^{o}C. Supernatant was extracted, inserted into a polystyrene cuvette (Fischer Scientific, Loughborough , UK) and absorbance was measured at 562 nm using a UV spectrophotometer (Shimazu, Tokyo, Japan). Stock solutions containing known amounts of protein samples were used to create standard curves to determine the amount of protein adsorbed.

2.4.6. Contact angle

Contact angles on modified glass slides were measured using deionised water to assess surface hydrophobicity. A 2 µL droplet of deionised water was deposited onto each type and the contact angle was measured using a DataPhysics OCA 20 system and device software (Data Physics Instruments GmBH, Filderstadt, Germany).

2.4.7. BET surface area

The Brunauer Emmett-Teller (BET) method was used to determine the surface area of aldehyde-functionalised glass beads. Weighed samples were degassed initially at 90 ^{o}C for 2,000 minutes and then at 140 ^{o}C for 600 minutes under a vacuum of < 10 µmHg. To determine the surface area the sample was cooled to a cryogenic temperature (77 K) and an adsorptive (nitrogen) was admitted to the sample in controlled increments. After each dose of nitrogen, the pressure was allowed to equilibrate and the quantity of gas was calculated, indicating the external surface area and pores of an assumed monolayer.

2.4.8. Fluorescent IgG staining and binding to cells

CD20 antigen distribution across Toldeo (CD20+) and CCRF-HSB-2 (HLA-A2+) cells was qualitatively assessed using fluorescein-tagged CD20 IgG. The CD20 IgG antibody was incubated with an NHS-fluorescein conjugate for 1 hour at room temperature, before the solution was purified in a 7 K MWCO Zeba spin column (Thermo Fischer Scientific, Cramlington, UK). The conjugate was subsequently incubated with Toledo and CCRF-HSB-2 cells respectively for 30 minutes at 4 ^{o}C in 1 % BSA (w/v) in DPBS. Cells were then centrifuged at 1,200 rpm and re-suspended in 1 % BSA (w/v) in PBS twice, prior to visualisation using a fluorescent microscope.

2.4.9. Cell counting

A high-throughput cell counting method was devised using computational software to quantify adherent cells. Images were recorded at x10 magnification on microscope and analysed with NIS-Elements AR software (Nikon, Tokyo, Japan) in MCH mode. Red, green and blue absorbance channels were adjusted to 60 – 130, 0 – 20 and 0 - 180 nm, respectively, to distinguish cells from the flow tube surface. Sizes above or below 10 – 50 pixels were eliminated from the analysis to avoid debris affecting the interpretation.

2.5. Results and Discussion

A range of tests were performed to assess the chemical functionality and morphological arrangement of deposited layers on the glass surface. XPS, based on the elemental composition of the first 100 nm depth of glass microslides was used to assess each surface following sequential cleaning, silanization (using 3-APTES) and glutaraldehyde treatment. Elemental compositions are presented in Table 2-2 and high resolution scans of nitrogen and carbon in Figures 2-6 and 2-7.

Nitrogen spectra, absent on cleaned glass, were present on APTES- and glutaraldehyde-treated glass. Peaks at 401.5 (NH_3^+) and 399 eV (NH_2) were detected. The protonated peak was attributed to terminal amine reactivity with adjacent hydroxyl groups of APTES molecules or glass, as reported elsewhere (Gao, 2006, Metwalli et al., 2006, Martin et al., 2007). A reduction in the nitrogen peak intensity and elemental content post-glutaraldehyde treatment was attributed to carbon content in glutaraldehyde (Martin et al., 2007). Nitrogen content in both APTES- and glutaraldehyde-treated APTES glass showed it to be several times higher than that observed for monolayers, which are typically 1 – 2 % (Metwalli et al., 2006), suggesting multilayer formation (Vandenberg et al., 1991, Williams et al., 2012).

Carbon was detected on all surfaces, although peaks at 284.8 eV (C-C), 286 eV (C-O-C) and 289 eV (O-C=O) on glass were attributed to adventitious carbon contamination (Smirnova, 2009) which was much higher (8.4 ±0.1 %) (mean ± SEM) than previous studies (< 2%) (Barr and Seal, 1995, Evans et al., 2004), suggesting that either the solvent-based cleaning method was ineffective and that a more aggressive acid-based washing (Chandradoss et al., 2014) is preferable, or that the cleaning environment was contaminated. More pronounced carbon peaks were identified on both the APTES- and glutaraldehyde-treated APTES surface: the 284.4 eV peak was attributed to the propyl group in APTES and the pentyl group in glutaraldehyde; 288.5 eV (present on glutaraldehyde-treated APTES slides only), was ascribed to the aldehyde group of glutaraldehyde (Smirnova, 2009).

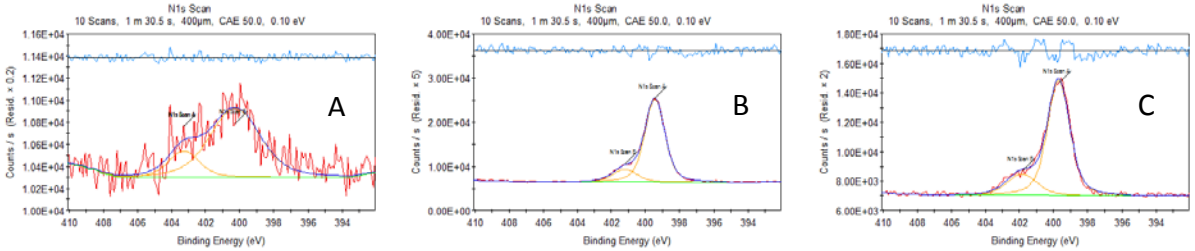

Figure 2-6. High resolution nitrogen 1s scans on cleaned glass (A), APTES-glass (B) and APTES-glass treated with glutaraldehyde (C).

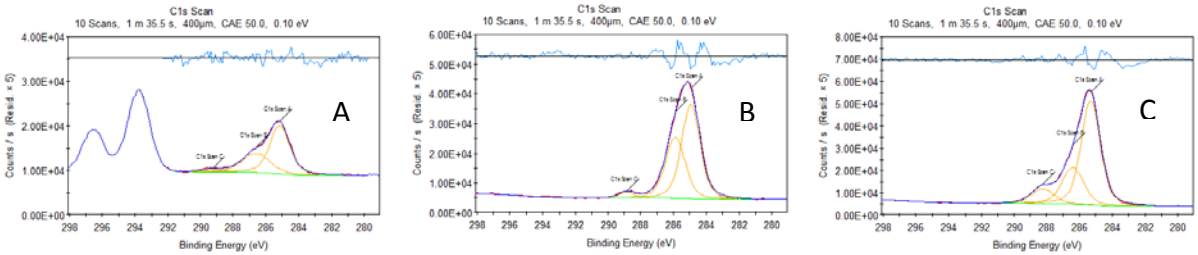

Figure 2-7. High resolution XPS carbon 1s scans on cleaned glass (A), APTES-glass (B) and APTES-glass treated with glutaraldehyde (C).

Table 2-2. XPS elemental composition of the first 100 nm depth of modified glass slides and contact angle measurements for modified glass slides

Material coating	Terminal layer	XPS elemental composition (%)			
		Carbon	Oxygen	Silicon	Nitrogen
Glass	Hydroxyl	8.4 ± 0.1	63.1 ± 0.3	28.5 ± 0.3	0 ± 0
APTES	Amine	46.1 ± 0.8	27.4 ± 0.0	16.1 ± 0.4	10.5 ± 1.2
Glutaraldehyde	Aldehyde	58.7 ± 2.6	24.6 ± 0.1	9.9 ± 1.6	6.8 ± 0.8

Data are displayed as the mean ± SEM for n = 2 runs for XPS and mean ± SD for n = 9 runs for Contact angle measurements

2.5.1. Surface analysis

The hydrophobicity of modified glass surfaces was determined using contact angle measurements. Data are displayed in Table 2-3 and images in Figure 2-8. Cleaned glass surfaces were hydrophilic (contact angle under 90^{o}), although measured contact angles were higher than those attained elsewhere (Hong et al., 2007, Williams et al., 2012), owing to the higher surface tension of contaminated glass (Ebnesajjad, 2006). Following APTES treatment, contact angles increased but remained hydrophilic, resembling those of thicker deposits (>40 ^{o}) (Williams et al., 2012). A small increase in hydrophobicity following glutaraldehyde treatment, contrasting with the more hydrophilic equivalents observed elsewhere (Hong et al., 2007), was attributed to the greater surface roughness of the slides (Yoshimitsu et al., 2002).

Table 2-3. Contact angle measurements for chemically modified glass slides.

Material coating	Terminal layer	Contact angle
Glass	Hydroxyl	32.2± 6.7[a]
APTES	Amine	55.7 ± 3.1[b]
Glutaraldehyde	Aldehyde	61.2 ± 2.7[c]

Surfaces with the same subscripts are not statistically different at the 5 % significance level based on a T-test. n = 9 runs were performed per sample. Data displayed as mean ± SD.

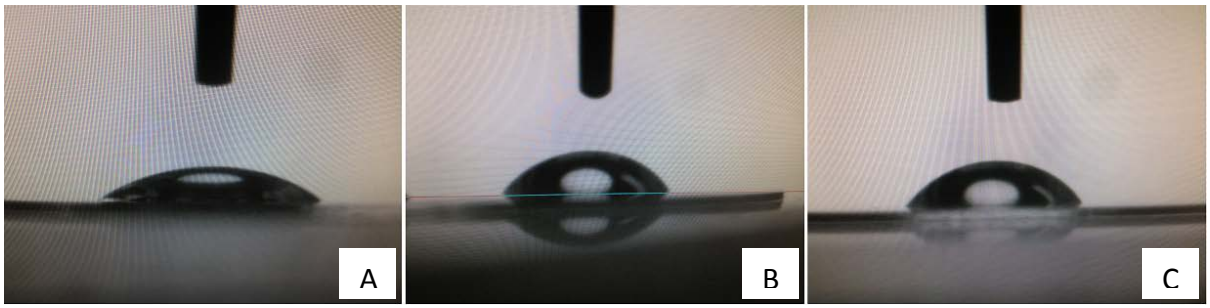

Figure 2-8. Contact angles for cleaned glass (A); APTES-treated glass (B) and APTES-glass treated with glutaraldehyde (C).

Surface roughness (Table 2-4) and representative micrographs (Figures 2-9 to 2-12) are presented below. Micrographs revealed that glass was flat, abrasive and with low surface roughness (Figure 2-9). Conversely, APTES treatment yielded smoother deposits, but was rougher and thicker due to aggregate formation (Figures 2-10 and 2-11), consistent with the high nitrogen content reported from XPS analysis (Williams et al., 2012). Glutaraldehyde-treated APTES revealed similar morphology, with large deposits and a rougher variable surface rendering it indistinguishable from APTES-treated glass (Figure 2-12).

Table 2-4. Surface roughness for modified glass slides using AFM

Terminal surface	Roughness (nm)		Thickness (nm)
	R_a	R_{rms}	
Glass	0.95 ± 0.10	1.60 ± 0.14	4.19 – 5.13
APTES	9.35 ± 2.08	12.75 ± 2.86	24.70 – 57.78
Glutaraldehyde	25.25 ± 4.84	33.90 ± 4.67	19.11 – 30.76

Roughness data are displayed as the mean ± SEM for n = 2 samples. R_a = roughness average; R_{rms} = root mean squared roughness. Image dimensions are 2 x 2 µm.

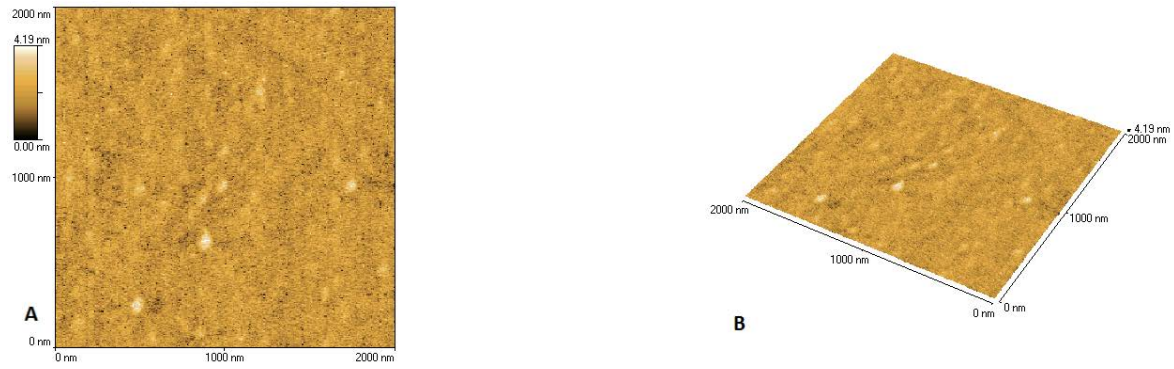

Figure 2-9. AFM images for glass (2 x 2 µm) in a two-dimensional display (A) and a three-dimensional display.

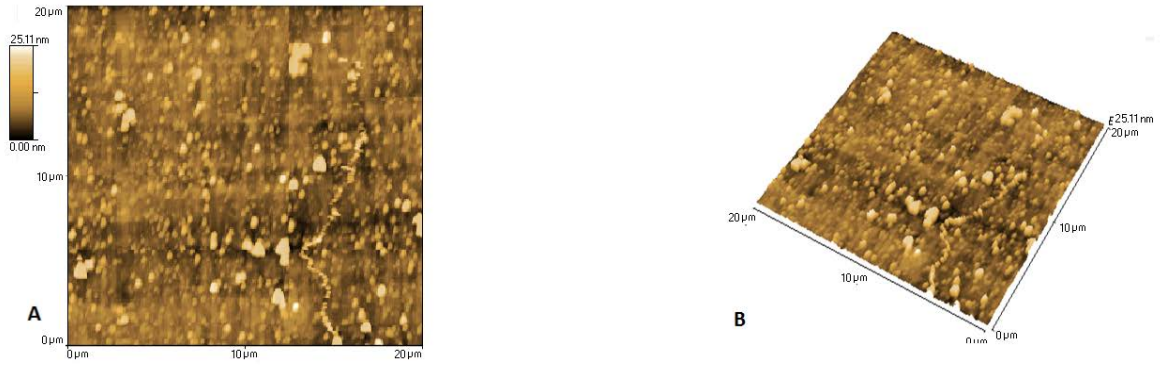

Figure 2-10. AFM images for aminated glass (2 x 2 µm) in a two-dimensional display (A) and a three-dimensional display.

Figure 2-11. AFM images for aminated glass (20 µm x 20 µm) in a two-dimensional display (A) and a three-dimensional display.

Figure 2-12. AFM images for aldehyde-treated aminated glass (2 x 2 μm) in a two-dimensional display (A) and a three-dimensional display.

Taken together, these findings indicate chemical deposition onto glass surfaces, but they also demonstrate excessive APTES physisorption through aggregation. APTES polymerisation, enhanced by time (Williams et al., 2012) and a higher APTES concentration (5 %) than typically used (Vandenberg et al., 1991), are most likely to blame for aggregate formation. The ineffective removal of these deposits from glass slide surfaces was attributed to the inability to employ aggressive washing procedures using glass microslides. This limited their usability in protein adsorption studies; physisorbed materials often lead to ligand leaching (Hong et al., 2007), which is undesirable for cell separation. Thus, glass beads were created using the same protocol, but were subjected to a more vigorous washing procedure to remove deposits.

2.5.2. Chemical group functionality measurements

BET surface area analysis performed on aldehyde-functionalised glass beads revealed an approximate surface area of 0.0296 ± 0.0013 m^2 per gram of aldehyde-functionalised beads (mean ± SD). This enabled aminosilane deposits to be quantified using the TNBS assay (Hermanson, 1992). A calibration chart (Figure 7-3) allowed surface APTES deposits to be estimated based on picric acid elution and data are presented in Table 2-5. APTES-treated

glass was consistent with monolayer formation (1 – 10 deposits/nm^2) (Kurth and Bein, 1993) and APTES beads treated with glutaraldehyde demonstrated a coverage efficiency above 90 %.

Table 2-5. Number of APTES deposits on APTES and glutaraldehyde-treated APTES glass beads.

Surface	No. of APTES deposits/nm^2
Amine	7.2 ± 2.5
Aldehyde	0.7 ± 0.6

Signals generated by glass were deemed to be negligible (< 0.2 per nm^2). Both surfaces were statistically significant at the 5 % level. The TNBS calibration chart is displayed in Figure 7-3.

Aldehyde functionalities were qualitatively measured using Tollen's reagent. APTES-coated glass slides stained a red/brown colour, possibly indicating reactivity with amine functionalities or contaminants (Ahluwalia, 2000), whilst the aldehyde-functionalised beads stained black (Figure 2-13). The latter reaction was consistent with the oxidation of aldehyde functional groups to create silver metal (represented by black precipitate) (Fieser, 1987, Ahluwalia, 2000).

Figure 2-13. Representative staining images of APTES (A) and glutaraldehyde-treated APTES (B) glass beads stained using Tollen's reagent.

2.5.3. Static protein binding studies

Protein adsorption capacities onto aldehyde-functionalised glass beads are presented in Table 2-6. The purpose was to estimate the adsorption capacities of glass flow tubes, which have a very low surface area-to-volume ratio by using non-porous glass beads, which have a much higher surface area-to-volume ratio. Accounting for the BET surface area, the rPrA density on aldehyde-modified beads ranged from 1,272 – 5,004 molecules per nm^2 (n = 5),

equating to approximately 12 – 17 nm per molecule, assuming monolayer formation and no aggregation. For BSA, the density was 1,004 – 1,673 molecules per μm^2 with spacing of 24 – 32 nm (n = 5). BSA adsorbed on rPrA-coupled beads was 1,039 – 2,430 molecules per nm^2 with spacing between 20 – 31 nm. Whilst variable, perhaps owing to functional group heterogeneity, these findings are similar to those reported for previous cell separation studies relying on affinity interactions (Colton, 1996).

Table 2-6. Protein binding onto aldehyde-functionalised glass beads

Adsorbed protein	Density (#/μm^2)	Distance (nm/molecule)
rPrA	1,272 – 5,004	12 – 17
BSA	1,004 – 1,673	24 – 32
rPrA-BSA[a]	1,809 – 2,266	20 – 31

Molecule arrangement assumes a monolayer with square-lattice formation. Data points are displayed as the minimum and maximum. Each rPrA and BSA molecule are assumed to represent a square 50 Å and each BSA molecule occupies a square 35 Å. [a] refers to BSA adsorption only. Data were subtracted from the mean values generated by aldehyde-functionalised beads, and in the care of rPrA-BSA, rPrA-coupled beads. Calibration curves for rPrA and BSA are displayed in Figure 7-1 and 7-2 respectively. Data are displayed as the range (minimum – maximum). BCA calibration charts are displayed in Figures 7-1 and 7-2 for rPrA and BSA respectively.

2.5.4. IgG binding capacity

Whilst a high ligand density is desirable, the IgG binding capacity of rPrA, will determine the number of affinity interactions between the cell and the surface. On most Protein A adsorbents, IgG:PrA ratios are approximately 1:1, in spite of the possible 5 – 7 Fc binding domains available (Moks et al., 1986, Hahn et al., 2003). Observed differences in the IgG:PrA ratio are often attributed to variable surface chemistries (Castilho et al., 2000). To deduce this, the binding capacity was determined from a binding saturation curve (Figure 2-14) with accompanying data Table 2-7.

The IgG binding capacity of BSA-blocked rPrA-coated surfaces was 0.042 ± 0.007 ng/cm^2 (1.37 ± 0.18 x 10^{11} IgG molecules per cm^2) of IgG for rPrA-coated beads. The binding equilibrium constant, K_d, was 2.16 ± 0.01 x 10^{-6} M and the non-specific binding was 0.0052 ± 0.0035 ng/cm^2. These equate to an approximate IgG to rPrA ratio of 0.71 ± 0.16, which is

lower than that observed in other studies (Colton, 1996, Castilho et al., 2000). The equilibrium constant, K_a, was ~4.6 x 10^5 M^{-1}, which is marginally in excess of that recommended for ligand leakage (Ohlson et al. 1997, Castilo et al., 2000). This could be either attributed to inefficient elution, rPrA aggregation or experimental inaccuracies in rPrA measurements.

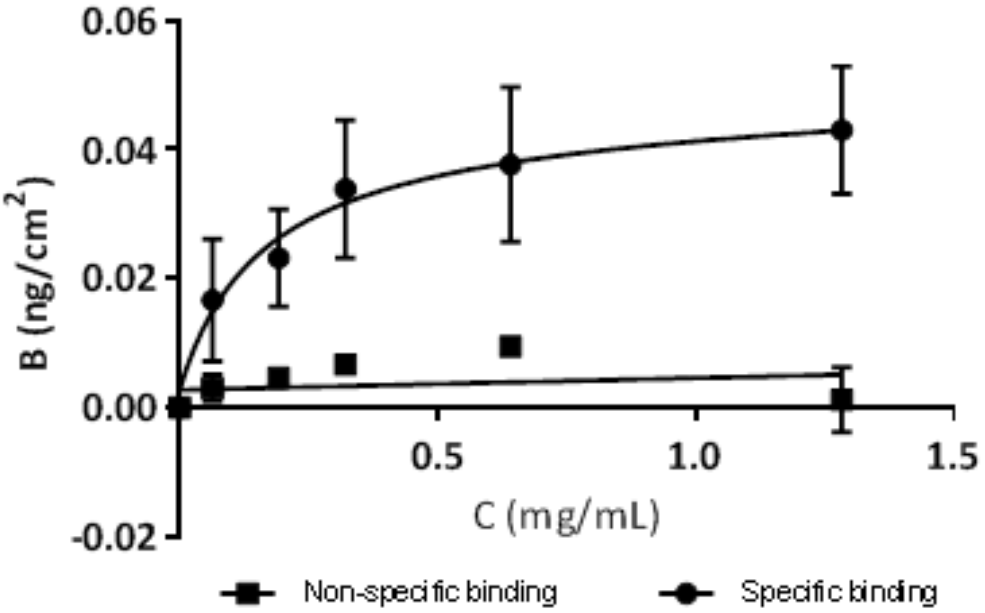

Figure 2-14. Binding saturation curve for IgG adsorption onto rPrA-coupled glass beads (specific) (n = 3) and onto BSA only beads (non-specific) (n = 5). B = IgG adsorption onto the substrate and C = the concentration of IgG in solution. Glass bead surface area was deduced from BET surface area analysis. Data are displayed as the mean ± SD.

Table 2-7. Binding data for IgG adsorption onto rPrA-coupled glass beads and onto BSA only beads.

Parameter	Value	Unit
B_{max}	0.042 ± 0.007	ng/cm^2
B_{max} (nsb)	0.005 ± 0.004	ng/cm^2
K_d	0.160 ± 0.006	mg/mL
	2.16 ± 0.01 x 10^{-6}	M
IgG:rPrA	0.71 ± 0.16	-

Glass bead surface area was deduced from BET surface area analysis. Data are displayed as the mean ± SD.

2.5.5. IgG binding to cells

CD20 IgG binding to cells was qualitatively assessed by conjugating fluorescein to the IgG antibody. Fluorescent microscopy revealed specific, heterogeneous and clustered CD20 IgG

antibody binding to CD20+ cells (Figure 2-12 A), but an absence of CD20 IgG antibody binding to HLA-A2+ cells (Figure 2.12 B). Based on an estimated number of CD20 antigens per CD20+ lymphocyte cell (mean = 109,000) (Ginaldi, 1998) and the density of rPrA on the surface, the number of possible immunoaffinity interactions between the cell and the surface is approximately 960 ± 126 per μm^2.

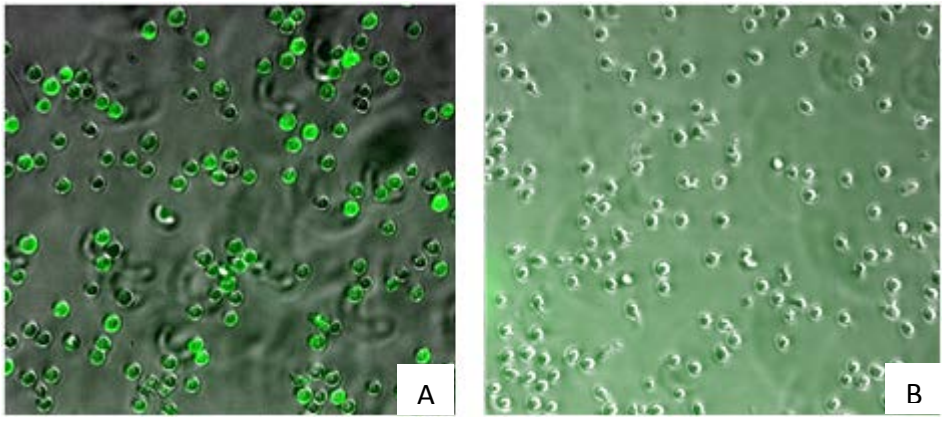

Figure 2.15. Fluorescent microscopy images at x10 magnification of (A) CD20+ cells stained with CD20 IgG antibody, indicated by green fluorescence and (B) HLA-A2+ cells showing no evidence of staining from CD20 IgG antibody. The difference in the image brightness is due to an attempt to maximise any fluorescent signal. The variation in CD20+ cell staining suggests that cells express a range of CD20 antigens across a given cell population.

2.5.6. Cell detachment studies

Differences in the adhesion strength of cells adsorbed to the surface with and without affinity interactions were investigated. Cells with affinity interactions have greater adhesive strengths than those without (Bell, 1978, Bell et al., 1984), requiring higher shear stresses to induce removal (Nordon et al., 1996 and Nordon et al., 2004, Slowiaczek, 1998). Lower shear stresses (0 – 25 dynes/cm^2) were preferred, since the purpose was to identify conditions to maximise product cell recovery (without affinity interactions) under milder conditions and retain cells with affinity interactions, providing a basis for the purification of mixed cell populations.

2.5.7. Counting adherent cells

Surface-adherent cells were quantified using image analysis software (Figure 2-16). To validate, a comparison of the software-based cell counting method versus manual cell counting (n = 12) was performed. Data (Figure 2-17), revealed good agreement, with an R^2 value of 0.94, although the software counting appeared to underestimate the number of adsorbed cells (intercept = 45), due to the inability to identify cells in very close proximity, indicating limitations in the method for higher densities (≥500 cells/cm^2 image). It is also worth noting that the cells exhibit negligible deformation, even after a 30 minute incubation period, meaning that shear stress-induced separation (Nordon et al., 1996) is more preferable to back-pressure (Pomianek, 1998) due to the greater surface area of the cell exposed to tangentially applied fluid flow.

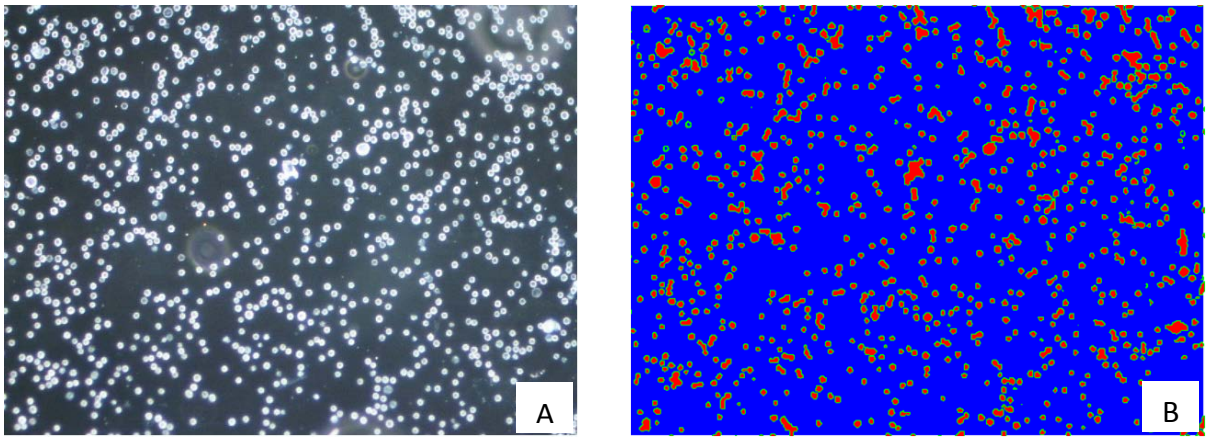

Figure 2-16. Actual image of adsorbed cells (A) and software-modified image of cells used for cell counting (B). Each image is at x10 magnification and equates to 1.125 mm^2. Cells are detected in red with green outlines.

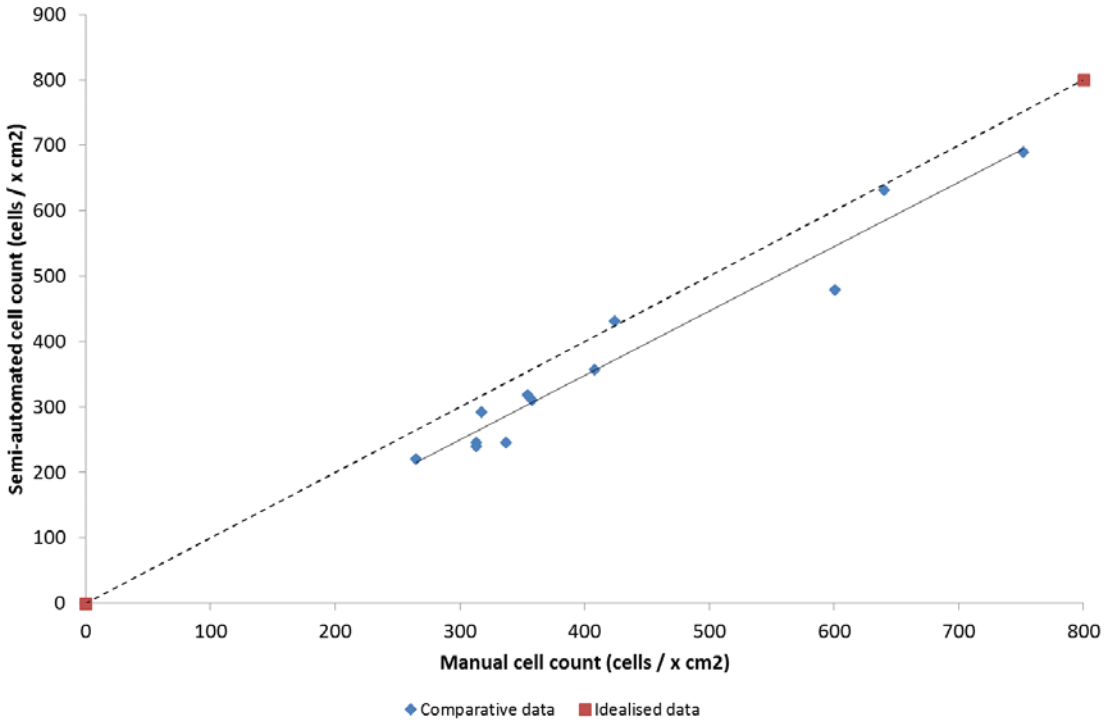

Figure 2-17. Calibration chart comparing software-based counting to manual counting (n = 12). A line of best fit was inserted (R^2 = 0.94). The slope is 0.98 and the intercept is 45. An idealised line is plotted through the centre of the y-x axis 0.

2.5.8. Cell detachment as a function of shear stress

Detachment isotherms using non-linear regression were fitted to experimental data (mean ± SEM) and are presented for cells without affinity interactions HLA-A2+ (n = 3) and CD20+ cells (n = 3) in Figures 2-18 and 2-19 respectively. The detachment of CD20+ cells with possible affinity interactions is presented in Figure 2-20 (n = 3), where linear regression was performed.

Cells without affinity interactions exhibited a lower resistance to detachment. The maximum detachment capacities (R_{max}) were 97 ± 1 % and 92 ± 1 % (after 25 dynes/cm^2) and the equilibrium constant (K_d) was 1.60 ± 0.56 dynes/cm^2 and 2.997 ± 1.40 dynes/cm^2 for CD20+ and HLA-A2+ cells respectively, indicating that cells without affinity interactions were more resistant to detachment than previous studies (Slowiaczek, 1998, Nordon et al., 2004) , where shear stresses ≤ 5 dynes/cm^2 were sufficient to remove ~95 % of cells. The increased

adhesion strength was primarily attributed to the longer incubation time used (30 minutes) versus that of previous studies (5 – 15 minutes) (Slowiaczek, 1998, Nordon et al., 2004). This is because cell deformation increases as a function of incubation time (Dong and Lei, 2000, Cuvelier et al., 2007), leading to a greater contact area and more cell-substrate attraction (Sagvolden et al., 1999, Zaidel-Bar et al., 2007), as well as a more hydrodynamic cell profile, so greater shear stresses are required to induce detachment. Positively charged amine groups of APTES which were not completely covered with glutaraldehyde (Section 2.5.2.) or blocked with BSA could have also increased adhesiveness with negatively charged cells (Bacakova et al., 2011, Christ, 2011).

Conversely, CD20+ cells pre-incubated with CD20 IgG were more resistant to detachment. Across 0 – 25 dynes/cm^2, only 20 ± 19 % of cells were removed. This greater cell resistance to detachment was attributed to affinity interactions, which were estimated to be up to 960 ± 126 per cell, assuming a 0.7 μm^2 contact area (determined from Equation 2.3). This increased resistance compared to non-affinity interactions was consistent with both practical (Xia et al., 1994, Pomianek, 1998) and theoretical studies reported elsewhere concerning force-induced cell detachment (Bell, 1978, Bell et al., 1984, Kuo and Lauffenburger, 1993) and is also consistent with the projections in Chapter 1.

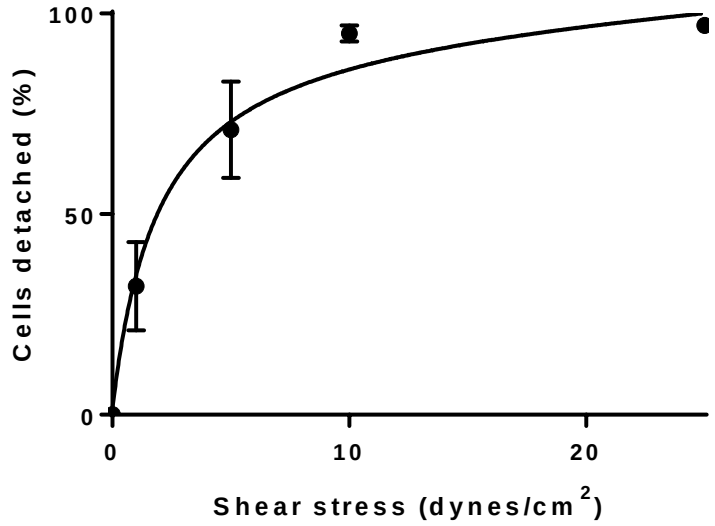

Figure 2-18. HLA-A2+ cell detachment without CD20 IgG affinity interactions with the rPrA-coupled glass flow tubes. Experimental data as a function of shear stress with detachment isotherm, where R_{max} = 97 %; K_d = 1.93 ± 0.79 dynes/cm^2. Data are displayed as the mean ± SEM (n = 3).

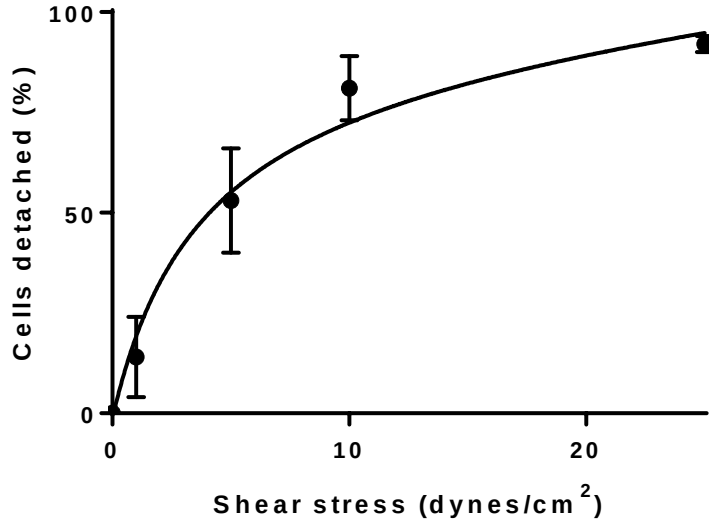

Figure 2-19. CD20+ cell detachment without CD20 IgG affinity interactions with the rPrA-coupled glass flow tubes. Experimental data as a function of shear stress with detachment isotherm, where R_{max} = 97 %; K_d = 3.63 ± 0.64 dynes/cm^2. Data are displayed as the mean ± SEM (n = 3).

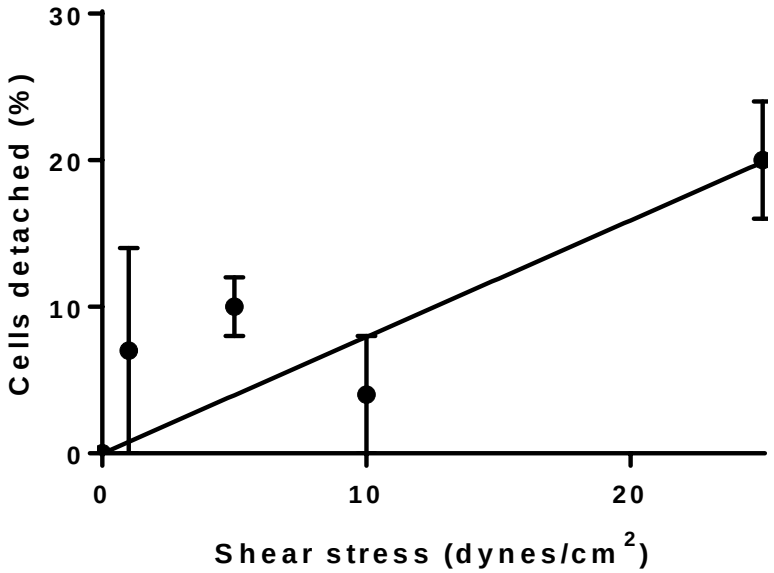

Figure 2-20. CD20+ cell detachment with CD20 IgG affinity interactions with the rPrA-coupled glass flow tubes. Experimental data as a function of shear stress with detachment isotherm, where R^2 = 0.84 and the slope = 0.79 ± 0.17 %/(dynes/cm^2). Data are displayed as the mean ± SEM (n = 3).

Representative images used to illustrate these findings across 0 – 25 dynes/cm^2 for CD20+ and HLA-A2+ cells without affinity interactions are displayed in Figure 2-21 and 2-22, whilst images for CD20+ cells with affinity interactions are displayed in Figure 2-23. The experimental setup was such that siz gated regions were created on each flow tube. Images were recorded at random within each region over a two minute period following the application of shear stress. The average number of cells in these siz images constituted one single run. These gated regions were utilised due to notable heterogeneity inside the flow tubes.

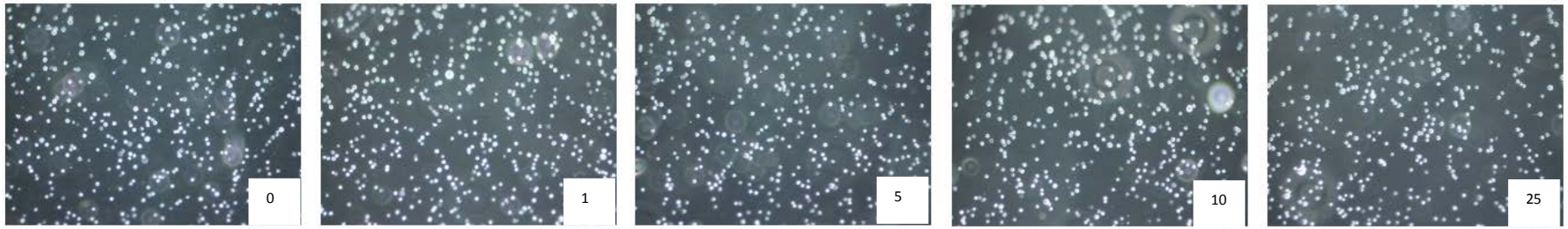

Figure 2-21. Microscope images of CD20 cells incubated with CD20 IgG antibody, introduced into the flow tubes and incubated for 30 minutes prior to washing over shear stresses of 0, 1, 5, 10 and 25 dynes/cm^2 applied sequentially for 3 minute intervals each.

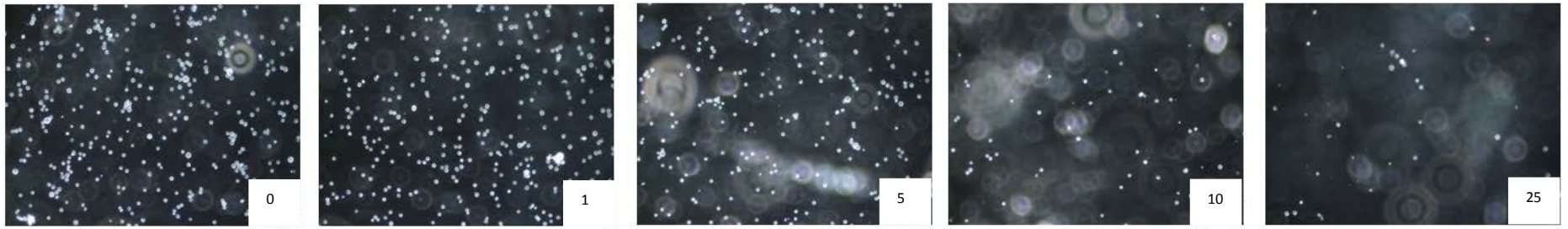

Figure 2-22. Microscope images of CD20 cells incubated without CD20 IgG antibody, introduced introduced into the flow tubes and incubated for 30 minutes prior to washing over shear stresses of 0, 1, 5, 10 and 25 dynes/cm^2 applied sequentially for 3 minute intervals each (control study for non-specific cell adhesion).

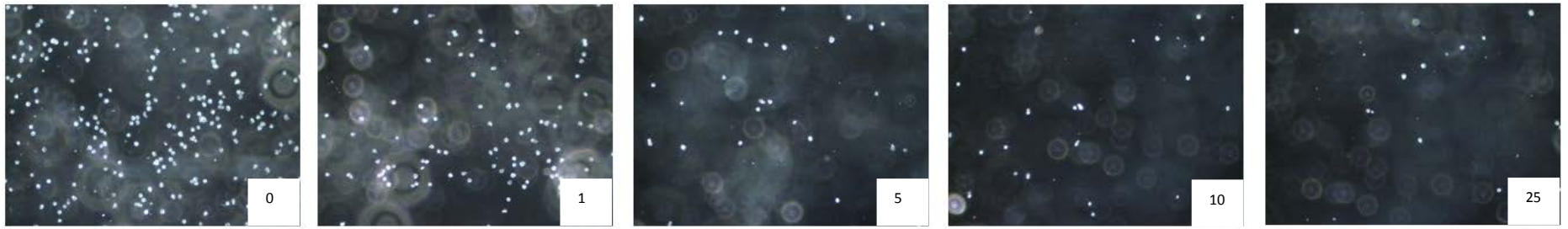

Figure 2-23. Microscope images of HLA-A2 cells (CD20-) incubated with IgG antibody, introduced into the flow tubes and incubated for 30 minutes prior to washing over shear stresses of 0, 1, 5, 10 and 25 dynes/cm^2 applied sequentially for 3 minute intervals each (control study for non-specific cell adhesion).

2.5.9. Cell detachment in real time

Responses of CD20+ cells with affinity interactions (Figures 2-24 and 2-25) and HLA-A2+ cells without affinity interactions (Figures 2-26 and 2-27) to shear stresses of 5 and 25 dynes/cm^2, respectively, were also monitored in real-time. From video analysis following exposure to shear stress, one of two scenarios occurred: (1) cells detached, usually within 2 seconds or (2) remained adherent, undergoing morphological change.

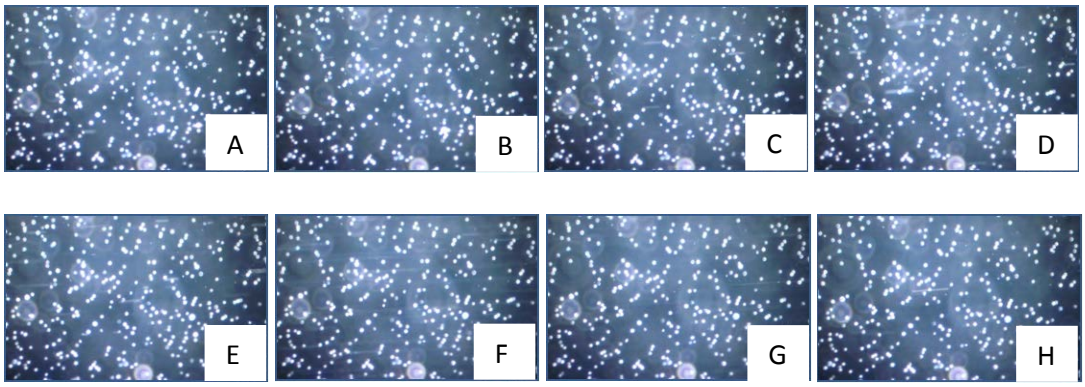

Figure 2-24. CD20+ cells adsorbed with affinity interactions subjected to a shear stress of 5 dynes/cm^2. Images (left to right) are recorded in real time over a 1-4 second period. Each image (A – H) is equivalent to 0.25 seconds. Cells in this instance remain adherent with negligible detachment after the application of shear stress. Negligible changes were observed over the full 2 minute period.

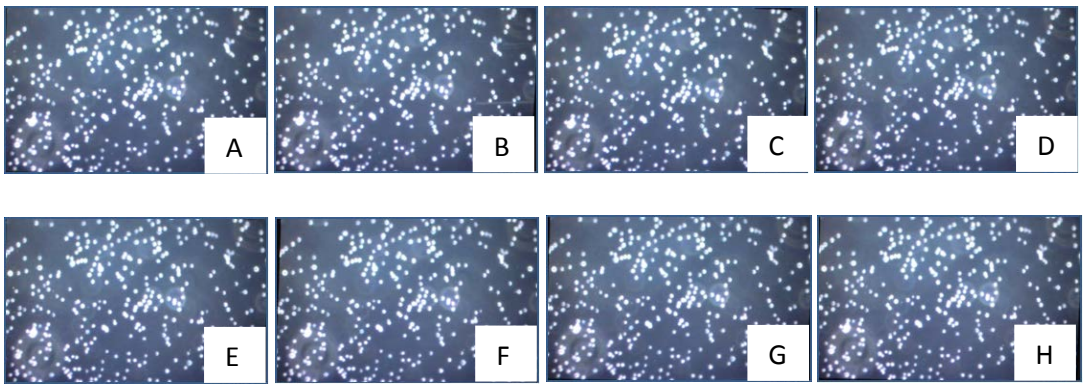

Figure 2-25. CD20+ cells adsorbed with affinity interactions subjected to a shear stress of 25 dynes/cm^2. Images (left to right) are recorded in real time over a 1-4 second period. Each image (A – H) is equivalent to 0.25 seconds. Cells in this instance remain adherent with negligible detachment after the application of shear stress. Negligible changes were observed over the full 2 minute period.

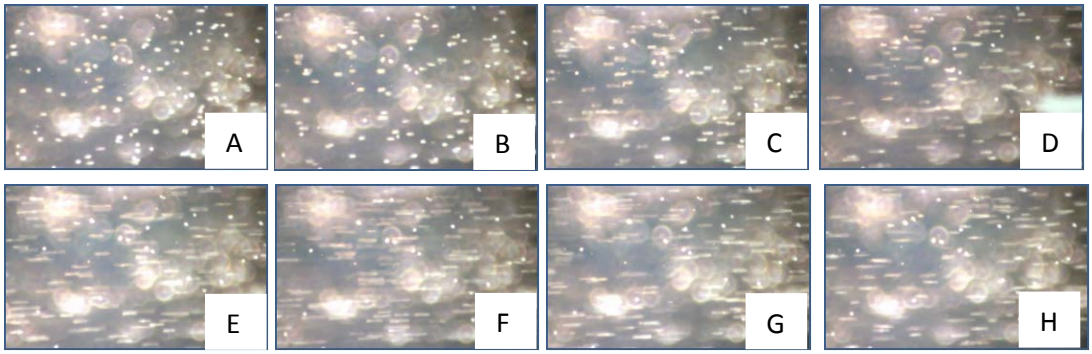

Figure 2-26. HLA-A2+ cells adsorbed without affinity interactions subjected to a shear stress of 5 dynes/cm^2. Images (left to right) are recorded in real time over a 1-4 second period. Each image (A – H) is equivalent to 0.25 seconds. Cells in this instance demonstrate a high level of detachment shortly after the application of shear stress. Negligible changes were observed over the full 2 minute period following initial detachment.

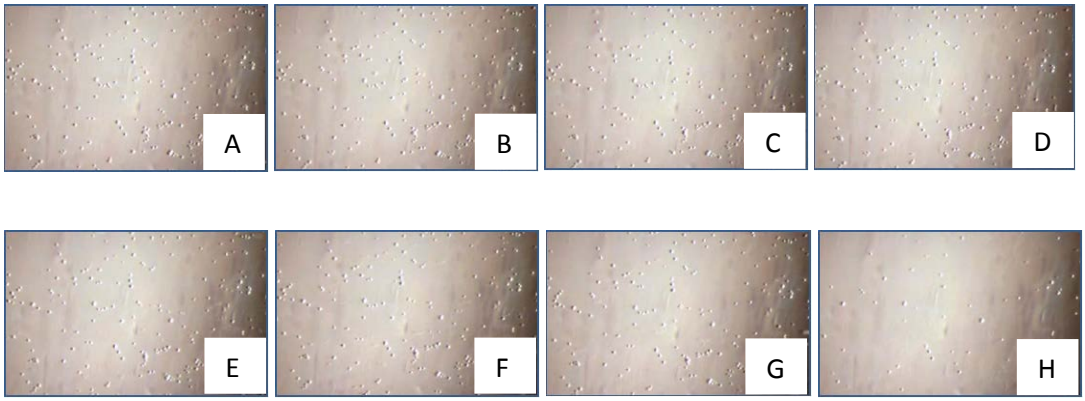

Figure 2-27. HLA-A2+ cells adsorbed without affinity interactions subjected to a shear stress of 25 dynes/cm^2. Images (left to right) are recorded in real time over a 1-4 second period. Each image (A – H) is equivalent to 0.25 seconds. Cells in this instance demonstrate a high level of detachment shortly after the application of shear stress. Negligible changes were observed over the full 2 minute period following initial detachment.

Cells resistant to detachment exhibited morphological and positional changes, usually forming ellipsoid shapes, with the bulk of the cytoplasm shifting away from the original anchor point (Figure 2-28). However, this observed phenomenon was temporary; cells returned to their original spherical shape once shear stress was ceased, irrespective of possible affinity interactions, contradicting previous work which suggested the change to be permanent and indicative of new affinity interaction formation (Nordon et al., 2004). Ascertaining whether cell detachment resembled that of a tensegrity system, where the cell adapted and stressed bonds equally (Ingber, 2014) or a peeling mechanism, where bonds

were stressed sequentially (Chang and Hammer, 1996) remained elusive, owing to experimental limitations.

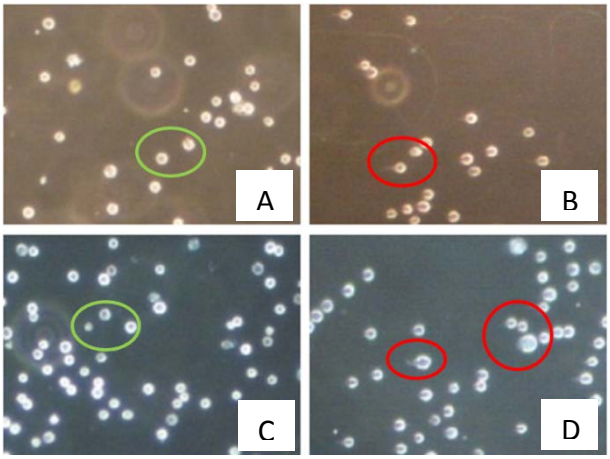

Figure 2-28. Cells exposed to shear stress undergo changes in morphology. Adherent cells with (C and D) and without (A and B) the potential for immuno-affinity interactions under static conditions (A and C) and following exposure to 25 dynes/cm^2 (B and D).

2.5.10. Cell viability

A loss of membrane integrity, often associated with but not indicative of cell death (Kroemer et al., 2005), was used to determine the effect of shear stress-induced detachment on desorbed cells. Data in Table 2-8 show no difference at a 5 % significance value in membrane integrity after applied shear stress or static incubation, where values were equal to or above 99 %. However, since the assay is a measure of membrane integrity and long-term cell viability was not determined, the actual effect on the cell could not be determined. Nevertheless, lower shear stresses (~≤ 25 dynes/cm^2) for cell recovery would expose cells to less physical stress than observed previously, where losses in cell viability, albeit minor (≤ 10 %), were observed (Nordon et al., 1996, Pomianek, 1998). Indeed, pluripotent cell differentiation is even enhanced under mild shear stresses (1.5 – 15 dynes/cm^2) (Yamamoto et al., 2005, Wlofe et al., 2012 and 2013, Nsiah et al., 2014).

Table 2-8. Cell viability assay using trypan blue staining.

	Affinity interaction	Before (%)	After (%)	Control (%)[a]
CD20[a]	Yes	99.5	99	100
CD20[b]	No	99.5	99	100
HLA-A2[b]		100	99.5	100

Represents cells collected over 1-25 dynes/cm^2 for n = 3 runs. [a] pre-incubation period with CD20 IgG; [b] pre-incubation period without CD20 IgG; [c] cells were not exposed to shear stress and were instead stored in the same solution.

2.5.11. Projected performances

Experimental data provide information about individual cell detachment in response to shear stress. When combined, these findings may project the purity of HLA-A2+ product cells recovered from the device relative to the retention of non-product 'impure' CD20+ cells, providing the basis for the separation of mixed cell populations. Thus, several assumptions were made:

1. Cells without affinity interactions (HLA-A2+) exhibit a range of adhesion strengths within a given population. This contradicts Chapter 1 which suggested that non-affinity cell adhesion strength was constant for a given cell type.

2. A mass balance on an idealised version of the separation system assumes three states:

$$In = Out + Adherent$$

, where In = the input fraction; Out = the detached and collected fraction and Adherent = cells adsorbed on the device surface.

3. The adhesion strength, represented by the purity of recovered cells, is assumed to be independent of the surface area of the device.

4. Two cell types are being separated: CD20 cells with affinity interactions (designated as impurities) and HLA-A2+ cells without affinity interactions (designated as product cells).

5. The effect on the health of the cell is neglected.

2.5.12. Large-scale separation device

The purpose of a depletion-based large scale cell separation device is to retain impurities (e.g. SSEA-4-positive undifferentiated pluripotent cells) and recover product cells (e.g. SSEA-4-negative differentiated cells, such as cardiomyocytes), therefore improving purity and minimising the risk of teratoma formation *in vivo*. Other extracellular pluripotent markers may also be targeted simultaneously as a means to further enhance purification performance, such as the SSEA-3 antigen (Thomson 1998). Projecting changes in purity as a function of shear stress will enable the selection of favourable operating constraints. Therefore, the following equations were generated to assess performance:

Separation performance

The recovery of CD20+ cells – those positive for target antigens – (%), $B_{C,n}$, may be given as a function of shear stress by considering a linear equation:

$$B_{C,n} = m.S_n + c \qquad 2.5$$

, where m = slope (% / (dynes/cm^2)); S_n = shear stress (dynes/cm^2); c = Y-intercept.

The recovery of HLA-A2+ cells – those negative for target antigens – (%), $B_{H,n}$ may be given as a function of shear stress using a detachment isotherm:

$$B_{H,n} = \frac{B_{H,n,max}.S_n}{K_d + S_n} \qquad 2.6$$

, where B_{max} = maximum HLA-A2 cell recovery using shear stress based on experimental output (%); K_d = detachment constant (dynes/cm^2); S_n = shear stress estimated to detach 50 % of cells (dynes/cm^2).

The log_{10} depletion for CD20+ cells removed from collected fractions of HLA-A2+ cells may be given by:

$$Log_{10}depletion = Log_{10}\left(\frac{N_{C,n0}}{RC_{C,n}.N_{C,n0}}\right) \quad 2.7$$

, where $N_{C,n0}$ = the number of adsorbed CD20+ cells prior to shear stress exposure; $RC_{C,n}$ = the fraction of CD20+ cells originally adsorbed that are recovered from the surface at a shear stress 'n' (to be determined through prior experimentation).

Output from these projections is shown in Table 2-9. As shown in the detachment isotherms, HLA-A2+ cell recovery, calculated from Equation 2.6, would increase with shear stress, although it is lower versus other studies; ≥95 % of cells adsorbed without affinity interactions were recovered after exposure to 5 dynes/cm^2 (Nordon 1996; Slowiaczek 1998). Here, the recovery of equivalent quantities would require higher shear stresses (25 dynes/cm^2), leading to greater amounts of CD20+ cells being recovered, ultimately reducing the purity of the collected fractions.

The CD20+ cell log_{10} depletion of collected fractions, calculated from Equation 2.5, shows comparable findings to those reported elsewhere, which range from 0.5 – 2.5 for depletion strategies (Barfield et al., 2004, Lara et al., 2006b) and 3 – 5 for enrichment (Martin-Henao et al., 2001, Handgretinger 2002).

Table 2.9. Projected cell depletion and recovery performance as a function of shear stress.

Shear stress (dynes/cm^2)	**0**	**1**	**5**	**10**	**25**
Cell recovery (%)	-	37	73	84	91
Log_{10} depletion	-	1.4	1.2	1.0	0.7

Note: data were based upon the average of n = 3 runs.

Estimating HLA-A2+ cell purity of detached cells

The log_{10} depletion expression indicates the removal of impure CD20+ cells but does not indicate the purity of HLA-A2+cells. Therefore the projected purity (%), $RP_{H,n}$, for recovered fractions of HLA-A2+ cells originally adsorbed at a given shear stress is determined instead from:

$$RP_{H,n} = \frac{RC_{H,n}.N_{H,n0}}{RC_{H,n}.N_{H,n0} + RC_{C,n}.N_{C,n0}} \quad 2.8$$

, where $RC_{H,n}$ = the fraction of HLA-A2+ cells originally adsorbed that are recovered at a specific shear stress (%) (to be determined prior through prior experimentation); $N_{H,n0}$ = the number of HLA-A2+ cells adsorbed prior to shear stress exposure (cells); $RC_{C,n}$ = the fraction of CD20+ cells originally adsorbed recovered using shear stress (%); $N_{C,n0}$ = the number of CD20+ cells adsorbed prior to shear stress exposure.

Using Equation 2.8, the projected purity of recovered fractions for mixed cell populations across purities of 1 – 90 % are presented in Figure 2-29 across 0 – 25 dynes/cm^2. The purity of HLA-A2+ cells in recovered fractions is projected to increase to a peak (estimated to be < 5 dynes/cm^2), before declining with increasing shear stress as more CD20+ cells are removed. The trend is in agreement with practical studies, where the majority of cells are recovered without affinity interactions (equivalent to HLA-A2+ cells here) at ≤ 5 dynes/cm^2 (Nordon 1996; Slowiaczek 1998).

Further, Figure 2-29 also shows that the purity of HLA-A2+ cells in collected fractions was projected to depend upon the starting purity. Populations with higher HLA-A2+ cell starting purities were projected to exhibit smaller increases in purity since fewer CD20+ cells with affinity interactions would be present for a given cell surface density.

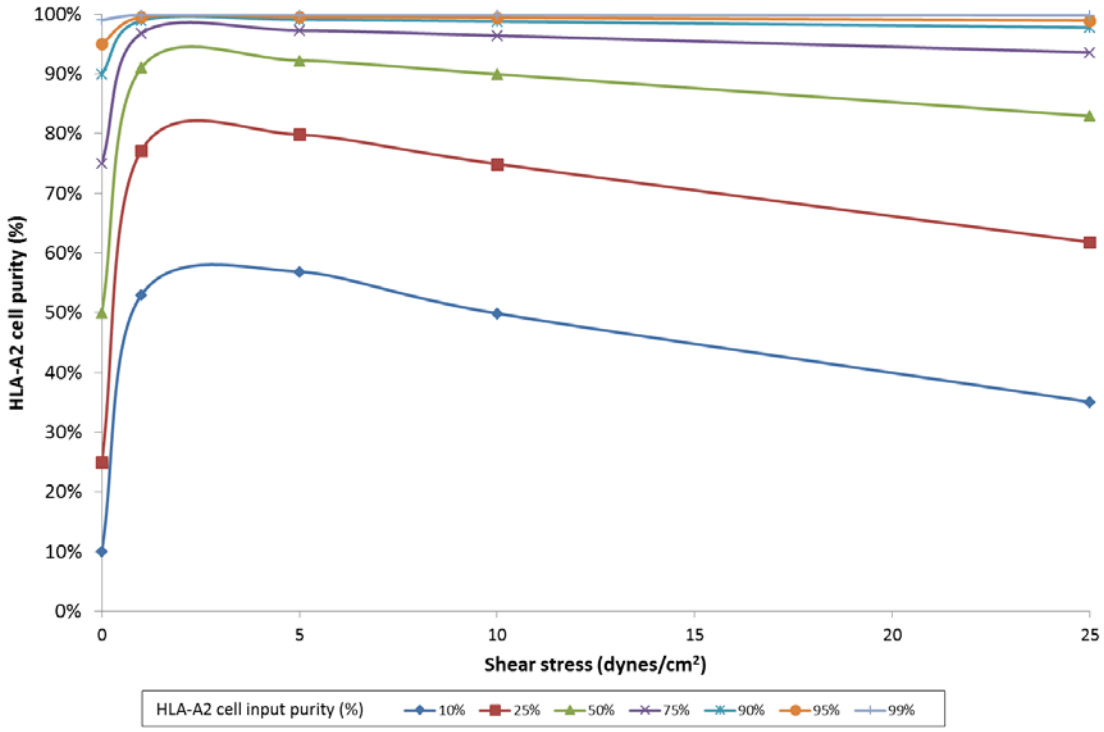

Figure 2-29. Projected HLA-A2+ cell purity as a function of shear stress for a range of starting purities (10 – 99 %). Relies upon adhesion data from individual studies using CD20+ and CD20- (HLA-A2+) cells. Assumes that adhesion strength is represented by a Guassian distribution for both cell types, where increasing fractions of cells are removed as a function of shear stress.

2.5.13. Biosensor development

For the QCM biosensor (Chapter 3), cell purity measurements will rely upon the net change in cells adsorbed on the sensor surface – before and after a designated shear stress is applied – to distinguish between cells adherent with and without affinity interactions. Here, adsorbed CD20+ cells (without affinity interactions) would need to be retained relative to

HLA-A2+ cells (with affinity interactions) following shear stress exposure to maximise the signal-to-noise ratio generated by the biosensor.

However, this chapter has shown that a higher proportion of HLA-A2+ cells (no affinity interactions) are resistant to shear stress-induced cell detachment compared to that observed elsewhere (Nordon 1994 and 2004) for cells without affinity interactions – and some CD20+ cells which should remain adherent with affinity interactions detach. Therefore, any projections must account for the fraction of these HLA-A2+ cells retained to accurately determine the purity of CD20+ cells present. To identify a shear stress capable of providing a sufficient signal-to-noise ratio, cell detachment data for CD20+ and HLA-A2+ cells was incorporated from Section 2.5.8.

Cell surface density

Initially, the number of surface adherent cells for a given cell density must be considered. This study utilised densities in the range of 2 – 4 %, although up to 8% (equivalent to 100,000 cells assuming a 10 μm diameter per cm^2 surface) have been reported (Nordon 1994). Assuming a cell density of 4 % over a surface of 1 cm^2 (the same surface area as the QCM sensor), the total number of cells present per unit surface area without shear stress exposure ($N_{T,n}$) is given by:

$$N_{T,n0} = \left(\frac{S_{SA}}{C_{SA}}\right).0 \qquad 2.9$$

, where S_{SA} = sensor surface area available for cell adsorption (cm^2); C_{SA} = surface area occupied per cell (cm^2/cell); 0 = percentage of the sensor surface occupied by cells, assuming a monolayer (%).

Effect of shear stress on the density of surface-adsorbed cells

CD20+ cells

The number of CD20+ cells on the sensor surface after washing at a given shear stress ($N_{C,n}$) may be calculated from:

$$N_{C,n} = SP_{C,n0}.RT_{C,n}.N_{T,n0} \quad 2.10$$

, where $SP_{C,n0}$ = surface purity of CD20+ cells adherent on the surface prior to shear stress exposure; $RT_{C,n}$ = fraction of CD20+ cells originally adsorbed on the surface retained at a given shear stress (-) (to be determined through experimental observation); $N_{T,n0}$ = total number of cells present prior to shear stress exposure.

HLA-A2+ cells

The number of HLA-A2+ cells on the surface after washing at a given shear stress ($N_{H,n}$) may be calculated from:

$$N_{H,n} = SP_{H,n0}.RT_{H,n}.N_{T,n0} \quad 2.11$$

, where $SP_{H,n0}$ = surface purity of HLA-A2+ cells adherent on the surface prior to shear stress exposure; $RT_{H,n}$ = fraction of HLA-A2+ cells originally adsorbed on the surface retained at a given shear stress (-) (to be determined through experimental observation).

Total cells

By combining CD20+ ($N_{C,n}$) and HLA-A2+ ($N_{H,n}$) cell quantities on the surface obtained from individual experimentation studies in Section 2.5.8., the total number of cells on the surface in a combined model at a given shear stress may be determined by:

$$N_{T,n} = N_{H,n} + N_{C,n} \quad 2.12$$

, where $N_{T,n}$ = the total number of cells retained on the surface following the application of a given shear stress (cells).

The total number of cells on the sensor surface for a range of starting purities across 0 – 25 dynes/cm^2 is projected in Figure 2.30 based on the individual studies conducted in Section 2.5. In scenarios where CD20+ cell purity is lower, the number of cells removed from the surface increases, owing to a higher proportion of HLA-A2+ cells, which do not possess affinity interactions strong enough to resist shear stress-induced detachment. Moreover, there are a limited number of affinity interactive sites on the surface, so these are more likely to be occupied by HLA-A2+ cells when those cells are in higher quantities than CD20+ cells.

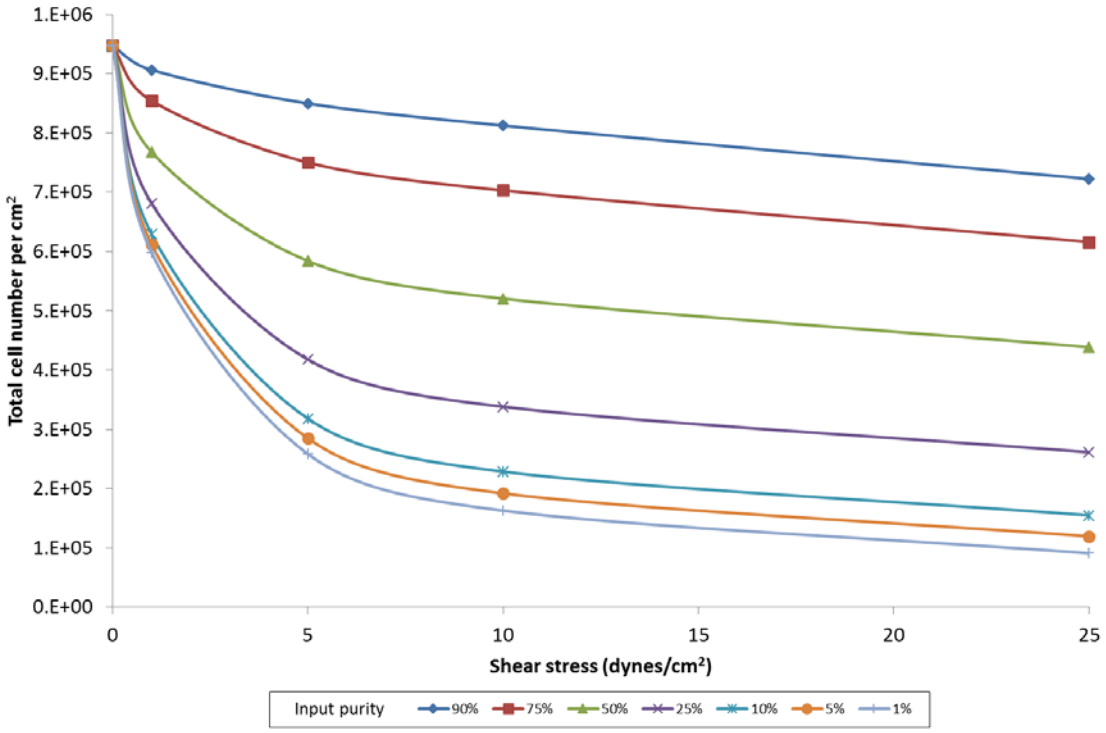

Figure 2.30. Total number of cells on the surface ($N_{T,n}$) as a function of shear stress (0 – 25 dynes/cm^2) for starting purities ranging from 1 – 90 %. Relies upon adhesion data from individual studies using CD20+ and CD20- (HLA-A2+) cells. Assumes that adhesion strength is represented by a Guassian distribution for both cell types, where increasing fractions of cells are removed as a function of shear stress.

CD20+ cell purity post-shear stress

Since the number of both cell types adsorbed at a given shear stress can be determined from Equations 2.10 and 2.11, the purity of CD20+ cells on the sensor surface ($SP_{C,n}$) may therefore be deduced:

$$SP_{C,n} = \frac{N_{C,n}}{N_{C,n} + N_{H,n}} \qquad 2.13$$

CD20+ cell surface purity has therefore been plotted as a function of shear stress for various starting purities (Figure 2-31).

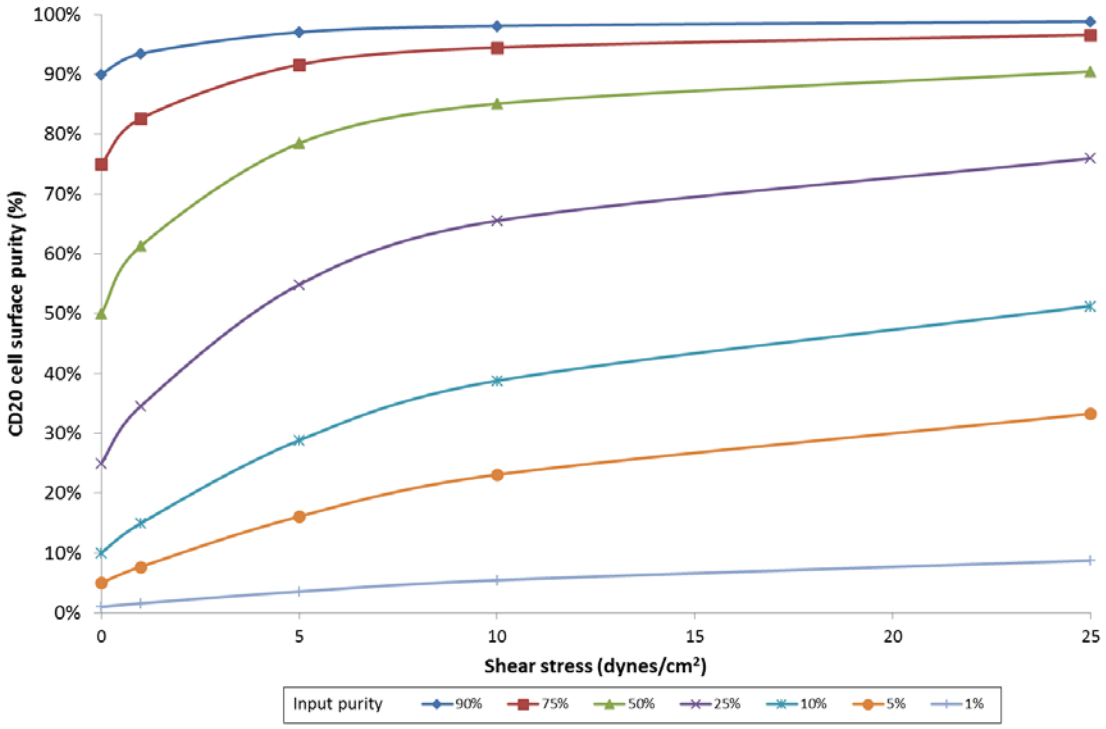

Figure 2-31. CD20+ cell purity on the sensor surface as a function of shear stress for starting purities ranging from 1 – 90 %. Relies upon adhesion data from individual studies using CD20+ and CD20- (HLA-A2+) cells. Assumes that adhesion strength is represented by a Guassian distribution for both cell types, where increasing fractions of cells are removed as a function of shear stress.

By calculating and plotting the total number of cells on the sensor surface post-shear stress ($N_{T,n}$) versus the purity of CD20+ cells also post-shear stress ($SP_{C,n}$) (determined from individual experimental studies), it is possible to determine the projected CD20+ cell purity retained on the surface.

Plotting ($SP_{C,n}$) versus ($N_{T,n}$) for a variety of starting purities at a given shear stress (in this instance using 25 dynes/cm^2) will yield Figure 2-32.

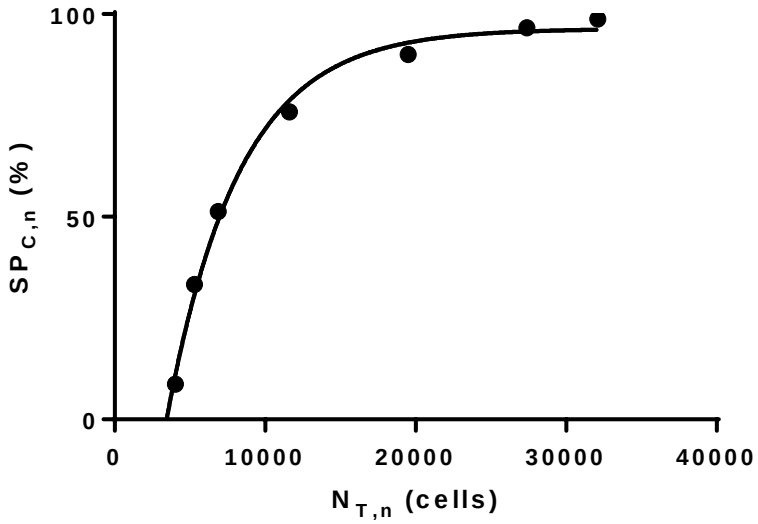

Figure 2-32. CD20+ cell purity on the sensor surface following washing at a given shear stress across a range of purities (based on Figure 2-28) versus the total number of cells on the surface. The R^2 value is 0.9943. Note: at 0 % CD20+ cell purity the number of cells retained on the surface after washing is > 0. This is because in spite of how much washing is applied when a 4 % cell coverage is used, around 9 % of HLA-A2+ cells will remain adherent. This is because the model assumes: (1) cells comprise a mixture of HLA-A2+ and CD20+ cells and (2) cell surface density must start at 4 %. The applicability of the model at CD20+ cell purities < 1 % is not deemed viable.

The equation used to estimate the CD20+ cell purity on the sensor surface ($SP_{C,n}$) is given by:

$$SP_{C,n} = SP_{C,n*} + \left(Plateau - SP_{C,n*}\right).\left(1 - \exp(-K.N_{T,n})\right) \quad 2.14$$

, where $SP_{C,n}$ = CD20+ cell purity on the surface for a given number of total cells ($N_{T,n}$) following washing at a given shear stress (25 dynes/cm^2) (cells); $SP_{C,n*}$ = calculated CD20+ cell purity on the sensor surface when zero cells are present (%); Plateau = the $SP_{C,n}$ value at an infinite number of cells on the surface (%); K = the rate constant expressed in reciprocal of the $N_{T,n}$ axis units (1/cells).

Note: there will always be cells on the surface since a residual amount of HLA-A2+ cells are resistant to detachment. (Look at the HLA-A2+ cell total on the surface – the graph

accounts for that – these cells cannot be removed at 25 dynes/cm^2). Second, the fact that a 4 % cell density is required means that there will always be a population of cells on the surface – in this instance HLA-A2+ cells, which remain adherent.

Table 2.10. Parameters used to determine cell purity.

Constant	Data	Unit
$SP_{C,n*}$	-100.9	%
K	0.0002077	1/cells
Plateau	96.40	%

The number of CD20+ cells on the surface after washing at a given shear stress can be calculated using:

$$N_{C,n} = SP_{C,n}.N_{T,n} \quad 2.15$$

, where $N_{C,n}$ = the number of CD20+ cells on the surface after washing at a given shear stress; $SP_{C,n}$ = the purity of CD20+ cells on the surface after washing at a given shear stress; $N_{T,n}$ = the total number of cells on the surface after washing at a given shear stress.

Recall the equation for the number of CD20+ cells on the sensor surface after washing at a given shear stress ($N_{C,n}$):

$$N_{C,n} = SP_{C,n0}.RT_{C,n}.N_{T,n0} \quad 2.16$$

, where $SP_{C,n0}$ = surface purity of CD20+ cells adherent on the surface prior to shear stress exposure; $RT_{C,n}$ = fraction of CD20+ cells originally adsorbed on the surface retained at a given shear stress (-) (to be determined through experimental observation); $N_{T,n0}$ = total number of cells present prior to shear stress exposure.

The determination of $SP_{C,n}$ for a given cell number can then be used to aid in the calculation of the original starting purity. By re-arranging Equation 2.7 and inserting Equation 2.12, the following may be derived to determine the purity of cells on the surface prior to washing:

$$SP_{C,n0} = \frac{SP_{C,n}.N_{T,n}}{RT_{C,n}.N_{T,n0}} \quad 2.17$$

, where $SP_{C,n}$ is known from Figure 2-29; $RT_{C,n}$ is known from initial experimental study using individual populations of cells to assess a range of adhesion strengths; $N_{T,n}$ and $N_{T,n0}$ are known from the determination of cells on the sensor surface (to be presented in Chapter 3). A worked example for this calculation is presented in Chapter 7 (Appendix).

2.6. Conclusions

rPrA-coupled glass flow tubes were generated using aldehyde-functionalised surface chemistry. Shear stresses (1, 5, 10 and 25 dynes/cm^2) were applied sequentially to identify differences in the adhesion strength of cells adsorbed with (CD20+) and without (CD20+ and HLA-A2+) affinity interactions.

Cells adsorbed with affinity interactions were thought to comprise multiple connections between surface-coupled rPrA and the Fc region of CD20 IgG antibody tagged to CD20+ cells. These interactions, estimated to be up to 960 ± 126 per μm^2 (mean ± SEM), provided greater cell adhesion strength relative to cells adsorbed without affinity interactions. For instance, at 25 dynes/cm^2, only 20 ± 19 % (mean ± SEM) of CD20+ cells adsorbed with affinity interactions detached. Yet for cells without affinity interactions – CD20+ and HLA-A2+ cells, around 97 ± 1 and 92 ± 1 % (mean ± SEM) detached, respectively. These findings

will enable performance projections to be made for large-scale cell separation and the development of a QCM biosensor utilising shear stress-induced affinity interactions.

Chapter 3. Biosensor development

3.1. Introduction

For several decades, the performance of mammalian cell culture has been enhanced with sensors that measure dissolved oxygen content, pH and temperature (Ahn et al., 2008, Sunley and Butler, 2010). However, successful CTP manufacture requires the measurement and control of more sophisticated characteristics (Table 3-1) inherent to the cell, such as cell antigen and gene expression, morphology, chromosomal stability, as well as the capacity to demonstrate biological functionality (Bravery et al., 2013). Such characteristics require much more sophisticated technologies in order to be measured. These cannot be easily integrated into existing bioreactor systems, often acting as separate devices that require extensive operator training, large bench spaces and high costs.

The large-scale manufacture of pluripotent-derived cells has the capacity to yield large quantities of cells for a variety of treatments. However, bioreactor inefficiencies at larger scales (> 10^{11} cells) are expected to generate impure cell populations. Safe thresholds for these cells are expected to be in excess of 99 % based on animal (Schriebl et al., 2012) and human studies (Schwartz et al., 2012). Undifferentiated pluripotent cells express the SSEA-4 antigen (Thomson et al., 1998), making affinity separation to selectively remove these cells possible (Shibata et al., 2006, Schriebl et al., 2012).

The measurement of cell purity during process development or routine lab-based research using simpler, cheaper alternatives to flow cytometry (> £60 k) is highly desirable. Many biosensors exist, primarily relying on acoustic (Pan et al., 2010) and optical (Brauchle et al., 2014) techniques. However, the majority of these will require complex analytical tools to

isolate specific parameters. Conversely, the quartz crystal microbalance (QCM) is a form of acoustic sensor, which can monitor mass and density related changes at the surface of a quartz disc, relying on the piezoelectric effect to provide quantitative data (Voinova et al., 2002) and are much cheaper (~£20 k).

The QCM has the potential to measure cell purity through affinity interactions, based on extracellular protein interactions with immobilised antibodies. The system is able to relay the mass of adsorbed components (e.g. cells) on a sensor surface via a measured output signal (frequency), thus providing quantitative data (Figure 3-1). Antibody-coupled sensors can be used to differentiate between cells adherent with and without affinity interactions. As detailed in Chapter 2, shear stress can be used to exploit differences in adhesion strength based on whether or not a cell has affinity interactions. This can be used to correlate net changes in the measured output signals with cell purity.

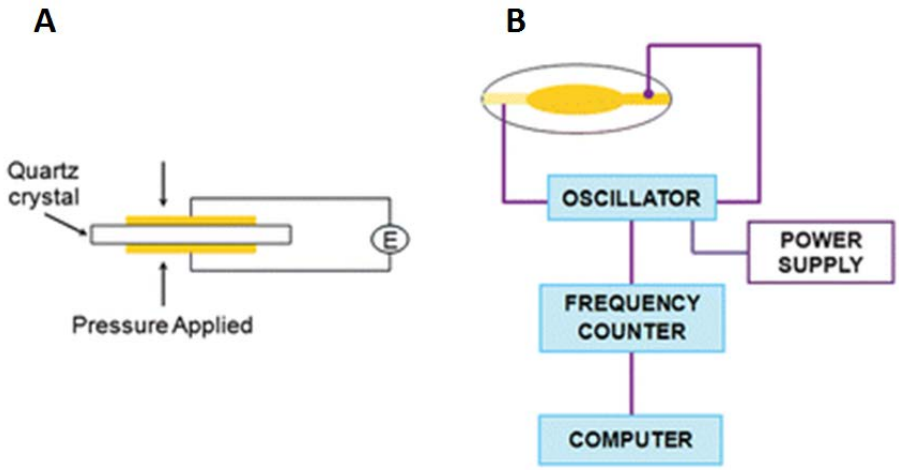

Figure 3-1. Key aspects of the QCM system: Gold-coated quartz crystal (A) and QCM system schematic (B): when mass is deposited on the surface of an oscillating gold-plated quartz crystal, it causes a change in the frequency of oscillation, which can be measured and quantified.

Chapter aims and objectives:

- Generate a surface capable of affinity interactions with proteins and cells

- Investigate the response of adherent cells to shear stress inside the QCM chamber
- Propose methods for converting measured output signal into a cell number and purity

3.2. Materials and methods

A protocol concerning the creation of a Protein A-terminated complex for oriented IgG antibody immobilisation onto quartz sensor chips treated with a PEG derivative to yield a surface added monolayer (SAM) was implemented (Nileback et al., 2011).

3.2.1. Chemical modification

Gold-coated AT-cut 5 MHz quartz crystals (Q-Sense AB, Gothenburg , Sweden) were cleaned in an ultraviolet ozone cleaner (UV/O3) (NL-UV253, Nippon Laser and Electronic Laboratory, Tokyo, Japan). After rinsing with de-ionised water, purified using a Milli-Q system (MilliPore, Molsheim, France), sensors were dried under a flow of nitrogen and placed 0.5 in a mM solution of an oligo(ethylene glycol) (OEG) disulfides with a hydroxyl terminal group (dS-OEG-OH) (PlasmChem GmbH, Berlin, Germany) with a mole fraction of 0.1 % for an oligo(ethylene glycol) (OEG) disulfides with a biotin terminal group (dS-OEG-biotin) (Polypure, Oslo, Norway) dissolved in spectroscopic-grade ethanol (Sigma-Aldrich, Munich, Germany). Following a 16 hour incubation period in a light-free dessicator, sensors were rinsed in ethanol (100 %) and ultra-sonicated in an Elma S10 ultrasonic bath (Fischer Scientific, Loughborough, UK) for 3–5 min in ethanol to remove non-covalently bound disulfides.

3.2.2. System operation

Successive protein layers and subsequent analyte studies were performed in the QCM-D system (Q-Sense AB, Gotenbugy, Sweden). The flow was controlled using an Ismatec IPC-N 4 peristaltic pump (Wertheim-Mondfeld, Germany). All measurements were performed at room temperature (22 °C). Data was collected at the fundamental frequency and overtones of 1 – 13 MHz, of which only the 7th overtone was used in analysis.

3.2.3. Surface characterisation

3.2.3.1. Contact angle measurements

Contact angle measurements on cleaned gold and PEG-treated gold sensors were used to indicate surface hydrophobicity. A 2 µL droplet of de-ionised water was deposited onto the sensor surface and the contact angle was measured with a DataPhysics OCA 20 system (Data Physics Instruments GmBH, Filderstadt, Germany).

3.2.3.2. Surface charge

Non-specific binding sites were estimated by incubating biotin-terminated sensors inside the chamber in a 1 % (w/v) BSA (Sigma-Aldrich, Munich, Germany) in PBS, prior to washing at 100 mL/min until the frequency change was approximately less than 5 Hz/hr. The net change in frequency was used to indicate the extent of adsorption.

3.2.4. Protein adsorption

A Protein A-terminated complex was created to provide a basis for future experiments (Figure 3-2) relying on a complex described previously (Nileback et al., 2011). Proteins were introduced, incubated and washed as detailed in Table 3-1. This complex was created to enable the immobilization of IgG antibody via the Fc region onto the sensor through a

Protein A interaction (all protein solutions diluted in PBS). Successive layers were rinsed in PBS at 100 µL/min.

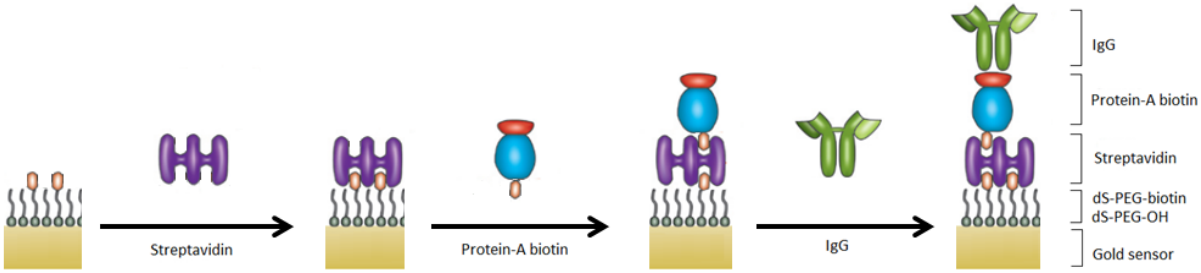

Figure 3-2. Protein A terminated surface. dS-PEG-OH/-biotin treated gold sensors were successively exposed to streptavidin, Protein A-biotin to create a platform for orientated IgG antibody adsorption via the Fc base.

Table 3-1. Analyte and component deposition

Step	Protein/chemical	Concentration	Static incubation time (minutes)
1	Streptavidin	25 µg/mL	10
2	SDS	50 mM	-
3	BSA	10 mg/mL	30
4	Protein A-biotin	25 µg/mL	10
	CD20 IgG[a]		
5	HLA-A2 IgG[b]	10 µg/mL	40
	Glycophorin A IgG[b]		

[a] = applied to CD20 IgG only ; [b] = applied to cells only

Protein L and A binding

CD20 IgG was introduced to bind to the underlying protein complex at a concentration of 10 µg/mL in PBS and incubated for 30 minutes at room temperature (~23 ^{o}C). Following washing, Protein L and A (100 µg/mL) were introduced into separate chambers and allowed to statically incubate for 20 minute prior to washing. The ratio of Protein L to Protein A was used as a basis to determine IgG presence and orientation.

3.2.5. Cell adsorption studies

3.2.5.1. Cell culture

CCRF-HSB-2 B-lymphocytes positive for the HLA-A2 antigen were cultured in 90 % RPMI-1640 with 2 mM glutamine and 10 % (v/v) foetal bovine serum (FBS) supplemented with 1 % Pen-Strep (Sigma-Aldrich, Munich, Germany). Cell cultures were maintained at 3x10^{5} to

$1x10^6$ cells/mL in 5 % CO_2 and 95 % O_2 atmospheric content at 37 ^oC using a Heracell 150i CO_2 incubator (Thermo Scientific, Loughborough, UK) and cultured every 2-3 days. Red blood cells were received from donor blood through the National Blood Transfusion Centre and were stored at 4 ^oC prior to use.

3.2.5.2. Cell adsorption

Exploratory cell binding studies were performed using two different cell types: B-lymphocyte cells across a range of $5 \times 10^4 – 5 \times 10^5$ cells/mL and red blood cells at 1×10^6 cell/mL (Table 3-2). For each experiment cells with a viability in excess of 99 % based on trypan blue exclusion were centrifuged at 1,200 rpm and re-suspended in 1 % BSA (w/v) in PBS.

Cells suspensions were injected into Q-Sense QCM-D chambers, (Gothenburg, Sweden) onto sensors with IgG antibodies immobilised. These antibodies had an affinity for the cells being introduced. Cells were then incubated for 30 minutes at room temperature prior to washing at 5 dynes/cm^2 with PBS until line stabilisation.

Table 3-2. Cell adsorption study conditions.

Cell type	Antibody	Cell concentration (cells/mL)	Incubation time (minutes)	Shear stress[a] (dynes/cm^2)
CCRF-HSB-2 B-lymphocytes	HLA-A2	$0.5 – 5 \times 10^5$	30	5
Red blood cells	Gly-A	1×10^6		

No control studies using cells negative for the target antigen or cells without adsorbed antibody were performed. [a] = shear stress applied during washing following a 30 minute incubation period of cell adsorption.

3.3. Theoretical considerations

Replicating the same hydrodynamic conditions inside the QCM chamber (Figure 3-3) as those used for the glass flow tube in Chapter 2 required the use of computational modelling software. The most sensitive location on the QCM sensor is the centre of the electrode and

it is important that the hydrodynamic conditions are more uniform here to provide a reliable signal.

COMSOL modelling software (Multiphysics 4.2a) was used to evaluate the fluid dynamics inside the chambers. Second order elements for velocity characteristics were discretized with first order characteristics for pressure for the fluid, which was assumed to be water, possess laminar flow characteristics (Reynolds number << 2,100) and obey the Navier-Stokes equation for fluid motion.

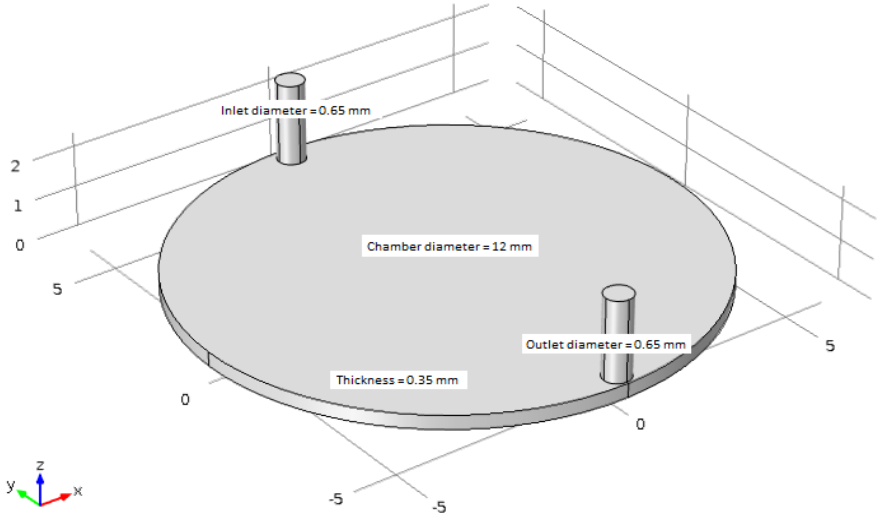

Figure 3-3. QCM chamber schematic. The chamber dimensions are: inlet/outlet diameter = 0.65 mm; height = 0.35 mm; diameter (also the sensor diameter) = 12 mm.

3.4. Results

3.4.1. Computational modelling

COMSOL-simulated fluid dynamics inside the QCM are presented in Figures 3-4 and 3-5. Surface shear stress and pressure gradients (Figure 3-4) are localised near the inlet and outlet ports with more uniform regions apparent at the centre. Fluid velocity gradients associated with depth (Figure 3-5) are evidently negligible. Taken together, these findings show that fluid flow within the QCM chamber is uniform near the central region, which is important for cell detection as this region provides the greatest signal strength.

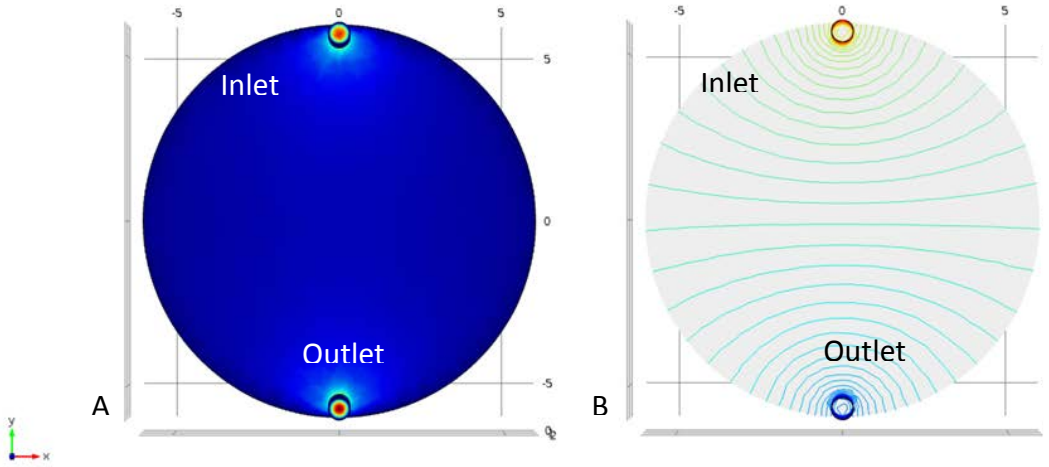

Figure 3-4. Top-down view of shear stress (A) and pressure (B) on the surface of the QCM chamber along the z-y axis of the QCM-D chamber. Red indicates a higher value, while blue indicates a lower one. Not to scale.

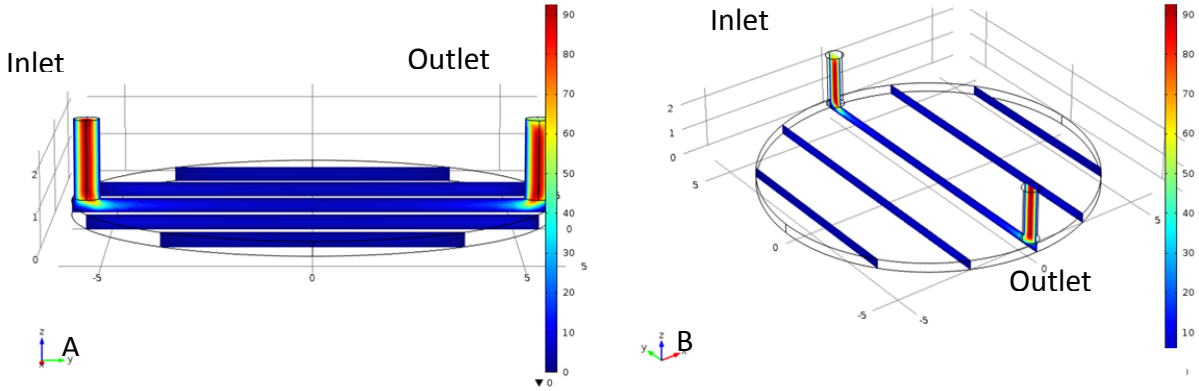

Figure 3-5. Side-views of fluid velocity in (A) and (B) inside the QCM chamber from the inlet to the outlet. Red indicates a higher value, while blue indicates a lower one. Not to scale.

3.4.2. Surface characterisation

The surface hydrophobicity of both clean gold (n = 3) and the dS-PEG-OH/-biotin (1%) treated gold sensors (n = 3), as well as the charge of the latter (n = 2) were investigated using contact angle measurements (mean ± SD) and BSA adsorption (Figure 3-6). Data in Table 3-3 show that the contact angle of gold was 85.0 ± 1.5 ^{o}, whilst that of the SAM is

much lower at 17.9 ± 0.8°. The frequency change for BSA adsorption on biotin-coupled surfaces was 2.6 – 6.4 Hz (Figure 3-7).

Table 3-3. Contact angle and frequency shifts for cleaned gold and dS-PEG-OH/-biotin (1%) treated gold sensors.

Surface	Contact angle (°)	Frequency shift (Hz) using 1% BSA (w/v)
Gold	85.0 ± 1.5	N/A
HS-PEG-OH -- HS-PEG-biotin (1 %)	17.9 ± 0.8	2.6 – 6.4

Contact angle measurements are displayed as the mean ± SEM. N/A = not applicable.

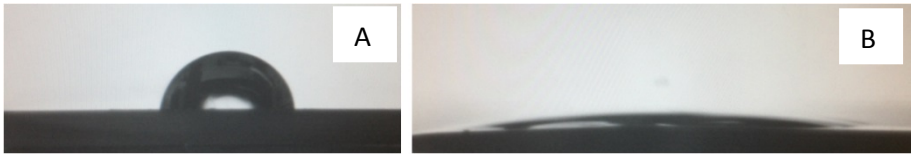

Figure 3-6. Contact angle images for (A) cleaned gold and (B) dS-PEG-OH/-biotin treated gold sensors.

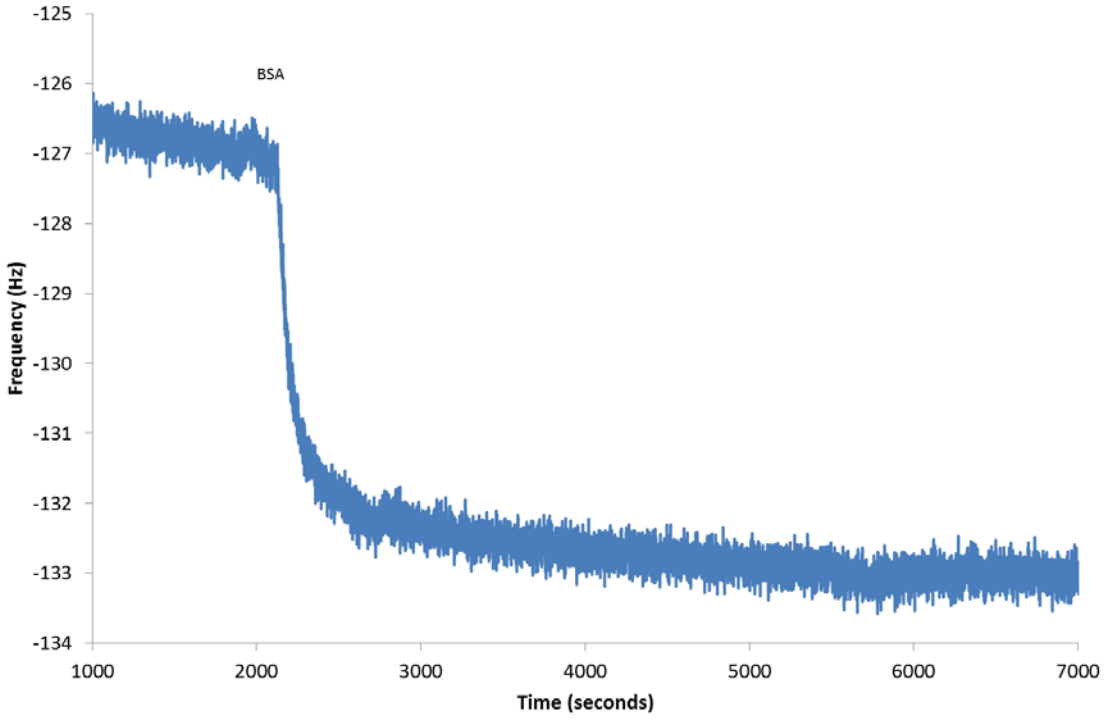

Figure 3-7. Frequency and dissipation vs. time for BSA adsorption onto gold-coated sensors treated with dS-PEG-OH/-biotin (1 %). Frequency is displayed on the blue line (left axis); dissipation is displayed on the red line (right axis).

3.4.3. Protein binding

Protein L and Protein A were used in replacement of a CD20 antigen to detect IgG presence and orientation. Data are summarised in Table 3-4 below. Protein L was shown only to elicit

a net change in frequency when IgG antibody was present, with a frequency change of 16.6 – 22.3 Hz (Figure 3-8) compared to only 1.1 Hz (Figure 3-9) without IgG antibody. Conversely, Protein A adsorption indicated a minor increase of -3.5 Hz, which was attributed to background variation (Figure 3-10).

Table 3-4. Protein L and Protein A analyte responses during QCM-D runs in the presence and absence of CD20 IgG antibody.

Ligand	Analyte	Frequency change (Hz)
IgG	Protein L	16.6 – 22.3
	Protein A	-3.5
No IgG	Protein L	1.1

IgG is the CD20 IgG antibody.

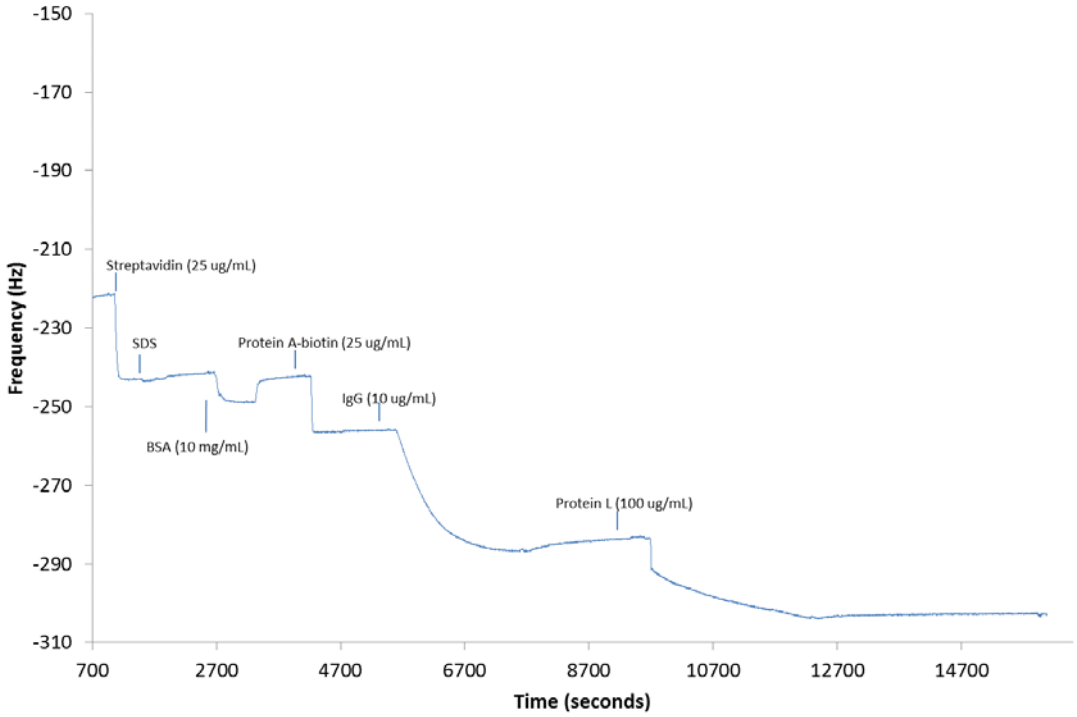

Figure 3-8. Frequency and dissipation changes vs. time for Protein L binding to CD20 IgG-based complex. Frequency is displayed on the blue line (left axis); dissipation is displayed on the red line (right axis).

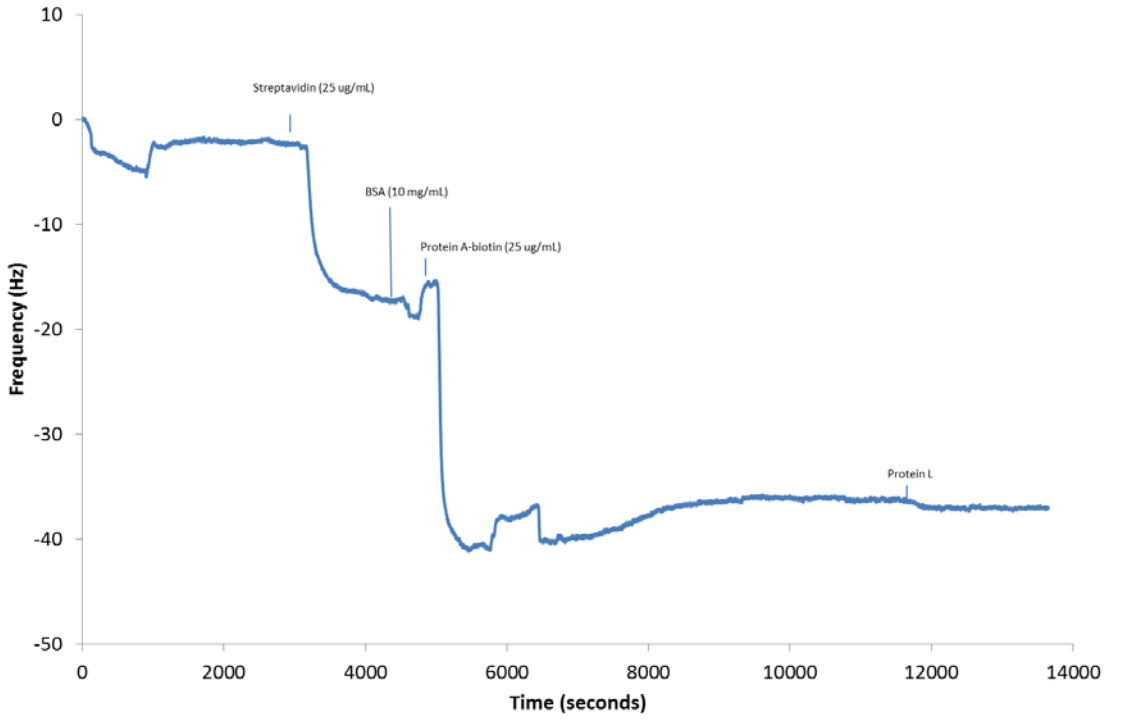

Figure 3-9. Frequency and dissipation vs. time Protein L binding to CD20 IgG-absent complex. Frequency is displayed on the blue line (left axis); dissipation is displayed on the red line (right axis).

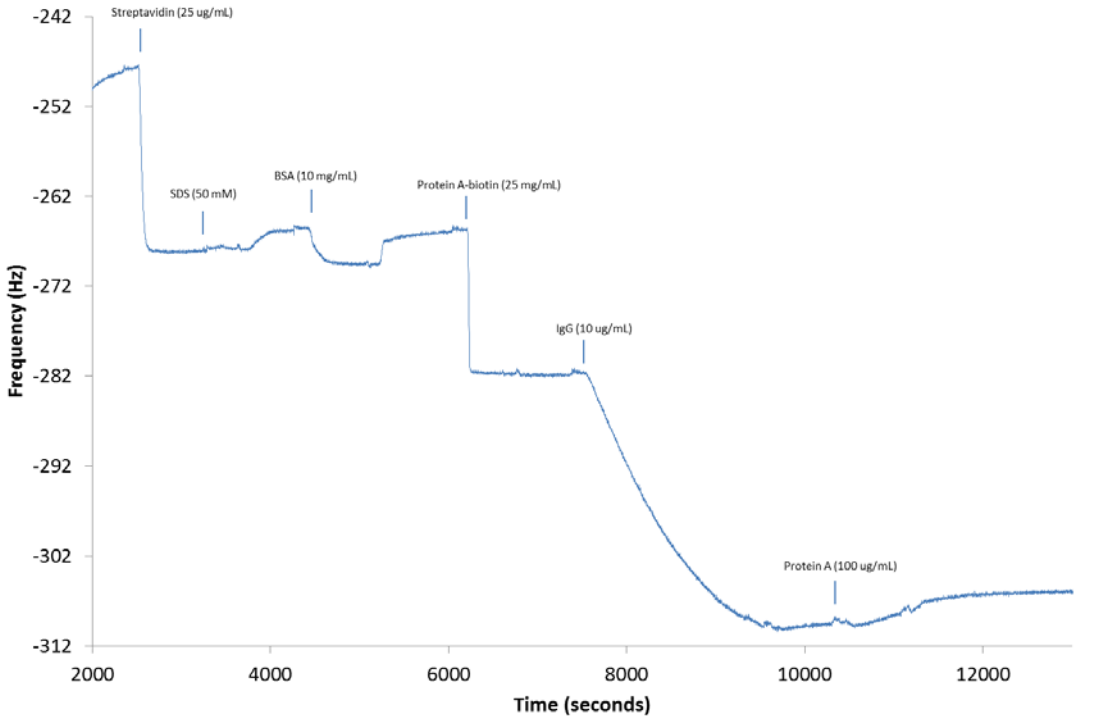

Figure 3-10. Frequency and dissipation vs. time for Protein A binding to CD20 IgG-based complex. Frequency is displayed on the blue line (left axis); dissipation is displayed on the red line (right axis).

3.4.4. Cell binding

Cell binding studies were used with Protein A-terminated sensors for HLA-A2 or Glycophorin A IgG antibody immobilisation to determine affinity interactions with B-lypmphocytes (n = 2) and red blood cells (n = 2) respectively (Table 3-5). B-lypmphocytes (Figure 3-11) exhibited a small net change in frequency following washing at 5 dynes/cm^2, ranging from 2.5 – 5.7 Hz. Conversely, red blood cells (Figure 3-12) exerted a much larger change in frequency ranging from 44 – 85 Hz. No control studies without corresponding IgG antibody were performed.

Table 3-5. Signal responses generated by cell adsorption onto IgG coupled surfaces

Cell type	Ligand surface	Cell concentration (cells/mL)	Frequency response (Hz)
CCRF-HSB-2	HLA-A2 IgG	4 x 10^4 – 5 x 10^5	5.7
		5 x 10^4	2.5
Red blood cells	Gly A	1 x 10^6	44 – 85

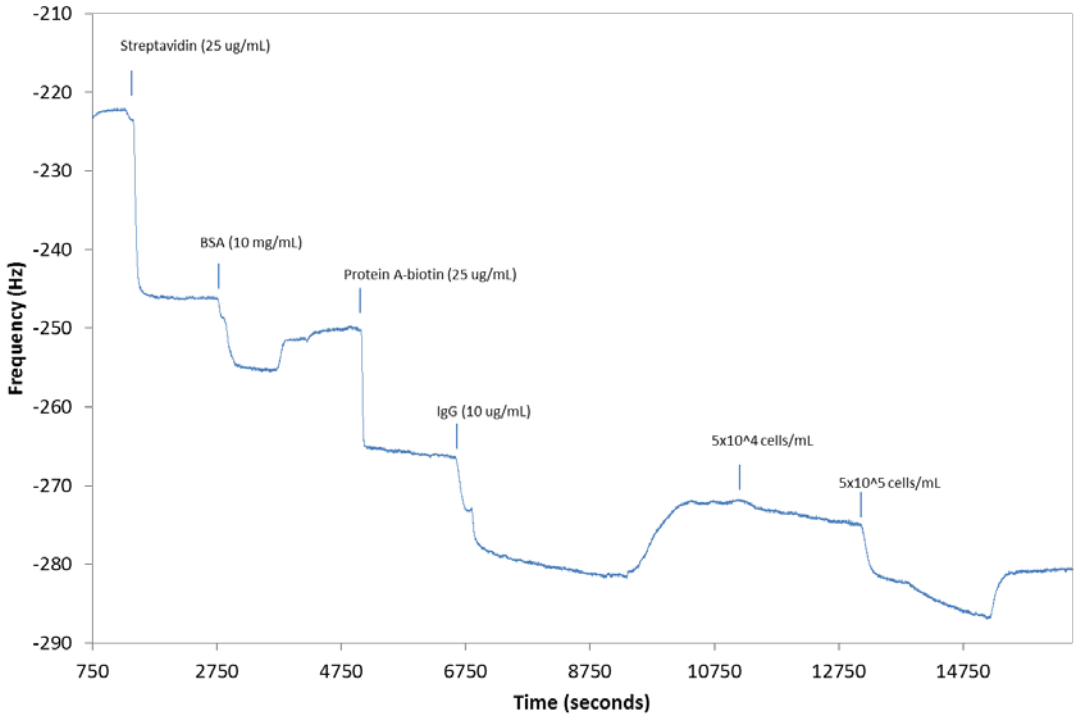

Figure 3-11. Frequency and dissipation vs. time for HLA-A2 B-lymphocyte cell binding to HLA-A2 IgG complex. Frequency = left y-axis, blue line, dissipation = right y-axis, red line.

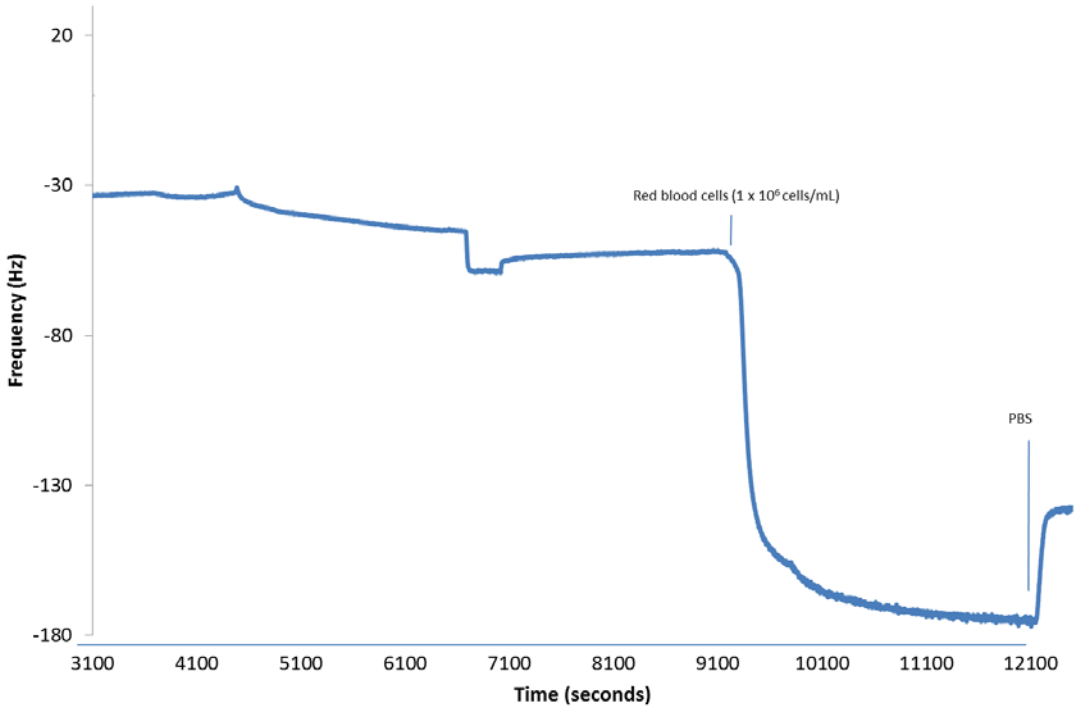

Figure 3-12. Frequency and dissipation vs. time for red blood cell binding to Glycophorein A IgG complex. Frequency = left y-axis, blue line, dissipation = right y-axis, red line.

3.5. Discussion

This chapter has proposed the use of shear stress-induced affinity cell separation inside a QCM as a means to measure cell purity. The application of shear stress has been shown to differentiate between cells adsorbed with and without affinity interactions, both theoretically (Kuo and Lauffenburger, 1993) and practically in previous studies (Nordon et al., 1996 and 2007) and in Chapter 2.

3.5.1. Surface hydrophobicity and charge

A functional surface for IgG immobilisation was created based on published work (Nileback et al., 2011). Briefly, gold-coated sensors were chemically modified to create a hydrophilic biotin-terminated surface added monolayer (SAM). The surface was hydrophilic, although atmospheric contamination via adventitious carbon (identified in Section 2.5.1.), was probably present given the high quantities of BSA content adsorbed compared to the cited

study (Nileback et al., 2011), as well as the contact angle of gold, which was greater than that characteristic of a cleaned gold surface (Abdelsalam et al., 2005).

3.5.2. Protein L and Protein A

IgG binding elicited a similar response to the aforementioned protocol, where the net change in frequency was 28.2 ± 3.6 Hz. IgG orientation was determined using Protein L and Protein A as analytes, which bind exclusively to the light kappa (Nilson et al., 1993) and Fc region (Moks et al., 1986) of IgG antibodies respectively. In this instance, a high Protein L to Protein A binding ratio would suggest orientated immobilisation of the adsorbed antibody. Protein L binding was almost 20 times greater when IgG was present compared to binding in the absence of IgG antibody. A similar trend was observed using Protein A, which was also markedly lower than Protein L. Conceivably, these findings show that it could be possible to use Protein L and A in replacement of antigens to indicate IgG orientation and presence, but this work is limited by the lack of experimental rigour and would be confined to certain antibodies that have an affinity for both Protein L and Protein A interactions.

3.5.3. Cell adsorption

B-lymphocytes and red blood cells were investigated for affinity interactions. Since no control study could be performed (i.e. antibody-free or using cells negative for the target antigen), it is not possible to determine whether cells were adherent with or without affinity interactions. Surfaces exposed to cells showed a net change in frequency following incubation and washing at 5 dynes/cm^2, consistent with the deposition of mass onto the sensor surface. B-lymphocytes exhibited a lower net change in frequency than red blood cells, which was attributed to the lower concentration of B-lymphocytes used (0.5 – 5 x 10^5 cells/mL), which was below concentrations (>3 x 10^6 cells/mL) typically used in previous

studies (Nordon et al., 1996, Slowiaczek, 1998, Nordon et al., 2004). Cell shape was also attributed to differences in signalling strength; Chapter 2 revealed that blood-bourne B-lymphocytes underwent no visible deformation over the incubation period, unlike that of most adherent cells, which flatten shortly after surface adsorption (Pierres et al., 2003). Conversely red blood cells are thin and flat, meaning that a higher proportion of the cytoplasm and nucleus is within range of the shear wave and were therefore able to generate a stronger signal.

3.5.4. Quantifying adherent cells

QCM methods for quantifying adsorbed material utilise density (Sauerbrey, 1959) and viscoelastic properties (Voinova et al., 2002). The application of such methods to quantify adsorbed cells is not considered feasible, owing to the complex structure of the cell, its dynamic nature (Kasza et al., 2007) and the fact that only a fraction of the cell would be in contact with the surface. Therefore, direct calibration to correlate changes in frequency with an adsorbed cell density (Redepenning et al., 1993), is deemed more appropriate. Correlating the number of adsorbed cells with frequency output will permit cell purity to be inferred using the same approach detailed in Section 2.5.12. This will allow shear stress to be used to differentiate between cells adherent with and without affinity interactions (Figure 3-13).

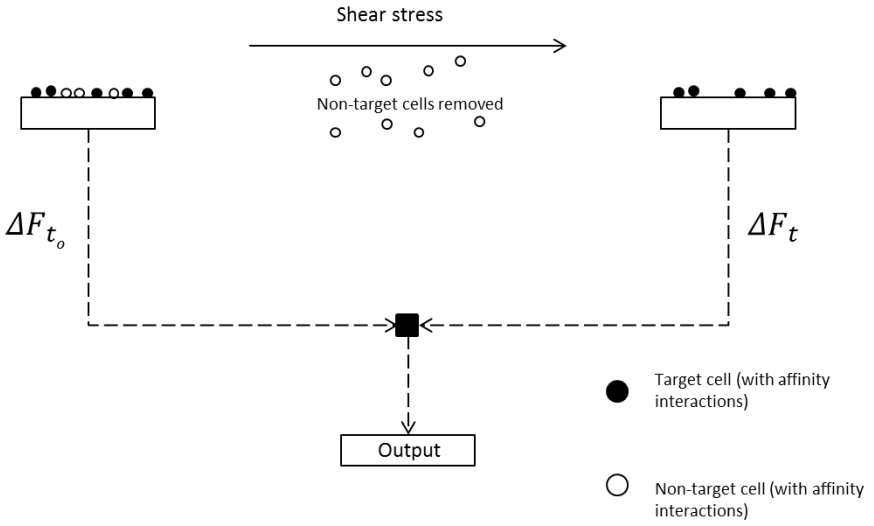

Figure 3-13. Output signal generated by difference in cell detachment. For a given number of adsorbed cells on the QCM sensor surface, determined through a correlation with the change in frequency, the purity may be determined using the approach developed in Chapter 2 (Section 2.5.11).

The following section assumes that two cell types are present; one positive for a specific antigen with an affinity for immobilised antibody and the other negative. These may represent a suspension of SSEA-4 antigen-negative product cells containing impure undifferentiated pluripotent cells negative for the SSEA-4 antigen. Therefore, for a given number of cells adsorbed on the sensor surface, the recorded change frequency (ΔF) relative to the baseline signal is given as:

$$\frac{\Delta F}{0 \rightarrow F_T} = N_T \qquad 3.3$$

, where F_T = the frequency for a population of adsorbed cells (Hz); N_T = the number of cells adsorbed on the sensor surface. By introducing a range of different cell numbers onto the sensor surface to quantify with microscope-based cell counting procedures, the change in

frequency per cell may be deduced from the following equation based on a linear plot of frequency versus cell number:

$$F_T = A_T . N_T \quad 3.4$$

, where A_T = the slope (Hz/cells). This allows the number of adsorbed cells to be estimated from the change in frequency without manual quantification. Chapter 2 proposed that based on the shear stress-induced detachment data of cells with and without affinity interactions, it is possible to correlate the number of adherent cells on a surface with their respective inlet purities. To determine the purity of cells adsorbed onto the sensor surface, the number of cells must be correlated with the resultant frequency change. The change in frequency for cells adsorbed onto the surface without washing (F_{To}) (Hz) may be given by:

$$F_{T_0} = F_{T,t_0} - F_o \quad 3.5$$

, where F_o = the baseline frequency prior to cell addition (Hz); $F_{T,to}$ = the change in frequency following the adsorption of cells on the surface, prior to washing (Hz); n = the shear stress applied (dynes/cm^2). Following washing at a critical shear stress able to differentiate between cells adherent with and without affinity interactions (e.g. 1 – 25 dynes/cm^2), the change in frequency for the total number of cells remaining on the surface (F_{Tn}) (Hz) is given by:

$$F_{T_n} = F_{T,n} - F_o \quad 3.6$$

, where $F_{T,n}$ = the change in frequency after washing at a given shear stress (e.g. 25 dynes/cm^2) (Hz). An example of the cell adsorption and detachment output signal that would be generated in response to shear stress is presented in Figure 3-14.

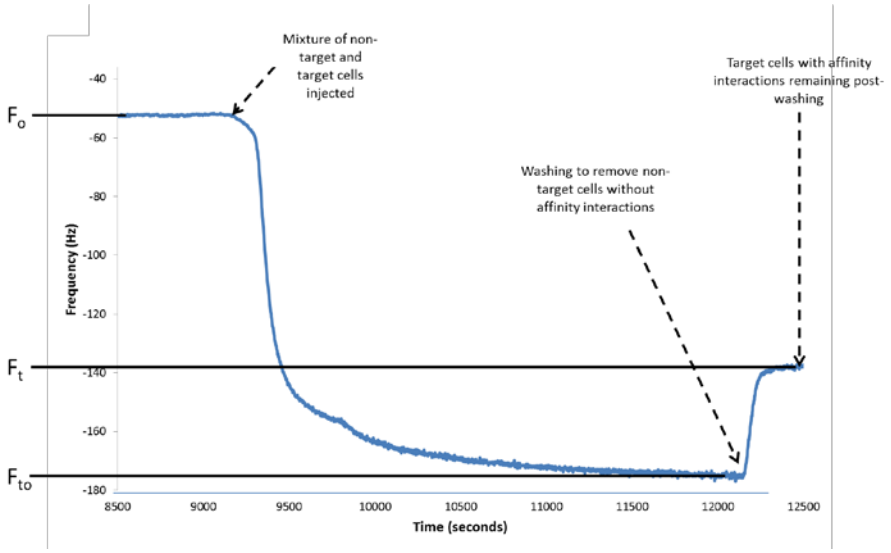

Figure 3-14. Example frequency vs. time plot. The graph plots a baseline signal (F_o) the static adsorption of cells onto a surface (F_{to}) and the subsequent detachment of cells (F_t) in response to shear stress. The net change in frequency (F_t - F_o) indicates the number of cells remaining on the surface.

The number of cells on the surface at any given point may be determined from by re-arranging Equation 3.4, generated from experimental data, to convert frequency into cell number:

$$\frac{F_{T,n}}{A_T} = N_{T,n} \qquad 3.7$$

, where $N_{T,n}$ = the total number of cells on the surface following washing at a given shear stress (cells).

The purity of target cells (e.g. CD20+ cells) on the surface following washing at a given shear stress ($SP_{C,n}$) may be given by utilising the approach devised in Chapter 2 to convert the

number of cells on the surface post-washing at a given shear stress into purity prior to washing ($SP_{C,n0}$):

$$SP_{C,n0} = \frac{SP_{\mathrm{C,n}}.N_{\mathrm{T,n}}}{RT_{C,n}.N_{T,n0}} \quad 2.17$$

, where $RT_{C,n}$ = fraction of CD20+ cells originally adsorbed on the surface retained at a given shear stress (-) (a constant determined through experimental observation); $N_{C,n}$ = the number of CD20 cells on the surface following washing at a given shear stress (cells); $N_{T,no}$ = the total number of cells on the surface prior to washing (cells); $SP_{C,n}$ = the purity of CD20+ cells on the surface after washing at a given shear stress. The purity of cells on the surface prior to washing would equate to the purity of the cells that would be injected into the device.

3.5.5. System feasibility

The QCM has many applications as a biosensor, but the purpose here would be to measure the level of impure SSEA-4 antigen-positive cells during a multi-day differentiation process (Figure 3-15) (Chen et al., 2014) to indicate the efficiency of the differentiation process. The feasibility of the QCM for this purpose would depend upon its practical operation and several quantitiative constraints that would need to be identified, as detailed below.

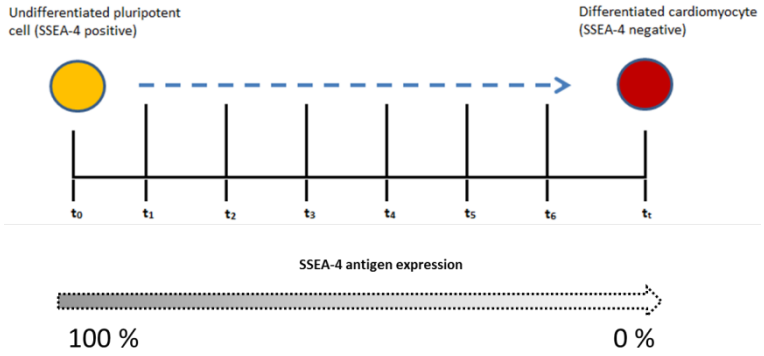

Figue 3-15. Sampling process for pluripotent cell differentiation towards a cardiomyocyte lineage. Undifferentiated pluripotent cells undergoing the transition to a differentiated state cease SSEA-4 antigen expression and this process can be measured as a function of time.

3.5.5.1. Operation

A proposed sampling and measurement protocol that is potentially faster than flow cytometry is presented in Table 3-6 below. The estimated time to measure a specific sample would range from 50 – 75 minutes for IgG-Protein A (utilised in this thesis) and 25 – 50 minutes if the IgG antibody is immobilised to the surface prior. Conversely, flow cytometry sample preparation typically ranges from 35 – 50 minutes.

Table 3-6. Protocol proposed for the detection of cells using the QCM biosensor

Task	Description	Time (minutes)
Sampling	Extraction of cell suspension from a bioreactor	2
Counting	Determination of cell number based on manual or automatic cell counting	5
Centrifugation	Centrifugation (1,200 rpm) to remove waste components	5
Re-suspension	Aspiration of waste supernatant and addition of a known volume of processing buffer (1 % BSA in PBS) to attain desired concentration	3
IgG incubation[a]	Addition of IgG antibody to cell suspension and subsequent incubation for a set period	15
Centrifugation[a]	Centrifugation (1,200 rpm) to remove waste components	5
Re-suspension[a]	Aspiration of waste supernatant and addition of a known volume of processing buffer (1 % BSA in PBS) to attain desired concentration	3
Sample injection	Injection of cell sample into biosensor unit	2
Sample incubation	Incubation of cells with ligands to promote binding and measurement	5 – 30
Washing	Application of shear stress deemed to be sufficient to differentiate between impure (undifferentiated pluripotent) cells and product (differentiated cells).	3
Output	Determination of net amount of cells on surface and subsequent purity	1

[a] only required if using Protein –coupled substrates where cell suspension is incubated with IgG prior to addition; [b] to be determined experimentally, depends on ligand choice and binding kinetics.

3.5.5.2. Performance criteria

In spite of the lack of cell-related studies, performance constraints can be inferred from some of these basic studies to determine the feasibility of this system for the detection of target cells. These performance constraints are detailed below and presented in Table 3-7.

Limit of Blank (LoB)

The Limit of Blank (LoB) can be used to determine the Limit of Detection (LoD) and the Limit of Quantitation (LoQ). The LoB may be estimated from the mean difference in frequency of a blank solution and an IgG-coupled sensor. The mean difference (mean +/- SD) was calculated to be 0.77 +/- 0.28 Hz (n = 8), equating to an LoB of 1.23 Hz.

Limit of Detection (LoD)

The LoD was estimated from two samples due to the limited amount of data available using a low-density sample (5 x 10^4 cells/mL x 40 µL chamber volume =~ 2,000 cells. The mean change following the deposition of cells was estimated to be 1.25 +/- 0.45 Hz (mean +/- SD) (n = 2), leading to an LoD of 1.97 Hz, approximating to ~ 2 Hz.

Limit of Quantitation (LoQ)

Previously, the change in frequency for a given sample was estimate to be 4 x 10^{-4} Hz per cell (Redepenning et al., 1993), meaning that the LoQ would equate to ~ 5,000 cells on the surface.

Table 3-7. Performance-related parameters for the QCM biosensor.

Parameter	Equation	Value (Hz)	Comment
LoB	$\boldsymbol{LoB = mean_{blank} + 1.645(SD_{blank})}$	0.77 +/- 0.28	Based upon unchallenged IgG-coupled sensors in buffer solution.
LoD	$\boldsymbol{LoD = LoB + 1.645(SD_{low\ density\ sample})}$	1.97	Two studies from experiments involving HLA-A2+ cells loaded at a concentration of 5 x 10^4 cells/mL
LoQ	$\boldsymbol{LoD = LoB + 1.645(SD_{low\ density\ sample})}$	2.00	In excess of the LoD. Would equate to 5,000 cells deposited on the sensor surface.

LoB = limit of blank; LoD = limit of detection; LoQ = limit of quantitation.

Minimum measurable purity for 4 % cell density

For a 4 % cell density prior to shear stress, the minimum measurable purity can be determined by first applying Equation 2.14 to determine $SP_{C,n}$, the surface purity of target cells after shear stress exposure, for an $N_{T,n}$, the total number of cells after shear stress exposure, of 5,000 cells (the LoQ), equating to 26.6 % CD20+ cell purity ($SP_{C,n}$) after washing at 25 dynes/cm^2.

By then using Equation 2.16 with a 4 % cell surface density (equating to 42,091 cells) and assuming that 84 % of the CD20+ cells remain adherent ($RT_{C,n}$) based on prior experimentation using individual cell subpopulations (as illustrated in Chapter 2), Equation 2.17 can then be applied to determine $SP_{C,n0}$, the purity of target cells on the surface prior to shear stress exposure and therefore the sample purity. When the LoQ is 5,000 cells, this would yield a 3.8 % CD20+ cell purity as a minimum quantifiable purity. As such, the minimum target cell purity for a 5,000 cell limit must be ≥ 4 %.

These estimates are extracted from the model developed in Chapter 2. In practice, significant variation across repeats is expected, which will limit the reliability of the data. The coefficient of variance for cells after washing is high, being up to 80 % HLA-A2+ (non-target) cells. In the QCM system, this would be reduced since the entire sensor surface would be utilised, instead of six-gated regions inside the flow tubes.

3.5.5.3. Challenges facing biosensor development

Whislt generic constraints have been described to account for instrument reliability, several limitations which cannot be addressed theoretically are presented in Table 3-8, along with potential solutions.

Table 3-8. Limitations and potential solutions for the QCM biosensor.

Problem	Description	Solution
Cell deformation	The cell will deform as a function of incubation time (Cuvelier et al., 2007, Gallant et al., 2005) and shear stress (Bose, 2009, Nordon et al., 2004), meaning that the signal will change irrespective of cell desorption.	Account for the change in signal strength at a given time and shear stress by using a converstion factor to measure cell deformation as a function of time and shear stress. The latter may be more complex.
Cell density	Pluripotent cells have a much higher cytoplasm-to-cell content ratio than more mature cell types (Thomson et al., 1998), so the measured frequency would be higher per pluripotent cell than per differentiated cell.	Account for cell density in models using a conversion factor based on the proportion of cells retained after washing at a given shear stress.
Non-specific cell adherence	The fraction of cells retained without affinity interactions was estimated to be ~ 5 % at 25 dynes/cm^2 (it was ~5 % at 5 dynes/cm^2 elsewhere (Nordon et al., 1996, Slowiaczek, 1998)), meaning that more impure cells would be removed, reducing the biosensor resolution.	Since differentiated cells upregulate certain extracellular antigens exclusive to their state, tagging the antigens of these cells with antibodies conjugated to hydrophilic PEG could reduce the adhesion of product cells, mitigate non-specific adherence further. Similar methods have been demonstrated for the inhibition of E-selectin-mediated cell adhesion (DeFrees et al., 1996).
System signal strength	An approximate 5 Hz change in frequency per 1 % cell coverage (equivalent to 12,500 cells) was reported (Redepenning et al., 1993). This would equate to 4 x 10^{-4} Hz per cell. In reality, a single cell could not be detected, owing to background noise and a lack of precision, but larger net changes (>0.5 Hz = ~ 1,250 cells) could indicate trends occurring within the system over a period of time. However, such measurements could not distinguish between minor changes in cell purity (e.g. from 99.9 to 99.9999 % purity)	Maximise the density of cells per unit surface area of sensor surface. According to the Sauerbrey equation (Sauerbrey, 1959), increasing the resonance frequency will magnify the output frequency signal (Uttenthaler et al., 2001). However, background noise (e.g. cell debris, proteins, etc.) would need to be minimised to ensure the highest signal-to-noise ratio.
Debris	The models assume that only two components exist: the cells and the buffer solution. In reality, other contaminent species may be present, namely cell debris (e.g. membrane segments, DNA, etc.). Such components, although smaller, are more dense and may generate a signal several orders of magnitude per single protein than per cell.	Subject the cell suspension to filtration and low-speed centrifugation procedures and confirm using a blank solution.
Antigen down-regulation	Models assumed that SSEA-4 antigen expression was binary. In reality it is transient, where cells gradually down-regulate the SSEA-	Identify a threshold based on shear stress studies to differentiate between cells with low levels of SSEA-4 antigen expression.

	4 antigen over a period of time during the differentiation process. This would lead to a change in the number of cells positive for the antigen adherent at a given shear stress, compromising system accuracy.

Whilst it is possible to detect changes in the density of surface-adherent cells the signal strength is very low (4×10^{-4} Hz/cell (Redepenning et al., 1993)) meaning that changes under 0.3 Hz would be hard to distinguish from background noise, so reliably detecting smaller changes in purity (e.g. from 99.9 to 99.99 %) may not be possible.

Ease of use is also a concern, given that extensive, albeit simple, preparation is required to prepare cell samples for measurement versus the flow cytometry benchmark, the procedure is similar and feedback is not immediate yet may compromise the reliability of measured data, questioning its use as a viable alternative.

Further, the mode of detachment is inherently reliant on pluripotent cell SSEA-4 antigen expression, which is typically representative for only 95 % of cells (Shibata et al., 2006). Methods such as RAMAN and FTIR may be more viable alternatives, relying upon the measurement of intracellular components (e.g. nucleic acid, collagen, phsopholipids, etc.) that direct cell fate (Chan et al., 2010), rather than antigenic markers which are associated with the state of a cell, but not necessarily representative of it (Fong et al., 2009).

3.6. Conclusion

This chapter has documented exploratory work into the QCM system as an affinity biosensor for impure cell detection. The specific purpose is to detect cells which have retained their pluripotent status (based on SSEA-4 antigen expression), through an affinity interaction with an SSEA-4 antibody-coated surface. Such information could be used to

improve a differentiation process during the development of a cell therapy product, offering a cheaper, easier to use alternative to flow cytometry. Preliminary data has been produced with cells using affinity-interactive surfaces, partially validated using Protein L and A analytes. It is thought that by replicating the same method of cell separation detailed in Chapter 2 (shear stress-induced affinity separation) and correlating frequency change with cell density, the net change in cells on the surface could be used to deduce the purity of a certain population of cells in a sample.

The results at this stage are far from conclusive. It is not clear what the QCM resolution is or how reliable it would be to operate practically for cell detection. Of the two cell types tested (B-lymphocytes and red blood cells), large differences were observed in measured frequencies and were attributed to (1) concentration differences and (2) cell shape; flatter, thinner red blood cells elicited a greater response in frequency than spherical B-lymphocytes. However, confirmation that cell-surface affinity interactions occurred was not possible, since no control studies could be performed.

The QCM system is not proposed as a universal biosensor, rather, one which is highly customised to a pluripotent cell line undergoing extensive testing for differentiation towards a specific lineage. Whilst theoretically feasible, it may not possess the resolution, ease of use or reliability to be considered a quality control (QC) instrument for a cell therapy manufacturing process, but rather, may be considered a routine lab tool.

Chapter 4. Affinity membrane development

4.1. Introduction

Chapter 2 presented a small-scale model to identify differences in cell adhesion strength using shear stress. Cells without affinity interactions proved to be more susceptible to detachment than cells with affinity interactions, consistent with theoretical (Bell, 1978, Bell et al., 1984) and practical (Kuo and Lauffenburger, 1993, Nordon, 1994) observations.

To replicate this concept for the separation of cell populations, a suitable device must be selected. Several formats derived from bioprocessing permit affinity separations in flow through modes (Ghosh, 2002; Moser and Hage, 2010). Beads for instance, have a surface area-to-volume ratio as high as 100 m^2/g of matrix (Bhattacharyya et al., 1996) and possible IgG adsorption densities of 55 – 70 g/L of resin (Coleman et al., 1990, Johansson, 1997, Hahn et al., 2005). However, the porous geometry of the beads, which promotes diffusion rather than convection-driven transport, is largely inaccessible to cells and would be inefficient for separation. Conversely, affinity membranes have lower surface areas (2-20 m^2/g) (Ulbricht et al., 2009) and lower ligand adsorption capacities (10 – 30 g/L of membrane volume) (Colton, 1996, Jia et al., 1999), but are more suited to cell separation because of their ability to transport cells via convection processes and apply uniform shear stresses tangentially (Slowiaczek, 1998).

Several membrane formats exhibit favourable geometry for cell separation, centring around flat sheet and hollow fibre membranes. Such membranes comprise chemically and mechanically stable polymers, such as polyethersulfone, nylon and methacrylate (Ghosh, 2002). Chemical functionalities present on these membranes enable covalent ligand

adsorption for protein (Hermanson, 1992, Castilho et al., 2000, Hahn et al., 2003) and cell separation (Nordon, 1994, Colton, 1996, Slowiaczek, 1998) through affinity interactions. Flat-sheet and hollow fibre membranes are particularly desirable because uniform shear stresses can be applied tangentially across the surface enabling similar conditions observed in Chapter 2 to be applied.

Chapter aims and objectives:

- Construct, chemically modify and characterise hollow fibre membranes.
- Characterise the hydraulic conditions inside both hollow fibre and flat sheet membranes
- Determine rPrA and IgG antibody adsorption capacities for both hollow fibre and flat sheet membranes and their adsorption capacity for IgG molecules

4.2. Materials and methods

This section concerns the development and characterisation of hollow fibre membrane modules constructed from Nephral ST200 dialysis cartridges (Gambro Lundia AB, Lund, Sweden) and a flat sheet microfiltration membrane cassette kindly supplied through Peter Levison (Pall Life Sciences, Uk) (Table 4-1). The purpose was to implement the same method developed for immunoaffinity cell separation in Chapter 2 using the affinity interaction created between immobilised rPrA and IgG-tagged cells, but to separate mixed cell populations CD20+ cells and HLA-A2+ cells) in scalable membrane units in Chapter 5.

Table 4-1. Comparison of hollow fibre and flat sheet microfiltration membranes

Membrane type	Physical properties	Chemical composition
Hollow fibre dialysis	Average pore size: < 1 um; length: 22 cm; wall thickness 42 um; outer diameter: 210 um; membrane volume per length: 1.25 mL/cm	Fibres are comprised of an acrylonitrile and sodium methallyl sulfonate copolymer treated with polyethyleneimine (PEI) (Figure 4-1 A). Amine terminal groups allow aldehyde functionalization with bi-functional aldehyde molecules via Schiff base formation.
Flat sheet microfiltration	Membrane type: flat sheet microfiltration; average pore size: 0.45 um	Sheets are made of polyethersulfone (PES) (Figure 4-1 B) and have been modified using proprietary techniques to create aldehyde functionality

Specifications were extracted from commercially available data.

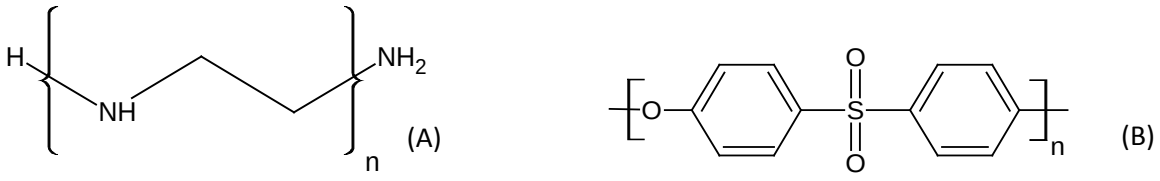

Figure 4-1. Basic chemical structures of (A) polyethyleneimine (PEI) (linear chain) and (B) polyethersulfone (PES).

4.2.1. Chemical modification

Since the Pall polyethersulfone (PES) membranes already have aldehyde functionalities, this section is devoted to the aldehyde functionalization of polyethylenimine (PEI) hollow fibres.

4.2.1.1. Hollow fibre aldehyde functionalisation

Nephral ST200 hollow fibre membrane dialysis cartridges were purchased from Gambro Lundia AB (Lund, Sweden). Cartridges were positioned vertically in a fume cabinet using a stand and clamp. A 2.5 % (v/v) solution of glutaraldehyde (Fischer Scientific, Loughborough, UK) in 0.1 M sodium phosphate buffer with 0.15 M NaCl (PBS) containing 0.075 M sodium cyanoborohydride (Sigma-Aldrich, Munich, Germany) (pH 7) was prepared. Each solution was then systematically alternated across both the shell and lumen side of the cartridge at 100 mL/min using Tygon tubing (Cole-Parmer, London, UK) and a peristaltic pump (Watson-Marlow, Falmouth, UK) for 4 hours. Excess glutaraldehyde solution was drained and

cartridges were rinsed at 10 minute intervals using de-ionised water, 50 % (v/v) methanol (Sigma-Aldrich, Munich, Germany) and de-ionised water for 1 hour. Cartridges were then stored at 4 ^{o}C in 20 % ethanol. Fibres were then extracted for characterisation or further modification by cutting the cartridge open with a saw.

4.2.2. Chemical assays

4.2.2.1. TNBS

The TNBS assay (detailed in Chapter 2 section 2.4.3) was prepared to qualitatively measure the change in amine functional groups before and after glutaraldehyde treatment through colour changes. Untreated and glutaldehyde-treated fibres were cut into 10 x 5 cm segments and soaked in TNBS solution for 15 minutes. Fibres were then rinsed three times successively in de-ionised water, 50 % methanol, 100 % methanol and de-ionised water and then blotted with absorbent paper. Photographic images of fibres were then recorded immediately.

4.2.2.2. Silver mirror test

Tollen's reagent (Fieser, 1987) was used to measure aldehyde functionalities on untreated PEI and glutaraldehyde-treated PEI membranes. Prior to conducting the reaction, the same procedure for solution preparation from Section 2.4.4. was implemented. Both untreated and glutaraldehyde-treated fibres were then soaked in this solution in a water bath at 37 ^{o}C for 15 minutes. Fibres were then removed with tweezers and rinsed three times in de-ionised water prior to imaging.

4.2.2.3. Fourier Transform Infra-Red (FTIR) spectroscopy

Dried fibres were mixed with potassium bromide and compressed under a 10-tonne force to form a disc. Fourier Transform Infra-Red (FTIR) analysis was performed using a Nicolet 380 instrument at The University of Birmingham. The discs of both unmodified and modified fibres were analysed using Intuitive EZ-OMNIC^{TM} software (Thermo Electron Corporation, Loughborough, UK).

4.2.2.4. BCA assay for aldehyde coating efficiency

Approximately 10 cm of glutaraldehyde-treated and untreated polyethyleneimine hollow fibres were soaked in liquid nitrogen then cut into < 1 mm sections using a scalpel. Fibres were then incubated in 0.225 mL of working reagent with 0.025 mL of deionised water for 30 minutes at 37 ^{o}C. (No calibration chart was generated since the purpose was to determine the net change in absorbance generated by the reaction of primary and secondary amines with BCA reagent.) Following incubation, 0.225 mL of supernatant was removed and absorbance was quantified in a Falcon black-walled 96 well plate using an Omega POLARstar plate reader (BMG Labtech, Bucks, UK) at 562 nm. The baseline absorbance was subtracted from recovered data. The net change in absorbance was then correlated with fibre length and used to indicate the coating efficiency of glutaraldehyde treatment.

4.2.3. Physical characterisation

The morphological and structural characterisation of both hollow fibre and flat sheet membranes was performed using a range of different techniques.

4.2.3.1. Atomic Force Microscopy

Atomic force microscopy was performed on both flat sheet and hollow fibre membranes. In all cases, the average roughness (R_a) and root mean square roughness (R_{rms}) were measured across dimensions of 20 x 20 um from duplicate samples.

4.2.3.2. Environmental scanning electron microscopy (ESEM)

Environmental scanning electron microscopy (ESEM) was performed on aldehyde-functionalised hollow fibre membranes only, owing to their tendency to dehydrate and disintegrate rapidly under atmospheric conditions. Fibres were stored in de-ionised water prior to use and then studied at 10 kV using an XL30 (FEI-Philips, Oregon, USA) in a saturated water vapour environment.

4.2.3.3. Field emission scanning electron microscopy (FESEM)

The structural stability of the PES membrane meant that Field Emission Gun Scanning Electron Microscopy (FEGSEM) could be performed. Prior to analysis, PES segments (1 x 1 cm) were sputter coated with gold. PES discs were then observed using a LEO 1530VP field emission scanning electron microscope, operating at 5 kV and 30 pA at Nottingham University.

Image analysis

The available surface area of the PES membrane electron microscope images were examined using NIOS-Element AR software (Nikon, Tokyo, Japan). Membrane pores were identified and quantified in MCH-mode. Absorbance channels were adjusted to differentiate between the top surface (red) and pores (green) as illustrated in Figure 4-2.

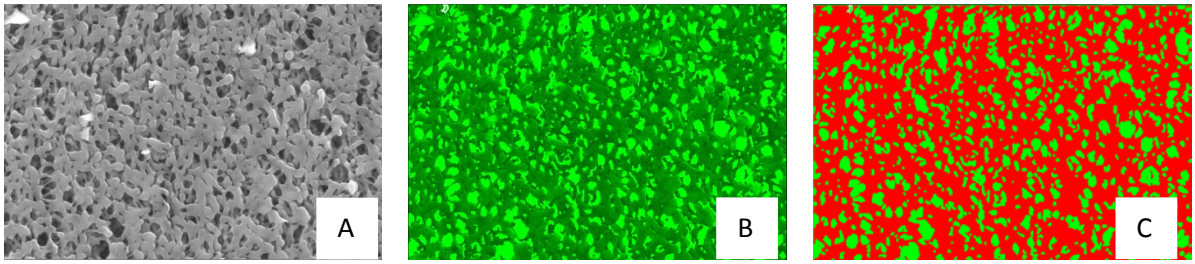

Figure 4-2. SEM porosity image analysis of (A) raw PES membrane, (B) green-inverted version and (C) red-/green-inverted to quantify porosity.

4.2.3.4. BET surface area

Brunauer-Emmett-Teller (BET) surface area measurements were performed on a Micromeritics ASAP2010 device (Hexton, UK) to determine the membrane surface area per unit volume of membrane. Weighed samples were degassed initially at 90 ^{o}C for 2,000 minutes and then at 140 ^{o}C for 600 minutes under a vacuum of < 10 umHg. The sample was cooled to 77 K and nitrogen was administered to the sample in controlled increments. After each dose of adsorptive, the pressure was allowed to equilibrate and the quantity of gas was used to indicate the available surface area of the membrane.

This measurement was only performed for the PES membranes as the hollow fibres were too fragile. Separate calculations were performed to determine the surface area of the hollow fibres.

4.2.4. Membrane sample preparation

Different hollow fibre and flat sheet membrane formats were generated for each experiment and the details are provided below.

4.2.4.1. Hollow fibres

Hollow fibres required preparation for each application, due to instability and difficulties in ensuring adequate liquid contact with the fibre lumen. These are detailed systematically for chemical modification followed by protein adsorption and cell separation purposes.

Static protein adsorption

rPrA and BSA protein adsorption studies required static conditions. Aldehyde-functionalised fibres were extracted from the cartridges and the length was measured for each batch before soaking in liquid nitrogen (< 10 seconds). Fibres were then immediately shredded with a scalpel. To avoid dehydration, shredded fibres were soaked in PBS until further use.

Fibre module preparation

Two different types of custom-made hollow fibre modules were created (Figure 4-3) to: (1) quantify IgG adsorption capacities and (2) conduct immunoaffinity cell separation (Chapter 4).

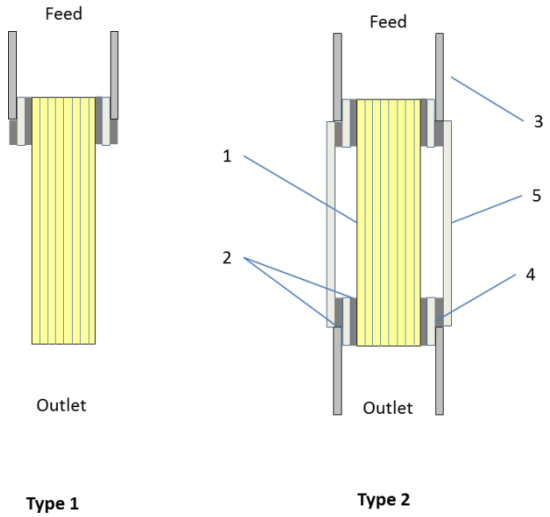

Figure 4-3. Schematic diagrams of constructed hollow fibre modules. Aldehyde-functionalised fibres (75 x 10 cm) were glued into tubing using resin. Two types of hollow fibre modules were utilised, which included the Type 1 module, where the fibres were sealed at the inlet for IgG adsorption capacity studies; and Type 2, fibres, which were sealed at the inlet and outlet and the shell was positioned only for cell separation studies. The numbers are represented by: (1) = aldehyde-functionalised hollow fibres; (2) resin glue; (3) tubing outer-module tubing; (4) inner-module tubing; and (5) module shell.

IgG protein adsorption modules (Type 1)

The fragility of shredded hollow fibres meant that a flow-through model was constructed to estimate IgG adsorption capacities. Here, 75 glutaldehyde-treated fibres were inserted into

5 cm of tygon tubing at a designated inlet. Fibres were then sealed into place by injecting EF80 epoxy resin (Easy Composites Ltd, Stoke-on-Trent, UK) using a plastipipette and the mixture was allowed to set for 2 hours. During this period the fibres, which dehydrate rapidly under atmospheric conditions, were sprayed with de-ionised water and kept moist by wrapping with foil. Once set, the tygon tubing inlet was cut with a scalpel to 3 cm and fibres were trimmed at the outlet to create a total module length of 10 cm. These were designated Type 1 modules (Figure 4-3). rPrA and BSA, as well as IgG adsorption procedures are detailed in Section 4.2.6.

Cell separation modules (Type 2)

For cell separation studies, the same method used to create Type 1 modules was used for module construction, except that a tygon tubing outlet port was also included. These were designated Type 2 fibre modules (Figure 4-3) and were stored in 20 % ethanol at 4 ^{o}C until use. Prior to rPrA adsorption and blocking with BSA (Section 4.2.6.1), modules were integrity tested and assessed for variability (section 4.5.2). Further modification involving rPrA and BSA adsorption and the positioning of a shell across Type 2 modules for cell separation is detailed (Chapter 5, Section 5.2.2.2).

4.2.4.2. Flat sheet microfiltration membrane

Static incubation studies

For rPrA, BSA and IgG adsorption capacities (protocols detailed in Section 4.2.6.2), discs (diameter: 0.6 cm^2; surface area: 0.283 cm^2) were created using a hole punch from aldehyde-functionalised flat sheet polyethersulfone (PES) microfiltration membrane supplied via Peter Levison at Pall Life Sciences (Portsmouth, UK).

4.2.5. Hydraulic studies

Pressure losses and hydraulic permeabilities were measured for both hollow fibre and flat sheet membrane units. A generic process schematic is provided in Figure 4-4. The purpose was to study the pressure drop for each unit as a function of the same shear stress (0 – 25 dynes/cm^2) to be used in cell separation studies, as well as the hydraulic permeability of each membrane material.

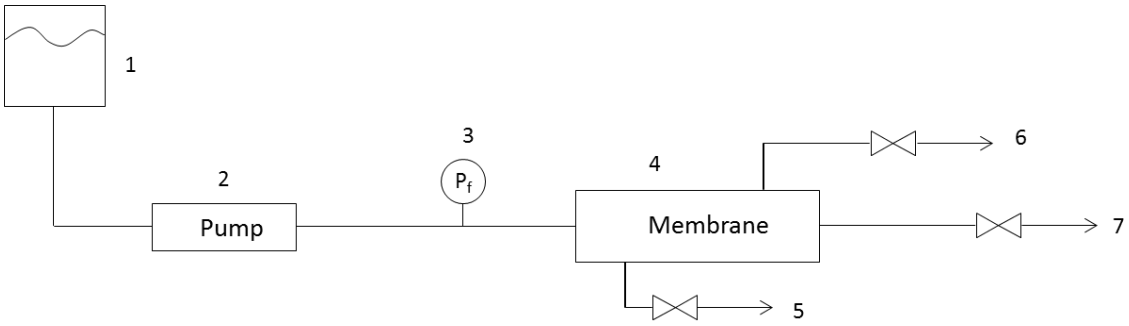

Figure 4-4. Representative schematic of process setup for TFF cassette and the HFM cartridge characterisation. Numbers are listed as: 1 = storage vessel with de-ionised water; 2 = pump (syringe pump for hollow fibre modules or a peristaltic pump for the microfiltration cassette); 3 = pressure sensor; 4 = membrane (hollow fibre or microfiltration); 5 = filtrate outlet (feed-side, microfiltration cassette only); 6 = filtrate outlet (outlet side, microfiltration cassette only); 7 = outlet.

For hollow fibres, the pressure drop of both the constructed Type 2 modules and the original Nephral ST200 cartridge were used owing to the absence of filtrate ports. The latter was only used for hydraulic permeability studies. For flat sheet membranes, a proprietary cassette containing the aldehyde-functionalised PES membrane was utilised in both pressure drop and hydraulic permeability studies.

4.2.5.1. Pressure loss

To determine the pressure loss, de-ionised water was pumped through each unit using an Alaris IVAC P7000 syringe pump (CareFusion, St Albans, UK) for fibre modules and a

peristaltic pump (Watson Marlow, Falmouth, UK) for the aldehyde-functionalised fibre cartridge and flat sheet membrane cassette. In each instance, the filtrate ports were closed, such that only the inlet and outlet were open, with the outlet being open to atmosphere. Pressure drop was measured using a Druck DPI 705 sensor (Cuthbertson Laird Group, Leeds, UK) as a function of shear stress applied sequentially for 3 minute intervals over 1, 5, 10 and 25 dynes/cm^2 for the hollow fibre membrane units and 1, 5 and 10 dynes/cm^2 for the flat sheet membrane cassette. The latter was restricted to a flowrate equivalent to 5 dynes/cm^2 to avoid damaging the membrane. Each flowrate was maintained for 30 seconds before extracting a reading.

4.2.5.2. Hydraulic permeability

Hydraulic permeability was determined across a range of 0 – 50 LMH for the aldehyde-functionalised Nephral ST200 cartridges and the Pall flat sheet membrane cassette. Device details were provided in Table 4-1. Prior to use membrane units were equilibrated with de-ionised water to remove air pockets. The inlet-side filtrate port and the outlet of each unit was closed, prior to the addition of de-ionised water.

4.2.6. Protein adsorption

The following section details rPrA and BSA adsorption onto both aldehyde-functionalised hollow fibre and flat sheet membrane surfaces.

4.2.6.1. Hollow fibre membrane

Static protein adsorption

rPrA and BSA adsorption capacities of aldehyde-functionalised fibres were performed under static conditions using segmented fibres (described in Section 4.2.4.1). Fibres were

incubated with recombinant Protein A (rPrA) (Prospec Bio, East Brunswick, USA) at a concentration of 1 mg/mL in 0.1 M sodium phosphate with 0.15 M sodium chloride (PBS) at pH 7 on an EW-51300 orbital shaker (Cole-Parmer, London, UK) for 4 hours. Fibres were then washed in PBS, 1 M NaCl and de-ionised water and then blotted with absorbent paper to remove excess moisture. The same procedure was performed using 1 % (v/v) BSA in PBS for 2 hours on both uncoupled and rPrA-coupled aldehyde-functionalised fibres to block charged sites. Protein densities were then determined according to the BCA assay (Section 4.2.2.4.), where fibres were incubated with 1.9 mL of working reagent and 0.1 mL of de-ionised water at 37 ^{o}C for 30 minutes. Samples were then centrifuged at 2,000 rpm in an Eppendorf 5416 centrifuge (Eppendorf UK, Stevenage, UK) to remove debris from the supernatant and transferred to a plastic cuvette (Fischer Scientific, UK). Sample absorbance was measured using a Shimadzu UV spectrophotometer (Shimadzu, Tokyo, Japan) at 562 nm. Protein content was determined using 0.1 mL stock solutions of known concentrations mixed with 1.9 mL of working reagent.

Flow-through protein adsorption

rPrA and BSA adsorption

To determine the IgG adsorption capacity of rPrA-coupled fibres, rPrA and BSA were adsorbed inside Type 1 modules. Modules were connected to two 3-way valves and a 1 mL micropipette using tygon tubing (Cole-Parmer, London, UK). Modules were then clamped into a vertical position suspended above a 2 mL eppendorf using a stand and clamp. A 1 mg/mL of rPrA solution in PBS was incubated for 4 hours and recycled every 30 minutes. During this period, modules were wrapped in foil to prevent dehydration and positioned horizontally to minimise fluid loss. Then, a 0.075 M solution of sodium cyanoborohydride in

PBS at pH 7 was injected into the column and incubated for 1 hour and recycled every 30 minutes. Control modules were also prepared for IgG adsorption studies using 1 % (w/v) BSA in PBS without rPrA. After incubation, modules were then washed successively in PBS, 1 M NaCl and de-ionised water. Fibres were then stored at 4 ^{o}C in 0.01 % (w/v) sodium azide in PBS.

IgG binding capacity

The IgG adsorption capacity of hollow fibre membranes was determined using Type 1 hollow fibre membrane modules. Module inlets of Type 1 hollow fibre modules were connected to the aforementioned setup (Figure 4-5). The side-inlet ports for the 3-way valves contained a 10 mL syringe containing air and a 10 mL syringe containing an elution buffer comprised of 0.1 M sodium citrate (pH 2.5) (Figure 4-5). A CD20 IgG antibody solution (0.25 mg/mL) was then injected into the module via a micropipette tip (1 mL) attached to the feed inlet and was recirculated through the column 3 times. The column was then detached, wrapped in foil and incubated horizontally at room temperature for 2 hours. The same protein adsorption process was also performed on control modules without rPrA, using BSA instead at 1 % (w/v) to determine non-specific adsorption. After incubation, modules were rinsed with PBS at 1 mL/min for 10 minutes. Air was injected to remove excess fluid, before the modules were rinsed 3 times with 0.5 mL of elution buffer. Eluted IgG concentrations from each collected fraction were determined using a Nanodrop 2000 UV spectrophotometric (ThermoScientific, Loughborough, UK) instrument by placing a 2 μL on the sensor and recording the absorbance at 280 nm.

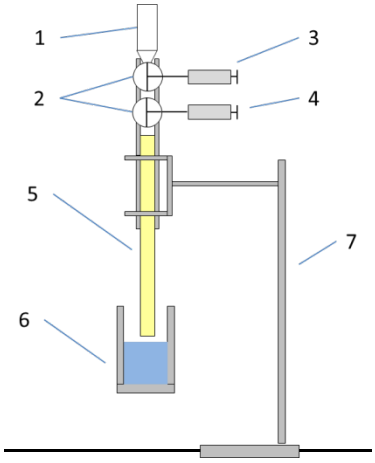

Figure 4-5. Schematic of a Type 1 hollow fibre module with immobilised rPrA for IgG binding capacity evaluation. Numbers represent: (1) = modified 1,000 uL micropipette; (2) = 3-way valve; (3) = 10 ml syringe containing 0.1 M PBS; (4) = 10 mL syringe containing air; (5) = Type 1 hollow fibre module; (6) = collection vessel; (7) = stand and clamp.

4.2.6.2. Flat sheet membrane

Protein adsorption

PES flat sheet membrane discs (Pall Life Sciences, Portsmouth, UK) were incubated in 1 mg/mL of rPrA for 4 hours under gentle agitation. Excess solution was removed and 0.075 M of sodium cyanoborohydride (Sigma-Aldrich, Munich, Germany) in PBS was injected and incubated for 1 hour (pH7). Discs were washed three times successively in PBS, 1 M NaCl and dH_2O for 15 minutes each under mild agitation. Absorbance was quantified using the BCA assay (Chapter 2, Section 2.4.4) with an Omega POLARstar plate reader (BMG Labtech, Slough, UK) at 562 nm and quantified using known stock solutions of protein concentrations in a black-walled 96 well plate. Modified fibres were then incubated in 0.225 mL of working reagent and 0.025 mL of de-ionised water at 37 ^{o}C for 30 minutes, after which 0.225 mL of supernatant was removed and the absorbance measured.

The IgG adsorption capacity of rPrA-coupled discs was then examined by incubating a range of CD20 IgG antibody across 0 – 1.28 mg/mL in 0.15 mL of PBS for 2 hours. Segments were

then rinsed three times in 0.2 mL of PBS to remove unbound IgG. Adsorbed IgG protein was then eluted in 0.2 mL of 0.1 M sodium citrate (pH 2.5) after 5 minutes of incubation with two washes. A control study to measure non-specific IgG binding was not performed. Eluted IgG protein was quantified at 280 nm using a Nanodrop 2000 UV-spectrophotometer (ThermoScientific, Loughborough, UK).

4.3. Theoretical considerations

4.3.1. Hydraulic characterisation

Pressure drop

Pressure loss, used to test device integrity and the batch-to-batch variability of constructed Type 2 hollow fibre modules was measured as a function of shear stress (0 – 25 dynes/cm^2) applied for 3 minute intervals. The filtrate lines of both the hollow fibre cartridge and the microfiltration cassette were closed. Laminar flow for a Newtonian fluid was confirmed using Equation 1.3 (Chapter 1). Shear stress at the wall of each fibre was then estimated assuming smooth tubes using (Bird, 2007):

$$\tau = \frac{4Q\mu}{\pi n r^3} \qquad 4.1$$

, where Q = flowrate (m^3/s); μ = dynamic viscosity (kg/m.s); r = fibre radius (m) and n = the number of fibres (-). Shear stress acting on the surface of the flat sheet membrane was then calculated assuming that the geometry resembled a parallel plate with laminar flow (Bacabac et al., 2005):

$$\tau = \frac{3Q\mu}{2w(h/2)^2} \qquad 4.2$$

, where Q = flowrate (m^3/s); μ = dynamic viscosity (kg/m.s); w = chamber width (m); h = chamber height (m).

Hydraulic permeability

The hydraulic permeability was determined for both PES flat sheet membranes and aldehyde-functionalised hollow fibre membranes. Inlet pressure was measured as a function of water flux (J_f) across the membrane and calculated using:

$$J_f = \frac{Q_f}{A_m} \quad 4.3$$

, where J_f = permeate flux rate ($L/hr/m^2$); Q_f = filtrate flowrate (L/hr); A_m = membrane area (m^2). The transmembrane pressure, TMP (psi), was then calculated from:

$$TMP = \left(\frac{P_{feed} + P_{retentate}}{2}\right) - P_{filtrate} \quad 4.4$$

, where P_{feed} = feed inlet pressure (psi); $P_{retentate}$ = retentate port pressure (psi); $P_{filtrate}$ = filtrate port pressure (psi). Both values enabled the hydraulic permeability to be calculated from:

$$HP = \frac{J_f}{TMP} \quad 4.5$$

, where hydraulic permeability = HP (LMH/psi); filtrate flux = J_f (LMH).

4.3.2. Protein adsorption capacities

The binding saturation capacity was estimated using Graphpad software (Prism, California, UK), assuming total binding (specific and non-specific):

$$B = \frac{B_{max}C}{K_d + C} \quad 4.6$$

, where B = the amount of IgG adsorbed per rPrA segment (mg/mL membrane volume); B_{max} = maximum IgG adsorbed (mg/mL of membrane volume); C = concentration of IgG in free solution (mg/mL); K_d = equilibrium binding constant (mg/mL).

4.3.3. Membrane size calculations

Hollow fibre membranes

The total surface area of hollow membrane (internal) available for cell adsorption (SA_i) is calculated from:

$$SA_i = \pi d_i . L \quad 4.7$$

, where d_i = inner fibre diameter (m); L = fibre length (m).

Total hollow fibre membrane volume including void volume (V_m) can be defined as:

$$V_{m-h} = \pi \frac{L}{4}\left(d_o^2 - d_i^2\right) \quad 4.8$$

, where d_o = outer fibre diameter (m); d_i = inner fibre diameter (m).

Flat sheet membranes

The total membrane volume including void volume for a circular segment of flat sheet membranes may be calculated as:

$$V_{m-F} = \pi . r^2 . h. \quad 4.9$$

, where r = segment radius (m); h = segment thickness (m). The thickness was taken to be 0.0152 m, based on personal communication with Pall Life Sciences.

4.4. Results and discussion

4.4.1. Physical

Membrane roughness and morphology were determined from atomic force microscope measurements. Data are displayed in Table 4-2 and force micrographs of untreated PEI fibres (Figure 4-6), glutaraldehyde-treated fibres (Figure 4-7) and flat sheet microfiltration membranes (Figure 4-8).

Glutaraldehyde treatment of PEI fibres yielded a reduction in surface roughness compared to untreated PEI fibres, where micrographs showed a flatter, but more abrasive surface. In particular for the glutaraldehyde-treated PEI fibres, the surface roughness (R_a = 32.2 ± 0.5 nm and R_{rms} = 45.8 ± 0.4 nm (mean ± SEM)) was comparable to that observed for glutaraldehyde-treated glass microslides detailed in Section 2.5.1, where R_a = 25.3 ± 4.8 nm and R_{rms} = 33.9 ± 4.6 nm (mean ± SEM) were observed.

In contrast, PES flat sheet membranes exhibited much greater morphological variation (R_a = 102.1 ± 9.9 nm and R_{rms} = 121.7 ± 10.6 nm (mean ± SEM)). Much larger height ranges were observed compared to both fibres, primarily owing to the porous nature of the membranes. The PES material surface itself was smooth, but exhibited surface-localised nodules (Figure 4-8).

Table 4-2. Membrane roughness for hollow fibre and flat sheet membrane formats.

Membrane format	Surface type	Roughness (nm)		Height measurements (nm)
		Ra	Rrms	
Hollow fibre	PEI[a]	39.9 ± 2.4	53.9 ± 1.9	376.5 – 678.9
	GA-PEI[b]	32.2 ± 0.5	45.8 ± 0.4	266.0 – 357.4
TFF	PES[c]	102.1 ± 9.9	121.7 ± 10.6	675.4 – 1,230.0

Samples performed in duplicates across two different areas. R_a = roughness average; R_{rms} = root mean square roughness. Data presented as mean ± SEM. n = 2. [a] untreated PEI (polyethylenmine); [b] glutaraldehyde-treated PEI; [c] aldehyde-functionalised polyethersulfone (PES).

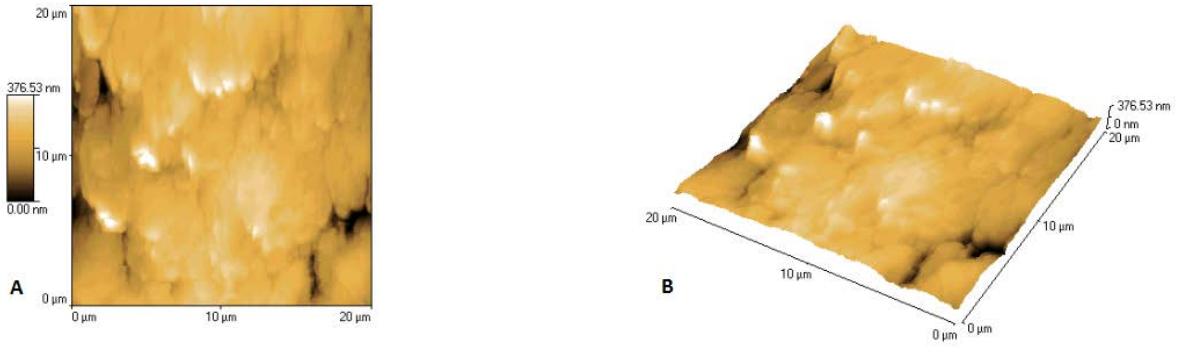

Figure 4-6. Atomic force micrographs of polyethylenimine hollow fibres in (A) 2D and (B) 3D formats.

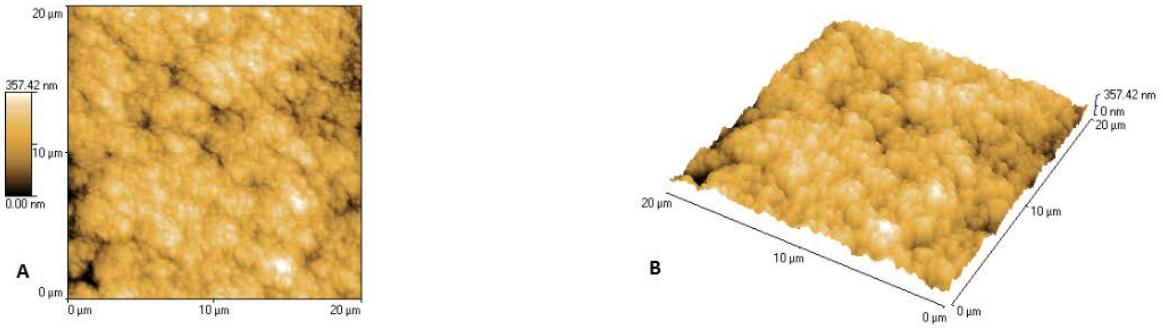

Figure 4-7. Atomic force micrographs of glutaraldehyde-treated polyethylenimine hollow fibres in (A) 2D and (B) 3D formats.

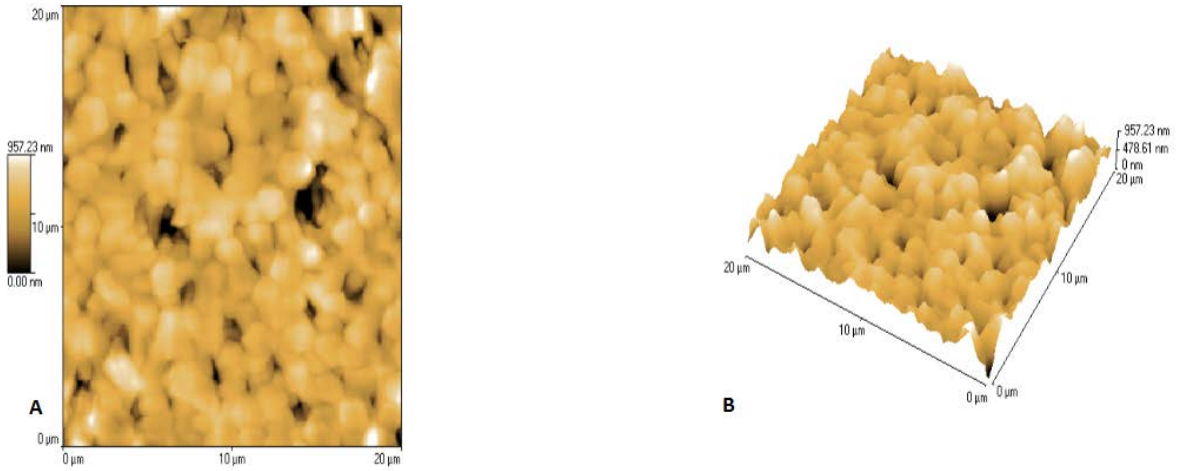

Figure 4-8. Atomic force micrographs of polyethersulfone segments in (A) 2D and (B) 3D formats.

Environmental scanning electron microscopy (ESEM) was performed on hydrated aldehyde-functionalised fibres only. Data are displayed in Table 4-3 and images in Figure 4-9. ESEM geometric measurements (Table 4-3) indicated a reduction in fibre wall thickness versus the commercial citations (Table 4-1), equating to ~ 7% increase in shear stress when utilising idealised conditions. Beyond possible measurement discrepancies, the primary reason was attributed to fibre dehydration prior to or during measurement. ESEM images possessed lower resolution than AFM, although demonstrated the absence of visible surface pores and an internal porous structure, unlike the PES membrane.

Table 4-3. Measured properties of aldehyde-functionalised hollow fibres.

Fibre property	Measurement	Unit
Porosity	N/A	-
Wall thickness	28.3 ± 1.5 (mean ± SD)	Um
Estimated average inner diameter	157	Um
Pore size	N/A	-

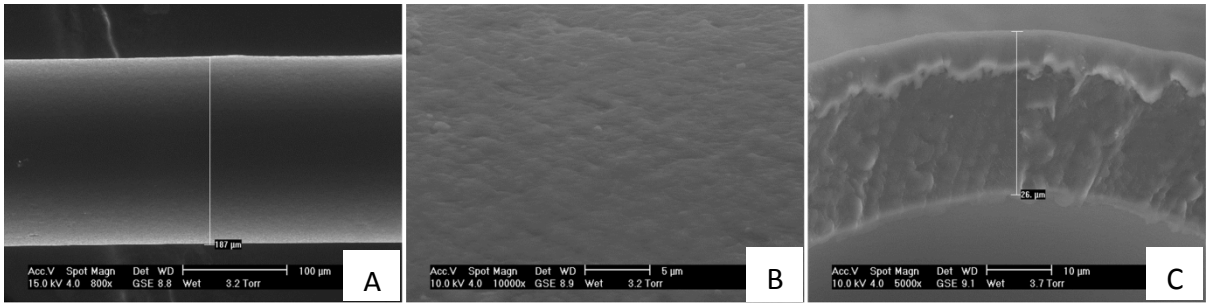

Figure 4-9. Representative images of hollow fibre membrane surfaces, where (A) the outer region of the fibre, (B) a high magnification scan of the fibre surface and (C) an image of the cross-section of the fibre.

BET surface area measurements of the aldehyde functionalised PEI fibres were not performed, as fibres were too delicate. A literature search failed to provide an estimate of the surface area per unit volume of dialysis fibres. However, the molecular weight cut-off of such fibres is low: the membranes permit the passage of molecules possessing molecular weights of up to 45 kDa in blood and have a molecular weight exclusion limit in water of about 200 kDa (Luttropp, 2014). (Protein molecular weights are approximated as: ~45 kDa

(BSA and rPrA) and 150 kDa (IgG).) Instead, the available surface area inside the tube was assumed to be equivalent to that of a smooth tube, since the BET method could not be performed on the fibres.

Data are presented in Table 4-4 and images are displayed in Figure 4-10 for PES microfiltration membranes. Membrane surfaces were highly porous (Figure 4-10 (A and B) with extensive internal cross-linking (Figure 4-10 (C and D)) and a surface area per unit volume characteristic of microfiltration membranes (Table 4-4) (Prasad, 2012, Coleman et al., 1990, Liu and Bai, 2006).

Also worth noting was the PES membrane (pore size: 0.45 µm), which is much smaller than most mammalian cells, which have diameters in the range of 10 – 20 µm. Whilst too small to allow cell transfer across the membrane surface, the potential for cell deformation into the pore, either during static incubation or due to shear stress is possible. Increased membrane roughness may also generate minor imbalances in the hydrodynamic forces that the cells are subjected to when compared to the idealised conditions assumed in Chapter 2 (Myers, 2002).

Table 4-4. Morphological properties of PES membranes

Membrane property	Measurement	Unit
Average pore size[a]	0.45	µm
Porosity	28	%
Surface area	2.16	m^2/mL membrane volume

[a] commercially available data.

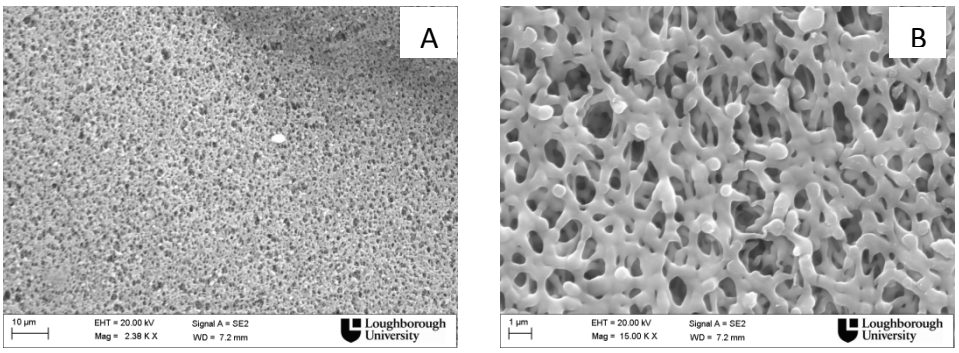

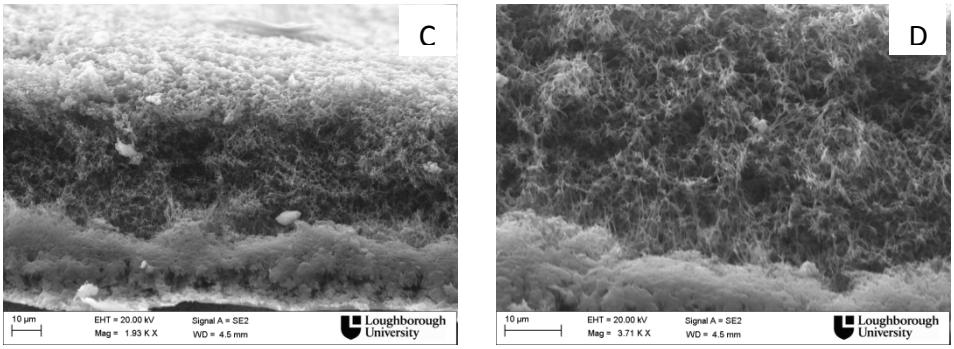

Figure 4-10. SEM Cross-sectional images of raw PES membranes. Top-down images of PES membranes, where the scale bar is at 10 µm in image A and 1 µm in image B. Side-view images of PES membranes, where the scale bar is 10 µm for both C and D.

4.4.2. Hydraulic properties

Pressure losses and hydraulic permeabilities of both membranes were measured and data are displayed in Table 4-4. The pressure losses were measured at flowrates equivalent to 25 dynes/cm^2 in Type 2 aldehyde-functionalised modules and up to 5 dynes/cm^2 in the microfiltration cassette, both used for cell separation in Chapter 4.

The removal of filtrate ports from the design specifications of hollow fibre modules meant that hydraulic permeability could not be determined. Therefore, glutaraldehyde-treated fibres in their original Nephral cartridges were examined. Table 4-5 shows that the hydraulic permeability of the hollow fibres was much lower than that of the microfiltration membranes and was characteristic of both membranes.

Table 4-5. Pressure drop and hydraulic permeability

Device	**Pressure drop/shear stress (psi/(dynes/cm^2))**	**Hydraulic permeability (LMH/psi)**
Type 2 fibre module (n=9)	0.036 ± 0.007	N/A
Hollow fibre cartridge (n = 3)	0.045 ± 0.004	2.25 ± 0.15
PES cassette (n = 1)	0.418	99.0

Note: all hollow fibre systems comprised aldehyde-functionalised membranes. [a] = at 25 dynes/cm^2; [b] up to 5 dynes/cm^2 only. N/A = not applicable. Data are displayed as the mean ± SD.

4.4.3. Chemistry

PEI-fibres were treated with glutaraldehyde to convert primary amine groups into functional aldehydes capable of covalent protein adsorption, using the same mechanism as described

in Figures 2.2 – 2.4 in Chapter 2. To confirm chemical bond formation and the extent of surface coverage, a range of tests were performed.

FTIR was used to identify differences in bond formation between PEI (n = 2) and glutaraldehyde-treated (n = 2) PEI fibres. Data are presented in Table 4-6 and a representative spectrograph is displayed in Figure 4-11. Amine bonds inherent to PEI were identified in both fibres, but the –C=N bond, indicative of Schiff base formation, was exclusive to glutaraldehyde-treated PEI and was absent in the untreated PEI at 1656 cm^{-1}, coinciding with previous studies (Wang et al., 2012a).

Table 4-6. Selected bands of diagnostic importance from FTIR spectra of PEI and aldehyde-functionalised PEI.

Detected wavelength (cm^{-1})	PEI	PEI-GA	Bond
3272	N	N	-N-H stretching
2940 – 2830	Y	Y	-C-H stretching
1576	N	N	-N-H bending
1465	Y	Y	-C-H bending
1350 – 1000	Y	Y	-C-N stretching
1656	N	Y	-C=N stretching

Note: Y = present; N = absent.

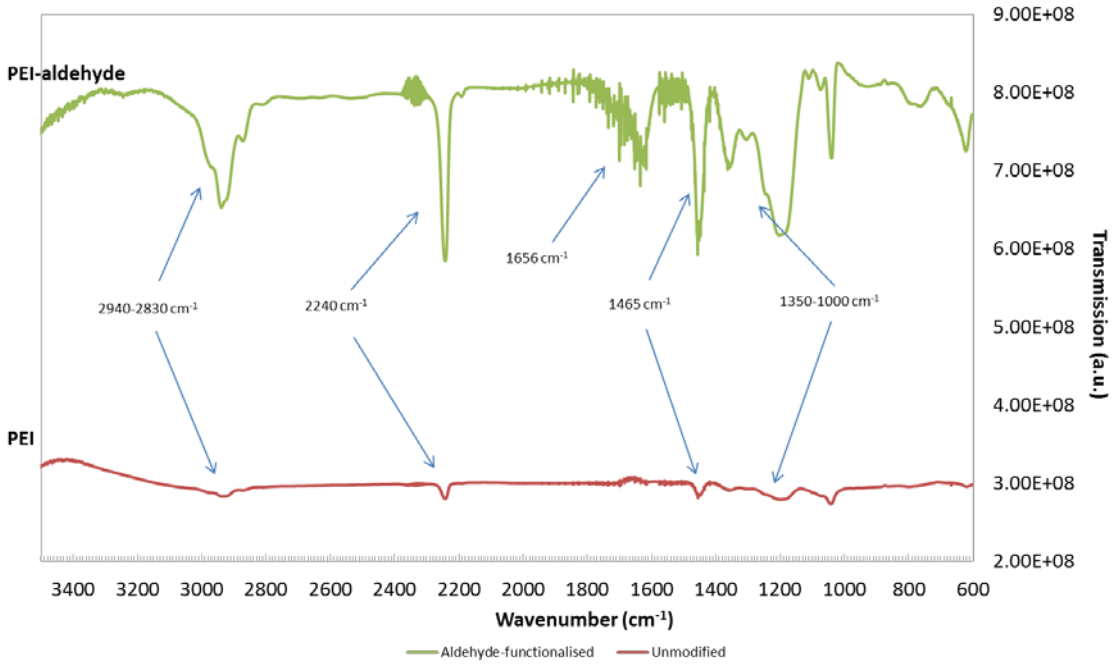

Figure 4-11. FTIR spectra for unmodified PEI membrane and aldehyde-functionalised PEI membrane.

Amine and aldehyde functionalities were assessed using TNBS and silver mirror stains, respectively. Untreated fibres exposed to TNBS solution stained yellow (Figure 4-112 A), owing to the formation of a chromogenic derivative resulting from the reaction between the nitro functional group of the TNBS molecule and a terminal amine group present on the PEI fibre (Hermanson, 1992, Pittner, 2002). (Whilst PEI is comprised of primary, secondary and tertiary amine groups, only primary amines possess reactivity with TNBS (Hermanson, 2008).) Glutaraldehyde-treated fibres exhibited a much paler yellow colour (Figure 4-12 B), indicating the reaction of amines with glutaraldehyde.

To indicate aldehyde functionalities, fibres were exposed to Tollen's reagent. Untreated PEI fibres stained brown (Figure 4-12 C), attributed to the sensitivity of the reagent to contaminants (Ahluwalia, 2000). Conversely, glutaraldehyde-treated fibres stained black (Figure 4-12 D), consistent with the oxidation of aldehyde functionalities with Tollen's reagent to create silver metal and carboxylic acid (Fieser, 1987).

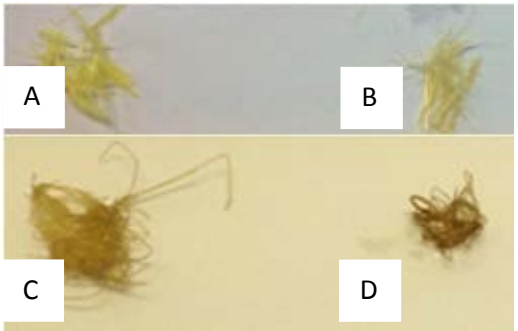

Figure 4-12. Representative staining images of untreated PEI fibres (A) and (C) and glutaraldehyde-treated fibres (B) and (D) stained with TNBS and Tollen's reagent respectively.

Hollow fibre fragility restricted attempts to quantify aldehyde functionality. The BCA assay was instead used to estimate the change in absorbance following glutaraldehyde treatment relative to untreated PEI fibres. Absorbance was less than 10 % of that for the untreated

fibres following glutaraldehyde treatment (Table 4-7). Incomplete coverage is perhaps attributable to the exposure of unreacted amine groups.

Table 4-7. Net change in absorbance between unmodified and aldehyde-functionalised PEI hollow fibre membranes.

	Net absorbance per 100 cm of fibre	
	Unmodified	Aldehyde-modified
Absorbance (Au)	0.026 ± 0.004^{a}	0.005 ± 0.001^{b}

Data with the same subscripts are not statistically different at the 5 % significance level based on a T-test. n = 9 runs were performed per sample. Data displayed as mean ± SD.

4.4.4. rPrA and BSA protein adsorption densities

High ligand densities per unit volume of substrate are desirable in protein separation, where target molecules can easily enter and exit pores (Bhattacharyya et al., 1996). However, cells cannot penetrate such pores (< 1 μm) as they are much larger (10 – 20 μm). Instead, the amount of protein accessible to cells on the substrate surface is a more important metric, enabling affinity interactions. rPrA and BSA adsorption densities onto aldehyde-functionalised hollow fibres and flat sheet microfiltration membranes are presented in Tables 4-8 and 4-9 below.

Hollow fibres exhibited comparatively high protein densities per unit volume of membrane, in spite of their low porosity. rPrA protein density per unit volume of membrane for the PES membranes was below that of other Protein A substrates, which typically ranged from 10 – 30 mg/mL of membrane volume (Colton, 1996, Dancette et al., 1999, Jia et al., 1999, Castilho et al., 2000). This was attributed to a lower Protein A incubation concentration, fewer aldehyde functionalities, or perhaps the lower surface area available per unit volume of membrane (2.1 m^2/mL of membrane). Importantly, both membranes exhibit similar (albeit slightly lower) Protein A surface densities to those used previously for cell separation

(27,000 – 35,000 per μm^2 of substrate) (Colton, 1996) and slightly higher than those obtained in Chapter 2.

Table 4-8. rPrA and BSA adsorption onto aldehyde-functionalised hollow fibre membranes.

Membrane type	Protein	Protein density		Protein spacing
		(mg/mL mv)	#/μm^2	(nm)
Hollow fibre	rPrA	0.46 ± 0.30	7,744 ± 5,065	9 – 42
	BSA	0.95 ± 0.71	10,753 ± 8,058	9 – 18
	rPrA-(BSA)	2.28 ± 1.21	25,760 ± 13,626	5 – 17

rPrA-(BSA) signifies the quantification of BSA on rPrA-coupled membranes. Protein spacing refers to the assumed distance between each adsorbed protein molecule, based on an idealised scenario of an assumed monolayer where proteins are arranged in a square lattice formation. Values are subtracted from an average baseline generated by uncoupled fibres for rPrA and BSA or rPrA-coupled fibres for rPrA-BSA. Protein density is displayed as the mean ± SD and protein spacing is displayed as the equivalent range for n = 5 runs. Calibration charts are displayed in Figures 7-4 and 7-5 for rPrA and BSA quantification using the BCA assay, respectively. Bead surface area was assumed to be equivalent to that determined from the BET surface area and neglected to account for size-restricted regions on the beaded glass surface that would be inaccessible to proteins. Calibration charts for rPrA and BSA quantitation are displayed in Figures 7-5 and 7-6.

Table 4-9. rPrA and BSA adsorption onto aldehyde-functionalised PES membranes

Membrane type	Protein	Protein density		Protein spacing
		(mg/mL mv)	#/μm^2	(nm)
Flat sheet PES	rPrA	0.80 ± 0.12	5,000 ± 759	13 – 16
	BSA	4.96 ± 0.22	20,750 ± 940	6.8 – 7.2
	rPrA-(BSA)	5.11 ± 0.33	21,394 ± 1,401	6.6 – 7.2

rPrA-(BSA) signifies the quantification of BSA on rPrA-coupled membranes. Protein spacing refers to the assumed distance between each adsorbed protein molecule, based on an idealised scenario of an assumed monolayer where proteins are arranged in a square lattice formation. Values are subtracted from an average baseline generated by uncoupled fibres for rPrA and BSA or rPrA-coupled fibres for rPrA-BSA. Protein density is displayed as the mean ± SD and Protein spacing is displayed as the equivalent range for n = 5 runs. Calibration charts are displayed in Figures 7-6 and 7-7 for rPrA and BSA quantification using the BCA assay, respectively. Bead surface area was assumed to be equivalent to that determined from the BET surface area and neglected to account for size-restricted regions on the beaded glass surface that would be inaccessible to proteins. Calibration charts for rPrA and BSA quantitation are displayed in Figures 7-7 and 7-8.

4.4.5. IgG binding

The IgG adsorption capacity is indicative of the number of possible affinity interactive sites between the rPrA-coupled membranes and IgG-tagged cells and more importantly the ability to differentiate between cells with and without affinity interactions through force-induced separation (Kuo and Lauffenburger, 1993, Nordon et al., 1996). More explicitly, the Fc binding domain of the immobilised rPrA and the Fc region of the IgG antibody.

However, the accuracy of these IgG adsorption studies is limited. It may be assumed that the adsorption capacities acquired indicate the number of affinity interactions taking place between the cell and the surface. However, there are very obvious differences in the

experimental approaches between each study limiting the accuracy of the measurements. IgG adsorption studies involved a 2 hour incubation period, whilst cell adsorption with IgG utilises a 30 minute incubation period with Protein A. For instance, static IgG antibody adsorption relies on the diffusion of IgG molecules onto the rPrA-coupled support, governed by the Stoke-Einstein equation (Young et al., 1980). IgG-tagged cell adsorption relies on cell sedimentation onto the surface, the rate of bond formation (Kuo and Lauffenburger, 1993) and the extent of cell deformation and therefore cell-substrate contact (Kasza et al., 2007, Bose, 2009), as well as the rPrA density and number of IgG-tagged antigens.

4.4.5.1. Hollow fibre Type 1 modules

The IgG adsorption capacity of rPrA-coupled hollow fibres was determined under semi-dynamic conditions. Type 1 hollow fibre modules were exposed to 0.25 mg/mL of IgG solution (in excess of that required for rPrA-coupled glass beads in Chapter 2) to saturate available binding sites. Data are presented (Table 4-10) based on the net amount of IgG affinity interactions with rPrA-coupled hollow fibres. Washing fractions for rPrA-coupled fibres blocked with BSA and a control containing only BSA blocked fibres only are both displayed in Figure 4-13, where the majority of IgG antibody was eluted during the first wash.

Table 4-10. Net IgG content for rPrA-coupled aldehyde-functionalised fibres

IgG	mg/mL mv	#/µm^{2a}	IgG : rPrA ratio
Net IgG	0.069 ± 0.032	1,946 – 9,245	0.25 – 1.19

Data are displayed as the mean ± SD for specific (n = 5) non-specific (n =5) IgG affinity interactions. [a] = assumes monolayer formation. IgG antibody incubated for 120 minutes.

The estimated IgG density per volume of membrane was comparably lower than more porous formats (Klein, 1994, Charcosset et al., 1995, Dancette et al., 1999). More relevant to cell separation was the IgG density per unit surface area, which was estimated assuming a

smooth, non-porous surface. Even though the calculated capacity may be inaccurate owing to the experimental method, the findings resemble densities reported previously for cell separation (Colton, 1996) and those reported in Section 2.5.4.

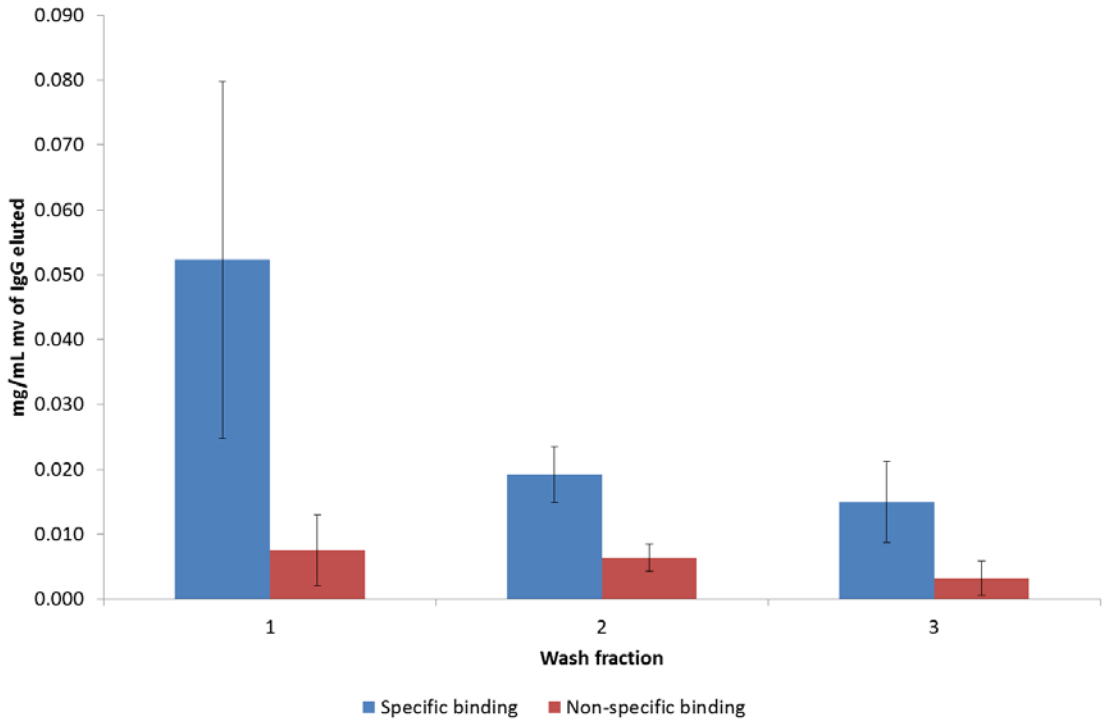

Figure 4-13. The elution of IgG from both rPrA-coupled (blue) and rPrA-free (red) Type 1 modules over three washes. Data points are displayed as the mean ± SD for n = 5 runs.

4.4.5.2. Flat sheet microfiltration membrane

The IgG adsorption capacity of rPrA-coupled PES discs was determined under static conditions across 0 – 1.28 mg/mL of IgG. Data (n = 4) are presented in Table 4-11 and a binding curve is displayed in Figure 4-14. No control study was performed, so the data comprises both specific and non-specific binding interactions.

Table 4-11. IgG adsorption capacity data for rPrA-coupled PES membranes

Parameter	Value	Unit
B_{max} [a]	7.17 ± 0.96	mg/mL membrane volume
	13,320 ± 1,791	#/µm^2
K_d [b]	0.15 ± 0.08	mg/mL
	2.0 ± 0.1 x 10^6	M^{-1}
IgG:rPrA	2.6 ± 0.4	-

Data are displayed as the mean ± standard deviation. [a] units refer to mg per mL of membrane volume; [b] units refer to mg per mL of challenge solution.

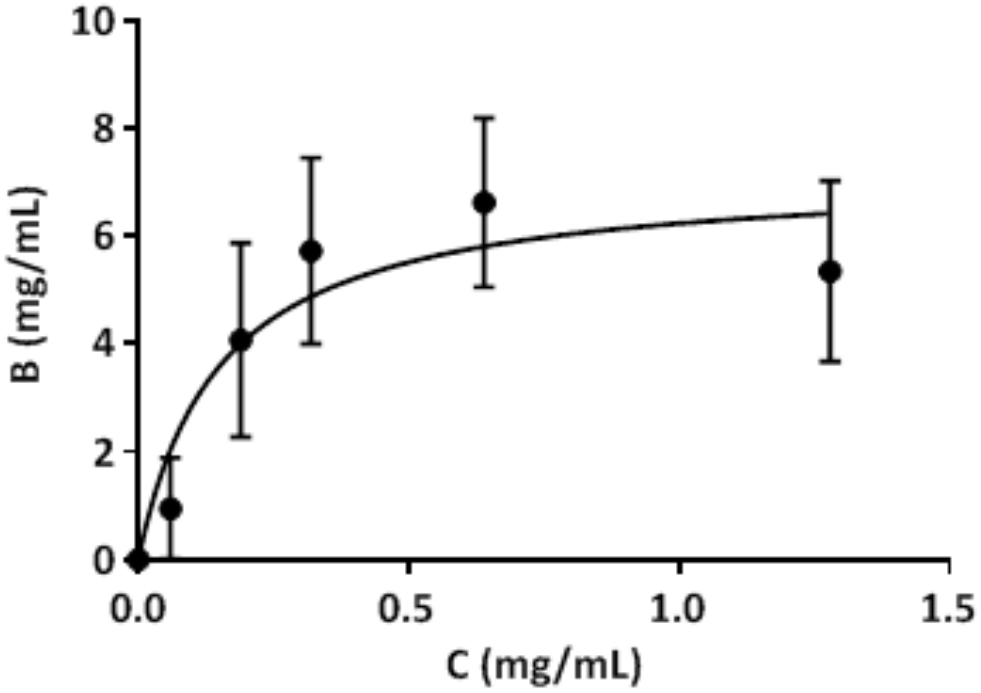

Figure 4-14. Binding curve for IgG binding for n = 4 runs comprised of the mean and calculated standard of the error mean. The data comprise both specific and non-specific protein adsorption, since no control study was performed.

IgG capacities per unit volume of membrane are lower than those reported elsewhere, which often cite a range of 10 – 30 mg/mLmv (Klein, 1994, Colton, 1996, Pomianek, 1998, Jia et al., 1999). The number of IgG antibody molecules per square micron was higher than those observed in Section 2.5.4 for aldehyde-functionalised glass beads and the fibres exhibited here. The equilibrium binding constant, K_a, was ~5 x 10^5 M^{-1}, determined from K_d, which was 2.0 ± 0.1 x 10^{-6} M. The value for K_a is slightly in excess of the recommended

minimum threshold of 10^5 M^{-1} to avoid ligand leakage (Ohlson et al., 1997, Castilho et al., 2000), but this may be attributed to the limitations of the experiment and may not be a true reflection.

Notably, the IgG : rPrA ratio (2.6 ± 0.4) (mean ± SEM) is very high compared to the aforementioned formats, suggesting an inaccuracy due to one or both of the following: (1) a lower rPrA density than that which was actually obtained (separate rPrA batches were used for rPrA and IgG adsorption studies); or (2) non-specific IgG adsorption is high and accounts for a large proportion of signal generation.

4.5. Conclusions

Aldehyde-functionalised surface chemistry was selected to immobilise proteins via Schiff base formation. Unlike flat sheet membranes, PEI hollow fibres did not possess aldehyde functionalities, so were chemically treated with glutaraldehyde. Chemical characterisation of glutaraldehyde-treated versus untreated fibres revealed: (1) a reduction in amine functionality and an increase in aldehyde functionality based on qualitative TNBS and silver mirror stains; (2) ~90 % reduction in amine functionality based on BCA assay staining; (3) Schiff base formation using FTIR spectra.

Physical characterisation indicated notable differences in membrane morphology. Hollow fibres exhibited no observable pores, with smooth, flat surfaces based on SEM and AFM with roughness (R_a) values of (32.2 ± 0.5 nm) (Mean ± SEM). Flat sheet membranes were rougher, with AFM revealing (102.1 ± 9.9 nm) and SEM indicating significant porosity (~28 %).

For hollow fibre and flat sheet membranes, rPrA densities were 7,744 ± 5,065 and 5,000 ± 759 per μm^2 (mean ± SEM), whilst IgG : rPrA adsorption ratios were 0.25 – 1.19 and 2.6 ± 0.4, respectively. Imprecision and possible inaccuracies were attributed to limitations in experimental models.

Protein adsorption densities were limited in accuracy and precision due to the experimental approach. These adsorption densities should be compared relative to each other rather than being considered absolute. These findings provide a platform for cell separation performance to be examined using constructed modules in Chapter 5.

Chapter 5. Affinity cell separation

5.1. Introduction

A side-effect of pluripotent-derived cell manufacture is anticpated to concern cells which have failed to differentiate (Schriebl et al., 2010b, Chen et al., 2014). These cells are expected to remain undifferentiated, retaining their pluripotent cell characteristics and potential for teratoma formation *in vivo*, if a pre-determined purity is not achieved (Lebkowski, 2011, Schriebl et al., 2012). This is deemed to be more probable at larger scales (>10^{11} cells per batch), where three-dimensional bioreactor heterogeneity is harder to control, leading to nutrient and growth factor gradients (Donati, 1997, Lara et al., 2006a). If existing purity thresholds (thought to be in excess of 99 % for safe transplantation (Section 1.7.1.)) cannot be met, downstream purification technologies may be required.

Affinity-based cell separation is a potential solution, offering the capacity to remove cells positive for the SSEA-4 antigen, which is expressed by ~ 95% of undifferentiated cells (Fong et al., 2009) and down-regulated on differentiated cells (Shibata et al., 2006, Thomson et al., 1998). Affinity separation has widespread applications in clinical medicine, from protein manufacture (Kelley et al., 2007, Moser and Hage, 2010) to bone marrow and haematological transplantation (Menendez et al., 2002, Ringhoffer et al., 2004). Affinity-based cell separation devices employ a variety of geometric arrangements and techniques ranging from magnetic bead- (Miltenyi et al., 1990) and fluorescence-based methods (Basu et al., 2010). The use of less commercially successfully polymer-based substrates, such as hollow fibres (Colton, 1996, Slowiaczek, 1998) and monoliths (Kumar and Srivastava, 2010) have since attracted limited attention owing to no immediate competitive advantage.

Magnetic bead separation is the existing benchmark technology for cell separation, with an apparent market share of ~70 %. Performance is suitable for clinical applictions, with log clearance rates typically ranging from 0.5 – 2.5 (Barfield et al., 2004; Lara et al., 2006b) for depletion (negative selection) and from 3 – 5 for enrichment (positive selection) (Handgretinger et al., 2002, Martin-Henao et al., 2001). The largest magnetic devices (CliniMACS®, which operates up to 10^{11} cells per unit) are however cumbersome, expensive and limited by the reduction in magnetic field strength as the distance from the magnetic increases (Ebner et al., 1997).

Membranes are considered scalable alternatives to magnetic separation devices, demonstrating similar separation performance to magnetic ones (Nordon et al., 1996, Slowiaczek, 1998). In such devices, shear stress-induced affinity separation is used to enrich cells with (Mandrusov et al., 1995, Nordon et al., 1996) or without additional agents (Nordon, 1994, Slowiaczek, 1998, Nordon et al., 2004) to enable cell recovery.

Whilst enrichment strategies yield higher purities useful for CD34+ enrichment (Nordon et al., 1996, Slowiaczek, 1998), the dissociation of an affinity interaction for cell separation using pH, force or enzymatic digestion used for more mature cell types (Mandrusov et al., 1995, Nordon et al., 1996, Slowiaczek, 1998) is considered too physiologically stressful for pluripotent-derived cells. Therefore, a depletion strategy, whereby impure cells are retained through affinity interactions and product cells without affinity interactions are recovered using lower shear stresses (≤ 25 dynes/cm^2) is deemed a more suitable method.

Chapter Aims:

- Investigate the performance of hollow fibre and flat sheet membranes using shear-stress-induced affinity cell separation to recover product cells and retain impure cells

- Investigate the impact of the separation process on cell physiology.

5.2. Materials and methods

5.2.1. Cell preparation

5.2.1.1. Cell culture

Two B-lymphocyte cell lines were used: (1) Toledo CD20 antigen-positive B-lymphocytes cells from ATCC (LGC Standards, Middlesex, UK) and (2) CCRF-HSB-2 HLA-A2 antigen-positive B-lymphocytes from Sigma-Aldrich (Dorset, UK). The purpose was for the CD20+ cells to mimic undifferentiated pluripotent stem cells expressing the SSEA-4 antigen, whilst HLA-A2+ cells were intended to mimic pluripotent-derived cells, such as cardiomyocytes, where the SSEA-4 antigen is absent.

Cells were maintained at 3 x 10^5 – 1 x 10^6 cells/mL in 90 % RPMI-1640 with 2 mM glutamine and 10 % (v/v) foetal bovine serum (FBS) supplemented with 1 % Pen-Strep (Sigma-Aldrich, Munich, Germany). Cell cultures were maintained at 3x10^5 to 1x10^6 cells/mL in 5 % CO_2 and 95 % O_2 atmospheric content at 37 ^oC using a Heracell 150i CO_2 incubator (Thermo Scientific, Loughborough, UK) and cultured every 2-3 days.

5.2.1.2. Cell harvesting for separation

Cell viability was measured using a trypan blue membrane exclusion assay prior to harvesting. Cells were only harvested if viability was ≥99 %. CD20+ and HLA-A2+ cells were centrifuged at 1,200 rpm, re-suspended in cell processing buffer (CPB) comprised of 1 % (w/v) BSA in Dulbecco's phosphate buffered saline (DPBS) (Life Technologies, Paisley, Ireland) prior to separation.

5.2.2. Separation units

Membrane-based affinity separation was compared to Miltenyi's Magnetic Activated Cell Separating (MACS) technology. CD20+ cells (impurities) were retained, whilst HLA-A2+ cells (product), were recovered as a means to increase purity. All separation was performed inside a Class II biological safety cabinet.

5.2.2.2. Magnetic Activated Cell Separation (MACS)

Magnetic separation was performed using Miltenyi ® Magnetic Activated Cell Separation (MACS) MS columns (Miltenyi Biotec, Surrey, UK) according to the manufacturer's instructions. Briefly, a mixture of HLA-A2+ and CD20+ cells were prepared in a 1:1 ratio equating to 2.4 x 10^7 cells in total. Cells were centrifuged at 1,200 rpm and re-suspended in 0.16 mL of CPB and 0.04 mL of anti-CD20 MACS microbeads then incubated at 4 ^oC for 30 minutes. Cells were then centrifuged and re-suspended twice in 0.6 mL of CPB. A sample of the cell suspension was taken for analysis. Miltenyi MS columns were prepared in advance and clipped into the magnet prior to the addition of 1.5 mL of CPB in 0.5 mL amounts was passed through the column. Thereafter, 0.5 mL of the cell suspension (equivalent to 2 x 10^7 cells) was fed into the column and was allowed to run through, followed by an additional 1.5 mL of CPB to collect remaining cells. Collected cells were then subjected to analysis.

5.2.2.3. Affinity membrane separation

Immuno-affinity-based membrane separation was performed inside a Class 2 biological cabinet through the sequential application of shear stress across 1, 5, 10 and 25 dynes/cm^2 and 1, 5 and 10 dynes/cm^2 for hollow fibre and flat sheet membranes respectively. Prior to separation in both formats, combined HLA-A2 and CD20 cells were pooled to create purities of approximately 1:1 containing 1.9 x 10^6 and 2.1 x 10^7 total cells for hollow fibre and flat

sheet membranes respectively. Cells were re-suspended and centrifuged in CPB to 3 x 10^7 cells/mL. CD20 IgG antibody purchased from The University of Birmingham Hospital (Birmingham, UK) was then added to mixed cell suspensions equivalent to a concentration of 10 µg/mL prior to incubation at 4 ^{o}C for 30 minutes. Cells suspensions were then diluted with CPB, centrifuged at 1,200 rpm and re-suspended twice in CPB to 3 x 10^6 cells/mL.

Hollow fibre membrane

Hollow fibre separation was performed using the modules developed and characterised in Chapter 4. The properties of these modules are presented in Table 5-1 below.

Table 5-1. Hollow fibre module properties

Property	**Value / comment**
Fibre internal diameter	168 µm
Fibre external diameter	210 µm
Number of fibres	75
Fibre length	10 cm
Membrane	Aldehyde-functionalised polyethylenimine
Affinity interaction	rPrA – interaction with the Fc domain of IgG-tagged cells
Supplier	Gambro (Nephral ST200)

[a] assuming an 8 % coverage of cells

In advance, Type 2 modules (prepared in Section 4.2.4.1), were removed from a storage solution of 0.01 % (w/v) sodium azide in 0.1 M sodium phosphate with 0.15 M sodium chloride (PBS) at 4 ^{o}C. They were then soaked in de-ionised water for 15 minutes and rinsed through with PBS at 30 mL/hr for 10 minutes. A solution of rPrA (1 mg/mL) in PBS (pH 7) was then injected into the modules via a connected a 1,000 µL micropipette tip. Modules were then wrapped with foil to prevent dehydration during a 4 hour incubation period at room temperature. The rPrA solution was recycled every 30 minutes to promote saturation, prior to rinsing with PBS using a manual syringe. Then, inside an air-tight glove box, a 0.075 M solution of sodium cyanoborohydride in PBS was injected and incubated at room temperature for 1 hour. Excess solution was drained and modules were rinsed in PBS, 1 M

NaCl and de-ionised water for 10 minutes each using a syringe pump at a flowrate of 60 mL/hr.

The tubing shell (tygon tubing) (Cole-Parmer, London, UK) was then positioned across the fibres and allowed to set using epoxy resin for 2 hours. Fibres were then manually rinsed with CPB containing 0.1 % (w/v) sodium azide using a syringe to test integrity and remove air from the shell side. Excess air was removed by inserting the needle of a 10 mL syringe into the shell side of the module to draw air out whilst CPB 0.1 % (w/v) sodium azide was simultaneously injected, prior to incubation for 4 hours at room temperature. Excess solution was then withdrawn and each module was washed with CPB prior to blocking in 1 % (w/v) BSA for 2 hours at room temperature. Fibres were then connected to the process setup (Figure 5-1) and subjected to the separation process detailed below.

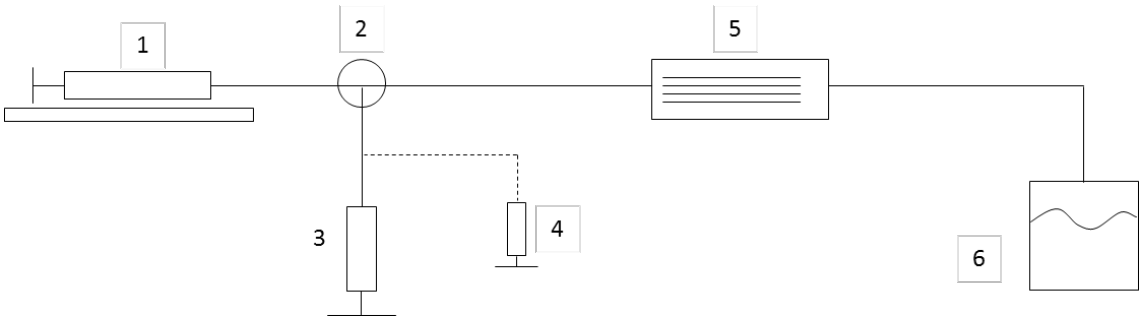

Figure 5-1. Hollow fibre membrane cell separation process. The instruments are listed as follows: (1) 50 mL syringe and syringe pump containing CPB (1 % BSA in 1 x DPBS); (2) 3-way valve; (3) 20 mL wash buffer syringe containing 1 % BSA; (4) 1 mL syringe of cell suspension in CPB with needle; (5) 75-fibre HFM Type 2 module; and (6) cell fraction collection vessel. Note: the dashed line represents the manual insertion of a needle into the tubing.

Flat sheet membrane cassette

A proprietary flat sheet microfiltration membrane cassette was kindly supplied by Peter Levison at Pall Life Sciences (Portsmouth, UK). The membrane material and the cassette were briefly characterised in Chapter 4 and fundamental characteristics are presented in Table 5-2 below.

Table 5-2. Flat sheet membrane properties

Property	Value / comment
Volume	6.4 mL
Membrane	Aldehyde-functionalised polyethersulfone
Affinity interaction	Immobilised rPrA – Fc interaction with IgG-tagged cells
Supplier	Pall Life Sciences
Membrane porosity (%)	28 %

Prior to modification, the flat sheet membrane cassette, stored in 20 % ethanol at 4 ^{o}C was drained thoroughly via the manual injection of de-ionised water followed by PBS using a 10 mL syringe. Inside a class 2 fume cabinet, excess PBS was then drained, and a 1 mg/mL solution rPrA was manually injected into the cassette to saturate the surface and promote the removal of air pockets. The solution was then incubated overnight at 4 ^{o}C on an EW 51300 orbital platform shaker at 1 rpm (Cole-Parmer, London, UK). Excess rPrA solution was then recovered for further use and the cassette was rinsed with PBS solution. Inside an air-tight glove box, 0.075 M sodium cyanoborohydride in PBS was injected and incubated at room temperature for 1 hour. Excess solution was drained and the cassette was sequentially rinsed in PBS, 1 M NaCl and de-ionised water for 10 minutes using an Alaris IVAC P7000 syringe pump (CareFusion, St Albans, UK) at 180 mL/hr. The membrane was then sterilised in 0.1 % (w/v) sodium azide in PBS for 4 hours at room temperature, prior to rising in PBS, 1 M NaCl and de-ionised water, before blocking in 1 % BSA in PBS (pH 7) for 2 hours, prior to rinsing again in PBS, 1 M NaCl and de-ionised water. The cassette was then connected (Figure 5-2) and separation studies were performed as detailed in Table 3.

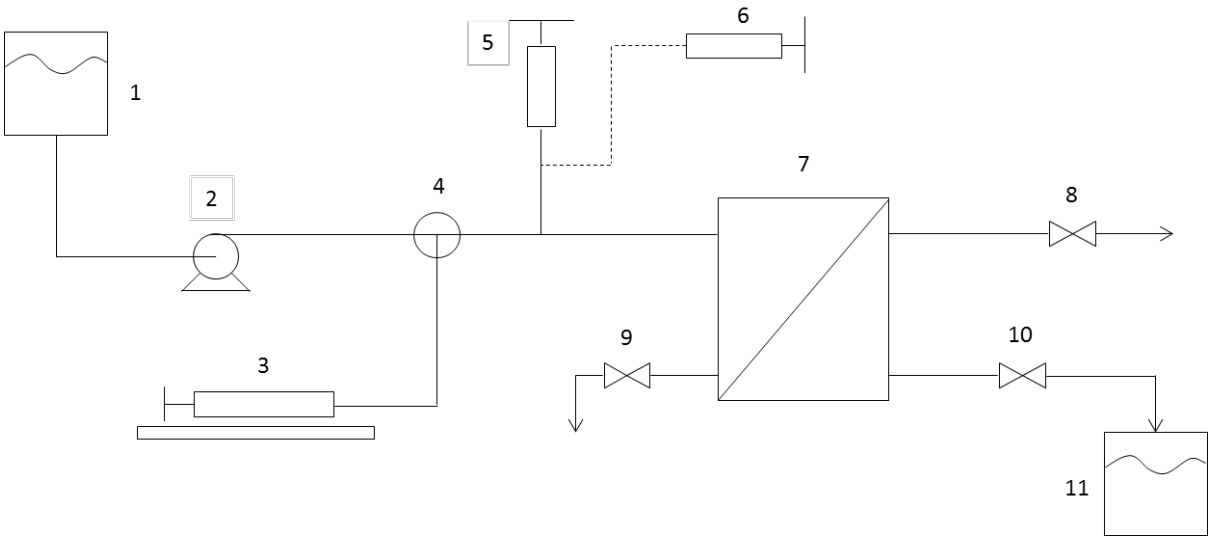

Figure 5-2. Flat sheet membrane cell separation process schematic. Numbers are represented accordingly, where: (1) = storage vessel containing wash buffer; (2) = peristaltic pump; (3) = 50 mL syringe and syringe pump containing wash buffer; (4) = 3-way valve; (5) = 20 mL wash buffer syringe containing CPB; (6) = 10 mL syringe of cell suspension in CPB with needle; (7) = flat sheet membrane cassette; (8) = Filtrate 1 port (closed); (9) = Filtrate 2 port (closed); (10) = outlet port.

5.2.3. Cell separation

Mixed cell suspensions containing known concentrations of cells were injected into respective membrane units at a concentration of 3 x 10^6 cells/mL in CPB and allowed to incubate for 30 minutes. Adherent cells were subjected to shear stresses of 1 – 25 dynes/cm^2 (hollow fibre membrane) and 1 – 10 dynes/cm^2 (flat sheet membrane) (Table 5-3). A process diagram details both magnetic- and membrane-based cell separation processes (Figure 5-3).

Table 5-3. Operating parameters for cell separation

Stage	Mobile phase	Total wash volume (mL)[a]	Shear stress (dynes/cm^2)	Time (minutes)[a]
Cell loading				
Cell injection	CS	0.4 (6.4)	0.5	1.7 (0.45)
Cell incubation				
	CS	-	-	30 (3)
Washing				
1st fraction	CPB	1.4 (86)	1	3 (3)
2nd fraction		6.9 (430)	5	3 (3)
3rd fraction		13.8 (286)	10	3 (1)
4th fraction[b]		34.5 (0)	25	3 (0)

[a] operating parameters are displayed for the hollow fibre membrane with the flat sheet membrane in brackets; [b] 25 dynes/cm2 was only applied for the hollow fibre membrane models, since the pressure limit was exceeded for the flat sheet membrane cassette. CPB = cell processing buffer comprised of 1 % BSA in 1 x Dulbecco's phosphate buffer solution.

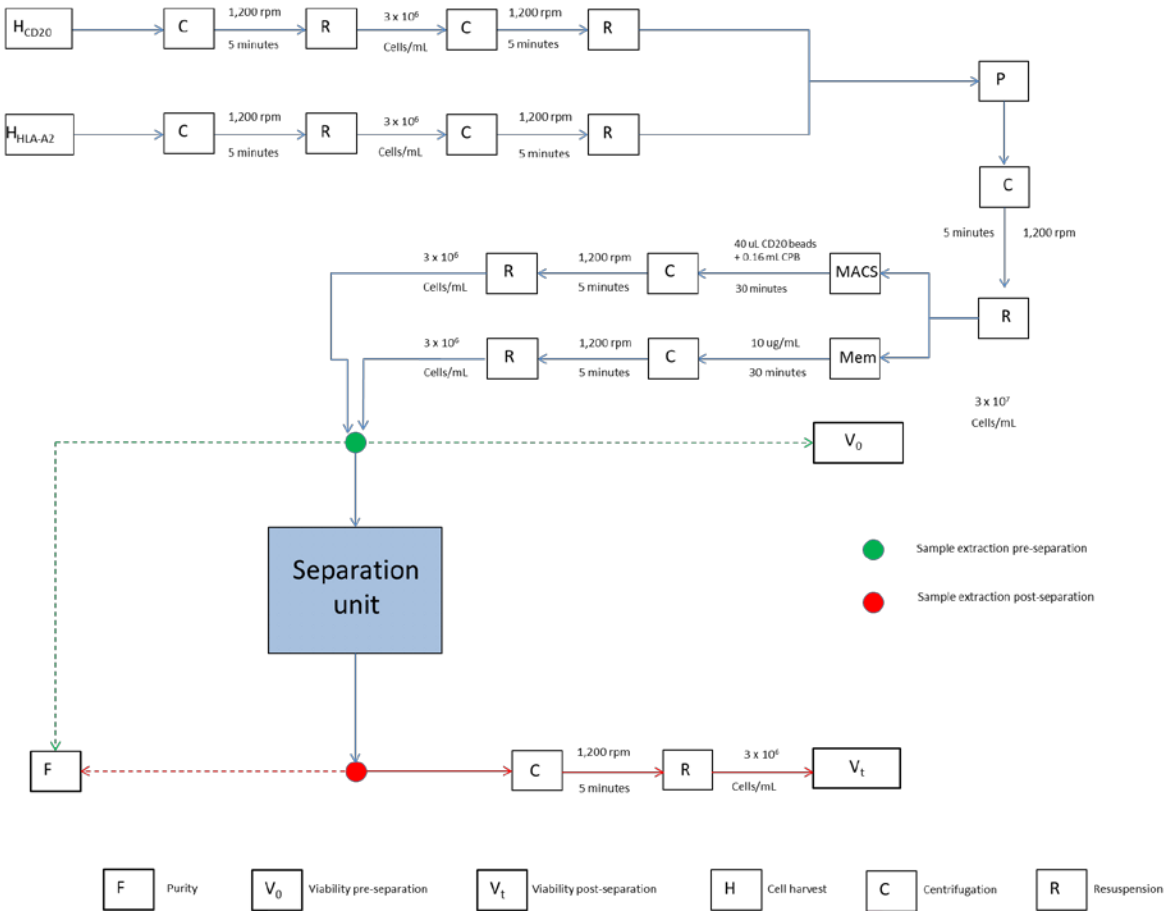

Figure 5-3. Process diagram for cell separation. Both magnetic and membrane-based separation protocols are detailed.

5.2.4. Characterisation

The separation performance of each system was measured based on changes in cell recovery, viability and purity. Assays are described below.

5.2.4.1. Cell membrane integrity and intracellular staining

Cells were concentrated to provide assay resolution by centrifuging at 1,200 rpm. No doubt, this could affect measurement accuracy by removing less dense dead or dying cells, but the concentrations of collected fractions were too dilute (<10^4 cells/mL).

Vita Bright-48/Propidium iodide (VB-48/PI)

A combination of membrane permeable (Vita Bright-48 fluorophore) and impermeable (Propidium iodide) compounds were used to measure reduced thiol content and membrane integrity. Cells undergoing apoptotic processes exhibit a reduction in cellular free thiol concentration detectable upon the formation of a fluorescent compound when reacted with VB-48 (Skindersoe et al., 2012). Propidium iodide (PI) is a membrane impermeable dye used to indicate losses in membrane integrity (Harrison and Vickers, 1990). Cell samples were mixed at a 19:1 ratio with Solution 5 (Chemotec, Gydevang, Denmark) equating to 8 µg/mL of VB-48 and 500 µg/mL of PI and content was measured using an A2 chip in an NC3000 (Chemotec, Gydevang, Denmark). Data were analysed using Nucleoview software (Chemotec, Gydevang, Denmark).

4',6-diamidino-2-phenylindolen (DAPI)

4',6-diamidino-2-phenylindolen (DAPI) is used to identify cells exhibiting losses in membrane integrity. It fluoresces when bound strongly to A-T rich regions of DNA of cells with permeable membranes, but is impermeable to cells with intact membranes (Hamada and Fujita, 1983). Cell samples were drawn up into a Via-1 cassette (Chemotec, Gydevang, Denmark) yielding a DAPI concentration of 1 µg/mL of cell suspension. The Via-1 cassette was immediately inserted into the NC3000 (Chemotec, Gydevang, Denmark) and data was analysed using Nucleoview software (Chemotec, Gydevang, Denmark).

7-Amino-Actinomycin (7AAD)

7-Amino-Actinomycin D (7-AAD) is a membrane impermeable dye indicative of losses in membrane integrity, by binding cells to DNA of cells with compromised membrane integrity, yielding a fluorescent complex detectable at 650 nm (Shapiro, 2003). 7-ADD (BD

Biosciences, Oxford, UK) was added to collected fractions (0.15 mL) at a concentration of 2 µg/mL cell suspension. Samples were gently mixed then incubated in the dark for 10 minutes. Fluorescence was measured using a Millipore Guava flow cytometer (Millipore, Cambridge, UK). Analysis was performed using the accompanying GuavaSoft software. The gate region for membrane permeable and impermeable cells was set at log $10^{1.7}$; cells above this threshold were considered to have lost membrane integrity, whilst cells below were deemed to have intact membranes.

Trypan blue

Trypan blue was used to stain cells with compromised membrane integrity. The methodology is described in Section 2.2.6.

5.2.4.2. Cell recovery

Acridine orange (AO) is a membrane permeable stain used to quantify cells by fluorescently staining DNA. Cell samples were drawn up into a Via-1 cassette, to yield an AO concentration of 1 µg/mL and immediately processed on the NC3000. Data were analysed using Nucleoview software.

5.2.4.3. Cell purity

Cell purity based on antigen expression was determined using flow cytometry. Cells were stained using CD20 IgG_3 (anti-human/mouse (H147) fluorescent with PE-Texas Red to detect CD20+ antigen expression and HLA-A2 IgG_{2b} (anti-human/mouse (BB7.2) IgG 2b fluorescent with FITC to detect HLA-A2+ antigen expression. Isotype controls were IgG_3 (anti-human/mouse fluorescent with PE (R&D Systems, Abingdon, UK) and anti-human/mouse IgG_{2b} fluorescent with FITC (BD Biosciences, Oxford, UK).

Samples were centrifuged at 1,200 rpm for 5 minutes then re-suspended in 0.1 mL of CPB. Fluorescent antibody was added to collected fractions separately, agitated on a MaxiMix™ vortex (Fischer Scientific, Loughborough, UK) for 5 seconds then incubated for 30 minutes at room temperature (~23 ^{o}C) in the dark. Samples were then diluted in CPB, centrifuged at 1,200 rpm for 5 minutes and re-suspended in 0.2 mL of CBP, twice. Re-suspended samples were measured using a Millipore Guava flow cytometer. Binding affinities were assessed for each cell type versus isotype controls (Figure 5-4). Analysis was performed using GuavaSoft software (Millipore, Watford, UK).

Gain settings were adjusted so that unstained cells resided within the first log decade of each detection channel on a four-log decade scale. Initial testing showed CD20+ and HLA-A2+ cells to be positive for respective antigens (>99 %), whilst the isotype controls and non-specific binding was estimated to be < 1 % (Figure 5-4).

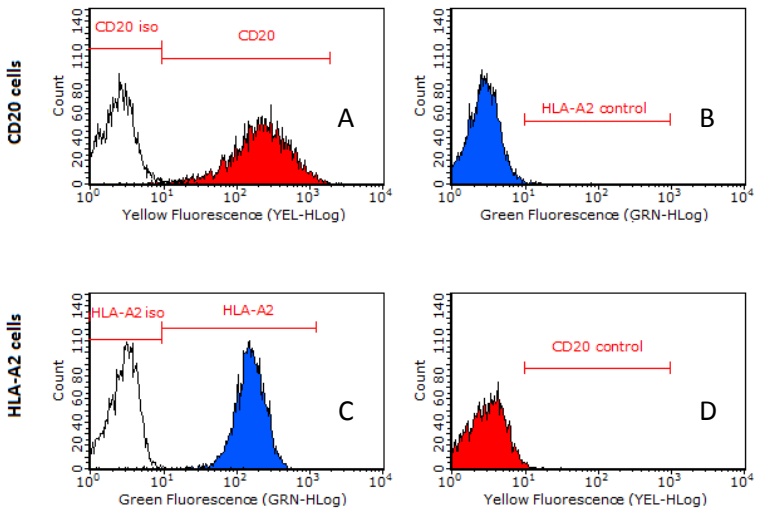

Figure 5-4. Cell staining histograms. (A) = CD20 cells (red) testing positive for CD20 IgG and negative for an isotype control; (B) = CD20 cells testing negative for HLA-A2 IgG control; (C) = HLA-A2 cells (blue) testing positive forHLA-A2 IgG and negative for an isotype control; (D) = HLA-A2 cells testing negative for CD20 IgG.

5.3. Theoretical considerations

5.3.1. Hydrodynamic conditions

Shear stress inside each membrane was determined assuming that fluid flow was predominantly laminar (Reynold's number << 2100) according to Equation 2.1. For hollow fibres, the shear stress at the wall of each fibre was calculated using Equation 4.1 and on the surface of the flat sheet membrane it was estimated using Equation 4.2.

Performance analysis

Output from each assay was evaluated using the following equations to identify changes in cell properties. As indicated earlier in Figure 2-12 and Figure 5-4, HLA-A2+ cells, designated product cells have no capacity for affinity interactions. Conversely, CD20+ cells, designated impurities, have the potential for affinity interactions via the interaction of the Fc region of IgG antibody tagged to cells with surface-adsorbed rPrA (Figure 2.4 Section 2.1.). HLA-A2+ cell purity ($F_{H,n}$) (%) for a recovered from a given fraction may be expressed by:

$$F_{H,n} = \frac{N_{H,n}}{N_{C,i} + N_{H,i}} \qquad 5.3$$

, where $N_{H,n}$ = the number of HLA-A2+ cells recovered from a given fraction (cells); $N_{C,i}$ =the number of CD20+ cells added to the device (cells); $N_{H,i}$ = the number of HLA-A2+ cells added to the device (cells). Subscripts 'i' and 'n' signify input and the collected fraction number, respectively. HLA-A2+ cell recovery relative to the original input quantity, $R_{H,n}$, (%) was calculated using:

$$R_{H,n} = \frac{Y_{H,n}}{Y_{H,i}} \qquad 5.4$$

Limitations meant that changes in membrane integrity for each cell type (CD20+ and HLA-A2+ lymphocytes) could not be measured. Instead, changes in vital dye uptake for all cells recovered at a given shear stress ($\Delta V_{T,n}$) (%) were used to assess the impact of shear-induced separation on cells from each fraction:

$$\Delta V_{T,n} = 1 - \frac{V_{T,n}}{V_{T,i}} \quad 5.5$$

, where $V_{T,n}$ = cell uptake of vital dye at a given shear stress; $V_{T,i}$ = cell uptake of vital dye prior to separation device addition. Log_{10} depletion (LCR) for each collected fraction was estimated as:

$$Log_{10}(negative\ cell\ depletion) = \log_{10}\left(\frac{Y_{C,i}}{Y_{C,n}}\right) \quad 5.6$$

, where $Y_{c,i}$ = CD20+ cell input yield; $Y_{c,n}$ = CD20+ cell output yield.

Because the starting purity was variable and collected fractions exhibited marginal changes in purity, performance trends based on the mean data points could not be deduced. Therefore an equation for the Relative Change in Purity (RCP) of product-designated HLA-A2+ cells was derived to compare the change in purity for each fraction relative to the original input.

$$RCP = \frac{P_{H,n} - P_{H,i}}{P_{C,n} - P_{C,i}} \quad 5.7$$

, where $P_{H,i}$ = HLA-A2+ cell input purity; $P_{H,n}$ = HLA-A2+ cell output purity at a given fraction; $P_{C,i}$ = CD20+ cell input purity; $P_{C,n}$ = CD20+ cell output purity at a given fraction. Subscript C = CD20 cells; H = HLA-A2 cells; i = input; n = fraction number. All purities are displayed in %.

5.4. Results

The following section presents the results for magnetic bead (n = 4) as well as hollow fibre (n = 5) and flat sheet membrane (n = 1) affinity separation. Hollow fibre membrane modules also included control studies without IgG pre-incubation incubation (n = 2). As stated previously, HLA-A2+ cells were designated product cells to be purified and recovered at lower shear stresses (≤ 25 dynes/cm^2) through the retention of CD20+ target cells using affinity interactions.

5.4.1. Recovery

HLA-A2+ cell recoveries from the magnetic column, as well as the hollow fibre and flat sheet membrane are presented in Figure 5-5. For the magnetic sepration column, approximately 2 x 10^7 cells (~ 50 % purity) were introduced. HLA-A2+ cell recovery ranged from 78 – 97 % per single column pass.

In the hollow fibre membrane modules, the application of 1 dynes/cm^2 of shear stress recovered 23 – 45 % of loaded HLA-A2+ cells. Sequentially increasing shear stress to 5, 10 and 25 dynes/cm^2 recovered 2 – 6 %, 3 – 9 % and 1 – 10 %. Overall HLA-A2+ cell recovery ranged from 37 – 55 % across the tested range. A control study for the hollow fibre model (excluding IgG incubation) yielded HLA-A2+ cell recoveries of 32 – 37 % at 1 dynes/cm^2 and 6 – 8 %, 3 % and 1 – 2 % at 5, 10 and 25 dynes/cm^2 respectively, with a cumulative recovery of 42 – 50 %.

For the flat sheet membrane, 1.92 x 10^7 cells (~53 % HLA-A2+ purity) were introduced. Recoveries of 4, 11 and 1 % of HLA-A2+ cells were achieved across 1, 5 and 10 dynes/cm^2, equating to a total recovery of around 16 %.

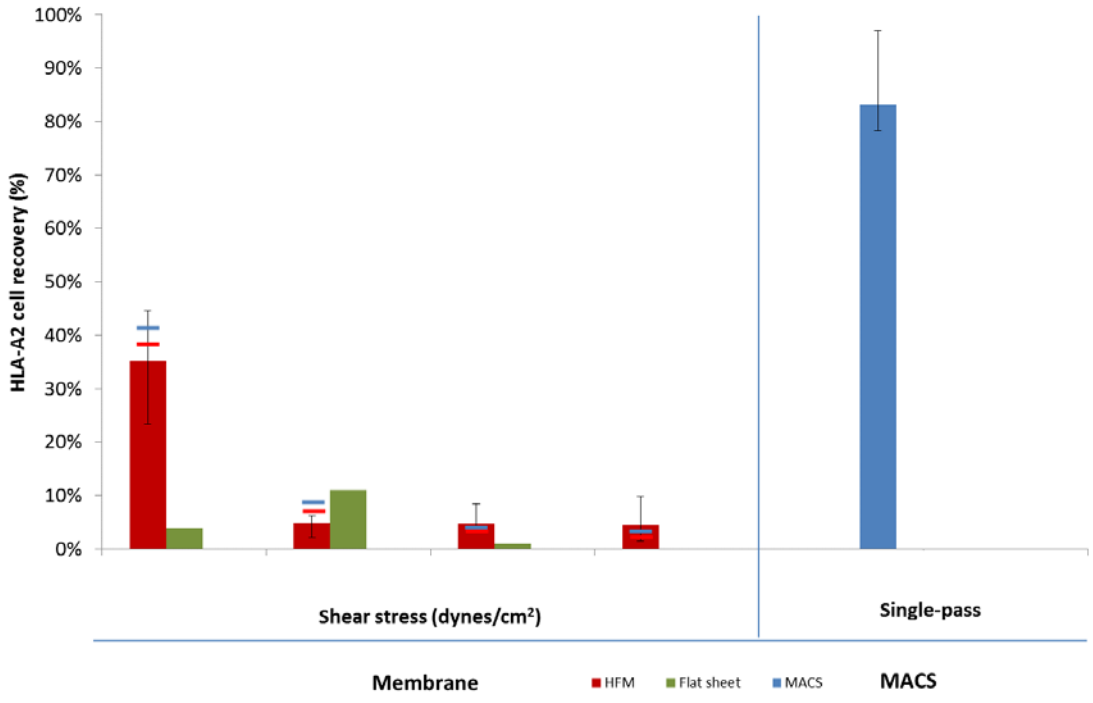

Figure 5-5. HLA-A2+ cell recovery across tested units. Separation of HLA-A2+ cell recovery as a % of the original input are compared for magnetic separation (MACS) (n = 4), hollow fibre membrane (n = 5) for IgG-exposed and flat sheet membrane (n = 1) devices. Data are displayed as the average, minimum and maximum data points. A control study for the hollow fibre membrane is also displayed (n = 2) as the range (minimum (red) and maximum (blue)). The data for CD20 cell recovery is displayed in Figure 7-9 and individual cell recoveries are displayed in Figure 7-10.

5.4.2. Purity

Changes in cell purity were quantified based only on HLA-A2 antibody staining. Isotype controls for both HLA-A2+ and CD20+ cells were used to indicate non-specific cell binding. Flow cytometry scatter plots and histograms are presented in Figure 5-6. CD20 IgG was not used for quantitative indication due to the inability to distinguish between positive and negative cells. In hindsight this may be attributed to incomplete antibody washing or

excessive incubation, since initial testing (Figure 5-4) showed identifying antigens to be exclusive to respective cell types.

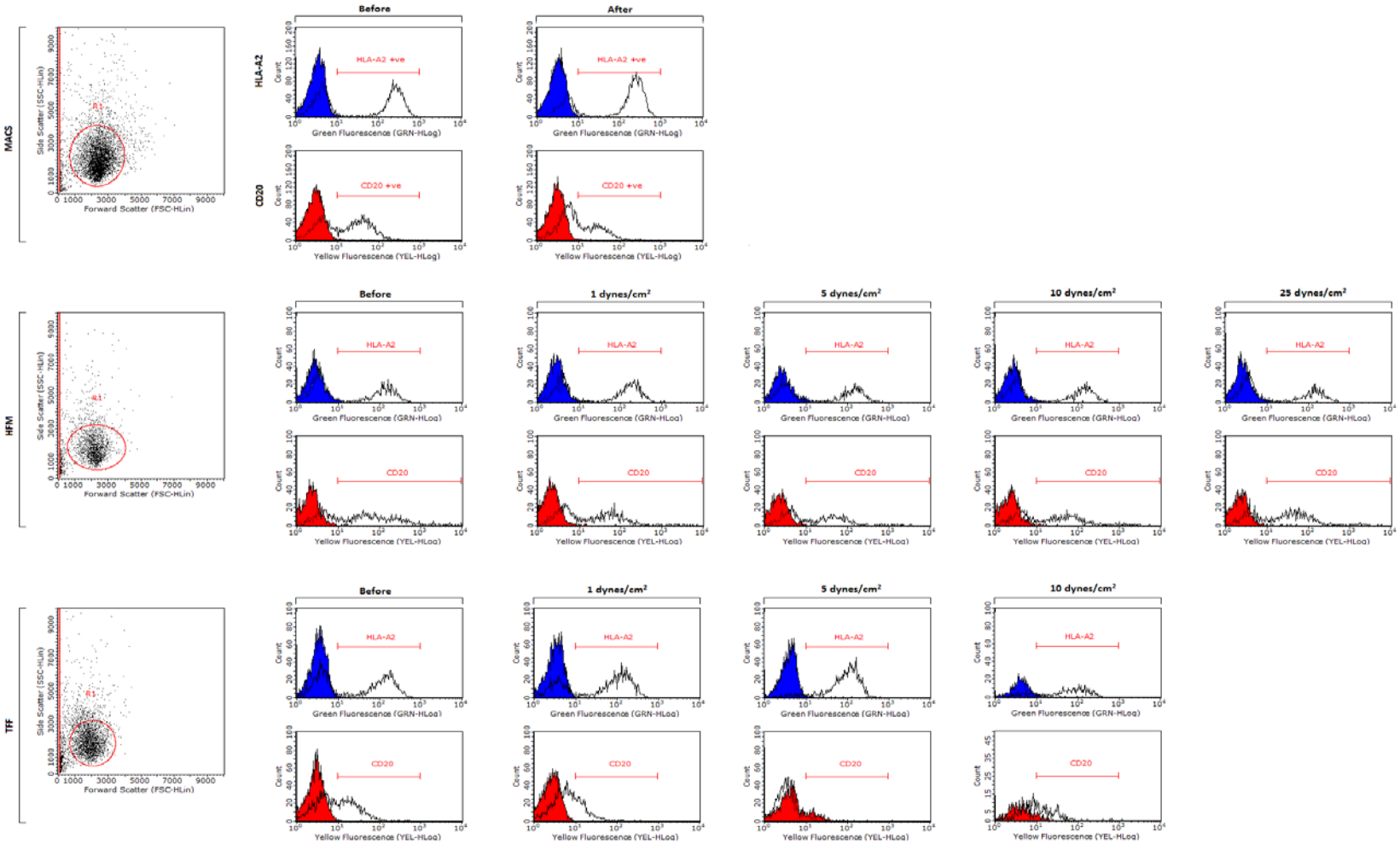

Figure 5-6. Scatter plots and histograms for separation devices. Graphs show magnetic separation (A), hollow fibre membrane (B) and flat sheet membrane (C) separation systems. Cell purity was quantified using HLA-A2-measured purity only. Blue = isotype control staining for HLA-A2+ cells; red = isotype control for CD20+ cells.

Since the average starting concentration varied across batches, individual data are displayed (Tables 5-4 – 5-6).

Magnetic separation

The relative change in HLA-A2+ cell purity and changes in purity for each individual run (n = 4) are presented for MACS (Table 5-4). Data show an increase in HLA-A2+ cell purity for one single column pass, ranging from 0.5 to 2.5, whilst the LCR (log_{10} depletion), ranged from 0.19 – 0.41.

Table 5-4. Relative change in purity for each collected fraction

Run	HLA-A2 Purity (%)		LCR	RCP
	Before	After		
1	51.8	69.5	0.34	1.2
2	71.5	83.4	0.41	2.5
3	62.4	68.1	0.22	0.5
4	77.3	80.4	0.19	0.7

Data displayed for n = 4 individual runs. Green indicates an increase in cell purity; RCP = relative change in purity of HLA-A2 cells; LCR = log10 depletion of CD20 cells.

Hollow fibre membrane

Individual HLA-A2 cell purities, as well as the RCP from hollow fibre membranes are presented in Table 5-5. Shear stress applied across 0 – 25 dynes/cm^2 yielded variable changes in purity. The RCP was calculated at specific fractions and ranged from 0.2 to 0.5 (1 dynes/cm^2); -0.1 to 0.4 (5 dynes/cm^2); -0.4 to -0.1 (10 dynes/cm^2) and -0.5 to 0.2 (25 dynes/cm^2). The purity of HLA-A2+ cells collected at lower fractions (≤ 5 dynes/cm^2) gradually increased, but decreased at higher shear stresses (≥ 5 – 25 dynes/cm^2). The control study without IgG showed negligible changes in cell purity across the 0 – 25 dynes/cm^2 range, where the RCP was 0.03 – 0.07, -0.01 – 0.1, -0.01 – 0.2 and -0.04 – -0.03 at 1, 5, 10 and 25 dynes/cm^2, respectively.

Table 5-5. HLA-A2 cell purification data for each fraction

Run	Shear stress (dynes/cm^2)				
	Input	**1**	**5**	**10**	**25**
1	42.1	51.7	47.1	44.2	36.2
2	47.7	53.6	49.7	44.4	30.2
3	40.4	47.9	47.1	38.6	33.0
4	42.4	51.5	41.6	37.6	35.7
5	40.0	54.0	51.6	40.6	34.3
Average RCP (-)	-	0.2 – 0.5	-0.1 – 0.4	-0.4 – -0.1	-0.5 – 0.2
1 (control)	53.7	54.1	54.7	50.4	51.7
2 (control)	47.6	47.4	47.3	48.1	46.5
Average RCP (control) (-)	-	0.03 – 0.07	-0.01 – 0.1	-0.01 – 0.02	-0.04 – - 0.03

Individual data points for hollow fibre separation with pre-incubation with IgG (n = 5) and without (n = 2) are displayed. Fractions exhibiting an increase in purity relative to the original input are displayed in green; those undergoing a reduction in red.

Flat sheet membrane

Changes in purity for each collected fraction across 1 – 10 dynes/cm^2 (n = 1) are displayed in Table 5-6. For an input purity of 53 % the collected purity increased to 65 % and 93 % for 1 and 5 dynes/cm^2, before declining to 79 % for 25 dynes/cm^2.

Table 5-6. Flat sheet membrane purification performance

	Shear stress (dynes/cm2)			
	Input	1	5	10
Purity (%)	53.2	65.3	92.8	78.5
RCP (-)	-	0.7	11.8	2.5

Individual data points for n = 1 runs across a range of 1 – 10 dynes/cm^2

5.4.3. Cell membrane integrity and intracellular staining

Plasma membrane permeable and impermeable vital stains were used to measure the impact of purification in each device on cells. Changes in cell staining relative to the original input were assessed using four different assays (three per device) for each separation system. Technical problems meant that the membrane permeable VB-48/PI stain was used only for magnetic separation and was replaced with 7-AAD for hollow fibre and flat sheet membrane systems.

Trypan blue

Trypan blue staining data are displayed in Figure 5-7. For magnetic separation, minor fluctuations were observed; percent cell uptake ranged from -0.2 to 1.5 % post-separation. In hollow fibres, an increase in cell staining was observed to 0.8 – 2.3 % at fractions collected at 25 dynes/cm^2. Flat sheet membranes exhibited much higher levels of cell staining, with 3, 14 and 23 % being recorded at 1, 5 and 10 dynes/cm^2 respectively.

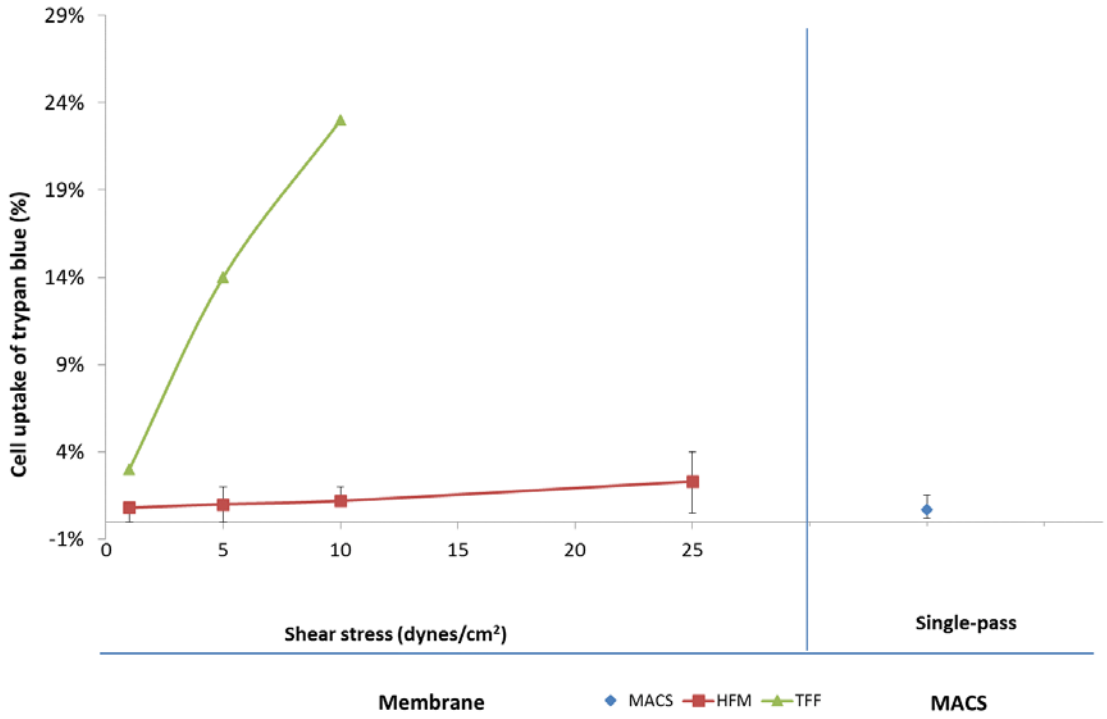

Figure 5-7. Percent cell uptake of trypan blue as a function of shear stress from collected fractions relative to the original input. Average, maximum and minimum data points are displayed for magnetic separation (n = 4), hollow fibre membranes (n = 5) and sole data point is displayed for flat sheet membranes (n = 1).

DAPI

Cells positive for DAPI staining across all three devices are represented in Figure 5-8. Gating was set at 2.00; cells above were considered to have lost membrane integrity by staining positive for DAPI, whilst cells below were considered to have retained membrane integrity, showing no DAPI staining.

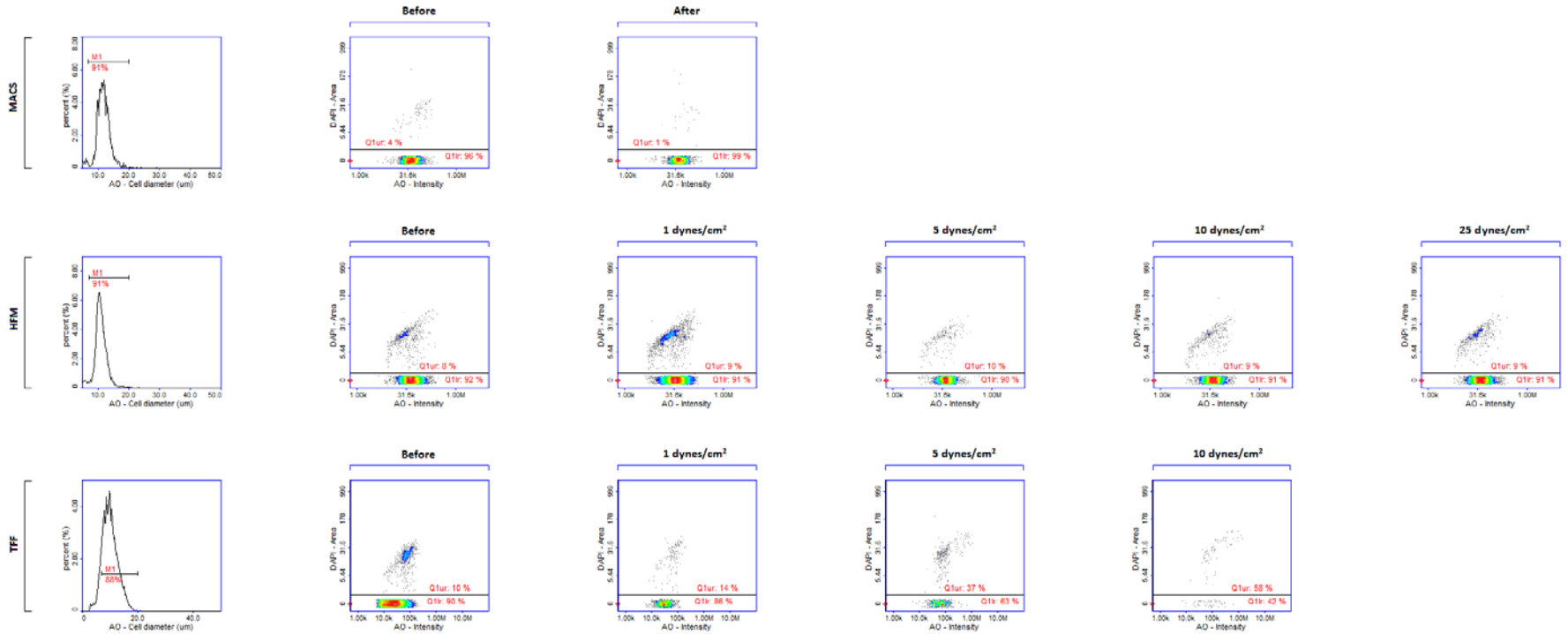

Figure 5-8. Scatter plots showing DAPI staining. Cells above or below an area intensity of 2.00 are considered positive or negative for DAPI staining, equating to cells with and without intact plasma membranes, respectively. Histograms have been used to gate cells into a size range of 7 – 20 µm.

The percentage of cells staining positive for DAPI increased following magnetic separation, equating to a gain of 2 - 23 % after one column pass. In hollow fibre membranes, staining increased gradually to 1 – 8 % at 25 dynes/cm^2. For the flat sheet membrane, particularly at a higher shear stress (10 dynes/cm^2), a 42 % loss was recorded. Data are displayed in Figure 5-9.

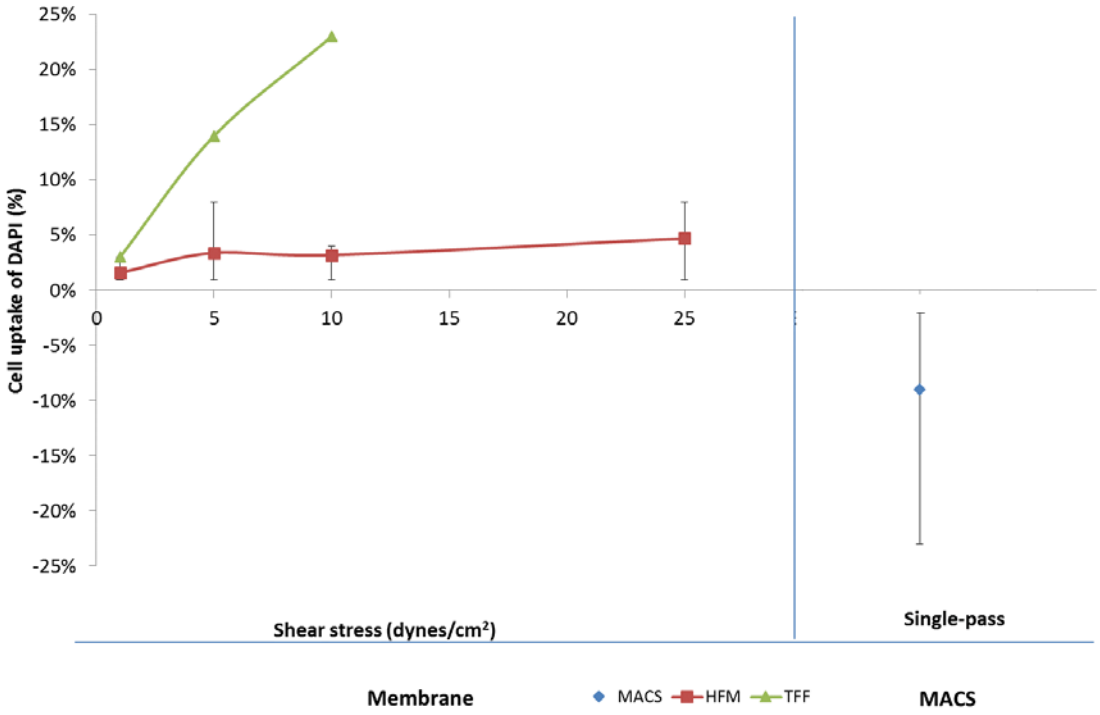

Figure 5-9. Percent cell uptake of DAPI as a function of shear stress from collected fractions relative to the original input. Average, maximum and minimum data points are displayed for magnetic separation (n = 4), hollow fibre membranes (n = 5) and sole data point is displayed for flat sheet membranes (n = 1).

VB-48/PI

VB-48/PI staining was performed for magnetic separation only, owing to technical constraints. Scatter plots and histograms for cell size gating were applied to plots presented in Figure 5-10 and data are in Table 5-7. Scatter plots were interpreted accordingly: cells in the lower right (VB-48 high and PI low) were deemed to have intact plasma membrane and no intracellular damage; those in the lower left (VB-48 low and PI low) were considered to have intracellular changes associated with pre-apoptotic processes in spite of intact

membranes; and cells in both regions above the line (PI high and VB-48 low or high) were considered necrotic.

7-AAD

Since VB-48/PI staining could not be used to assess cells processed in both affinity membranes, the 7-AAD assay was used instead. Representative scatter plots are displayed in Figure 5-10 and fractions of cell uptake of 7-AAD are displayed in Figure 5-11. The percentage of cells staining positive for 7-AAD collected from the hollow fibre membrane ranged from 0 – 1.6 % at 25 dynes/cm^2. For the flat sheet cassette, cell staining was much higher, having increased to 22 and 54 % at 5 and 10 dynes/cm^2 respectively (Figure 5-12).

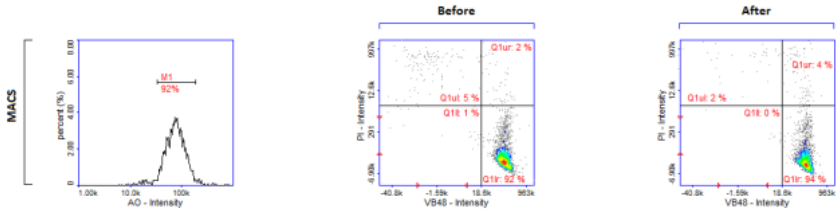

Figure 5-10. Scatter plots of B-lymphocyte cells showing VB-48 intensity vs. PI staining intensity before and after magnetic depletion using MACS MS columns. Cells staining in these regions is represented accordingly: upper right = VB-48-negative/PI positive; upper left = VB-48-positive/PI-positive; lower right = VB-48-positive/PI-negative; lower left = VB 48 negative/PI-positive.

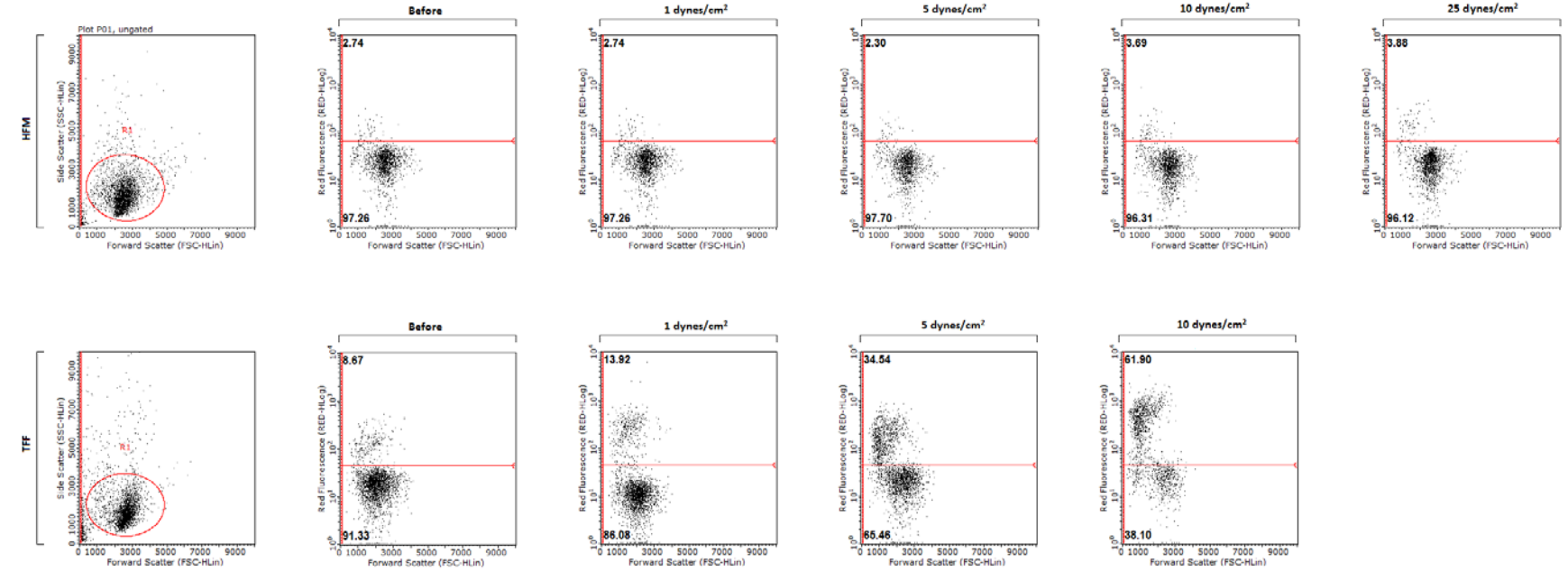

Figure 5-11. Scatter plots of gated cells before and after cell separation in hollow fibre and flat sheet membranes over ranges of 1 – 25 and 1 – 10 dynes/cm2 respectively.

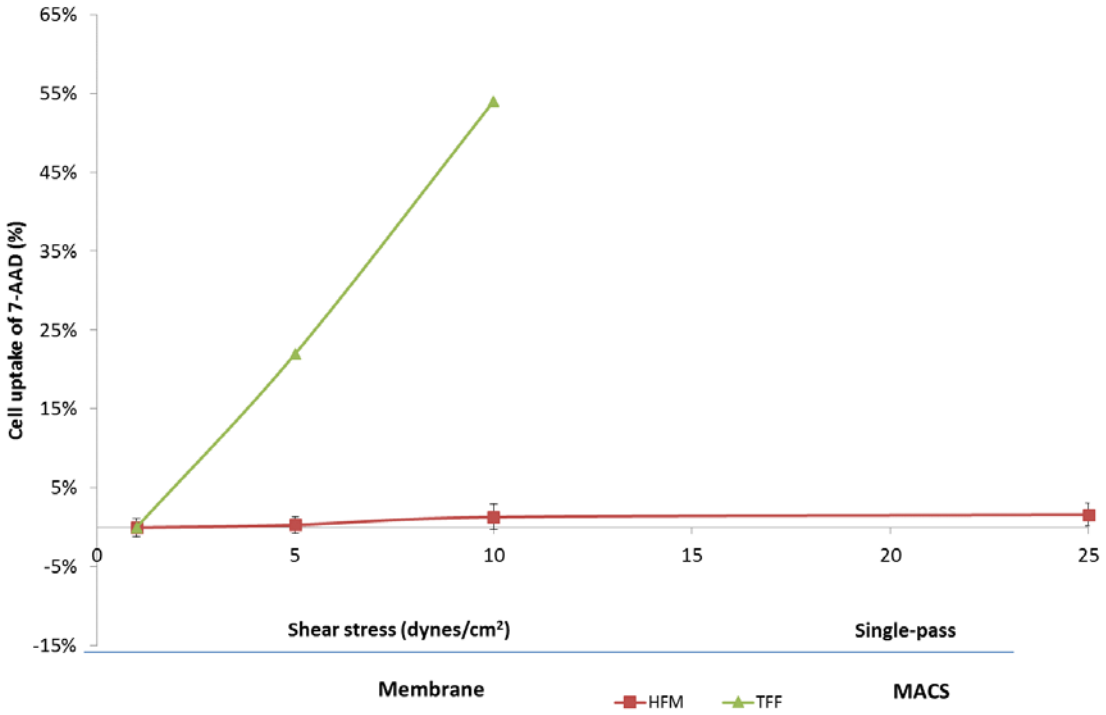

Figure 5-12. Percent cell uptake of 7-AAD as a function of shear stress from collected fractions relative to the original input. Average, maximum and minimum data points are displayed for hollow fibre membranes (n = 5) and a sole data point is displayed for flat sheet membranes (n = 1).

Table 5-7. Cell staining based on VB-48/PI.

	Upper right	Upper left	Lower right	Lower left
Change (%)	-1.1 – 4.3	4.5 – 8.9	0.1 – 0.2	-8.2 – 2.9

Cells staining in these regions is represented accordingly: upper right = VB-48-negative/PI positive; upper left = VB-48-positive/PI-positive; lower right = VB-48-positive/PI-negative; lower left = VB-48 negative/PI-positive. Data are displayed as the minimum and maximum data points for n = 5 runs.

In this chapter, the shear stress-induced separation of cells adsorbed with and without affinity interactions was performed. The purpose was to retain CD20+ cells (impurities) through affinity interactions and recover HLA-A2+ cells (product) free of affinity interactions to increase purity. This depletion (negative selection) strategy is in contrast to previous studies, committed to recovering cells adsorbed with affinity interactions, using shear stresses as high as 200 dynes/cm^2 (Colton, 1996, Slowiaczek, 1998) or potentially harmful acidic (Mandrusov et al., 1995) or enzymatic agents (Nordon et al., 1996). This work aimed to simulate the removal of impure, undifferentiated cells from pluripotent-derived cells

using more gentle conditions (shear stresses ≤ 25 dynes/cm^2) considered physiologically compatible to pluripotent-derived cells (Yamamoto et al., 2005, Wolfe et al., 2012 and 2013).

Magnetic separation

Miltenyi's magnetic cell separation technology, used as a benchmark, achieved HLA-A2+ cell recoveries in excess of 75 %, consistent with other studies (Schriebl et al., 2010b). However, both the $\log_{10}$ depletion (LCR) of impure CD20+ cells and the relative change in HLA-A2+ cell purity (RCP), were lower versus previous studies (Lara et al., 2006b, Schriebl et al., 2010b, Schriebl et al., 2012), perhaps due to lower antibody affinities, inefficient incubation protocols or the presence of CD20+ subpopulations with reduced antigen densities. The latter was observed in Figure 2.11 (Section 2.5.5); a subpopulation of CD20+ cells exhibited little-to-no staining perhaps due to limited antigen expression, a phenomenon which has limited the removal of such cells (Nordon et al., 1996, Schriebl et al., 2012). Cell viability was measured using membrane permeable and impermeable assays. Surprisingly, an increase in dye uptake was observed in collected fractions, owing to a higher propensity to remove non-viable cells during centrifugation and aspiration. Cells are less likely to incur process-induced damage inside the column since cell recovery is gravity-driven and shows no change in the biological attributes of magnetically separated cells (Li et al., 2012).

Membrane separation

Recovery

For hollow fibre and flat sheet membranes, HLA-A2+ cell recovery was highest in lower fractions (≤5 dynes/cm^2) presumably due to a high proportion of cells with weaker non-

affinity cell-substrate interactions. Cumulative HLA-A2+ cell recovery across 0 – 25 dynes/cm^2 was comparably lower versus previous studies, where ~95 % of cells without affinity interactions were recovered at lower shear stresses (≤ 5 dynes/cm^2). This is attributed to the longer incubation periods used here (30 minutes) and versus other studies (5 – 15 minutes) (Colton, 1996, Nordon et al., 2004). Longer incubation times prior to shear stress exposure are associated with increased bond formation and therefore greater resistance to cell detachment (Gallant et al., 2005, Cuvelier et al., 2007).

Purity

The purity of collected fractions, evaluated using the RCP ratio, was highest at lower shear stresses (≤ 5 dynes/cm^2) and declined when shear stress increased. Differences in the RCP ratios in both membrane formats and versus previous studies (Nordon et al., 1996, Slowiaczek, 1998) were attributed to different adhesion strengths. Chapter 4 showed that for hollow fibres, the number of possible affinity interactions per cell was 5,272 ± 1,102 (mean ± SEM), assuming a 0.7 μm^2 cell-surface contact area. For flat sheet membranes, there were 13,320 ± 1,791 possible affinity interactions. Whilst these numbers are rough estimates, differences in the number of affinity interactions could account for the different selectivities between both membranes, with greater resistance for the flat sheet membranes. For instance, theoretical (Bell, 1978, Bell et al., 1984, Kuo and Lauffenburger, 1993) as well as practical models (Xia et al., 1994), have shown that cell adhesion strength is proportional to the number of affinity interactions for a given dissociation constant and contact area. So for the hollow fibre membrane, the lower ligand density could have generated weaker adhesion strengths for CD20+ cells – similar to those for HLA-A2+ cells compared to the flat sheet cassette. Other possible causes could include: (1) fibres

possessing regions with lower rPrA densities, owing to ineffective coupling methods and therefore regions with lower affinity-interactive sites and/or (2) blocked fibres, most likely via instances where the resin had penetrated fractured or damaged fibres (Figure 5-13). In such instances, blocked fibres could inadvertently lead to higher shear stresses being applied, creating lower cell recoveries and purities.

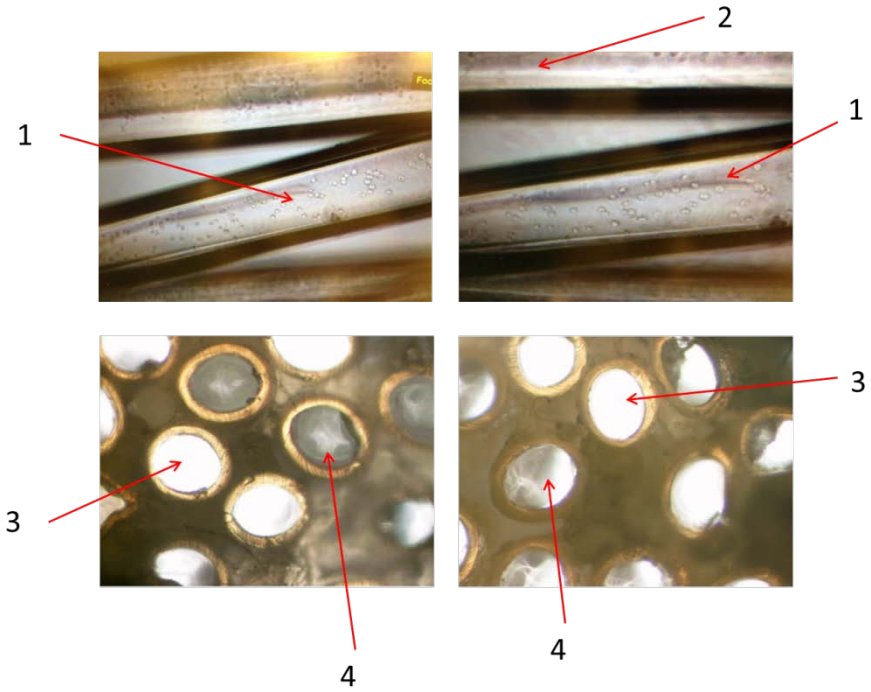

Figure 5-13. Dissected hollow fibre membrane modules post-separation: (A) and (B) show images of fibres containing adherent cells (x10 magnification) and (C) and (D) indicate microscopic images of fibre module cross-sections. Numbers are: 1 = fibres containing adsorbed cells; 2 = fibres without cells; 3 = dissected fibre open; and 4 = dissected fibre with possible blockage.

Membrane integrity

Changes in cell membrane integrity were radically different between hollow fibre and flat sheet membranes. Cells collected from hollow fibres exhibited increased dye uptake (up to 10 %) after 25 dynes/cm^2. Conversely, cells recovered from flat sheet membranes exhibited higher losses after 10 dynes/cm^2, where up to 50 % stained positive. Assays shared trends,

but not sensitivity, mostly likely due to different reagent concentrations and incubation times.

Generally, losses in cell membrane integrity were attributed to: (1) shear stress-induced damage where the surface tension acting on the cell membrane exceeded a critical limit sufficient to cause a rutpure (4 – 6 dynes/cm was previously deemed sufficient (Vlahakis and Hubmayr, 2000)); (2) membrane tearing through force-induced rPrA-IgG or IgG-antigen dissociation, as discussed in Chapter 1, or the possible rupture of the antigen out of the cell membrane (Pomianek, 1998). Ascertaining the impact on individual cell types (CD20+ or HLA-A2+ cells) was not possible since single- rather than multi-parameter flow cytometry staining was performed.

The more extreme reduction in cell membrane integrity in the flat sheet membrane cassette could be attributed to: (1) turbulent eddies generated from spacers used to improve mixing (Da Costa et al., 1994), leading to forces sufficient for rupture being applied to the membrane; (2) increased fluid pressure exerted on cells due to a reduction in internal geometry during the transition from the membrane to the outlet ports and tubing; and (3) turbulent conditions inside the collection vessel (a plastic beaker), again leading to cell membrane rupture.

Measurements to assess the cell response to shear stress were restricted to membrane integrity assays and the true effect on the cell is unknown. Moreover, losses in cell membrane integrity apparently indicate cell death (Kroemer et al., 2009), but this is contradicted in some instances, such as those caused by pore-forming proteins (Bischofberger et al., 2012) or mechanical stress, which is repairable by calcium influx-dependent mechanisms (McNeil and Steinhardt, 2003). Moreover, cells with apparently

intact plasma membranes may have incurred more subtle damage, such as a loss in functionality, manifesting much sooner than cell death and independent of membrane integrity. For instance, myocardial cells become non-contractile 1 to 2 minutes post-ischemia, but do not die until 20 to 30 minutes later and visible cell death is not even apparent until 6 to 12 hours later (Kumar, 2013). Cardiomyocytes derived from pluripotent cells, require a range of different tests to be performed to validate functionality. These concern electrophysiology, beating rates, contractility as well as extra- and intracellular-related characteristics (Blazeski et al., 2012).

5.5. Conclusion

This chapter has presented membrane-based methods for shear stress-induced affinity cell separation. Shear stress (0 – 25 dyes/cm^2) was applied to surface-adsorbed cells to exploit differences in the adhesion strength of those adsorbed with and without affinity interactions. Affinity interactions were attributed to substrate-adsorbed rPrA interacting with the Fc region of CD20 IgG-antibody-tagged CD20+ cells, increasing adhesion strengths relative to HLA-A2+cells without.

Membrane separation performances versus magnetic bead-based separation was poor. Cell recovery was very variable, ranging from 37 – 55 %, further indicating the limitations of the particular models used in this study. Cell purity increased (up to 10 % from an input purity of 50 %) in fractions collected ≤ 5 dynes/cm^2 and it decreased in fractions collected ≥ 5 dynes/cm^2. This lower selectivity was attributed to fewer affinity interactions between CD20+ cells and the substrate, perhaps owing to the lower rPrA density, which was variable, ranging from 13,320 ± 1,791 per μm^2 (mean ± SEM). Vital dye uptake, used to indicate a loss of cell plasma membrane integrity, was under 10 % across the 0 – 25 dynes/cm^2 range.

Conversely, the flat sheet membranes exhibited a larger increase in the purity of collected fractions in the single run that was performed (increasing from 53 % at the inlet to 65, 93 and 79 % at fractions collected at 1, 5 and 10 dynes/cm^2. However, cells collected from fractions at 5 and 10 dynes/cm^2 showed a very high uptake of vital dye, indicating extensive damage to cell membrane integrity. However, recovery was also poor, totalling 16 % across the collected range.

Direct comparisons in performance between both membrane formats are of limited use for several reasons: (1) the poor quality of the hollow fibre modules and (2) the fact that only a single run could be performed using the flat sheet membrane. However, these findings show that membranes have the capacity to increase the purity of cells, although compared to existing magnetic bead and previous membrane separation devices, aforementioned limitations must first be addressed. These primarily centre on membrane design and construction, as well as the incubation times used. Further, more detailed assessments regarding the impact on cell health and functionality should also be performed.

Chapter 6. Thesis summary and future work

6.1. Thesis output

6.1.1. Flow tube model

A small scale model was used to determine differences in the resistance of cells adherent with and without affinity interactions using shear stress. The purpose was to exploit these differences for cell separation studies for two proposed uses: (1) as an acoustic quartz crystal microbalance biosensor to measure cell purity based on net changes in surface-localised cells and (2) a membrane device capable of scale-up or scale-out to address larger batch sizes containing impure cell populations.

6.1.2. Biosensor

A quartz crystal microbalance was proposed as a biosensor to measure the purity of cells in a given sample. Here, shear stress-induced affinity cell separation is proposed as a means to remove cells without affinity interactions (product) and retain cells adherent with affinity interactions (impurities), ultimately to detect impure cell populations. A method for quantifying cells and converting the change in cell number on the surface with purity was proposed. However, the lack of practical output meant that the concept could not be investigated and further work is recommended to determine its feasibility.

6.1.3. Separation devices

Hollow fibre and flat sheet microfiltration membranes were utilised for cell separation. The purpose was to mimic the removal of impure cell populations by exploiting differences in the adhesion strength of cells with and without affinity interactions. However, compared to

magnetic separation studies, performance (recovery, purity and cell membrane integrity) was poor. In short, a possible re-consideration of operating parameters (in particular incubation time prior to washing and ligand density) is recommended, along with a re-design of the system and the use of more advanced methods to study the impact on cells are also recommended.

6.2. Improvements and future work

Incubation time and ligand density

The shear stress required to remove 95 % of cells adherent without affinity interactions was approximately 25 dynes/cm^2 in flow tube models. This is higher than cited papers and is primarily attributed to the longer incubation time used (30 minutes versus 5 – 15 minutes used elsewhere). This reduced cell selectivity and recovery in both membrane separation devices and would translate to a lower resolution in the QCM biosensor. In order to improve this, a reduced incubation time is therefore proposed in conjugation with studies that vary ligand density, which has also been shown to affect cell selectivity (Pomianek, 1998, Colton, 1996).

Studying the physiological effects of shear stress on cells

Since the flow tube is limited to shear stress-induced cell detachment, which relies upon practical models that are difficult to operate for cell collection, the use of a conventional rotating plasma separation unit is instead proposed. Here, cells may be exposed to a range of shear stresses and collected as a function of rotation rate (Ohashi et al., 1988, Kaplan and Halley, 1990). Collected cells may then be assessed for short- and long-term effects of shear stress using high-throughput, multiparameter methods.

Correlation with cell potency

Another functionality of this separation device concerns the purification of cells based on potency. Recent evidence suggests that non-pluripotent mesenchymal stem cells are in fact split into sub-populations during culture that contain cells with and without key potency factors (Crigler et al., 2006, Mabuchi, 2013). Increasing the proportion of potent cells in a transplant could increase the therapeutic effect of a dose. However, enriching these cells may compromise cell functionality, as observed in fluorescent cell sorting methods (Li et al., 2012). Rather, by identifying extracellular markers exclusive to cells incapable of therapeutic action, a depletion separation strategy targeting inert cells could be implemented without compromising cell functionality.

Backpressure-induced cell separation

Backpressure-induced cell detachment, demonstrated elsewhere (Colton, 1996, Pomianek, 1998), may be more appropriate in instances where cells deform and spread across the surface (Cuvelier et al., 2007) more quickly than the rate at which new affinity interactions could occur. The cells used here are non-adherent lymphocytes and do not deform unless subjected to increased external force, irrespective of the incubation time. However, the majority of adherent cells do undergo deformation when statically incubated (Itano et al., 2003, Gallant et al., 2005, Cuvelier et al., 2007), so the use of membranes with larger pores would perhaps be more useful in such applications, as demonstrated previously (Colton, 1996).

6.3. New system design

Provides overview of device design and implementation.

Cartridge design

A method of scaling-out the system in order to scale-up is presented. Here, up to 100 cartridges are stacked 10 x 10 to achieve a system comprised of 100 cartridges. A method to process multiple cartridges is highly desirable for large-scale cell separation, since the direct scale-up of such systems is limited by the reduction in shear stress as a function of distance from the centre of the cartridge at larger scales. The proposed cartridge and system design is presented in Figure 6-1 below.

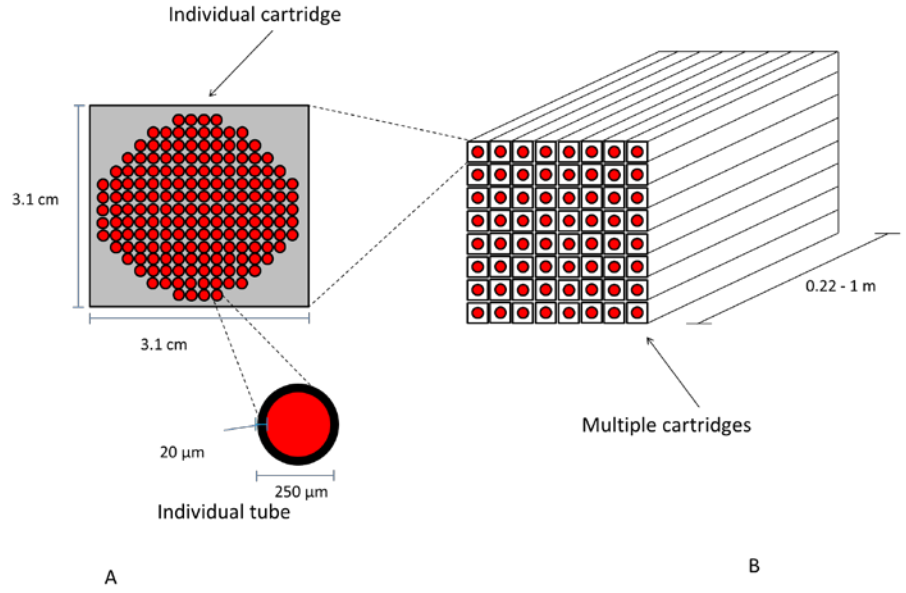

Figure 6-1. Individual cartridge components (not to scale) where (A) = dimensions of an individual cartridge; (B) = multiple cartridges stacked in a combined system.

Cartridge and tube sizes are presented in Tables 6-1 and 6-2. Thinner tube walls, owing to a non-porous nature enable tubes to be more closely packed together. Since radial mass transfer is not a requirement, the tube may be made non-porous.

Table 6-1. Cartridge sizing.

	Actual	Compact	Units
# tubes	20,000	20,000	-
Length	0.22	1	*m*
CS-area	9.8	9.8	cm^2
Width	3.1	3.1	*cm*

Table 6-2. Tube sizing.

	Actual	Compact	Units
Tube length	0.22	1	*m*
Outer diameter	250	250	*um*
Inner diameter	230	230	*um*
Wall thickness	20	20	*um*
SA tube total	1.60E-04	7.20E-04	m^2
SA/cm tube	7.20E-06	7.20E-06	m^2/cm
SA/cartridge	3.18	14.45	m^2

System design

The cartridge system for 10 cartridges in a row is presented in Figures 6-2 and 6-3. Up to 90 additional cartridges may be stacked underneath, also in rows of 10, equating to 100 cartridges in total.

The basic process involves the following: (1) the 3-way valve (**2**) is adjusted to allow the injection of a cell suspension (**1**) into 10 channel valve (**4**), which systematically controls the injection of suspension into each of the cartridge units (**5**) (the outlet 3-way valve (**9**) is adjusted to allow waste to be removed from the system (**10**)); (2) an incubation period occurs whereby cells are allowed to form affinity interactions with ligand-coupled surfaces; (3) the feed 3-way valve (**2**) is adjusted to inject wash buffer (**3**) to recover cells from cartridges, again by selectively adjusting the 10-channel valve (**4**) to permit the systematic recovery of cells from each cartridge in series and the outlet 3-way valve (**9**) is adjusted to allow cell recovery for further downstream processing (**8**).

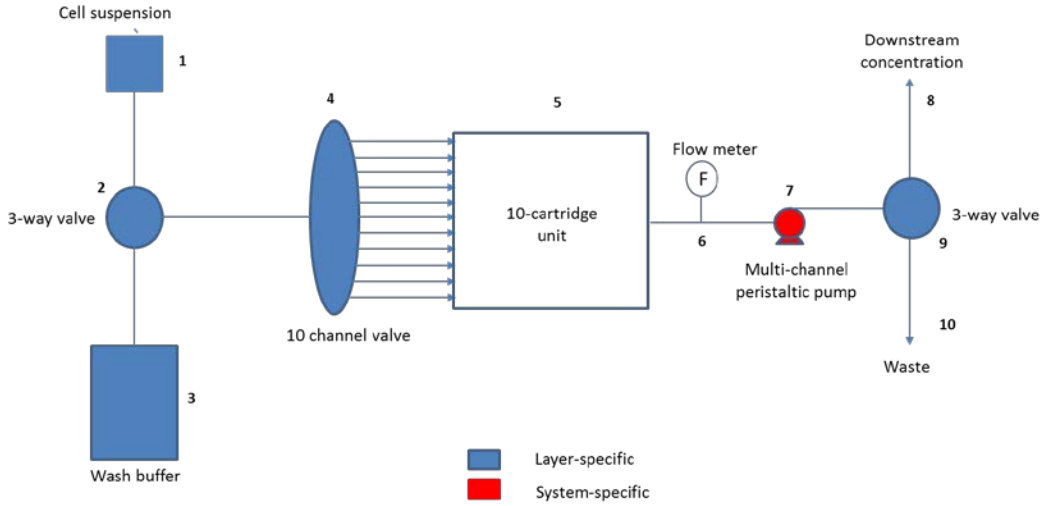

Figure 6-2. Top-down view of basic setup for 10 cartridges. The potential for adding additional rows of 10 cartridges underneath also exists, enabling up to 100 cartridges to be processed in a system. Each layer is represented by blue symbols, whereas units used by multiple layers simultaneously are represented by red symbols.

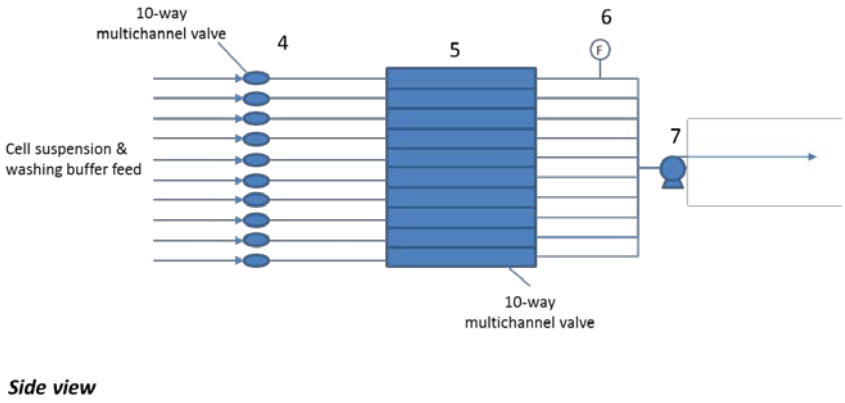

Figure 6-3. Side view of 10 layers of 10 cartridges stacked and connected to a single peristaltic pump.

Importantly, the system could also be engineered to comply with the following criteria deemed instrumental in a cell therapy manufacturing process (Table 6-3).

Table 6-3. Technology requirements recommended for implementation into a cell therapy manufacturing process.

Property	Description	Justification
Closed system	Functionally closed unit permitting operation in non-GMP settings	Cell suspension is not exposed to the atmospheric environment and can be integrated into a flow-based manufacturing process. Utilises closed-system compatible components.
Single-use	Disposable device	Critical components are disposable after use
Cost-effective	Exerts minimal costs on the process development or operation	Components account for a low cost of the overall process
Scalable	Capacity to increase batch sizes whilst maintaining process performance	The technology may purify up to 1.5 x 10^{12} cells per batch[a].
Capable of automated operation	Integration into robotic processing steps	The system may be capable of automation and integration into a manufacturing process.
GMP compliant	Consistent with regulatory constraints surrounding product manufacture	Maintains cells in a sterile environment. Utilises GMP-compatible components.
ISO9001 certification	Demonstration of dependable quality	Ensures that necessary standards have been met and that if the system is manufactured in house, that all components received from suppliers are validated.

[a] based upon a density of 8 % coverage – up to 90 % has been reported elsewhere (**Nordon 1996 and patent**)

System operation

Each cartridge will operate a 1.5 minute injection time, 10 – 15 minute incubation period for cell adsorption and the formation of affinity interactions and a 2 minute recovery period (Figure 6-4).

Figure 6-4. Operating regime for an individual cartridge.

As detailed above, rows of 10 cartridges in each system can be operated in series; the injection of cells into one cartridge is immediately followed by the injection of cells into the adjacent cartridge until complete. Since the incubation time of the first cartridge in a row of 10 ends prior to cell recovery, multiple cartridges may be processed using the same pump.

The outlet from the 10-cartridge cassette (**5**) may be connected to a peristaltic pump (**7**). Since peristaltic pumps can process multiple feed lines, additional layers of 10 cartridges may be added underneath and operated in parallel with the top layers. As such, Figure 6-5 shows how rows of 10 may be processed in series. By using the same peristaltic pump for each layer of 10 cartridges, multiple feed lines and therefore multiple cassettes containing 10 cartridges may be processed in

simultaneously. As such, the processing time will remain the same in spite of additional layers of cassettes, meaning that additional cartridges (e.g. 9 cassettes of 10 cartridges each) may be added, equating to a system of 100 cartridges.

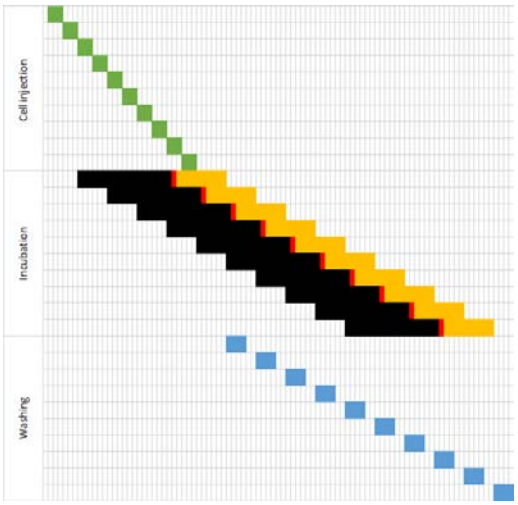

Figure 6-5. Operating regime for 10 cartridges in series.

Cartridge system performance

The nature of the design is such that performance may be assumed to be independent of scale. It is assumed that performance projections extracted from the scaled-down flow tube models can be replicated inside each individual cartridge. Since the cartridge system itself is comprised of several individual cartridges, separation performance would be replicated in each of the cartridges.

Figure 6-6 presents the performance projections for each of the cartridges assuming separation performance based upon that of the data gathered in Chapter 2. Here, performance was sub-optimal versus previous studies: ~91 % of product cells were recovered at 25 dynes/cm^2, whilst a similar amount were recovered at 5 dynes/cm^2 elsewhere (Nordon 1996). This lower recovery would mean that higher amounts of impure cells would be recovered, diluting the purity of recovered fractions.

Notably, system performance is independent of scale and has the capacity to recover the majority of product cells (~ 75 %) and raising purity above 99 % (up from an original starting purity of 90 % or

above). Although not addressing more stringent requirements (Section 1.7), it would satisfy those for some clinical standards where ≥99 % is deemed sufficient for therapeutic application (Schwartz et al., 2012).

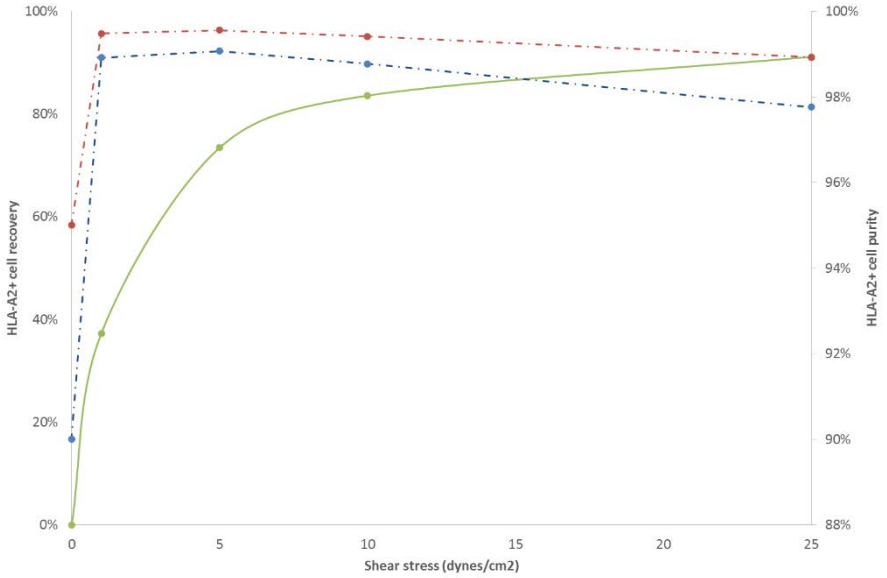

Figure 6-6. System performance projections based on experimental data obtained in Chapter 2.

Processing capacity

Idealised estimates (Tables 6-4 and 6-5) using projections from Chapter 2 indicate that the number of cells which can be purified in 100 cartridges ranges from 1.6 – 3.2 x 10^{11} cells for the 0.22 m length unit and 0.74 – 1.5 x 10^{12} cells for the 1 m length unit for densities of 4 and 8 % respectively. Ultimately the system size will depend upon the number of cartridges, the length of the cartridges and adsorption density of cells on the surface.

Table 6-4. Cell adsorption capacity per cartridge.

	Actual (0.22 m)		**Compact (1 m)**	
Cell surface coverage	4 %	8 %	4 %	8 %
Total cells	1.8 x 10^{9}	3.2 x 10^{9}	0.75 x 10^{9}	1.5 x 10^{10}

Cartridge dimensions: tube height: 3.1 cm; width: 3.1 cm; number of tubes: 20,000. Assumed cell size = 10 µm diameter.

Table 6-5. Large-scale cell adsorption capacity per 100-cartridge system.

	Actual (0.22 m)		Compact (1 m)	
Cells surface density	4%	8%	4%	8%
Total cells	1.6×10^{11}	$3.2E \times 10^{11}$	$7.4E \times 10^{11}$	$1.5E \times 10^{11}$

Cartridge quantity: 100; height: 31 cm; width: 31 cm. These values are based upon the assumption that cell adsorption is homogeneous across all surfaces. Whilst cells settle under gravity, it is thought that cartridge rotation will encourage cell adsorption onto all surfaces. Cell surface adsorption is assumed to be homogeneous, since cells are transported via convective processes and would be mixed prior to injection.

It should be noted that the cell densities assumed here are low compared to those utilised previously (Nordon, 1996, Slowiaczek 1998), which were as high as 90 % and independent of performance. Such an increase in density would yield a more compact system. The previous design where a 90 % starting density was used (Nordon 1996) was 20 cm in length and assuming 20,000 fibres were compacted together, as calculated in this section, each device could accommodate ~2.5 x 10^{10} cells, which would mean that ~60 units would be required to purify 1.5 x 10^{12} cells. No doubt an increase in length would translate to a reduction in the number of cartridges required, but the higher densities of cells utilised in such systems could increase the likelihood of aggregation, tubular clogging, imbalances in shear stress applied and therefore reduced purification performance. As such the precise densities, lengths and number of cartridges utilised could only be determined practically but would no doubt benefit from the design presented in Figures 2 and 3 to ensure the rapid purification of multiple cartridges.

Volume generated

The internal volume of the cartridges must be removed in order to recover the cells from the system. Figure 6-7 displays the internal volumes of 100-cartridge systems comprised of 0.22 m-length cartridges and 1 m-length cartridges. The volumes from each system alone are significant and present several technical challenges that would require additional processing in order to overcome.

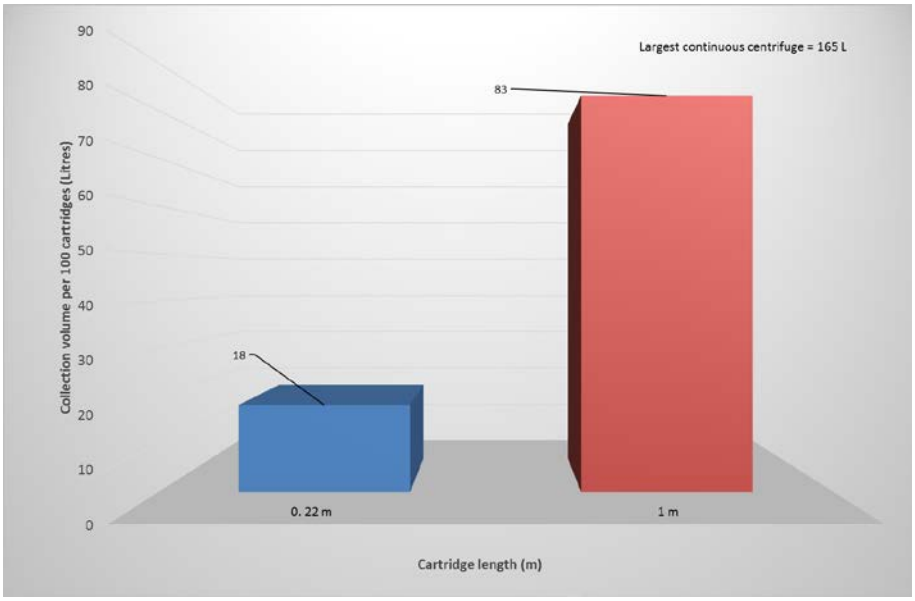

Figure 6-7. Internal volumes inside the 100 cartridge units of length 0.22 m and 1 m with the purification capacity of 3.2 x 10^{11} and 1.5 x 10^{12} cells respectively, assuming an 8 % density.

This highlights a significant increase in the volume of cells that would recovered from the system versus that for magnetic separation technologies. The final capacity will depend upon the shear stress utilised for detachment (applied for ≤ 1 – 2 seconds), as well as the volume of fluid inside the system. This means that additional downstream processing to concentrate the cells to a required amount (10^7 – 10^8 cells/mL) will need to be large-scale – in the order of 100 litres. Such technology has been patented previously as either a hollow fibre membrane unit [WO2011091248A1] or a continuous centrifugation device.

Chapter 7. Appendix

The following section provides the calibration charts used to quantify various protein and chemical contents present on glass and membrane substrates.

Chapter 2 data

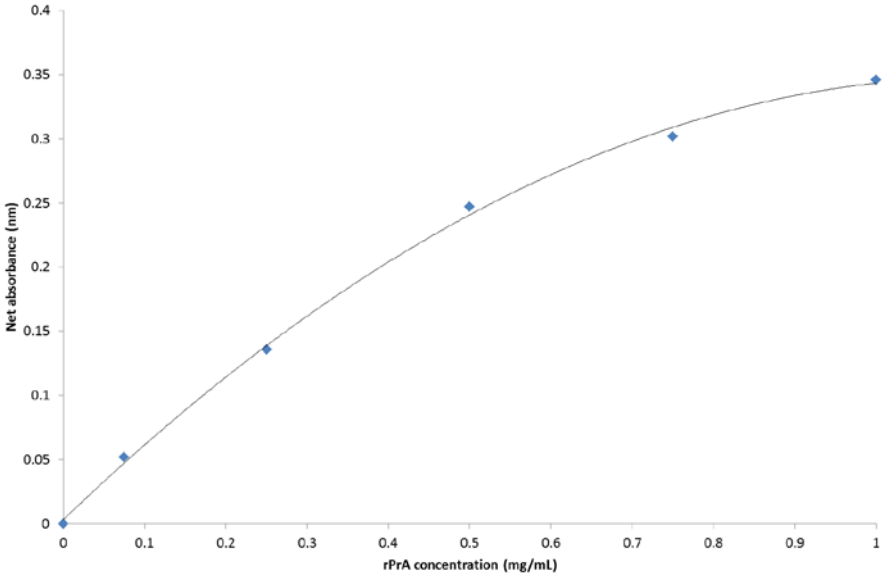

Figure 7-1. Calibration chart for rPrA quantification onto aldehyde-functionalised glass beads using the BCA assay. A range of known concentrations (0 – 1 mg/mL) were plotted versus absorbance. The R^2 value is 0.993.

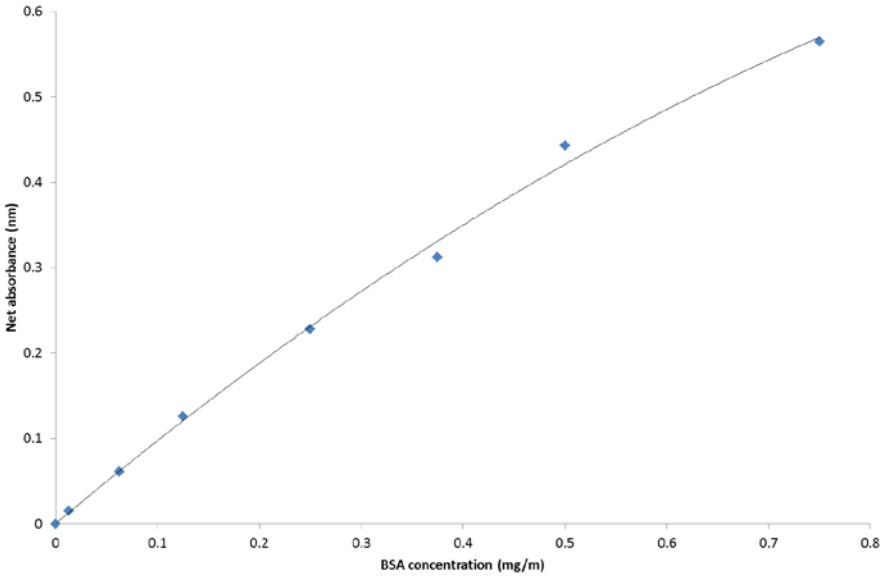

Figure 7-2. Calibration chart for BSA quantification onto aldehyde-functionalised glass beads using the BCA assay. A range of known concentrations (0 – 0.75 mg/mL) were plotted versus absorbance. The R^2 value is 0.989.

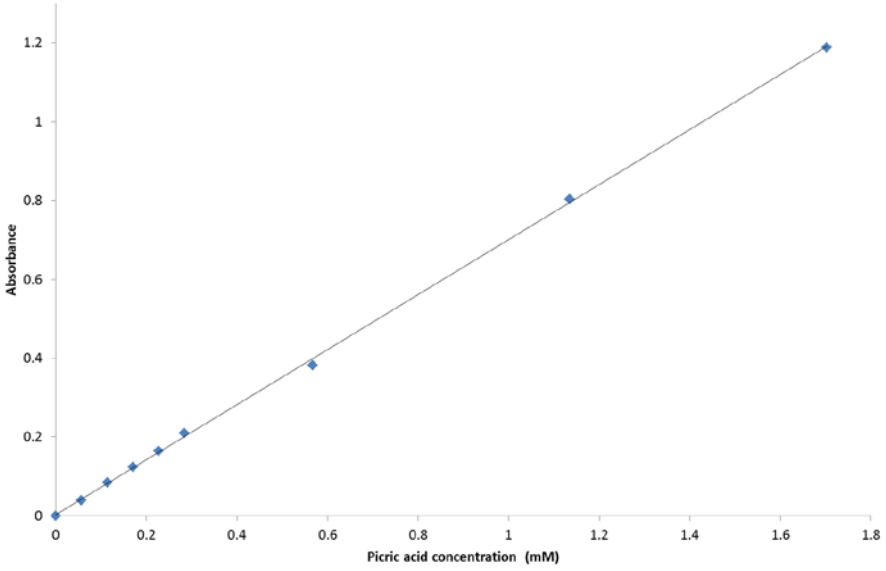

Figure 7-3. Calibration chart using to convert absorbance at 410 nm into picric acid concentration for TNBS data interpretation. The R^2 value = 0.9996.

Worked example (Section 2.5.13.)

Assuming a 4 % density of cells on the sensor surface are washed at 25 dynes/cm^2, the following approach may be applied:

1. Present equations:

$$N_{C,n} = SP_{C,n0}.RT_{C,n}.N_{T,n0} \quad 2.16$$

$$N_{C,n} = SP_{C,n}.N_{T,n} \quad 2.15$$

2. Rearrange equations to determine $SPC_{n,0}$:

$$SP_{C,n0} = \frac{SP_{C,n}.N_{T,n}}{RT_{C,n}.N_{T,n0}} \quad 2.17$$

3. Present known and unknown parameters from calibration chart:

Table 7-1. Parameters used to determine cell purity.

	Data	Unit
$SP_{C,n}$	Unknown	%
$N_{T,n0}$	42,091	Cells
$N_{T,n}$	32,111	Cells
$RT_{C,n}$	84	%

Note: $RT_{C,n}$ is to be obtained through prior experimental determination – to be customised for each cell line.

4. Determine the unknown parameter ($SP_{C,n}$):

Use Equation 2.11 to determine:

$$SP_{C,n} = SP_{C,n*} + \left(Plateau - SP_{C,n*}\right).\left(1 - \exp(-K.N_{T,n})\right) \quad 2.14$$

, and insert the following data.

Table 7-2. Constants used in Equation 2.14.

Constant	Data	Unit
$SP_{C,n*}$	-100.9	%
K	0.0002077	1/cells
Plateau	96.40	%

, such that at 25 dynes/cm^2, where $N_{T,n}$ is 32,111 cells , $SP_{C,n}$ would equate to 96.1 % (the actual value is 98.8 %).

5. Insert the data into Equation 2.13 to determine the original starting purity of cells on the sensor surface:

$$SP_{C,n0} = \frac{0.96 \times 32{,}111}{0.84 \times 42{,}091}$$

, such that $SP_{C,n0}$ = 87.2 % (the actual value would be 90 % based on the projections made in Section 2.5.8.).

A comparison of the calculated versus actual $SP_{C,n0}$ purities is presented below based on shear stress exposure at 25 dynes/cm^2.

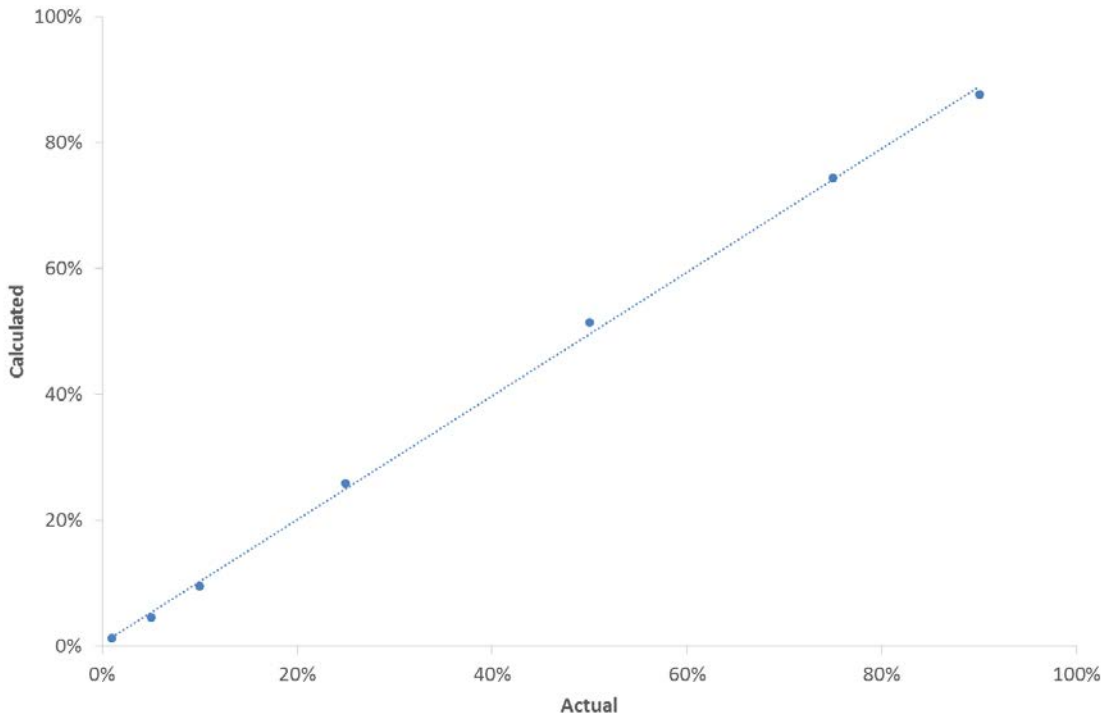

Figure 7-4. Comparison of actual purities versus those calculated with Equation 2.13 $SP_{C,n0}$ purities. The R^2 value is 0.9991 and the equation is y = 0.9822x + 0.0046. The comparison shows good agreement, with an R^2 value of 0.9991. *Note*: the actual values are based on the original data generated from the model, which considered cell recoveries.

Table 7-3. Comparison of actual purities versus calculated purities.

Actual	90%	75%	50%	25%	10%	5%	1%
Calculated	87.6%	74.3%	51.4%	25.9%	9.6%	4.6%	1.3%

Note: CD20+ cell purities below 1 % are not considered measurable due to limitations in the model.

Chapter 3 data

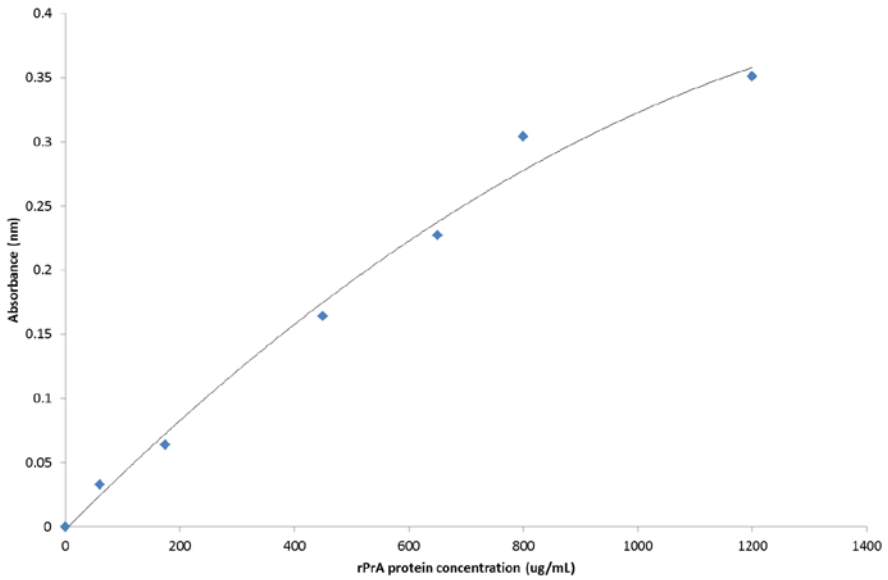

Figure 7-5. Calibration chart for rPrA quantification onto aldehyde-functionalised hollow fibre membranes using the BCA assay. A range of known concentrations (0 – 1,250 µg/mL) were plotted versus absorbance. The R^2 value is 0.990.

6

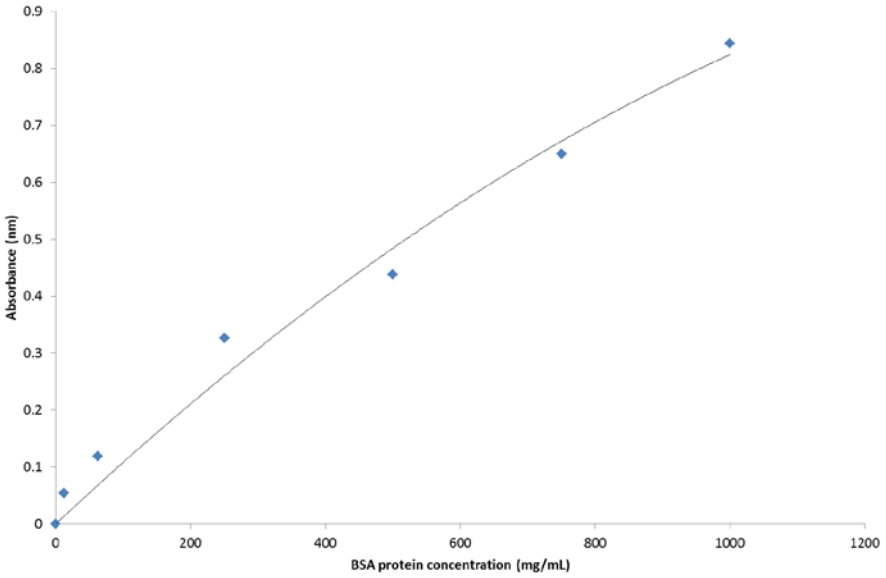

Figure 7-6. Calibration chart for BSA quantification onto aldehyde-functionalised hollow fibre membranes using the BCA assay. A range of known concentrations (0 – 1,000 µg/mL) were plotted versus absorbance. The R^2 value is 0.981.

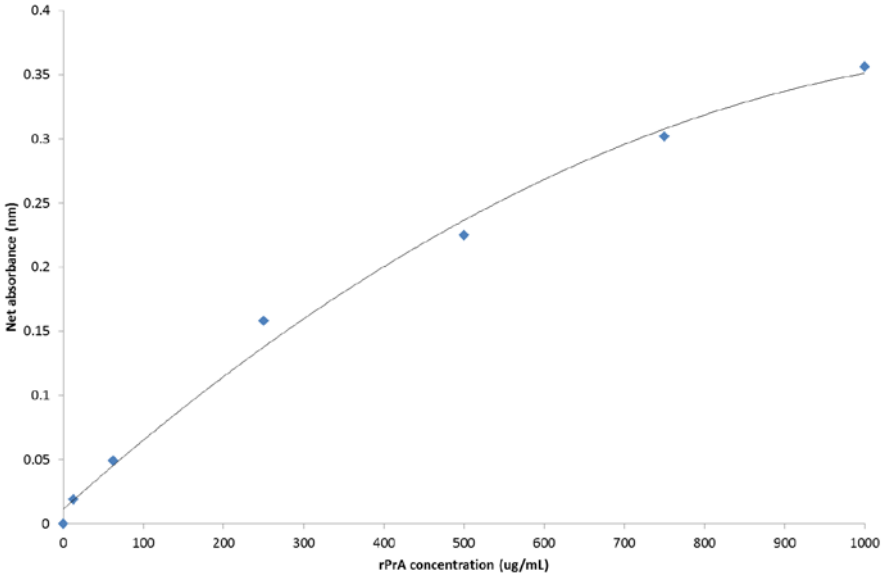

Figure 7-7. Calibration chart for rPrA quantification onto aldehyde-functionalised PES membranes using the BCA assay. A range of known concentrations (0 – 1,000 µg/mL) were plotted versus absorbance. The R^2 value is 0.994.

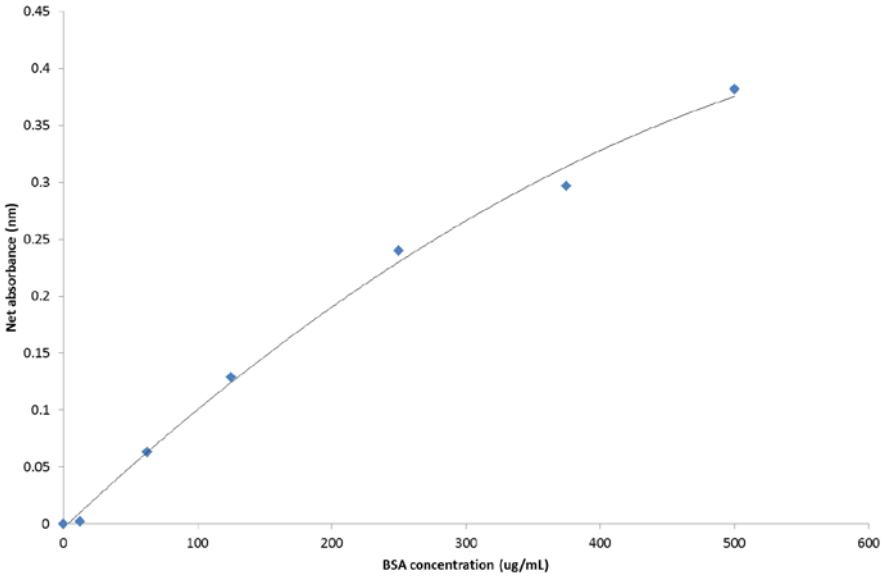

Figure 7-8. Calibration chart for rPrA quantification onto aldehyde-functionalised PES membranes using the BCA assay. A range of known concentrations (0 – 1,000 µg/mL) were plotted versus absorbance. The R^2 value is 0.996.

Chapter 5 data

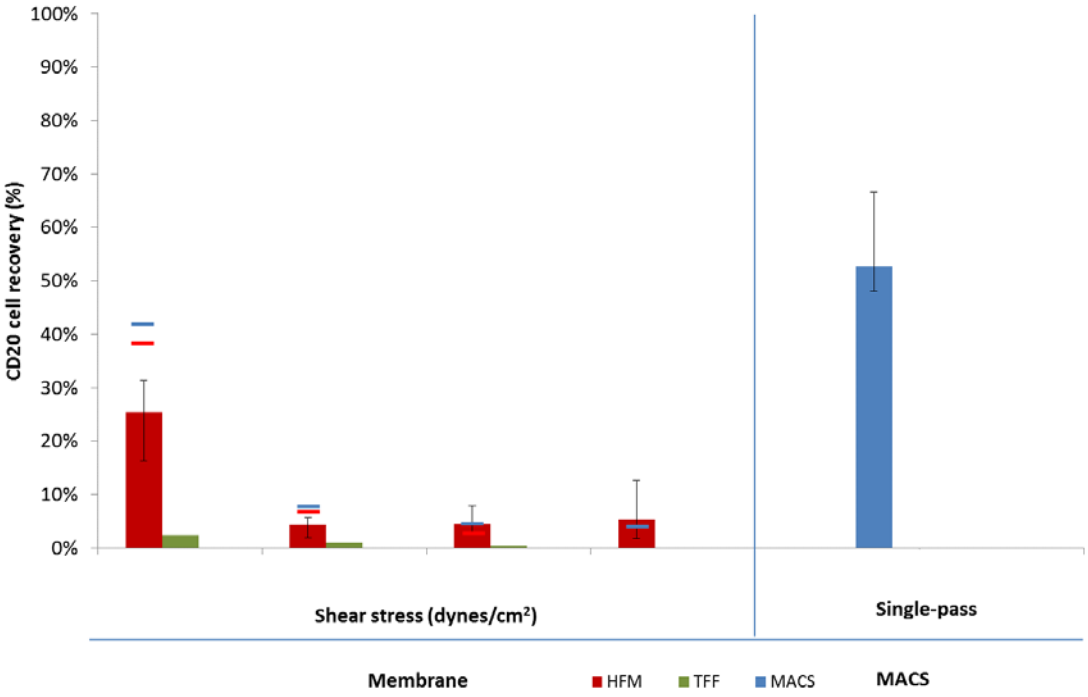

Figure 7-9. CD20+ cell recovery across tested units. Separation of CD20+ cell recovery as a % of the original input are compared for magnetic separation (MACS) (n = 4), hollow fibre membrane (n = 5) for IgG-exposed and flat sheet membrane (n = 1) devices. Data are displayed as the average, minimum and maximum data points. A control study for the hollow fibre membrane is also displayed (n = 2) as the range (minimum (red) and maximum (blue)).

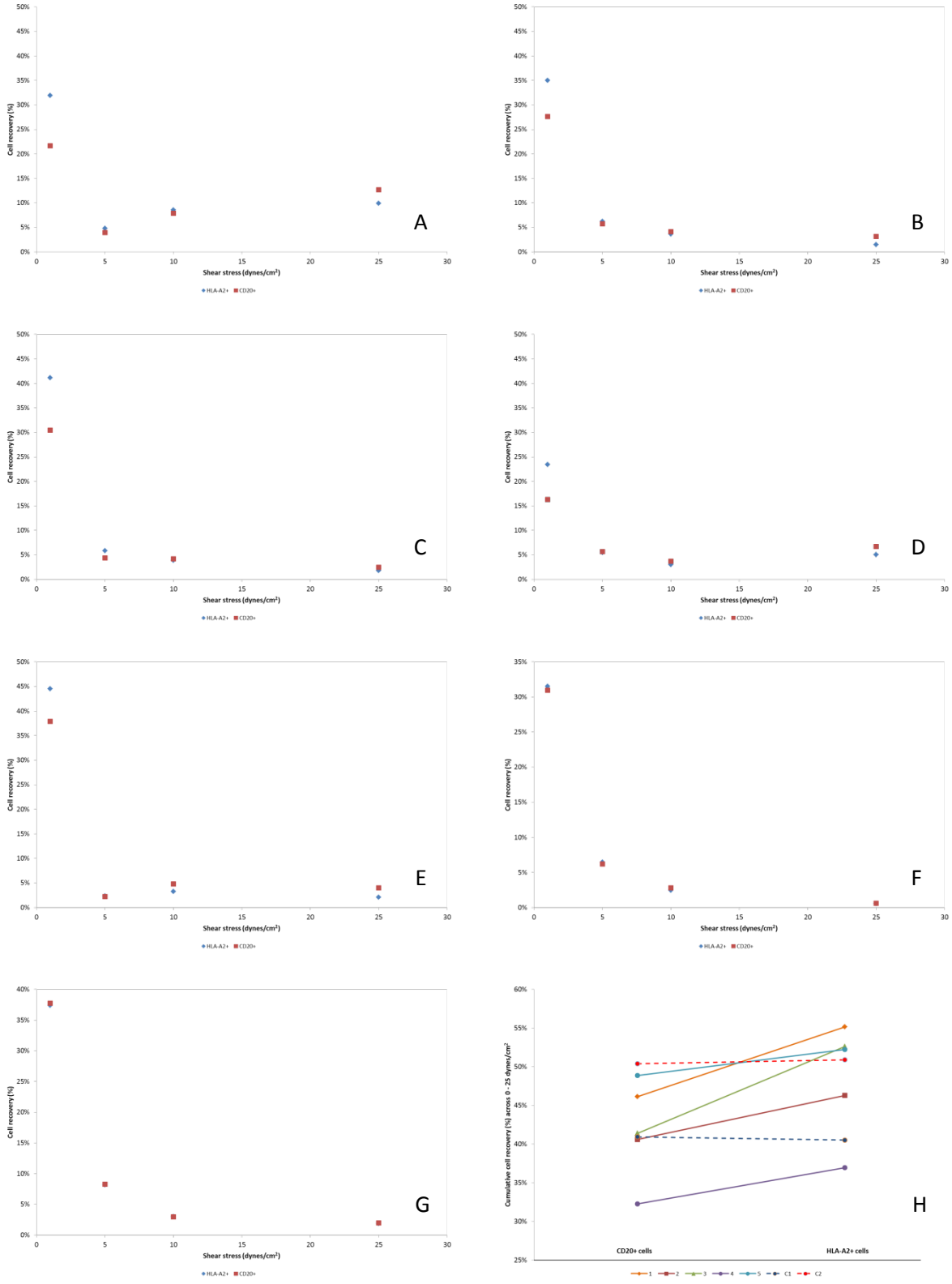

Figure 7-10. Individual cell recoveries from hollow fibre membranes across 1, 5, 10 and 25 dynes/cm^2 for CD20+ and HLA-A2+ cells with affinity interactions (A-E) and without (F-G). Total cell recovery across 0 – 25 dynes/cm^2 (H), where undashed lines = main runs and dashed lines control runs (without IgG antibody incubation).

Chapter 8. Appendix

(CTGTAC), F. 2008. Cellular Therapies Derived from Human Embryonic Stem Cells – Considerations for Pre-Clinical Safety Testing and Patient Monitoring

ABDELSALAM, M. E., BARTLETT, P. N., KELF, T. & BAUMBERG, J. 2005. Wetting of regularly structured gold surfaces. *Langmuir,* 21, 1753-7.

ADAMO, L., NAVEIRAS, O., WENZEL, P. L., MCKINNEY-FREEMAN, S., MACK, P. J., GRACIA-SANCHO, J., SUCHY-DICEY, A., YOSHIMOTO, M., LENSCH, M. W., YODER, M. C., GARCIA-CARDENA, G. & DALEY, G. Q. 2009. Biomechanical forces promote embryonic haematopoiesis. *Nature,* 459, 1131-1135.

ADAMSON, S. R. 1998. Experiences of virus, retrovirus and retrovirus-like particles in Chinese hamster ovary (CHO) and hybridoma cells used for production of protein therapeutics. *Dev Biol Stand,* 93, 89-96.

AHLUWALIA, V. K. D., S. 2000. Comprehensive Practical Organic Chemistry: Qualitative Analysis. Hyderabad, India: Universities Press (India).

AHN, W. S., JEON, J. J., JEONG, Y. R., LEE, S. J. & YOON, S. K. 2008. Effect of culture temperature on erythropoietin production and glycosylation in a perfusion culture of recombinant CHO cells. *Biotechnol Bioeng,* 101, 1234-44.

AL-RUBEAI, M. S., R. P.; EMER, A.; ZHANG, Z. 1995. Cell cycle and cell size dependence of susceptibility to hydrodynamic forces. *Biotechnol Bioeng,* 46, 88-92.

ALEXANDER, P. B., WANG, J. & MCKNIGHT, S. L. 2011. Targeted killing of a mammalian cell based upon its specialized metabolic state. *Proceedings of the National Academy of Sciences,* 108, 15828-15833.

AMI, D., NERI, T., NATALELLO, A., MEREGHETTI, P., DOGLIA, S. M., ZANONI, M., ZUCCOTTI, M., GARAGNA, S. & REDI, C. A. 2008. Embryonic stem cell differentiation studied by FT-IR spectroscopy. *Biochimica et Biophysica Acta (BBA) - Molecular Cell Research,* 1783, 98-106.

ARMBRUSTER, D. A. & PRY, T. 2008. Limit of Blank, Limit of Detection and Limit of Quantitation. *The Clinical Biochemist Reviews,* 29, S49-S52.

ATKINS, H. L. & FREEDMAN, M. S. 2013. Hematopoietic stem cell therapy for multiple sclerosis: top 10 lessons learned. *Neurotherapeutics,* 10, 68-76.

AVRAHAM-CHAKIM, L., ELAD, D., ZARETSKY, U., KLOOG, Y., JAFFA, A. & GRISARU, D. 2013. Fluid-Flow Induced Wall Shear Stress and Epithelial Ovarian Cancer Peritoneal Spreading. *PLoS ONE,* 8, e60965.

BABACAN, S., PIVARNIK, P., LETCHER, S. & RAND, A. 2002. Piezoelectric Flow Injection Analysis Biosensor for the Detection of Salmonella Typhimurium. *Journal of Food Science,* 67, 314-320.

BACABAC, R. G., SMIT, T. H., COWIN, S. C., VAN LOON, J. J. W. A., NIEUWSTADT, F. T. M., HEETHAAR, R. & KLEIN-NULEND, J. 2005. Dynamic shear stress in parallel-plate flow chambers. *Journal of Biomechanics,* 38, 159-167.

BACAKOVA, L., FILOVA, E., PARIZEK, M., RUML, T. & SVORCIK, V. 2011. Modulation of cell adhesion, proliferation and differentiation on materials designed for body implants. *Biotechnol Adv,* 29, 739-67.

BARFIELD, R. C., OTTO, M., HOUSTON, J., HOLLADAY, M., GEIGER, T., MARTIN, J., LEIMIG, T., GORDON, P., CHEN, X. & HANDGRETINGER, R. 2004. A one-step large-scale method for T- and B-cell depletion of mobilized PBSC for allogeneic transplantation. *Cytotherapy,* 6, 1-6.

BARR, T. L. & SEAL, S. 1995. Nature of the use of adventitious carbon as a binding energy standard. *Journal of Vacuum Science & Technology A,* 13, 1239-1246.

BASU, P., JOGLEKAR, G., RAI, S., SURESH, P. & VERNON, J. 2008. Analysis of Manufacturing Costs in Pharmaceutical Companies. *Journal of Pharmaceutical Innovation,* 3, 30-40.

BASU, S., CAMPBELL, H. M., DITTEL, B. N. & RAY, A. 2010. Purification of specific cell population by fluorescence activated cell sorting (FACS). *J Vis Exp*.

BELL, G. I. 1978. Models for the specific adhesion of cells to cells. *Science,* 200, 618-27.

BELL, G. I., DEMBO, M. & BONGRAND, P. 1984. Cell adhesion. Competition between nonspecific repulsion and specific bonding. *Biophysical Journal,* 45, 1051-1064.

BHATTACHARYYA, D., GANAPATHI, S., VISHWANATH, S., SUMMERS, M. & BUTTERFIELD, D. A. 1996. Immobilized Enzyme Reactions on Beads and Membranes. *In:* BUTTERFIELD, D. A. (ed.) *Biofunctional Membranes.* Springer US.

BIRD, R. B. S., W. E.; LIGHTFOOT, E. N. 2007. *Transport Phenomena*, John Wiley & Sons.

BISCHOFBERGER, M., IACOVACHE, I. & GISOU VAN DER GOOT, F. 2012. Pathogenic Pore-Forming Proteins: Function and Host Response. *Cell Host & Microbe,* 12, 266-275.

BLAZESKI, A., ZHU, R., HUNTER, D. W., WEINBERG, S. H., BOHELER, K. R., ZAMBIDIS, E. T. & TUNG, L. 2012. Electrophysiological and contractile function of cardiomyocytes derived from human embryonic stem cells. *Progress in biophysics and molecular biology,* 110, 178-195.

BORN, C., ZHANG, Z., AL-RUBEAI, M. & THOMAS, C. R. 1992. Estimation of disruption of animal cells by laminar shear stress. *Biotechnology and Bioengineering,* 40, 1004-1010.

BOSE, S. 2009. *A microvillus-based approach to model cell rolling.* Master of Science in Mechanical Engineering, Massachusettes Institute of Technology.

BRAAM, S. R., TERTOOLEN, L., VAN DE STOLPE, A., MEYER, T., PASSIER, R. & MUMMERY, C. L. 2010. Prediction of drug-induced cardiotoxicity using human embryonic stem cell-derived cardiomyocytes. *Stem Cell Res,* 4, 107-16.

BRANDENBERGER, R. B., S.; CAMPBELL, A.; FONG, T.; ROWLEY, J. 2011. Cell Therapy Bioprocessing. *BioProcess International*.

BRAUCHLE, E., THUDE, S., BRUCKER, S. Y. & SCHENKE-LAYLAND, K. 2014. Cell death stages in single apoptotic and necrotic cells monitored by Raman microspectroscopy. *Sci. Rep.,* 4.

BRAVERY, C. A., CARMEN, J., FONG, T., OPREA, W., HOOGENDOORN, K. H., WODA, J., BURGER, S. R., ROWLEY, J. A., BONYHADI, M. L. & VAN'T HOF, W. 2013. Potency assay development for cellular therapy products: an ISCT review of the requirements and experiences in the industry. *Cytotherapy,* 15, 9-19.

BRILLHART, K. L. & NGO, T. T. 1991. Use of microwell plates carrying hydrazide groups to enhance antibody immobilization in enzyme immunoassays. *J Immunol Methods,* 144, 19-25.

BRINDLEY, D. A. F., A. L.; BAPTISTA, R.; TIMMINS, N.; WALL, I.; BURE, K. 2014. Cell Therapy Bioprocessing Technologies and Indicators of Technological Convergence.

BROOKS, S. A. T., A. 1996. Flow past an array of cells that are adherent to the bottom plate of a flow channe. *Computers and Fluids*, 25, 741-757.

BROUSSEAU, L. C. & MALLOUK, T. E. 1997. Molecular Design of Intercalation-Based Sensors. 1. Ammonia Sensing with Quartz Crystal Microbalances Modified by Copper Biphenylbis(phosphonate) Thin Films. *Analytical Chemistry,* 69, 679-687.

BRYERS, D. 2005. Processes governing bacterial colonization of biomaterials. *In:* DEYSINE, M. (ed.) *Hernia Infections: Pathophysiology, Diagnosis, Treatment and Prevention.* New York, USA: Marcel Dekker, Inc. .

BURRIDGE, P. W., ANDERSON, D., PRIDDLE, H., BARBADILLO MUNOZ, M. D., CHAMBERLAIN, S., ALLEGRUCCI, C., YOUNG, L. E. & DENNING, C. 2007. Improved human embryonic stem cell embryoid body homogeneity and cardiomyocyte differentiation from a novel V-96 plate aggregation system highlights interline variability. *Stem Cells,* 25, 929-38.

CAO, J., NG, E., MCNAUGHTON, D., STANLEY, E., ELEFANTY, A., TOBIN, M. & HERAUD, P. 2013. The Characterisation of Pluripotent and Multipotent Stem Cells Using Fourier Transform Infrared Microspectroscopy. *International Journal of Molecular Sciences,* 14, 17453-17476.

CASTILHO, L. R., DECKWER, W.-D. & ANSPACH, F. B. 2000. Influence of matrix activation and polymer coating on the purification of human IgG with protein A affinity membranes. *Journal of Membrane Science,* 172, 269-277.

CHAN, J. W., HUSER, T. R., LANE, S. M., RUTLEDGE, J. C., TAYLOR, D. S., ZWERDLING, T. & LI, R. 2010. Single-Cell Raman Spectroscopy for the Non-Destructive, Non-Invasive Analysis of Cells and Cellular Components. Google Patents.

CHAN, J. W. & LIEU, D. 2013. Label-free identification of stem cell-differentiated cells. Google Patents.

CHANDRADOSS, S. D., HAAGSMA, A. C., LEE, Y. K., HWANG, J.-H., NAM, J.-M. & JOO, C. 2014. Surface Passivation for Single-molecule Protein Studies. e50549.

CHANG, K.-C. & HAMMER, D. A. 1996. Influence of Direction and Type of Applied Force on the Detachment of Macromolecularly-Bound Particles from Surfaces. *Langmuir,* 12, 2271-2282.

CHARCOSSET, C., SU, Z., KAROOR, S., DAUN, G. & COLTON, C. K. 1995. Protein A immunoaffinity hollow fiber membranes for immunoglobulin G purification: Experimental characterization. *Biotechnology and Bioengineering,* 48, 415-427.

CHEN, A., TING, S., SEOW, J., REUVENY, S. & OH, S. 2014. Considerations in designing systems for large scale production of human cardiomyocytes from pluripotent stem cells. *Stem Cell Res Ther,* 5, 12.

CHEN, A. K., CHEN, X., CHOO, A. B., REUVENY, S. & OH, S. K. 2011. Critical microcarrier properties affecting the expansion of undifferentiated human embryonic stem cells. *Stem Cell Res,* 7, 97-111.

CHISTI, Y. 2000. Animal-cell damage in sparged bioreactors. *Trends Biotechnol,* 18, 420-32.

CHOQUET, D., FELSENFELD, D. P. & SHEETZ, M. P. 1997. Extracellular matrix rigidity causes strengthening of integrin-cytoskeleton linkages. *Cell,* 88, 39-48.

CHRIST, K. V. 2011. Methods to measure the strength of cell adhesion to substrates. *In:* CARRÉ, A. M. (ed.) *Surface and Interfacial Aspects of Cell Adhesion.* CRC Press.

CHUCK, R. S. 2011. Methods and systems for identifying and isolating stem cells and for observing mitochondrial structure and distribution in living cells. Google Patents.

COLEMAN, P. L., WALKER, M. M., MILBRATH, D. S., STAUFFER, D. M., RASMUSSEN, J. K., R. KREPSKI, L. & HEILMANN, S. M. 1990. Immobilization of Protein A at high density on azlactone-functional polymeric beads and their use in affinity chromatography. *Journal of Chromatography A,* 512, 345-363.

COLLIER, R. 2009. Drug development cost estimates hard to swallow. *CMAJ,* 180, 279-80.

COLTON, C. K. P., M. J. 1996. *Selective cell separation*. United States patent application.

COZENS-ROBERTS, C., LAUFFENBURGER, D. A. & QUINN, J. A. 1990. Receptor-mediated cell attachment and detachment kinetics. I. Probabilistic model and analysis. *Biophysical Journal,* 58, 841-856.

CRIGLER, L., ROBEY, R. C., ASAWACHAICHARN, A., GAUPP, D. & PHINNEY, D. G. 2006. Human mesenchymal stem cell subpopulations express a variety of neuro-regulatory molecules and promote neuronal cell survival and neuritogenesis. *Experimental Neurology,* 198, 54-64.

CUVELIER, D., THERY, M., CHU, Y. S., DUFOUR, S., THIERY, J. P., BORNENS, M., NASSOY, P. & MAHADEVAN, L. 2007. The universal dynamics of cell spreading. *Curr Biol,* 17, 694-9.

DA COSTA, A. R., FANE, A. G. & WILEY, D. E. 1994. Spacer characterization and pressure drop modelling in spacer-filled channels for ultrafiltration. *Journal of Membrane Science,* 87, 79-98.

DAMMER, U., HEGNER, M., ANSELMETTI, D., WAGNER, P., DREIER, M., HUBER, W. & GUNTHERODT, H. J. 1996. Specific antigen/antibody interactions measured by force microscopy. *Biophys J,* 70, 2437-41.

DANCETTE, O. P., TABOUREAU, J.-L., TOURNIER, E., CHARCOSSET, C. & BLOND, P. 1999. Purification of immunoglobulins G by protein A/G affinity membrane chromatography. *Journal of Chromatography B: Biomedical Sciences and Applications,* 723, 61-68.

DAVIDSON, K. C. D., M.; PEBAY, A. 2008. Human embryonic stem cells: Key characteristics and main applications in disease research. *In:* SORENSEN, M., L. (ed.) *Stem Cell Applications in Diseases.* Nova Science Publishers.

DAVILA, M. L. & PAPAPETROU, E. P. 2014. CARs Move To the Fast Lane. *Mol Ther,* 22, 477-478.

DAVIS-SPROUL, J. M., MOORMAN, M. A., MCNEIL, R. M., SIMONETTI, D. W., HAMMILL, L. C. & CRAIG, S. 1999. Cd45 humain + et/ou fibroblaste + cellules mesenchymales humaines. Google Patents.

DAVIS, J. 2007. *Medicines from Animal Cell Culture*, John Wiley & Sons, Ltd.

DÉCAVÉ, E., GARRIVIER, D., BRÉCHET, Y., FOURCADE, B. & BRUCKERT, F. 2002. Shear Flow-Induced Detachment Kinetics of Dictyostelium discoideum Cells from Solid Substrate. *Biophysical Journal,* 82, 2383-2395.

DEFREES, S. A., PHILLIPS, L., GUO, L. & ZALIPSKY, S. 1996. Sialyl Lewis x Liposomes as a Multivalent Ligand and Inhibitor of E-Selectin Mediated Cellular Adhesion. *Journal of the American Chemical Society,* 118, 6101-6104.

DEMALI, K. A. 2004. Vinculin--a dynamic regulator of cell adhesion. *Trends Biochem Sci,* 29, 565-7.

DEMETRIUS, L. 2005. Of mice and men. *EMBO Reports,* 6, S39-S44.

DOMINICI, M., LE BLANC, K., MUELLER, I., SLAPER-CORTENBACH, I., MARINI, F., KRAUSE, D., DEANS, R., KEATING, A., PROCKOP, D. & HORWITZ, E. 2006. Minimal criteria for defining multipotent mesenchymal stromal cells. The International Society for Cellular Therapy position statement. *Cytotherapy,* 8, 315-7.

DONATI, G. P., R. 1997. Scale up of chemical reactors. *Catalysis Today,* 34, 483-533.

DONG, C. & LEI, X. X. 2000. Biomechanics of cell rolling: shear flow, cell-surface adhesion, and cell deformability. *J Biomech,* 33, 35-43.

DOS SANTOS, F., ANDRADE, P. Z., EIBES, G., DA SILVA, C. L. & CABRAL, J. M. 2011. Ex vivo expansion of human mesenchymal stem cells on microcarriers. *Methods Mol Biol,* 698, 189-98.

DREWS, A. 2010. Membrane fouling in membrane bioreactors—Characterisation, contradictions, cause and cures. *Journal of Membrane Science,* 363, 1-28.

DUDA, G. N., WINKLER, T., MATZIOLIS, G., VON, R. P. & PERKA, C. 2013. Skeletal muscle regeneration using mesenchymal stem cells. Google Patents.

EBNER, A. D., RITTER, J. A. & PLOEHN, H. J. 1997. Feasibility and limitations of nanolevel high gradient magnetic separation. *Separation and Purification Technology,* 11, 199-210.

EBNESAJJAD, S. E., C. 2006. *Surface Treatment of Materials for Adhesive Bonding*, Elselvier.

EDMONSON, P. J., HUNT, W. D. & STUBBS, D. D. 2010. Acoustic wave biosensor for the detection and identification of characteristic signaling molecules in a biological medium. Google Patents.

EIBL, R. E., D; PÖRTNER, R. 2009. *Mammalian cell culture technology: an emerging field*, Springer.

ENGLER, A. J., CHAN, M., BOETTIGER, D. & SCHWARZBAUER, J. E. 2009. A novel mode of cell detachment from fibrillar fibronectin matrix under shear. *J Cell Sci,* 122, 1647-53.

EVANS, E., LEUNG, A., HEINRICH, V. & ZHU, C. 2004. Mechanical switching and coupling between two dissociation pathways in a P-selectin adhesion bond. *Proceedings of the National Academy of Sciences of the United States of America,* 101, 11281-11286.

FAIR, J. R. 1984. Liquid-Solid Systems. *In:* PERRY, R. H. G., D. (ed.) *Perry's Chemical Engineering Handbook.* 6 ed. New York, USA: McGraw-Hill International.

FAN, X., WHITE, I. M., SHOPOVA, S. I., ZHU, H., SUTER, J. D. & SUN, Y. 2008. Sensitive optical biosensors for unlabeled targets: a review. *Anal Chim Acta,* 620, 8-26.

FIESER, L. F. W., K. L. 1987. *Organic Experiments,* Toronto, D. C. Heath and Co.

FIRER, M. A. 2001. Efficient elution of functional proteins in affinity chromatography. *J Biochem Biophys Methods,* 49, 433-42.

FONG, C. Y., PEH, G. S., GAUTHAMAN, K. & BONGSO, A. 2009. Separation of SSEA-4 and TRA-1-60 labelled undifferentiated human embryonic stem cells from a heterogeneous cell population using magnetic-activated cell sorting (MACS) and fluorescence-activated cell sorting (FACS). *Stem Cell Rev,* 5, 72-80.

FOSTER, J. S. & GRUMMITT, D. W. 2014. Particle manipulation system with cytometric capability. Google Patents.

FOSTER, J. S., GRUMMITT, D. W., HARLEY, J. C., LINTON, J. P. & SPONG, J. K. 2014. Cartridge for MEMS particle sorting system. Google Patents.

FREEMAN, W. H. 2000. Molecular Cell Biology. *In:* LODISH, H. B., A.; ZIPURSKY, S. L. (ed.) *Cell-Cell Adhesion and Communication.* New York.

FUKUDA, H., TAKAHASHI, J., WATANABE, K., HAYASHI, H., MORIZANE, A., KOYANAGI, M., SASAI, Y. & HASHIMOTO, N. 2006. Fluorescence-activated cell sorting-based purification of embryonic stem cell-derived neural precursors averts tumor formation after transplantation. *Stem Cells,* 24, 763-71.

FUNK, C., DIETRICH, P. M., GROSS, T., MIN, H., UNGER, W. E. S. & WEIGEL, W. 2012. Epoxy-functionalized surfaces for microarray applications: surface chemical analysis and fluorescence labeling of surface species. *Surface and Interface Analysis,* 44, 890-894.

GALLANT, N. D., MICHAEL, K. E. & GARCÍA, A. J. 2005. Cell Adhesion Strengthening: Contributions of Adhesive Area, Integrin Binding, and Focal Adhesion Assembly. *Molecular Biology of the Cell,* 16, 4329-4340.

GAO, X. M., H. 2006. Surface functionalization for biomedical applications. *In:* BLITZ, J. (ed.) *Surface Chemistry in Biomedical and Environmental Science.* The Netherlands: Springer.

GHOSH, R. 2002. Protein separation using membrane chromatography: opportunities and challenges. *Journal of Chromatography A,* 952, 13-27.

GINALDI, L. D. M., M.; MATUTES, E.; FARAHAT, N.; MORILLA, R.; CATOVSKY, D. 1998. Levels of expression of CD19 and CD20 in chronic B cell leukaemias. *Journal of Clinical Pathology,* 51, 364-369.

GIZELI, E. & SAITAKIS, M. 2009. Analysing the binding of cell membrane bound molecules. Google Patents.

GOLDMAN, A. J., COX, R. G. & BRENNER, H. 1967. Slow viscous motion of a sphere parallel to a plane wall—II Couette flow. *Chemical Engineering Science,* 22, 653-660.

GOSTJEVA, E. V. & THILLY, W. G. 2010. Methods for identifying stem cells by detecting fluorescence of cells and syncytia. Google Patents.

GRANGER, J., DODDS, J. & MIDOUX, N. 1989. Laminar flow in channels with porous walls. *The Chemical Engineering Journal,* 42, 193-204.

GRATWOHL, A. B., H.; ALJURF, M.; PASQUINI, M. C.; BOUZAS, L. F.; YOSHIMI, A.; SZER, J.; LIPTON, J.; SCHWENDENER, A.; GRATWOHL, M.; FRAUENDORFER, K.; NIEDERWIESER, D.; HOROWITZ, M.; KODERA, Y. 2010. Hematopoietic stem cell transplantation: a global perspective. *JAMA,* 303, 1617-24.

GRONEMEYER, P. D., R.; STRUBE , J. 2014. Trends in Upstream and Downstream Process Development for Antibody Manufacturing. *Bioengineering,* 1, 188-212.

GRUTZKAU, A. & RADBRUCH, A. 2010. Small but mighty: how the MACS-technology based on nanosized superparamagnetic particles has helped to analyze the immune system within the last 20 years. *Cytometry A,* 77, 643-7.

GUARDIA, M. J. H., W. 1999. *Encyclopedia of Bioprocess Technology: Fermentation, Biocatalysis and Bioseparation*, John Wiley & Sons.

GUPTA, P. K., DAS, A. K., CHULLIKANA, A. & MAJUMDAR, A. S. 2012. Mesenchymal stem cells for cartilage repair in osteoarthritis. *Stem Cell Res Ther,* 3, 25.

GUTIERREZ-ARANDA, I., RAMOS-MEJIA, V., BUENO, C., MUNOZ-LOPEZ, M., REAL, P. J., MÁCIA, A., SANCHEZ, L., LIGERO, G., GARCIA-PAREZ, J. L. & MENENDEZ, P. 2010. Human Induced Pluripotent Stem Cells Develop Teratoma More Efficiently and Faster Than Human Embryonic Stem Cells Regardless the Site of Injection. *STEM CELLS,* 28, 1568-1570.

HAHN, R., BAUERHANSL, P., SHIMAHARA, K., WIZNIEWSKI, C., TSCHELIESSNIG, A. & JUNGBAUER, A. 2005. Comparison of protein A affinity sorbents: II. Mass transfer properties. *Journal of Chromatography A,* 1093, 98-110.

HAHN, R., SCHLEGEL, R. & JUNGBAUER, A. 2003. Comparison of protein A affinity sorbents. *J Chromatogr B Analyt Technol Biomed Life Sci,* 790, 35-51.

HAMADA, S. & FUJITA, S. 1983. DAPI staining improved for quantitative cytofluorometry. *Histochemistry,* 79, 219-226.

HANDGRETINGER, R., LANG, P., IHM, K., SCHUMM, M., GEISELHART, A., KOSCIELNIAK, E., HERO, B., KLINGEBIEL, T. & NIETHAMMER, D. 2002. Isolation and transplantation of highly purified autologous peripheral CD34(+) progenitor cells: purging efficacy, hematopoietic reconstitution and long-term outcome in children with high-risk neuroblastoma. *Bone Marrow Transplant,* 29, 731-6.

HANSON, M. A., GE, X., KOSTOV, Y., BRORSON, K. A., MOREIRA, A. R. & RAO, G. 2007. Comparisons of optical pH and dissolved oxygen sensors with traditional electrochemical probes during mammalian cell culture. *Biotechnol Bioeng,* 97, 833-41.

HARRISON, R. A. & VICKERS, S. E. 1990. Use of fluorescent probes to assess membrane integrity in mammalian spermatozoa. *J Reprod Fertil,* 88, 343-52.

HASS, R., KASPER, C., BOHM, S. & JACOBS, R. 2011. Different populations and sources of human mesenchymal stem cells (MSC): A comparison of adult and neonatal tissue-derived MSC. *Cell Commun Signal,* 9, 12.

HENRY, S. D. 2009. Materials and Coatings for Medical Devices: Cardiovascular. The Materials Information Society.

HERAUD, P., NG, E. S., CAINE, S., YU, Q. C., HIRST, C., MAYBERRY, R., BRUCE, A., WOOD, B. R., MCNAUGHTON, D., STANLEY, E. G. & ELEFANTY, A. G. 2010. Fourier transform infrared microspectroscopy identifies early lineage commitment in differentiating human embryonic stem cells. *Stem Cell Res,* 4, 140-7.

HERDRICH, B. J., LIND, R. C. & LIECHTY, K. W. 2008. Multipotent adult progenitor cells: their role in wound healing and the treatment of dermal wounds. *Cytotherapy,* 10, 543-50.

HERMANSON, G. 2008. *Bioconjugate Techniques*, Academic Press.

HERMANSON, G. M., A. K.; SMITH, P. K. 1992. *Immobilized affinity ligand techniques*, Academic Press.

HOLTON, O. D., 3RD & VICALVI, J. J., JR. 1991. Optimization of monoclonal antibody immobilization on hydrazide-preactivated hollow fiber membrane. *Biotechniques,* 11, 662-7.

HONG, S., LEE, D., ZHANG, H., ZHANG, J. Q., RESVICK, J. N., KHADEMHOSSEINI, A., KING, M. R., LANGER, R. & KARP, J. M. 2007. Covalent immobilization of p-selectin enhances cell rolling. *Langmuir,* 23, 12261-8.

HOURD, P., GINTY, P., CHANDRA, A. & WILLIAMS, D. J. 2014. Manufacturing models permitting roll out/scale out of clinically led autologous cell therapies: regulatory and scientific challenges for comparability. *Cytotherapy,* 16, 1033-1047.

HOWE, M. S. 2006. *Hydrodynamics and Sound*, Cambridge University Press.

HUNG, P.-S., KUO, Y.-C., CHEN, H.-G., CHIANG, H.-H. K. & LEE, O. K.-S. 2013. Detection of Osteogenic Differentiation by Differential Mineralized Matrix Production in Mesenchymal Stromal Cells by Raman Spectroscopy. *PLoS ONE,* 8, e65438.

INGBER, D. E. 2006. Cellular mechanotransduction: putting all the pieces together again. *FASEB J,* 20, 811-27.

INGBER, D. W., N.; STAMENOVIC, D. 2014. Tensegrity, cellular biophysics, and the mechanics of living systems. *Reports on Progress in Physics,* 77.

ITANO, N., OKAMOTO, S., ZHANG, D., LIPTON, S. A. & RUOSLAHTI, E. 2003. Cell spreading controls endoplasmic and nuclear calcium: a physical gene regulation pathway from the cell surface to the nucleus. *Proc Natl Acad Sci U S A,* 100, 5181-6.

JAALOUK, D. E. & LAMMERDING, J. 2009. Mechanotransduction gone awry. *Nat Rev Mol Cell Biol,* 10, 63-73.

JIA, L., YANG, L., ZOU, H., ZHANG, Y., ZHAO, J., FAN, C. & SHA, L. 1999. Protein A tangential flow affinity membrane cartridge for extracorporeal immunoadsorption therapy. *Biomed Chromatogr,* 13, 472-7.

JING, D., PARIKH, A. & TZANAKAKIS, E. S. 2010. Cardiac cell generation from encapsulated embryonic stem cells in static and scalable culture systems. *Cell Transplant,* 19, 1397-412.

JOHANSSON, I. 1997. *IgG separation medium*. Germany patent application.

JONES, E. A., KINSEY, S. E., ENGLISH, A., JONES, R. A., STRASZYNSKI, L., MEREDITH, D. M., MARKHAM, A. F., JACK, A., EMERY, P. & MCGONAGLE, D. 2002. Isolation and characterization of bone marrow multipotential mesenchymal progenitor cells. *Arthritis Rheum,* 46, 3349-60.

JUNGBAUER, A. & HAHN, R. 2004. Monoliths for fast bioseparation and bioconversion and their applications in biotechnology. *J Sep Sci,* 27, 767-78.

JUOPPERI, T. A., SCHULER, W., YUAN, X., COLLECTOR, M. I., DANG, C. V. & SHARKIS, S. J. 2007. Isolation of bone marrow-derived stem cells using density-gradient separation. *Exp Hematol,* 35, 335-41.

KAPLAN, A. A. & HALLEY, S. E. 1990. Plasma exchange with a rotating filter. *Kidney Int,* 38, 160-166.

KASZA, K. E., ROWAT, A. C., LIU, J., ANGELINI, T. E., BRANGWYNNE, C. P., KOENDERINK, G. H. & WEITZ, D. A. 2007. The cell as a material. *Current Opinion in Cell Biology,* 19, 101-107.

KEATING, A. 2012. Mesenchymal stromal cells: new directions. *Cell Stem Cell,* 10, 709-16.

KELLEY, B. 2007. Very large scale monoclonal antibody purification: the case for conventional unit operations. *Biotechnol Prog,* 23, 995-1008.

KEMPKEN, R., PREIßMANN, A. & BERTHOLD, W. 1995. Clarification of animal cell cultures on a large scale by continuous centrifugation. *Journal of Industrial Microbiology,* 14, 52-57.

KIM, N. & CHO, S.-G. 2013. Clinical applications of mesenchymal stem cells. *The Korean Journal of Internal Medicine,* 28, 387-402.

KING, J. A. & MILLER, W. M. 2007. Bioreactor development for stem cell expansion and controlled differentiation. *Current Opinion in Chemical Biology,* 11, 394-398.

KISAALITA, W. S. 1992. Biosensor standards requirements. *Biosensors and Bioelectronics,* 7, 613-620.

KLEIN, E. E., E.; THEIMER, F.; YEAGER, D. 1994. Chitosan Modified Sulfonated Poly(Ethersulfone) as a Support for Affinity Separations. *Journal of Membrane Science,* 95, 199-204.

KRETZMER, G. & SCHÜGERL, K. 1991. Response of mammalian cells to shear stress. *Applied Microbiology and Biotechnology,* 34, 613-616.

KROEMER, G., EL-DEIRY, W. S., GOLSTEIN, P., PETER, M. E., VAUX, D., VANDENABEELE, P., ZHIVOTOVSKY, B., BLAGOSKLONNY, M. V., MALORNI, W., KNIGHT, R. A., PIACENTINI, M., NAGATA, S. & MELINO, G. 2005. Classification of cell death: recommendations of the Nomenclature Committee on Cell Death. *Cell Death Differ,* 12, 1463-1467.

KROEMER, G., GALLUZZI, L., VANDENABEELE, P., ABRAMS, J., ALNEMRI, E. S., BAEHRECKE, E. H., BLAGOSKLONNY, M. V., EL-DEIRY, W. S., GOLSTEIN, P., GREEN, D. R., HENGARTNER, M., KNIGHT, R. A., KUMAR, S., LIPTON, S. A., MALORNI, W., NUNEZ, G., PETER, M. E., TSCHOPP, J., YUAN, J., PIACENTINI, M., ZHIVOTOVSKY, B. & MELINO, G. 2009. Classification of cell death: recommendations of the Nomenclature Committee on Cell Death 2009. *Cell Death Differ,* 16, 3-11.

KUMAR, A., PLIEVA, F. M., GALAEV, I. Y. & MATTIASSON, B. 2003. Affinity fractionation of lymphocytes using a monolithic cryogel. *J Immunol Methods,* 283, 185-94.

KUMAR, A. & SRIVASTAVA, A. 2010. Cell separation using cryogel-based affinity chromatography. *Nat Protoc,* 5, 1737-47.

KUMAR, K. A., A.; ASTER, J. 2013. *The Morphology of Cell and Tissue Injury*.

KUO, S. C. & LAUFFENBURGER, D. A. 1993. Relationship between receptor/ligand binding affinity and adhesion strength. *Biophys J,* 65, 2191-200.

KUROSAWA, H. 2007. Methods for inducing embryoid body formation: in vitro differentiation system of embryonic stem cells. *J Biosci Bioeng,* 103, 389-98.

KURTH, D. G. & BEIN, T. 1993. Surface reactions on thin layers of silane coupling agents. *Langmuir,* 9, 2965-2973.

LARA, A. R., GALINDO, E., RAMIREZ, O. T. & PALOMARES, L. A. 2006a. Living with heterogeneities in bioreactors: understanding the effects of environmental gradients on cells. *Mol Biotechnol,* 34, 355-81.

LARA, O., TONG, X., ZBOROWSKI, M., FARAG, S. S. & CHALMERS, J. J. 2006b. Comparison of two immunomagnetic separation technologies to deplete T cells from human blood samples. *Biotechnol Bioeng,* 94, 66-80.

LE BLANC, K., FRASSONI, F., BALL, L., LOCATELLI, F., ROELOFS, H., LEWIS, I., LANINO, E., SUNDBERG, B., BERNARDO, M. E., REMBERGER, M., DINI, G., EGELER, R. M., BACIGALUPO, A., FIBBE, W. & RINGDEN, O. 2008. Mesenchymal stem cells for treatment of steroid-resistant, severe, acute graft-versus-host disease: a phase II study. *Lancet,* 371, 1579-86.

LEBKOWSKI, J. 2011. *Geron's Embryonic Stem Cell Clinical Trial for Spinal Cord Injury* [Online]. Available: https://www.youtube.com/watch?v=c46ANweHGNw 2014].

LEBLEBICI, P., LEBLEBICI, M. E., FERREIRA-DA-SILVA, F., RODRIGUES, A. E. & PAIS, L. S. 2014. Separation of human immunoglobulin G subclasses on a protein A monolith column. *J Chromatogr B Analyt Technol Biomed Life Sci,* 962, 89-93.

LECINA, M., TING, S., CHOO, A., REUVENY, S. & OH, S. 2010. Scalable platform for human embryonic stem cell differentiation to cardiomyocytes in suspended microcarrier cultures. *Tissue Eng Part C Methods,* 16, 1609-19.

LEE, C.-F., YAN, T.-R. & WANG, T.-H. 2012. Long-term monitoring of Caco-2 cell growth process using a QCM-cell system. *Sensors and Actuators B: Chemical,* 166–167, 165-171.

LEE, D. W., KOCHENDERFER, J. N., STETLER-STEVENSON, M., CUI, Y. K., DELBROOK, C., FELDMAN, S. A., FRY, T. J., ORENTAS, R., SABATINO, M., SHAH, N. N., STEINBERG, S. M., STRONCEK, D., TSCHERNIA, N., YUAN, C., ZHANG, H., ZHANG, L., ROSENBERG, S. A., WAYNE, A. S. & MACKALL, C. L. 2013. T cells expressing CD19 chimeric antigen receptors for acute lymphoblastic leukaemia in children and young adults: a phase 1 dose-escalation trial. *The Lancet*.

LI, H. & FU, X. 2012. Mechanisms of action of mesenchymal stem cells in cutaneous wound repair and regeneration. *Cell Tissue Res,* 348, 371-7.

LI, Q., ZHANG, X., PENG, Y., CHAI, H., XU, Y., WEI, J., REN, X., WANG, X., LIU, W., CHEN, M. & HUANG, D. 2012. COMPARISON OF THE SORTING EFFICIENCY AND INFLUENCE ON CELL FUNCTION BETWEEN THE STERILE FLOW CYTOMETRY AND IMMUNOMAGNETIC BEAD PURIFICATION METHODS. *Preparative Biochemistry and Biotechnology,* 43, 197-206.

LIPOWSKY, H. H., KOVALCHECK, S. & ZWEIFACH, B. W. 1978. The distribution of blood rheological parameters in the microvasculature of cat mesentery. *Circ Res,* 43, 738-49.

LIU, C. & BAI, R. 2006. Preparing highly porous chitosan/cellulose acetate blend hollow fibers as adsorptive membranes: Effect of polymer concentrations and coagulant compositions. *Journal of Membrane Science,* 279, 336-346.

LIU, M., LIU, N., ZANG, R., LI, Y. & YANG, S. T. 2013. Engineering stem cell niches in bioreactors. *World J Stem Cells,* 5, 124-35.

LUCKLUM, R. & HAUPTMANN, P. 2006. Acoustic microsensors--the challenge behind microgravimetry. *Anal Bioanal Chem,* 384, 667-82.

LUTTROPP, D. K., B.; NEUBAUER, M.; BAER, P. 2014. *Hybrid bioartificial kidney*. Sweden patent application.

MA, S., XIE, N., LI, W., YUAN, B., SHI, Y. & WANG, Y. 2014. Immunobiology of mesenchymal stem cells. *Cell Death Differ,* 21, 216-225.

MABUCHI, Y. M., S.; HARADA, S.; NIIBE, K.; OKANO, H.; MATSUZAKI, Y. 2013. LNGFR+THY-1+VCAM-1hi+ Cells Reveal Functionally Distinct Subpopulations in Mesenchymal Stem Cells. *Stem Cell Reports,* 1, 152-165.

MACMILLAN, M. L., BLAZAR, B. R., DEFOR, T. E. & WAGNER, J. E. 2009. Transplantation of ex-vivo culture-expanded parental haploidentical mesenchymal stem cells to promote engraftment in pediatric recipients of unrelated donor umbilical cord blood: results of a phase I-II clinical trial. *Bone Marrow Transplant,* 43, 447-54.

MAK, I. W. Y., EVANIEW, N. & GHERT, M. 2014. Lost in translation: animal models and clinical trials in cancer treatment. *American Journal of Translational Research,* 6, 114-118.

MALMSTRÖM, J., AGHELI, H., KINGSHOTT, P. & SUTHERLAND, D. S. 2007. Viscoelastic Modeling of Highly Hydrated Laminin Layers at Homogeneous and Nanostructured Surfaces: Quantification of Protein Layer Properties Using QCM-D and SPR. *Langmuir,* 23, 9760-9768.

MANDALAM, R. L., Y.; POWELL, S.; BRUNETTE, E.; LEBKOWSKI, J. 2005. HES cell-derived cellular product for therapeutic use. *In:* ODORICO, J. Z., S.; PEDERSEN, R. (ed.) *Human embryonic stem cells.* New York: Garland Science.

MANDRUSOV, E., HOUNG, A., KLEIN, E. & LEONARD, E. F. 1995. Membrane-based cell affinity chromatography to retrieve viable cells. *Biotechnol Prog,* 11, 208-13.

MARTIN-HENAO, G. A., PICON, M., AMILL, B., QUEROL, S., FERRA, C., GRANENA, A. & GARCIA, J. 2001. Combined positive and negative cell selection from allogeneic peripheral blood progenitor cells (PBPC) by use of immunomagnetic methods. *Bone Marrow Transplant,* 27, 683-7.

MARTIN, H. J., SCHULZ, K. H., BUMGARDNER, J. D. & WALTERS, K. B. 2007. XPS Study on the Use of 3-Aminopropyltriethoxysilane to Bond Chitosan to a Titanium Surface. *Langmuir,* 23, 6645-6651.

MARX, K., BRAUNHUT, S., ZHOU, T. & MONTRONE, A. 2003. Biosensor for use in the detection preferential particles in quartz crystal microbalance. Google Patents.

MASON, C. & DUNNILL, P. 2009. Quantities of cells used for regenerative medicine and some implications for clinicians and bioprocessors. *Regenerative Medicine,* 4, 153-157.

MASON, C. & HOARE, M. 2006. Regenerative medicine bioprocessing: the need to learn from the experience of other fields. *Regen Med,* 1, 615-23.

MASON, C., MCCALL, MARK J., CULME-SEYMOUR, EMILY J., SUTHASAN, S., EDWARDS-PARTON, S., BONFIGLIO, GREGORY A. & REEVE, BROCK C. 2012. The Global Cell Therapy Industry Continues to Rise during the Second and Third Quarters of 2012. *Cell Stem Cell,* 11, 735-739.

MATEO, C., FERNANDEZ-LORENTE, G., ABIAN, O., FERNANDEZ-LAFUENTE, R. & GUISAN, J. M. 2000. Multifunctional epoxy supports: a new tool to improve the covalent immobilization of proteins. The promotion of physical adsorptions of proteins on the supports before their covalent linkage. *Biomacromolecules,* 1, 739-45.

MATTIASSON, B. G., I.; KUMAR, A.; DAINIAK, M. 2011. *Process for absorption-based separation of bioparticles from an aqueous suspension*.

MAZIARZ, R., KOVACSOVICS, M., STREETER, P., DEANS, R. & HOF, W. V. 2012. Immunomodulatory properties of multipotent adult progenitor cells and uses thereof. Google Patents.

MAZUR, P. 1984. Freezing of living cells: mechanisms and implications. *Am J Physiol,* 247, C125-42.

MAZUR, P. 1988. Stopping biological time. The freezing of living cells. *Ann N Y Acad Sci,* 541, 514-31.

MCNEIL, P. L. & STEINHARDT, R. A. 2003. PLASMA MEMBRANE DISRUPTION: Repair, Prevention, Adaptation. *Annual Review of Cell and Developmental Biology,* 19, 697-731.

MEHTA, S., HERMAN, T., ROSS, H., IQBAL, K. & MCMAHON, J. 2011. Methods and systems for manipulating particles using a fluidized bed. Google Patents.

MENENDEZ, P., PEREZ-SIMON, J. A., MATEOS, M. V., CABALLERO, M. D., GONZALEZ, M., SAN-MIGUEL, J. F. & ORFAO, A. 2002. Influence of the different CD34+ and CD34- cell subsets infused on clinical outcome after non-myeloablative allogeneic peripheral blood transplantation from human leucocyte antigen-identical sibling donors. *Br J Haematol,* 119, 135-43.

MERYMAN, H. T. 2007. Cryopreservation of living cells: principles and practice. *Transfusion,* 47, 935-45.

METWALLI, E., HAINES, D., BECKER, O., CONZONE, S. & PANTANO, C. G. 2006. Surface characterizations of mono-, di-, and tri-aminosilane treated glass substrates. *J Colloid Interface Sci,* 298, 825-31.

MIKKOLA, H. K. A. & ORKIN, S. H. 2006. The journey of developing hematopoietic stem cells. *Development,* 133, 3733-3744.

MILLER, A. W. & ROBYT, J. F. 1983. Sodium cyanoborohydride in the immobilization of proteins to glutaraldehyde-activated aminoalkyl silica. *Biotechnology and Bioengineering,* 25, 2795-2800.

MILTENYI, S., MULLER, W., WEICHEL, W. & RADBRUCH, A. 1990. High gradient magnetic cell separation with MACS. *Cytometry,* 11, 231-8.

MINAMI, I., YAMADA, K., OTSUJI, T. G., YAMAMOTO, T., SHEN, Y., OTSUKA, S., KADOTA, S., MORONE, N., BARVE, M., ASAI, Y., TENKOVA-HEUSER, T., HEUSER, J. E., UESUGI, M., AIBA, K. & NAKATSUJI, N. 2012. A small molecule that promotes cardiac differentiation of human pluripotent stem cells under defined, cytokine- and xeno-free conditions. *Cell Rep,* 2, 1448-60.

MITCHELL, P. D., RATCLIFFE, E., HOURD, P., WILLIAMS, D. J. & THOMAS, R. J. 2014. A Quality-by-Design Approach to Risk Reduction and Optimization for hESC Cryopreservation Processes. *Tissue Eng Part C Methods*.

MOKS, T., ABRAHMSEN, L., NILSSON, B., HELLMAN, U., SJOQUIST, J. & UHLEN, M. 1986. Staphylococcal protein A consists of five IgG-binding domains. *Eur J Biochem,* 156, 637-43.

MOREHEAD, H. W., TALMADGE, K. W., O'SHANNESSY, D. J. & SIEBERT, C. J. 1991. Optimization of oxidation of glycoproteins: An assay for predicting coupling to hydrazide chromatographic supports. *Journal of Chromatography A,* 587, 171-176.

MOSER, A. C. & HAGE, D. S. 2010. Immunoaffinity chromatography: an introduction to applications and recent developments. *Bioanalysis,* 2, 769-90.

MULHALL, H., PATEL, M., ALQAHTANI, K., MASON, C., LEWIS, M. P. & WALL, I. 2011. Effect of capillary shear stress on recovery and osteogenic differentiation of muscle-derived precursor cell populations. *J Tissue Eng Regen Med,* 5, 629-35.

MUMMERY, C., WARD-VAN OOSTWAARD, D., DOEVENDANS, P., SPIJKER, R., VAN DEN BRINK, S., HASSINK, R., VAN DER HEYDEN, M., OPTHOF, T., PERA, M., DE LA RIVIERE, A. B., PASSIER, R. & TERTOOLEN, L. 2003. Differentiation of human embryonic stem cells to cardiomyocytes: role of coculture with visceral endoderm-like cells. *Circulation,* 107, 2733-40.

MURRY, C. E. & KELLER, G. 2008. Differentiation of Embryonic Stem Cells to Clinically Relevant Populations: Lessons from Embryonic Development. *Cell,* 132, 661-680.

MYERS, T. G. 2002. Modeling laminar sheet flow over rough surfaces. *Water Resources Research,* 38, 1230.

NESS, K. K., BHATIA, S., BAKER, K. S., FRANCISCO, L., CARTER, A., FORMAN, S. J., ROBISON, L. L., ROSENTHAL, J. & GURNEY, J. G. 2005. Performance limitations and participation restrictions among childhood cancer survivors treated with hematopoietic stem cell transplantation: the bone marrow transplant survivor study. *Arch Pediatr Adolesc Med,* 159, 706-13.

NIENOW, A. W., RAFIQ, Q. A., COOPMAN, K. & HEWITT, C. J. 2014. A potentially scalable method for the harvesting of hMSCs from microcarriers. *Biochemical Engineering Journal,* 85, 79-88.

NILEBACK, E., FEUZ, L., UDDENBERG, H., VALIOKAS, R. & SVEDHEM, S. 2011. Characterization and application of a surface modification designed for QCM-D studies of biotinylated biomolecules. *Biosens Bioelectron,* 28, 407-13.

NILSON, B. H., LOGDBERG, L., KASTERN, W., BJORCK, L. & AKERSTROM, B. 1993. Purification of antibodies using protein L-binding framework structures in the light chain variable domain. *J Immunol Methods,* 164, 33-40.

NISTOR, G. I. & KEIRSTEAD, H. S. 2004. Oligodendrocytes derived from human embryonic stem cells for remyelination and treatment of spinal cord injury. Google Patents.

NIWA, H. 2006. Mechanisms of Stem Cell Self-Renewal. *In:* LANZA, R. (ed.) *Essentials of Stem Cell Biology.* Burlington, USA: Elselvier Academic Press.

NORDON, R. E. & CRAIG, S. 2007. Hollow-fibre affinity cell separation. *Adv Biochem Eng Biotechnol,* 106, 129-50.

NORDON, R. E., HAYLOCK, D. N., GAUDRY, L. & SCHINDHELM, K. 1996. Hollow-fibre affinity cell separation system for CD34+ cell enrichment. *Cytometry,* 24, 340-7.

NORDON, R. E. & SCHINDHELM, K. 1997. Design of hollow fiber modules for uniform shear elution affinity cell separation. *Artif Organs,* 21, 107-15.

NORDON, R. E., SHU, A., CAMACHO, F. & MILTHORPE, B. K. 2004. Hollow-fiber assay for ligand-mediated cell adhesion. *Cytometry Part A,* 57A, 39-44.

NORDON, R. E. M., K. M.; SCHINDHELM, K.; SLOWIACZEK, P. R. 1994. An Experimental Model of Affinity Cell Separation. *Cytometry,* 16, 25-33.

NSIAH, B. A., AHSAN, T., GRIFFITHS, S., COOKE, M., NEREM, R. M. & MCDEVITT, T. C. 2014. Fluid shear stress pre-conditioning promotes endothelial morphogenesis of embryonic stem cells within embryoid bodies. *Tissue Eng Part A,* 20, 954-65.

O'GARRA, A. & VIEIRA, P. 2004. Regulatory T cells and mechanisms of immune system control. *Nat Med,* 10, 801-805.

OHASHI, K., TASHIRO, K., KUSHIYA, F., MATSUMOTO, T., YOSHIDA, S., ENDO, M., HORIO, T., OZAWA, K. & SAKAI, K. 1988. Rotation-induced Taylor vortex enhances filtrate flux in plasma separation. *ASAIO Trans,* 34, 300-7.

OHLSON, S., BERGSTRÖM, M., PÅHLSSON, P. & LUNDBLAD, A. 1997. Use of monoclonal antibodies for weak affinity chromatography. *Journal of Chromatography A,* 758, 199-208.

PAN, Y., GUO, M., NIE, Z., HUANG, Y., PAN, C., ZENG, K., ZHANG, Y. & YAO, S. 2010. Selective collection and detection of leukemia cells on a magnet-quartz crystal microbalance system using aptamer-conjugated magnetic beads. *Biosens Bioelectron,* 25, 1609-14.

PANICKER, M. M., MENON, R., THANGASELVAM, M. & MUKHERJEE, O. 2014. A method to identify and isolate pluripotent stem cells using endogenous blue fluorescence. Google Patents.

PAS83 2012. PAS83:2012. *Developing human cells for clinical applications in the European Union and the United States of America – Guide.* British Standards Institute.

PAS93 2011. PAS93. *Characterization of human cells for clinical applications.* British Standards Institute.

PATEL, S. K. J., R. N.; KHATIK, N. 2008. Effect of grafting technique on peel strength, contact angle, particle size and viscosity of butyl acrylate-PUD hybrid adhesives for plastic laminates. *In:* MITTAL, K. L. (ed.) *Contact angle, Wettability and Adhesion.* The Netherlands: Brill Academic Publishers.

PATTASSERIL, J. V., H.; LOCK, L.; ROWLEY, J. A. 2013. Downstream Technology Landscape for Large-Scale Therapeutic Cell Processing. *BioProcess International*.

PFAUNMILLER, E. L., PAULEMOND, M. L., DUPPER, C. M. & HAGE, D. S. 2013. Affinity monolith chromatography: a review of principles and recent analytical applications. *Anal Bioanal Chem,* 405, 2133-45.

PIERRES, A., EYMERIC, P., BALOCHE, E., TOUCHARD, D., BENOLIEL, A. M. & BONGRAND, P. 2003. Cell membrane alignment along adhesive surfaces: contribution of active and passive cell processes. *Biophys J,* 84, 2058-70.

PIJANKA, J. K., KUMAR, D., DALE, T., YOUSEF, I., PARKES, G., UNTEREINER, V., YANG, Y., DUMAS, P., COLLINS, D., MANFAIT, M., SOCKALINGUM, G. D., FORSYTH, N. R. & SULE-SUSO, J. 2010. Vibrational spectroscopy differentiates between multipotent and pluripotent stem cells. *Analyst,* 135, 3126-32.

PINXTEREN, J. A. M. & CRAEYE, D. 2012. Expansion of Stem Cells in Hollow Fiber Bioreactors. Google Patents.

PITTNER, F. 2002. Immobilized Biomolecules in Bioanalysis. *In:* SCHALKHAMMER, T., G., M. (ed.) *Analytical Biotechnology.* Springer.

POMIANEK, M. J. 1998. *Selective cell separation utilizing porous immunoaffinity membranes.* PhD, Massachusetts Institute of Technology.

PRASAD, K. 2012. *Downstream Process Technology: A New Horizon in Biotechnology,* Delhi, PHI Learning Private Limited.

PROCKOP, D. J. 2010. Defining the Probability that a Cell Therapy Will Produce a Malignancy. *Mol Ther,* 18, 1249-1250.

PROWSE, A. B. J., TIMMINS, N. E., YAU, T. M., LI, R.-K., WEISEL, R. D., KELLER, G. & ZANDSTRA, P. W. 2014. Transforming the promise of pluripotent stem cell derived cardiomyocytes to a therapy: Challenges and solutions for clinical trials. *Canadian Journal of Cardiology*.

QUINTANILLA, R. H., JR. 2013. Cellular characterization of human pluripotent stem cells. *Methods Mol Biol,* 997, 179-90.

RAFIQ, Q., BROSNAN, K., COOPMAN, K., NIENOW, A. & HEWITT, C. 2013. Culture of human mesenchymal stem cells on microcarriers in a 5 l stirred-tank bioreactor. *Biotechnology Letters,* 35, 1233-1245.

RAND, R. 1964. Mechanical Properties of the Red Cell Membrane II. Viscoelastic Breakdown of the Membrane. *Biophysical Journal,* 4, 303-316.

REDEPENNING, J., SCHLESINGER, T. K., MECHALKE, E. J., PULEO, D. A. & BIZIOS, R. 1993. Osteoblast attachment monitored with a quartz crystal microbalance. *Anal Chem,* 65, 3378-81.

RESCH-GENGER, U., HOFFMANN, K. & HOFFMANN, A. 2008. Standardization of fluorescence measurements: criteria for the choice of suitable standards and approaches to fit-for-purpose calibration tools. *Ann N Y Acad Sci,* 1130, 35-43.

REVERBERI, R. & REVERBERI, L. 2007. Factors affecting the antigen-antibody reaction. *Blood Transfusion,* 5, 227-240.

REYES, P. I., DUAN, Z., LU, Y., KHAVULYA, D. & BOUSTANY, N. 2013. ZnO nanostructure-modified QCM for dynamic monitoring of cell adhesion and proliferation. *Biosens Bioelectron,* 41, 84-9.

RINGHOFFER, M., WIESNETH, M., VON HARSDORF, S., SCHLENK, R. F., SCHMITT, A., REINHARDT, P. P., MOESSNER, M., GRIMMINGER, W., MERTENS, T., RESKE, S. N., DÖHNER, H. & BUNJES, D. 2004. CD34+ cell selection of peripheral blood progenitor cells using the CliniMACS device for allogeneic transplantation: clinical results in 102 patients. *British Journal of Haematology,* 126, 527-535.

ROTHFUS, R. R., ARCHER, D. H., KLIMAS, I. C. & SIKCHI, K. G. 1957. Simplified flow calculations for tubes and parallel plates. *AIChE Journal,* 3, 208-212.

ROWLAND, S. A., SHALABY, S. W., LATOUR, R. A. Effectiveness of cleaning surgical implants: Quantitative analysis of contaminant removal. Journal of applied biomaterials, 6, 1-7.

ROWLEY, A. J. How Today's Manufacturing Innovations can be Leveraged by Tomorrow's Living Cell-Based Products. IBC, 2014 Arlington, VA, USA.

ROWLEY, J., PATTASSERIL, J. & LOCK, L. T. 2013. Scalable process for therapeutic cell concentration and residual clearance. Google Patents.

ROWLEY, J., PATTASSERIL, J. & MOHAMED, A. 2012. High yield method and apparatus for volume reduction and washing of therapeutic cells using tangential flow filtration. Google Patents.

ROWLEY, J. A. A., E.; CAMPBELL, A.; OH, S. 2012. Meeting Lot-Size Challenges of Manufacturing Adherent Cells for Therapy. *BioProcess International*, 16 - 22.

RUBBI, C. P., PATEL, D. & RICKWOOD, D. 1993. Evidence of surface antigen detachment during incubation of cells with immunomagnetic beads. *J Immunol Methods,* 166, 233-41.

SAGVOLDEN, G., GIAEVER, I., PETTERSEN, E. O. & FEDER, J. 1999. Cell adhesion force microscopy. *Proceedings of the National Academy of Sciences,* 96, 471-476.

SANDT, C., FÉRAUD, O., OUDRHIRI, N., BONNET, M. L., MEUNIER, M. C., VALOGNE, Y., BERTRAND, A., RAPHAËL, M., GRISCELLI, F., TURHAN, A. G., DUMAS, P. & BENNACEUR-GRISCELLI, A. 2012. Identification of Spectral Modifications Occurring during Reprogramming of Somatic Cells. *PLoS ONE,* 7, e30743.

SATHANANTHAN, A. H. & TROUNSON, A. 2005. Human embryonic stem cells and their spontaneous differentiation. *Ital J Anat Embryol,* 110, 151-7.

SATO, J., KAWANO, Y., TAKAUE, Y., HIRAO, A., MAKIMOTO, A., OKAMOTO, Y., ABE, T., KURODA, Y., SHIMOKAWA, T. & IWAI, A. 1995. Quantitative and qualitative comparative analysis of gradient-separated hematopoietic cells from cord blood and chemotherapy-mobilized peripheral blood. *STEM CELLS,* 13, 548-555.

SAUERBREY, G. 1959. Verwendung von Schwingquarzen zur Wägung dünner Schichten und zur Mikrowägung. *Zeitschrift für Physik,* 155, 206-222.

SCHELLER, F. W., HINTSCHE, R., PFEIFFER, D., SCHUBERT, F., RIEDEL, K. & KINDERVATER, R. 1991. Biosensors: Fundamentals, applications and trends. *Sensors and Actuators B: Chemical,* 4, 197-206.

SCHRIEBL, K., LIM, S., CHOO, A., TSCHELIESSNIG, A. & JUNGBAUER, A. 2010a. Stem cell separation: A bottleneck in stem cell therapy. *Biotechnology Journal,* 5, 50-61.

SCHRIEBL, K., LIM, S., CHOO, A., TSCHELIESSNIG, A. & JUNGBAUER, A. 2010b. Stem cell separation: a bottleneck in stem cell therapy. *Biotechnol J,* 5, 50-61.

SCHRIEBL, K., SATIANEGARA, G., HWANG, A., TAN, H. L., FONG, W. J., YANG, H. H., JUNGBAUER, A. & CHOO, A. 2012. Selective removal of undifferentiated human embryonic stem cells using magnetic activated cell sorting followed by a cytotoxic antibody. *Tissue Eng Part A,* 18, 899-909.

SCHWARTZ, S. D., HUBSCHMAN, J.-P., HEILWELL, G., FRANCO-CARDENAS, V., PAN, C. K., OSTRICK, R. M., MICKUNAS, E., GAY, R., KLIMANSKAYA, I. & LANZA, R. 2012. Embryonic stem cell trials for macular degeneration: a preliminary report. *The Lancet,* 379, 713-720.

SERRA, M., BRITO, C., COSTA, E., SOUSA, M. & ALVES, P. 2009. Integrating human stem cell expansion and neuronal differentiation in bioreactors. *BMC Biotechnology,* 9, 82.

SHANTILATHA, P. V., S.; MITRA, C. 2003. Designing a simple biosensor. *In:* MALHOTRA, B. T., A. (ed.) *Advances in Biosensors: Perspectives in Biosensors.* Amsterdam, The Netherlands: Elselvier Science B.V.

SHAPIRO, H. 2003. *Practical Flow Cytometry*, John Wiley & Sons.

SHEPPARD, N. F., MIAN, A., KELLOGG, G., KIEFFER-HIGGINS, S. G. & CARVALHO, B. L. 2005. Affinity binding-based system for detecting particulates in a fluid. Google Patents.

SHI, Y., HU, G., SU, J., LI, W., CHEN, Q., SHOU, P., XU, C., CHEN, X., HUANG, Y., ZHU, Z., HUANG, X., HAN, X., XIE, N. & REN, G. 2010. Mesenchymal stem cells: a new strategy for immunosuppression and tissue repair. *Cell Res,* 20, 510-518.

SHIBATA, H., AGEYAMA, N., TANAKA, Y., KISHI, Y., SASAKI, K., NAKAMURA, S., MURAMATSU, S.-I., HAYASHI, S., KITANO, Y., TERAO, K. & HANAZONO, Y. 2006. Improved Safety of Hematopoietic Transplantation with Monkey Embryonic Stem Cells in the Allogeneic Setting. *STEM CELLS,* 24, 1450-1457.

SHUKLA, A. A. E., M. R.; GADAM, S. 2007. *Process Scale Bioseparations for the Biopharmaceutical Industry,* Florida, USA, Taylor & Francis.

SKINDERSOE, M. E., ROHDE, M. & KJAERULFF, S. 2012. A novel and rapid apoptosis assay based on thiol redox status. *Cytometry A,* 81, 430-6.

SLOWIACZEK, P. R. N., R. E.; SCHINDHELM, K.; MILTHORPE, B. 1998. *Cell Separation Device*.

SMIRNOVA, A. H., Y.; ZHANG, L.; RHINE, W. 2009. Synthesis of novel electrode materials using supercritical fluids. *In:* MINTEER, S. (ed.) *Novel Electrode Materials, Issue 21.* New Jersey: The Electrochemical Society.

STOLBERG, S. & MCCLOSKEY, K. E. 2009. Can shear stress direct stem cell fate? *Biotechnol Prog,* 25, 10-9.

SUNLEY, K. & BUTLER, M. 2010. Strategies for the enhancement of recombinant protein production from mammalian cells by growth arrest. *Biotechnol Adv,* 28, 385-94.

TAKEI, S., ICHIKAWA, H., JOHKURA, K., MOGI, A., NO, H., YOSHIE, S., TOMOTSUNE, D. & SASAKI, K. 2009. Bone morphogenetic protein-4 promotes induction of cardiomyocytes from human embryonic stem cells in serum-based embryoid body development. *Am J Physiol Heart Circ Physiol,* 296, H1793-803.

TANG, C., LEE, A. S., VOLKMER, J.-P., SAHOO, D., NAG, D., MOSLEY, A. R., INLAY, M. A., ARDEHALI, R., CHAVEZ, S. L., PERA, R. R., BEHR, B., WU, J. C., WEISSMAN, I. L. & DRUKKER, M. 2011. An antibody against SSEA-5 glycan on human pluripotent stem cells enables removal of teratoma-forming cells. *Nat Biotech,* 29, 829-834.

TERRACCIANO, M. R., I.; DE STEFANO, L. 2013. Optical characterization of aminosilane-modified surface for biosensing. *Journal of the European Optical Society: Rapid publications,* 8, 13075 1-6.

THOMAS, R. J., ANDERSON, D., CHANDRA, A., SMITH, N. M., YOUNG, L. E., WILLIAMS, D. & DENNING, C. 2009. Automated, scalable culture of human embryonic stem cells in feeder-free conditions. *Biotechnol Bioeng,* 102, 1636-44.

THOMSON, J. A., ITSKOVITZ-ELDOR, J., SHAPIRO, S. S., WAKNITZ, M. A., SWIERGIEL, J. J., MARSHALL, V. S. & JONES, J. M. 1998. Embryonic stem cell lines derived from human blastocysts. *Science,* 282, 1145-7.

TIWARI, A., PUNSHON, G., KIDANE, A., HAMILTON, G. & SEIFALIAN, A. M. 2003. Magnetic beads (Dynabead) toxicity to endothelial cells at high bead concentration: implication for tissue engineering of vascular prosthesis. *Cell Biol Toxicol,* 19, 265-72.

TRINH, L. & SHILOACH, J. 1995. Recovery of insect cells using hollow fiber microfiltration. *Biotechnology and Bioengineering,* 48, 401-405.

UCCELLI, A., MORETTA, L. & PISTOIA, V. 2008. Mesenchymal stem cells in health and disease. *Nat Rev Immunol,* 8, 726-736.

ULBRICHT, M., ANSORGE, W., DANIELZIK, I., KÖNIG, M. & SCHUSTER, O. 2009. Fouling in microfiltration of wine: The influence of the membrane polymer on adsorption of polyphenols and polysaccharides. *Separation and Purification Technology,* 68, 335-342.

UTTENTHALER, E., SCHRAML, M., MANDEL, J. & DROST, S. 2001. Ultrasensitive quartz crystal microbalance sensors for detection of M13-Phages in liquids. *Biosens Bioelectron,* 16, 735-43.

VAN KOOTEN, T. G., SCHAKENRAAD, J. M., VAN DER MEI, H. C. & BUSSCHER, H. J. 1992. Development and use of a parallel-plate flow chamber for studying cellular adhesion to solid surfaces. *J Biomed Mater Res,* 26, 725-38.

VAN OSS, C. J. 2006. Adsorption and adhesion in aqueous media, including ligand-receptor interactions. *Interfacial Forces in Aqueous Media, Second Edition.* Taylor & Francis Group.

VANDENBERG, E. T., BERTILSSON, L., LIEDBERG, B., UVDAL, K., ERLANDSSON, R., ELWING, H. & LUNDSTRÖM, I. 1991. Structure of 3-aminopropyl triethoxy silane on silicon oxide. *Journal of Colloid and Interface Science,* 147, 103-118.

VARLEY, J. & BIRCH, J. 1999. Reactor design for large scale suspension animal cell culture. *Cytotechnology,* 29, 177-205.

VELEZ-SUBERBIE, M. L., TARRANT, R. D., TAIT, A. S., SPENCER, D. I. & BRACEWELL, D. G. 2013. Impact of aeration strategy on CHO cell performance during antibody production. *Biotechnol Prog,* 29, 116-26.

VLAHAKIS, N. E. & HUBMAYR, R. D. 2000. *Invited Review: Plasma membrane stress failure in alveolar epithelial cells*.

VOINOVA, M. V., JONSON, M. & KASEMO, B. 2002. 'Missing mass' effect in biosensor's QCM applications. *Biosensors and Bioelectronics,* 17, 835-841.

WAGNER, M. & SIDDIQUI, M. A. 2007a. Signal transduction in early heart development (I): cardiogenic induction and heart tube formation. *Exp Biol Med (Maywood),* 232, 852-65.

WAGNER, M. & SIDDIQUI, M. A. 2007b. Signal transduction in early heart development (II): ventricular chamber specification, trabeculation, and heart valve formation. *Exp Biol Med (Maywood),* 232, 866-80.

WANG, F., LIU, P., NIE, T., WEI, H. & CUI, Z. 2012a. Characterization of a polyamine microsphere and its adsorption for protein. *Int J Mol Sci,* 14, 17-29.

WANG, N., TYTELL, J. D. & INGBER, D. E. 2009. Mechanotransduction at a distance: mechanically coupling the extracellular matrix with the nucleus. *Nat Rev Mol Cell Biol,* 10, 75-82.

WANG, S., ESFAHANI, M., GURKAN, U. A., INCI, F., KURITZKES, D. R. & DEMIRCI, U. 2012b. Efficient on-chip isolation of HIV subtypes. *Lab Chip,* 12, 1508-15.

WANG, X., CHEN, S., KONG, M., WANG, Z., COSTA, K. D., LI, R. A. & SUN, D. 2011. Enhanced cell sorting and manipulation with combined optical tweezer and microfluidic chip technologies. *Lab Chip,* 11, 3656-62.

WARR, S. R. 2014. Microbioreactors and scale-down models: growth of CHO cells using the Pall Micro24 MicroReactor system. *Methods Mol Biol,* 1104, 149-65.

WATERHOUSE, G. I. N., BOWMAKER, G. A. & METSON, J. B. 2001. The thermal decomposition of silver (I, III) oxide: A combined XRD, FT-IR and Raman spectroscopic study. *Physical Chemistry Chemical Physics,* 3, 3838-3845.

WILCHEK, M. & MIRON, T. 1999. Thirty years of affinity chromatography. *Reactive and Functional Polymers,* 41, 263-268.

WILCHEK, M. A. C., I. 2000. An Overview of Affinity Chromatography. *Affinity chromatography: methods and protocols. Methods in molecular biology, vol. 147.* New Jersey: Humana Press.

WILCHEK, M. A. M., T. 1999. Thirty years of affinity chromatography. *Reactive and Functional Polymers*, 41, 263-268.

WILLIAMS, E. H., DAVYDOV, A. V., MOTAYED, A., SUNDARESAN, S. G., BOCCHINI, P., RICHTER, L. J., STAN, G., STEFFENS, K., ZANGMEISTER, R., SCHREIFELS, J. A. & RAO, M. V. 2012. Immobilization of streptavidin on 4H–SiC for biosensor development. *Applied Surface Science,* 258, 6056-6063.

WILLOUGHBY, N. 2009. Too big to bind? Will the purification of large and complex therapeutic targets spell the beginning of the end for column chromatography? *Journal of Chemical Technology & Biotechnology,* 84, 145-150.

WOLFE, R. P. & AHSAN, T. 2013. Shear stress during early embryonic stem cell differentiation promotes hematopoietic and endothelial phenotypes. *Biotechnol Bioeng,* 110, 1231-42.

WOLFE, R. P., LELEUX, J., NEREM, R. M. & AHSAN, T. 2012. Effects of shear stress on germ lineage specification of embryonic stem cells. *Integrative Biology,* 4, 1263-1273.

WONG, S. S. Y. & BERNSTEIN, H. S. 2010. Cardiac regeneration using human embryonic stem cells: producing cells for future therapy. *Regenerative Medicine,* 5, 763-775.

XIA, Z., GOLDSMITH, H. L. & VAN DE VEN, T. G. 1994. Flow-induced detachment of red blood cells adhering to surfaces by specific antigen-antibody bonds. *Biophys J,* 66, 1222-30.

YAMAMOTO, K., SOKABE, T., WATABE, T., MIYAZONO, K., YAMASHITA, J. K., OBI, S., OHURA, N., MATSUSHITA, A., KAMIYA, A. & ANDO, J. 2005. Fluid shear stress induces differentiation of Flk-1-positive embryonic stem cells into vascular endothelial cells in vitro. *Am J Physiol Heart Circ Physiol,* 288, H1915-24.

YAMANAKA, S. & TAKAHASHI, K. 2011. Oct3/4, Klf4, c-Myc and Sox2 produce induced pluripotent stem cells. Google Patents.

YING, Z., JIANG, Y., DU, X., XIE, G., YU, J. & TAI, H. 2008. Polymer coated sensor array based on quartz crystal microbalance for chemical agent analysis. *European Polymer Journal,* 44, 1157-1164.

YOSHIMITSU, Z., NAKAJIMA, A., WATANABE, T. & HASHIMOTO, K. 2002. Effects of Surface Structure on the Hydrophobicity and Sliding Behavior of Water Droplets. *Langmuir,* 18, 5818-5822.

YOSHIOKA, M., MUKAI, Y., MATSUI, T., UDAGAWA, A. & FUNAKUBO, H. 1991. Immobilization of ultra-thin layer of monoclonal antibody on glass surface. *J Chromatogr,* 566, 361-8.

YOUNG, M. E., CARROAD, P. A. & BELL, R. L. 1980. Estimation of diffusion coefficients of proteins. *Biotechnology and Bioengineering,* 22, 947-955.

ZAIDEL-BAR, R., ITZKOVITZ, S., MA'AYAN, A., IYENGAR, R. & GEIGER, B. 2007. Functional atlas of the integrin adhesome. *Nat Cell Biol,* 9, 858-67.

ZANDSTRA, P. W., BAUWENS, C., YIN, T., LIU, Q., SCHILLER, H., ZWEIGERDT, R., PASUMARTHI, K. B. & FIELD, L. J. 2003. Scalable production of embryonic stem cell-derived cardiomyocytes. *Tissue Eng,* 9, 767-78.

ZBOROWSKI, M. C., J. J. 2008. *Magnetic Cell Separation,* Oxford, UK, Elsevier.

ZHANG, F., SAUTTER, K., LARSEN, A. M., FINDLEY, D. A., DAVIS, R. C., SAMHA, H. & LINFORD, M. R. 2010. Chemical vapor deposition of three aminosilanes on silicon dioxide: surface characterization, stability, effects of silane concentration, and cyanine dye adsorption. *Langmuir,* 26, 14648-54.

ZORO, B. J., OWEN, S., DRAKE, R. A. & HOARE, M. 2008. The impact of process stress on suspended anchorage-dependent mammalian cells as an indicator of likely challenges for regenerative medicines. *Biotechnol Bioeng,* 99, 468-74.